NASA Contractor Report 4387

Orbital Transfer Vehicle
Engine Technology

*Baffled Injector Design,
Fabrication and Verification*

J. A. Schneider

NASA

NASA Contractor Report 4387

Orbital Transfer Vehicle Engine Technology

Baffled Injector Design, Fabrication and Verification

J. A. Schneider
GENCORP
Aerojet Propulsion Division
Sacramento, California

NASA

National Aeronautics and
Space Administration

Office of Management

Scientific and Technical
Information Program

1991

Page intentionally left blank

FOREWORD

This document represents the final report to the National Aeronautics and Space Administration for work performed under Task Order C.4 to Contract NAS 3-23772. The task work span was from May 1988 to June 1989.

This is a summary report in that all material discussed herein was presented to NASA program personnel at oral presentations or in the contractually required monthly reports submitted while the work was in progress.

The author wishes to acknowledge the contributions of the following:

Mike Murphy   —   Materials & Processes
Section 1.0 Baffle Fabrication Study
Section 3.4 Injector Fabrication Study

Rob Simin   —   Producibility Engineer
Section 2.0 Channel Machining Study
Section 3.4 Injector Fabrication Study

Karen Niiya   —   Performance Analyst
Section 3.0 Injector Studies

TABLE OF CONTENTS

iv

LIST OF TABLES

LIST OF FIGURES

LIST OF FIGURES (cont.)

I.   INTRODUCTION

A.   BACKGROUND

New technologies for space-based, reusable, throttleable, cryogenic orbit transfer propulsion are being evaluated under NASA Contract NAS3-23772. The supporting tasks for the design of a dual-expander cycle engine thrust chamber design are documented in this report. This supports the NASA-OAST plans for development of a new Orbit Transfer Vehicle (OTV) to be operational in the late 1990s. Critical to the economical operation of a space based OTV is a new H_2/O_2 rocket engine with capabilities superior to available engines. Table I summarizes the available engine characteristics and those required of a new engine. In total, these requirements represent a substantial advance in the state-of-the-art technologies and a considerable challenge to rocket engine designers. In support of this effort Aerojet TechSystems has selected a unique engine cycle and thrust chamber configuration in response to these requirements.

OTV engine studies have identified a dual-propellant expander cycle as offering advantages over either staged combustion or gas generator cycles. In a conventional expander cycle engine, hydrogen is routed through passages in the combustion chamber wall where it both cools the wall and acquires sufficient thermal energy to power the turbine drives of pumps for both the hydrogen and oxygen flow circuits. It is then routed to the injector for combustion. This cycle is fairly simple and offers good performance potential. Since all propellant is burned in the combustion chamber it does not have the losses of open cycles. The limitations of the conventional expander cycle engine are related to dependence on only one working fluid for turbine drive energy. To supply the energy for the high turbopump and engine chamber pressures required, the hydrogen must exit the regeneratively-cooled chamber at temperatures near the design limits for the chamber liner.

A marked improvement in engine operating flexibility and high chamber pressure capability is available if oxygen can be used as a working fluid driving the turbine on the oxidizer circuit Turbine Pump Assembly (TPA). This reduces the demands on the hydrogen circuit and allows the TPAs to be designed without inter

1

TABLE I

TECHNOLOGY GOALS FOR THE NEW OTV ENGINE

Parameters	Reference Engine System Characteristics	October 1986 NASA Goals and/or Requirements	1988 Updated Goals or Requirements
Basing	Earth	Not Specified	Space
Human-rating	No	Not Specified	Yes
Safety Criteria	Not Specified	Not Specified	Fail Operational, Fail Safe
Propellants – Fuel	Hydrogen	Hydrogen	Hydrogen
– Oxidizer	Oxygen	Oxygen	Oxygen
Vacuum Thrust (Design Point)	15,000 lbF	10,000 - 25,000 lbF*	7500 lbF (per engine)
Number of Engines per Vehicle	Not Specified	Not Specified	2 Minimum
Engine Mixture Ratio, O/F (Design Point)	5.0	6.0	6.0
Engine Mixture Ratio Range, O/F (Design Point)	4.4 to 5.6	5 - 7	5 - 7
Propellant Inlet Temperature - Hydrogen	38.3°R	37.8°R	37.8°
Oxygen	175.3°R	162.7°R	162.7°R
Gimbal	±4.0 Degrees	±6.0 Degrees (Sq. Pattern)	±20 degrees Pitch & Yaw
Aerobraking Design Criteria	The engine must be compatible with aeroassist return of the vehicle to low-earth-orbit.		
Vacuum Specific Impulse	444 lbF-sec/lbm	520 lbF-sec/lbm	490 lbF-sec/lbm
Vacuum Thrust Throttling Ratio	No Throttling	30:1	10:1
Net Positive Suction Head (NPSH) - Hydrogen	133.0 ft-lbf/lbm	0	15 ft-lbf/lbm
Oxygen	16.7 ft-lbf/lbm	0	2 ft-lbf/lbm
Weight	290 lbm	360 lbm	360 lbm (2 engines)
Length	70.1 in.	40	TBD (Assume 60", Stowed)
Reliability (90% Confidence Level)	0.9982	1.0	.9975 Single engine, .99958 Dual engine**
Operational Life	3 Starts, 4000 sec	500 Starts, 20 Hours	500 Starts, 20 Hours
Service Free-Life		100 Starts, 4 Hours	100 Starts, 4 Hours
Start Cycle		Chilldown with propulsive dumping of propellants, tankhead start, pumped idle operation, autogenous tank pressurization required	

Updated 4 January 1989

---

*Vehicle engine set total thrust must be in this range

**MSFC/Boeing vehicle studies

propellant seals or mechanical gear train connections. Operation at high chamber pressure is enhanced due to the increase in thermal energy available to drive the turbopumps.

This engine cycle proposed by Aerojet for the OTV engine, illustrated in Figure 1 is called the dual-propellant expander cycle. This engine cycle is fairly simple, plumbing is straightforward, and the cycle offers excellent performance potential. Gasification of both propellents provides a convenient source of tank pressurant and allows gas-gas injector elements to be used. Gas-gas injection is desirable in that it enables full range throttling with a single injector without resulting in significant performance or stability degradation.

The purpose of the studies documented in this report was to research the materials used in the thrust chamber design, the supporting fabrication methods necessary to complete the design, and the modification of the injector element for optimium injector/chamber compatibility.

B.   BASELINE DESIGN, 7.5K THRUST LEVEL TCA

The 7.5K thrust level TCA was based on the demonstrated design of the 3K thrust level TCA. The primary difference between the two designs is within the combustion chamber. The 3K chamber contains an oxygen cooled centerbody structure housing the oxygen TPA encircled by an annular injector. For maintainability, reliability, and scaleability, the oxygen TPA was removed from within the combustion chamber. To maintain enthalpy gain by the hydrogen without increasing the chamber length, hydrogen cooled baffles were designed with a segmented injector pattern.

The baseline chamber for the 7.5K TCA design was a single pass regenerative design to be made from NASA-Z Copper with conventionally milled coolant channels. A high strength electroformed NiCo alloy forms the channel backside closeout. The nominal L' (injector face to throat) length is 9.8 inches with a contraction ratio of 25:1. An oxygen cooled tube bundle nozzle extension is attached at an area ratio of 28:1. This concept is shown in Figure 2.
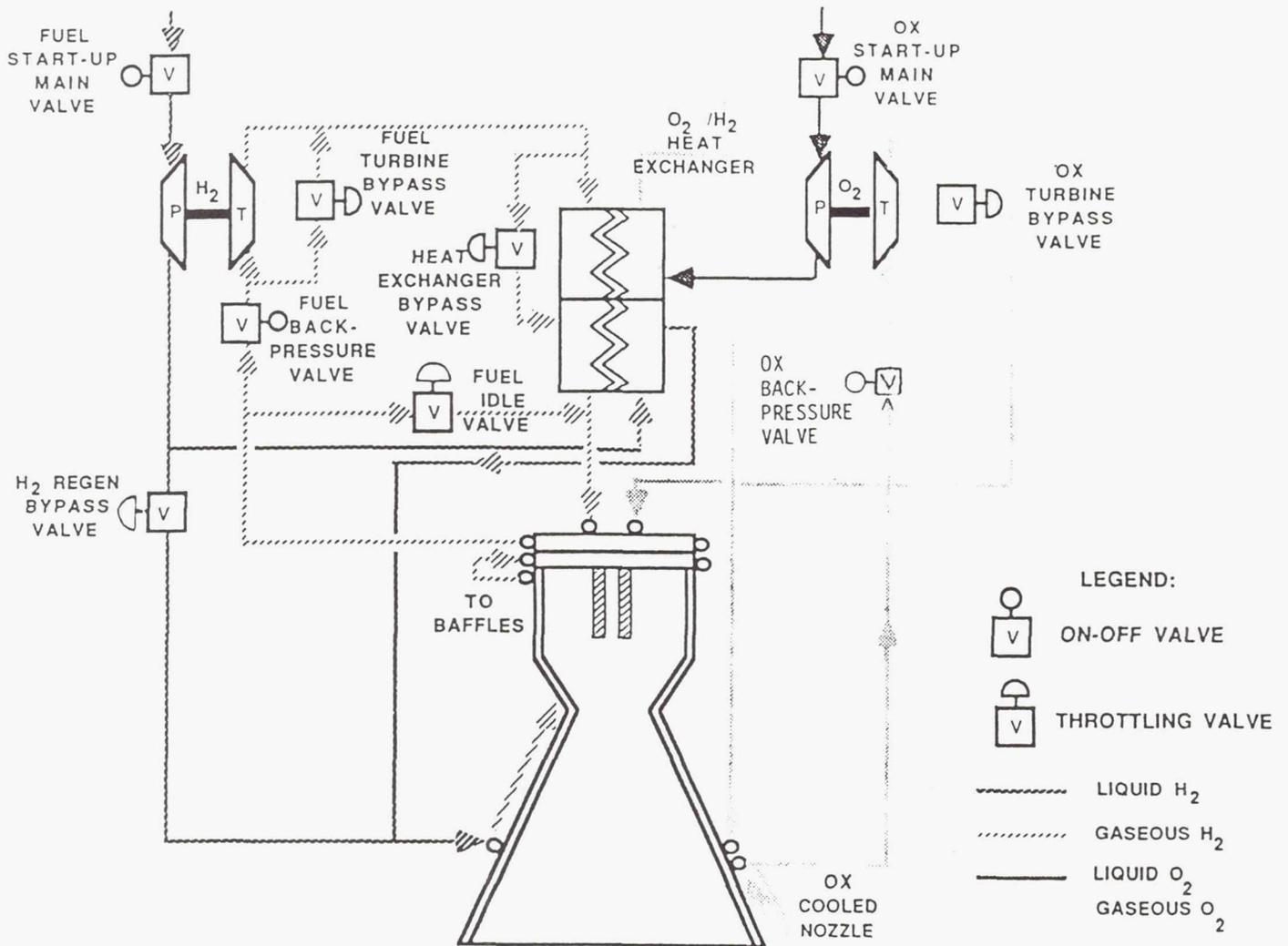
Figure 1. 7.5K Thrust Level OTV Engine Schematic

The schematic includes the following labeled components:

- FUEL START-UP MAIN VALVE
- OX START-UP MAIN VALVE
- FUEL TURBINE BYPASS VALVE
- O_2/H_2 HEAT EXCHANGER
- OX TURBINE BYPASS VALVE
- HEAT EXCHANGER BYPASS VALVE
- FUEL BACK-PRESSURE VALVE
- FUEL IDLE VALVE
- OX BACK-PRESSURE VALVE
- H_2 REGEN BYPASS VALVE
- TO BAFFLES
- OX COOLED NOZZLE
- H_2
- O_2
- P / T

LEGEND:
- ON-OFF VALVE
- THROTTLING VALVE
- LIQUID H_2
- GASEOUS H_2
- LIQUID O_2
- GASEOUS O_2

Component Packaging Envelope

37.9"

Engine/Vehicle Interface Plane

4"

10"

10"

$\varepsilon = 28$

Oxygen Regen Cooled

Hydrogen Inlet Manifold
Oxygen Inlet Manifold

39.0"

$\varepsilon = 300$ Oxygen Outlet Manifold
(Pass and 1/2)

1"

121.8"

Gas Seal = 1" Width
$\varepsilon = 623$ Extendible Dia = 37.9"

91.8"

49.3"

Radiation Cooled

$D_{Barrel} = 7.6"$
$D_{Throat} = 1.5"$

$\varepsilon = 1430$
Exit Dia = 57.6"

Scale 20:1

100% Bell Nozzle

Updated 4 Jan 1987

Figure 2. OTV 7.5K TCA Engine

5

I, B, Baseline Design, 7.5K Thrust Level TCA (cont.)

Sizing of the coolant channels is based on demonstrated fabrication capability with copper chamber liners. The minimum channel and land widths have been demonstrated to be 0.01" wide with aspect ratios (depth to width) up to a maximum of 10:1 using NASA-Z copper. (Reference 12)

C. SCOPE OF WORK ·

The work performed on Task C.4 focused on the identified material technologies required to complete the preliminary design task for the 7.5K thrust level TCA. Material selection and fabrication technique demonstration for the major TCA components were required to be verified prior to the final design of the TCA. These components include the hydrogen-cooled baffles, regeneratively-cooled combustion chamber, and injector. This will result in verification of the proposed fabrication methods for final design of the TCA. By utilizing improved materials for the TCA the potential for increased chamber cycle life and weight reductions are obtainable.

Baffles - Construction of the hydrogen cooled baffles takes advantage of Aerojet's platelet technology. To maximize the enthalpy gain by hydrogen cooling the baffles, materials with high thermal conductivity properties are required. In addition, use of high pressure hydrogen necessitates use of increased material strength. Diffusion bonding of the copper alloys can sometimes result in degradation of the base material properties due to (1) the presence of a diffusion aid or (2) the bonding temperatures and resulting effects of alloy element precipitation and grain growth. Development work on diffusion bonding of ZrCu has as its goal, to produce a diffusion bonded part with base material properties.

Past work on diffusion bonding of ZrCu has evaluated use of the solid phase aids: copper, gold, silver, and nickel (Reference 3). Based on preliminary visual evaluations, use of nickel and silver was pursued. Nickel aided bonds were theorized to produce parts with tensile strength approaching that of the base material but with a decrease in thermal conductivity. Silver aided bonds were theorized to produce parts with thermal conductivity properties approaching that of the parent material but with a decrease in tensile strength. Hence the design

6

philosophy has been to use nickel aid in designs where strength was the driver and silver in designs where thermal conductivity was the driver.

Improvements in the diffusion bonding process modified the bonding parameters in an effort to preclude void formation within the joints which is theorized to reduce the tensile strength properties. These improvements have eliminated the voids yielding silver aided bond stacks with recently documented mechanical properties approaching those of the parent material. This has demonstrated silver aided diffusion bonded ZrCu to be a viable fabrication method for the hydrogen cooled baffles where both strength and thermal conductivity are design drivers. In addition, Aerojet's analytical predictions for thermal conductivity of diffusion bonded parts has been validated with measured properties.

Regeneratively-Cooled Chamber - Design requirements for the regeneratively-cooled chamber are based on engine goals of a 100 start, 4 hour service free operational life. For lower thrust engines, this was achieved by utilization of the "mini" channel technology to maximize heat input to the hydrogen while minimizing the thermally induced stress in the chamber. At higher thrust levels, stronger materials are required to realize increased chamber life.

Utilization of GlidCop, pure copper dispersion strengthened by fine particles of alumina, is being pursued. Analysis of the relationship between the elevated-temperature mechanical-properties of copper alloys and their performance in test combustion chambers suggests that GlidCop may out perform the current state-of-the-art, high conductivity copper alloys by a significant margin.

Use of a new material for the combustion chamber relies on demonstration of the adaptability of the material to the fabrication methods imposed by the design. Use of GlidCop for the "mini" channel design was validated by establishment of the required machining parameters to successfully reproduce the channel geometry of the 7.5K TCA throat region.

Injector Element - Increased reliability of the injector can be obtained by examination of the performance and design issues. The 7.5K TCA injector design is based on the element used for the 3K injector design. Expansion of the existing data

base was undertaken for the "I"triplet premix element to improve the thermal environment for the chamber and gas-side baffle wall. Examination of the 3K injector by a post test, flow coefficient (Kw) check verified no anomalies which may have resulted in the increased heat flux levels noted during hot fire tests.

This element was selected for the OTV engine due to its very high (approximately 100%) Energy Release Efficiency (ERE) in a very short (<8") chamber length. The chamber was designed for average heat flux levels of 10 BTU/in ^{2} sec. Higher than anticipated heat flux levels were noted during hot fire testing of the 3K injector. Earlier studies of this element had indicated that the element could be modified to lower the heat flux levels without seriously compromising the performance. The purpose of this study was to see if slight modifications to the fuel flow cross-section of an "I" triplet premix element would enhance the wall compatibility by providing fuel-rich regions around the periphery of the spray fan. The results of the splash test and milkmaid tests documented herein prove that this program was successful. The baffle element and center element modifications both gave increased fuel-rich regions along with increased mixing efficiencies due to the more uniform mixture ratios in the spray fan. These element modifications are also beneficial since the effective flow area (CdA) of the modified elements are within 15% of the baseline element CdA and therefore will receive about the same flow per element when incorporated into a full scale injector

The modifications documented in this report form the basis for the design of the new injector where customizing of the element will be undertaken according to its location to improve the thermal environment for the hydrogen-cooled chamber and gas-side baffle walls.

Injector Fabrication and Material Selection - Weight reductions are obtainable through use of higher strength materials. Initially, the 3K injector manifolds and face platelets were made from nickel. Nickel is easy to machine and diffusion bonding parameters have been established. Use of higher-strength super-alloys are of interest. Aerojet has had recent success in diffusion bonding nickel base superalloys. Selection of materials for the injector manifolds and face platelets is based on compatibility with the propellants and the ability to join the materials to

I, C, Scope of Work (cont.)

form the injector. A survey was made of the compatible materials for use in a hydrogen/ oxygen system. Adaptability of these to diffusion bonding of the face plate material was evaluated. Ability to diffusion bond was based on Aerojet demonstration in either the same or similar materials. For lighter weight engines, use of a zirconium copper face plate would best accommodate Inconel 718 oxygen manifolds and Incoloy 909 hydrogen manifolds. These materials offer the highest strength to density ratios for compatible materials.

Significant cost savings for fabrication of the injector faceplate was realized by laser cutting of element features. Tolerances equivalent to those achieved by chemical milling were achieved. Simple, acceptable methods of dross removal were demonstrated.

1.0 BAFFLE FABRICATION STUDY

1.1 BAFFLE DESIGN

A 7.5K or higher thrust level OTV engine will utilize a hydrogen cooled baffled injector. The baffles serve a dual purpose by providing a heat transfer surface for the heating of the hydrogen in addition to ensuring stable injector operation. Construction of the baffles will utilize Aerojet's platelet technology. To finalize the design of this component, the mechanical properties of the diffusion bonded structure need to be documented. Utilization of the diffusion bonded fabrication technique enables construction of a homogeneous parent material structure with integral cooling passages. This process is desirable because the mechanical properties of the diffusion bonded joint theoretically approach those of the parent material, unlike the degradation of ZrCu caused by traditional fabrication methods of welding or brazing.

The baffle assemblies are to be fabricated from ZrCu platelets diffusion bonded together. Each baffle is a separate integral assembly as shown in Figure 1.1-1. Hydrogen passages are chemically etched in the ZrCu platelets prior to diffusion bonding. The baffle plates are cooled with hydrogen which flows down one side, across the radius bottom, and back up the opposite side. The two opposing ends of the baffles are cooled in a similar manner. Common manifolding in the baffle plate feeds the inlets to the side and end passages (Figure 1.1-2). Exiting hydrogen is collected in a separate common manifold adjacent to the inlet. External lines are connected to these manifolds for further routing of the fuel.

1.2 TASK OBJECTIVE

The work under this task included documenting the tensile strength and thermal conductivity of the diffusion bonded stacks. Theoretical values for thermal conductivity had been determined from the diffusion aid thickness and resulting alloying of the aid into the parent material. This task was to correlate actual values with the predicted thermal conductivity properties and documented the resulting effect on the tensile strength through tensile testing.

Early Aerojet research (Reference 3) had identified use of a nickel aid as a reliable, reproducible method of achieving a leak free diffusion bonded part. On-

Baffles

Injector Face

H₂ Inlet

H₂ Exit
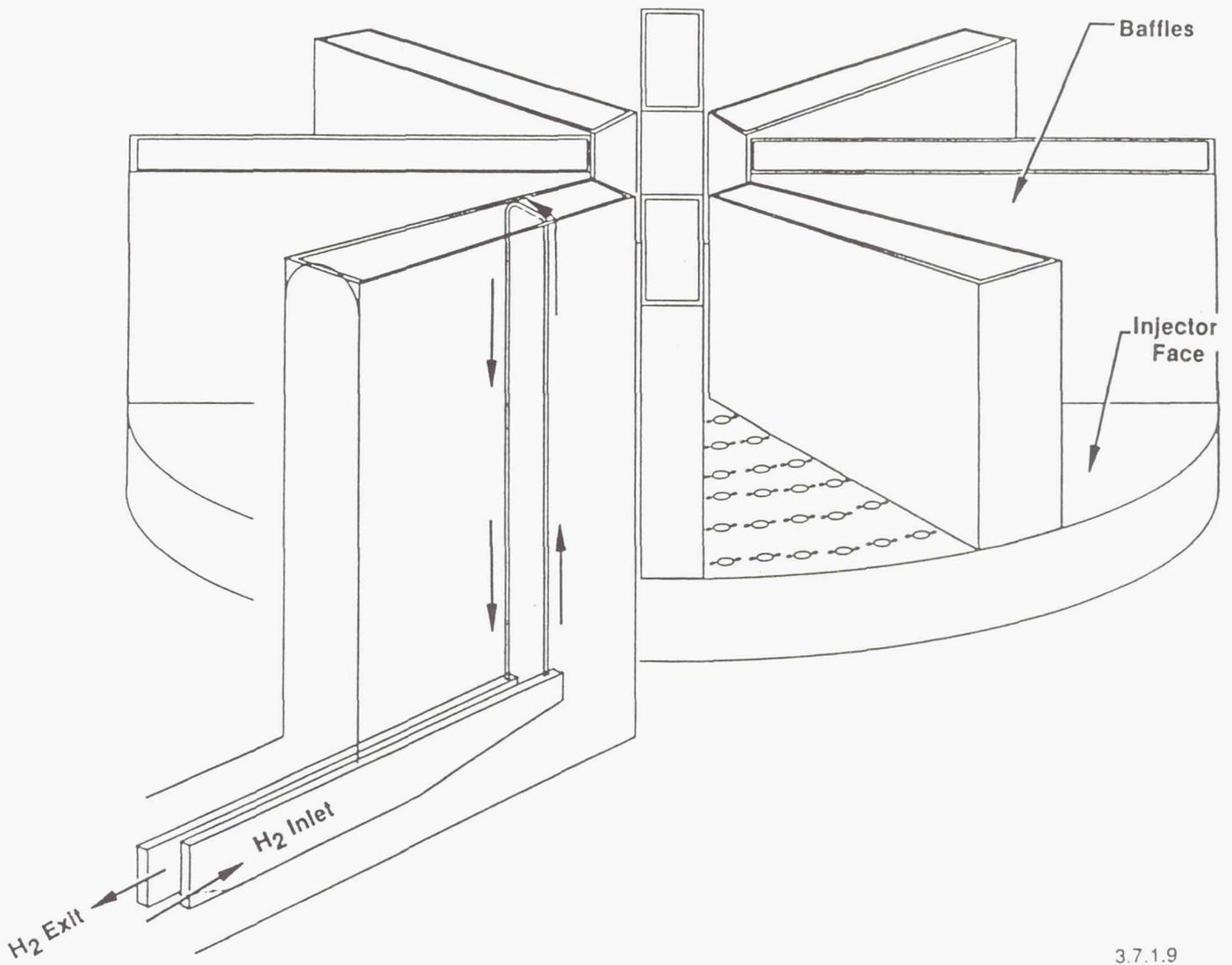
Figure 1.1-1. Baffle Assembly

Fuel Inlet Manifold

Fuel Exit Manifold

Top View

0.5"
0.375"
0.125"

Fuel Inlet

Fuel Exit

Baffle Feed Manifold

3.25"

Side View
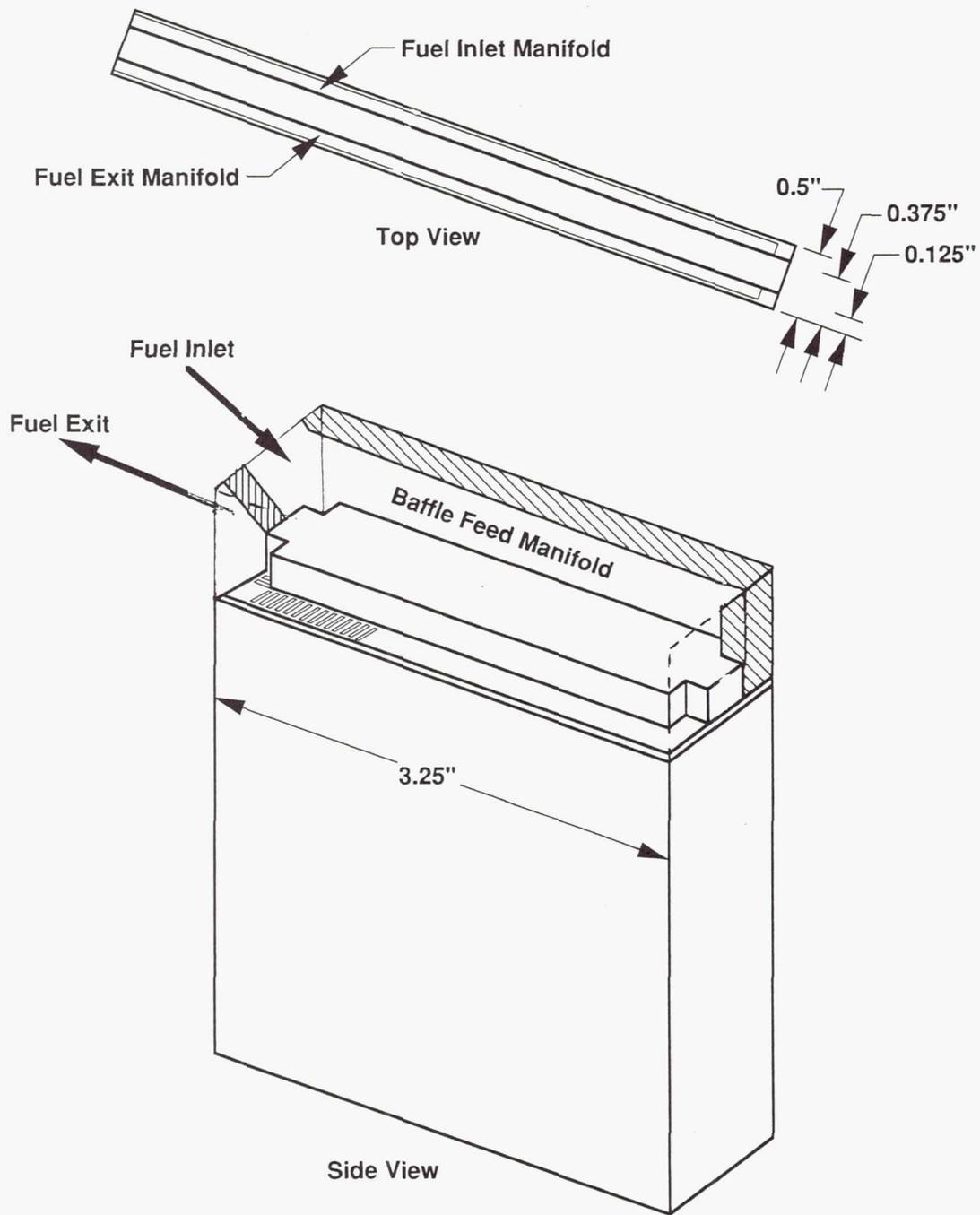
Figure 1.1-2. Baffle Manifolding Details

1.2, Task Objective (cont.)

going diffusion bond investigation at Aerojet for the SSME HEX program, has demonstrated success with a modified diffusion bond process for ZrCu using silver as a bond aid.

1.3 FABRICATION TECHNIQUES

1.3.1 Diffusion Bonding History

1.3.1.1 Background - Previous Aerojet Studies

Zirconium copper (ZrCu) is normally chosen for combustion chamber and heat exchanger applications where high heat flux conditions are encountered because of its combination of good mechanical properties and high thermal conductivity. Past brazing experience with ZrCu has shown the necessity of plating the ZrCu surface to prevent formation of zirconium oxide which inhibits braze alloy wetting. Thus, all diffusion bonding development of ZrCu has utilized some type of bonding aid to control oxide formation.

The bonding aids themselves may form an oxide film, such as NiO or AG_2O, but these oxide films are unstable and will disassociate during the heat-up phase of the bonding cycle. A completely oxidation resistant bonding aid such as gold, does not appear to offer a measurable advantage over less oxidation resistant aids as long as no stable zirconium oxides are formed.

Aids used in diffusion bonding fall into two general categories: 1) liquid phase aids which melt and flow to help break up oxides and bridge small joint gaps; and 2) solid phase aids which remain solid at bonding temperatures and serve to isolate the oxidation prone substrata alloying elements from the bonding environment.

The selection of a solid state vs a liquid state bonding aid is not a straight forward decision. A liquid phase may be necessary where perfect intimate

contact cannot be achieved in 100% of the joint, such as in cases where non-columnar loading configurations prevent adequate pressure on some areas of the bond. The liquid phase aid can the "bridge" small gaps in the joint, allowing diffusion to proceed. Also, a liquid phase may prove to be more effective in breaking up a tenaceous oxide film on the substrate. On the other hand, particular care must be taken to preclude the possibility of the liquid phase from flowing into undesirable areas, such as small channels, where plugging can occur. The solid state aid will obviously stay in the desired locations, but must be accompanied by perfect physical contact between bond faying surfaces in order to achieve a sound bond. As a rule, the solid state bonding aids are preferred unless shown to be unsatisfactory in a given application because of poor physical joint contact or extremely tenaceous oxide films between the aid and the substrate.

The selection of a solid vs liquid phase aid will have some affect on bonding parameters. Typically, lower bonding pressures are desired with liquid phase aids. Bonding time is most influenced by temperature, not aid composition. A liquid phase bonding aid does not necessarily dictate a higher bonding temperature, depending on the specific aid used. For instance, silver will be a liquid phase aid above 1761°F on stainless steel, but nickel will be a solid state aid well above this temperature. The choice of bonding aid in this case is not driven by a desired bonding temperature, but rather the requirement of the liquid phase itself.

Diffusion bonding ZrCu using liquid phase bonding aides has produced parts with relatively good bond quality. However, rejection rates were noted due to excessive porosity in the bond. Based on less observed random porosity with solid phase aids, all follow on work targeted the solid phase aids.

An investigation was undertaken in 1987 in support of Aerojet work for the National Aerospace Plane (NASP) program (Reference 3). This investigation evaluated the use of solid phase aids to further improve bond quality. The aids were chosen based on metallurgical compatibility with copper, oxidation resistance (or low oxide thermal stability), and minimal impact on the thermal conductivity of the copper alloy. The final set of selected diffusion bond aids included copper, silver, and gold.

1.3, Fabrication Techniques (cont.)

Copper was considered for both metallurgical and thermal com-
patibility with the ZrCu substrata. Although copper is subject to oxidation, its oxides
have low thermal stability and dissassociates on heating. This enables the copper to
act as an oxygen barrier.

Silver was considered based on its solubility in copper at low
concentrations and at the temperatures experienced during bonding. Since silver is
oxidation resistant, it should provide a good oxidizer barrier for the ZrCu.

Gold was considered for the same reasons as silver and had the
potential for being better metallurgically compatible with copper since gold is
soluable at all concentrations.

With the selection of any of the above aids, the effects of alloying
on the thermal conductivity properties of copper need to be experimentally
quantified.

Bonding temperatures represent the spread of practical tempera-
tures. The upper limit was defined by the lower limit solution heat treatment tem-
perature of ZrCu (1650 deg F). The lower limit was determined empirically from
earlier work (Reference 13) that observed poor diffusion bond quality when bonded
at less than 60% of the melting point of the bonded species. For ZrCu, the melting
point is 1981 deg F defining a lower limit of 1188 deg F for bonding. A midpoint
temperature of 1425 deg F was also evaluated. Bonding pressures were selected
based on anticipated deformation of the ZrCu platelet structure.

1.3.1.2 Metallographic Evaluation of Background Experiments

The results of the diffusion bonding experiments for the NASP
program (Reference 3) were evaluated using visual metallographic techniques. The
experiments utilized 0.020" thick ZrCu (0.015% Zr) sheets. After cleaning and
plating, the sheets were sheared into 2" x 2" coupons. Bonding stacks consisted of
approximately 10 coupons of each diffusion aid. Stop-off coated stainless steel plates
separated the different diffusion aided groups as represented by Figure 1.3.1-1. This
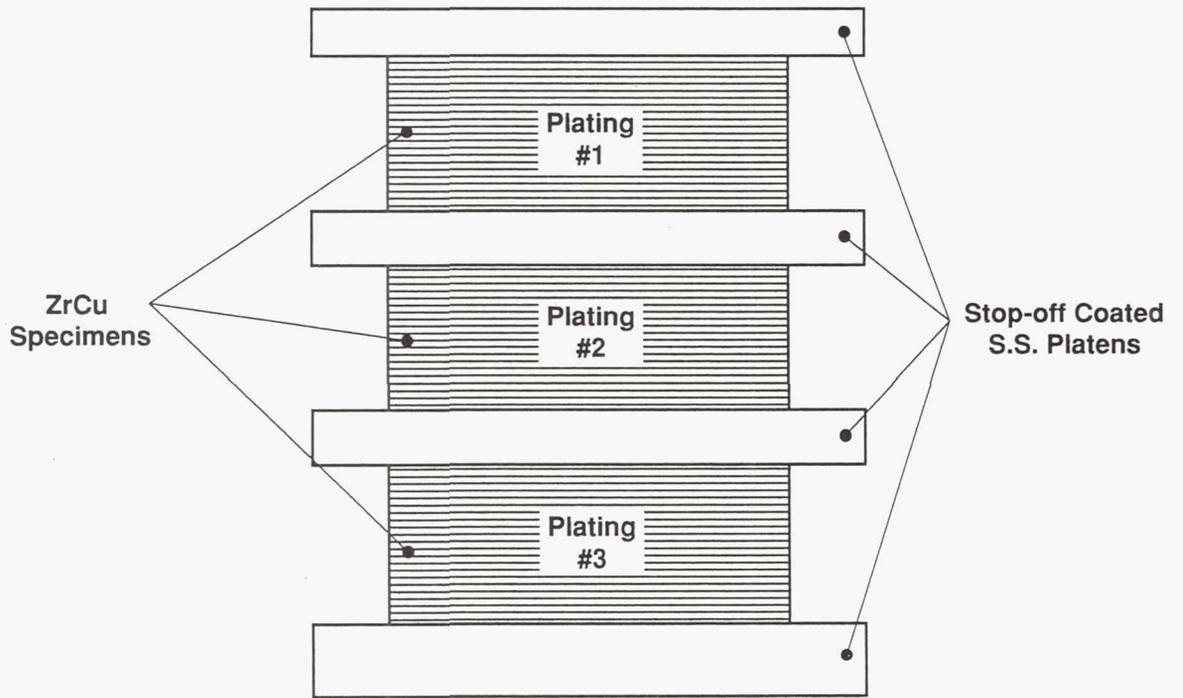
Figure 1.3.1-1 ZrCu Bonding Stock Configuration

1.10.1.11

configuration cancelled out any variables due to nonuniform loading or variance in furnace parameters. All diffusion aided stacks were subjected to the same load and the same furnace run.

The coupons were visually evaluated by Scanning Electron Microscope (SEM). After documentation of the bond joints, each coupon was subjected to bend tests at room temperature. Results of this evaluation follows.

Maintaining parent material properties after diffusion bonding is desirable. Some degradation in tensile strength is anticipated due to the heat cycle in the bonding furnace. Some degradation of thermal conductivity is expected with the use of bonding aids. Preliminary inspection of the data ruled out the 1650 deg F bonding temperature because of the resulting copper grain growth as shown in Figures 1.3.1-2 thru -4 for each of the bond aids. Excessive grain growth usually results in degradation of the tensile strength of the bonded stack.

Evaluation of the bond joints made at the other two temperatures showed different degrees of diffusion of the aid into the base metal. The variation in void formation at the joint was evaluated for each of the diffusion aids.

The copper aided bonds in Figures 1.3.1-5 thru - 7 show distinct bond lines with no grain growth across the joints. This suggests that there may be a layer of oxide particles at the joint which could have a detrimental affect on bond strength.

The silver aided bonds are shown in Figures 1.3.1-8 thru - 10. The extent of silver diffusion into the copper substrata is shown by the less effective etching adjacent to the bonds. The bonds made at 1200 deg F show a significant amount of residual silver at the joints. This was felt to possibly be a desirable effect since minimal diffusion should result in less degradation of the thermal conductivity of the joint. This reduction in thermal conductivity is assumed since solid solution alloys have lower conductivities than the pure form of either alloying species. The degree of diffusion of the bonding aid into the base material is expected to increase
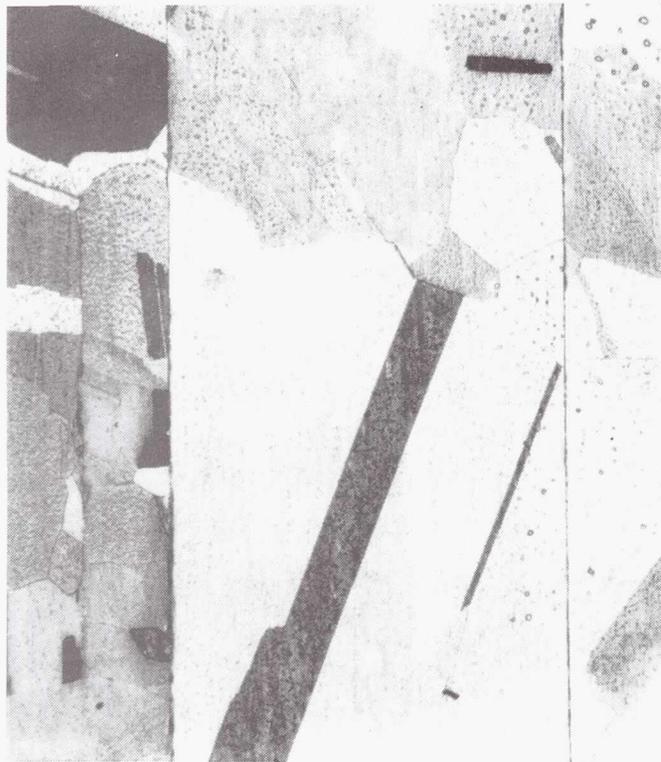
Figure 1.3.1-2. Zirconium Copper Diffusion Bonded With Copper Aid at 1650°F With Low Bonding Loads
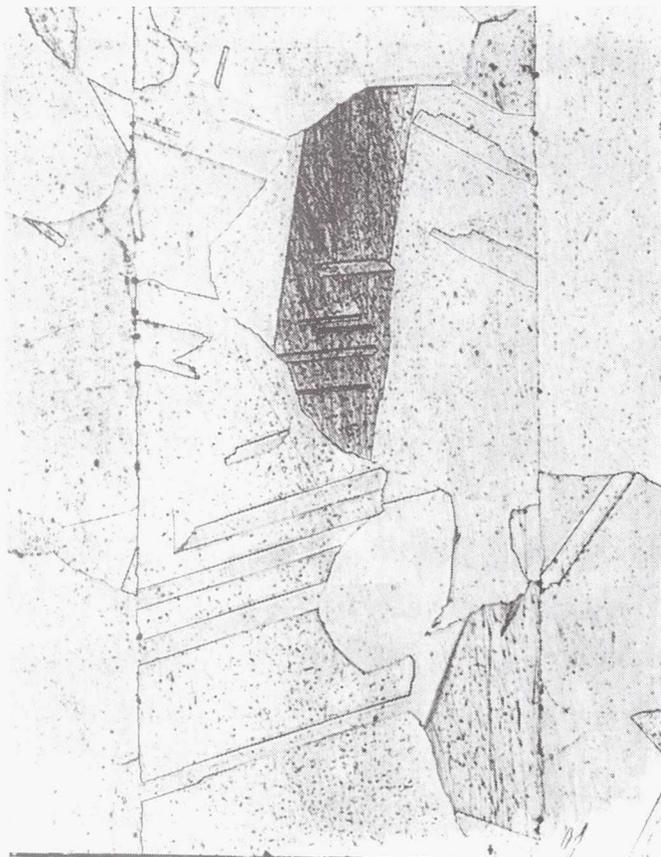
Figure 1.3.1-3. Zirconium Copper Diffusion Bonded With Silver Aid at 1650°F With Low Bonding Loads

18

Figure 1.3.1-4. Zirconium Copper Diffusion Bonded With Gold Aid at 1650°F With Low Bonding Loads

Figure 1.3.1-5. Zirconium Copper Diffusion Bonded With Copper Aid at 1200°F With Higher Bonding Loads

Figure 1.3.1-6. Zirconium Copper Diffusion Bonded With Copper Aid at 1425°F With Low Bonding Loads

Figure 1.3.1-7. Zirconium Copper Diffusion Bonded With Copper Aid at 1425°F With Higher Bonding Loads

20

Figure 1.3.1-8. Zirconium Copper Diffusion Bonded With Silver at 1200°F With Higher Bonding Loads

Figure 1.3.1-9. Zirconium Copper Diffusion Bonded With Silver Aid at 1425°F With Low Bonding Loads

21

Figure 1.3.1-10. Zirconium Copper Diffusion Bonded With Silver Aid at 1425°F
With Higher Bonding Loads

22

1.3, Fabrication Techniques (cont.)

with temperature. The 1425 deg F bonds show this wider silver diffusion zone. Bond quality appears good even though there is a visible bond line with a few point defects.

The gold aided bonds are shown in Figures 1.3.1-11 thru - 13. As in the silver aided bonds, gold diffusion into the copper substrata has improved the copper's corrosion resistance adjacent to the bonds. The 1200 deg F bond shows what appears to be an interlayer between copper platelets. This interlayer represents the gold diffusion layer. Some preferential grain boundary diffusion is noted near the bonds.

1.3.1.3   Diffusion Bonding Summary of Background Experiments

Bond quality of the specimens discussed in Section 1.3.1.2 was determined solely by visual metallurgical examination, and therefore remains subjective. This study was the first step taken to identify viable bonding aid candidates. Additional work, including that undertaken on the OTV task C.4, resulted in quantitatively documenting the resulting mechanical properties. This work, funded under the OTV task, is discussed in Section 1.3.2.

Based on the visual observations of the early work, the effectiveness of copper as a bonding aid was suspect. Very distinct bond lines, representing numerous fine defects along a continuous bond line grain boundary, were observed.

Silver and gold visually appeared to be effective as bonding aids. No significant bond voids were noted, and the interdiffusion of copper/silver and copper/gold might yield improved bond strength. However, the concern remained that the effects of this interdiffusion might degradate the thermal conductivity properties of the bonded joint.

Silver and gold appear to improve the corrosion/oxidation resistance of copper as was shown by resistance to etching in the diffusion zone of the bonds. This may be critical in preventing oxidation on the oxygen side of hot
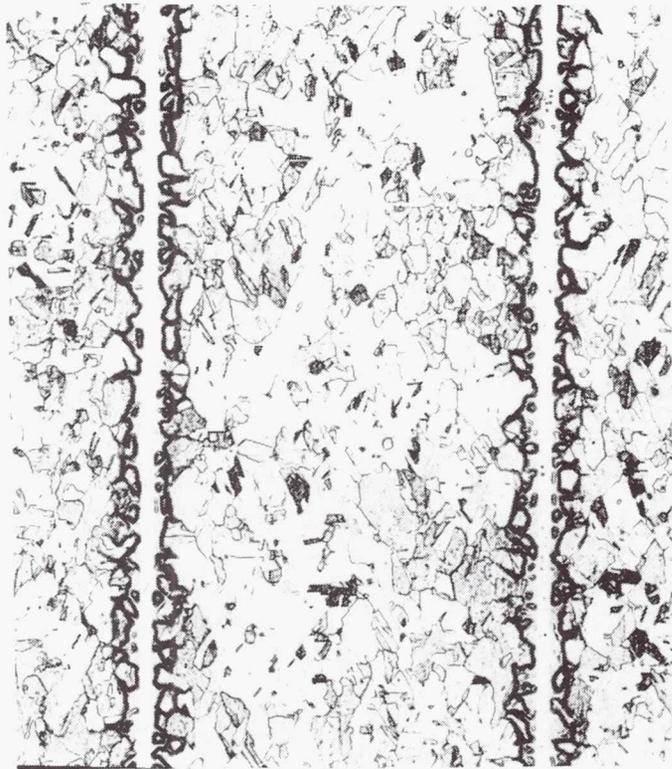
Figure 1.3.1-11.   Zirconium Copper Diffusion Bonded With Gold Aid at 1200°F
With Higher Bonding Loads

Figure 1.3.1-12.   Zirconium Copper Diffusion Bonded With Gold Aid at 1425°F
With Low Bonding Loads

24
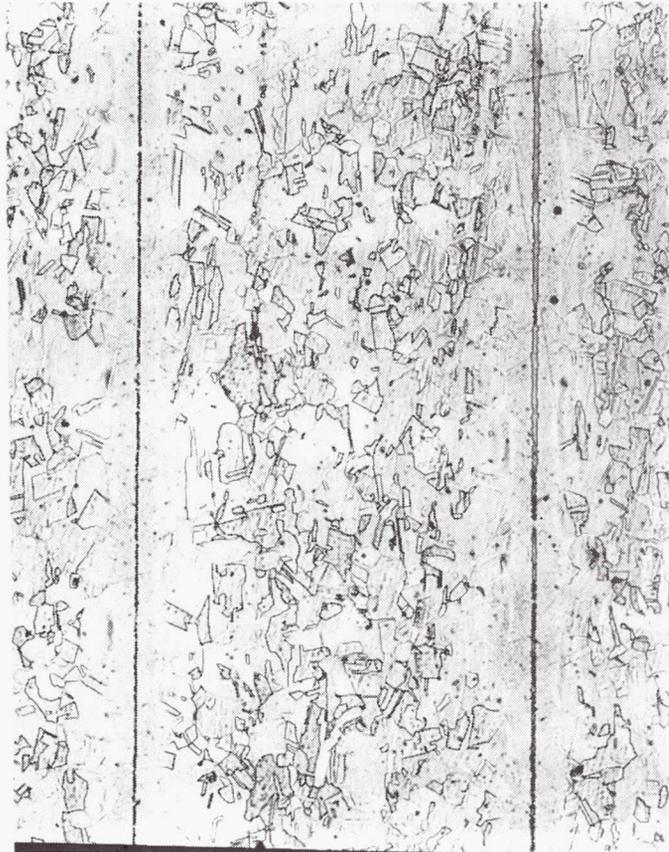
Figure 1.3.1-13. Zirconium Copper Diffusion Bonded With Gold Aid at 1425°F With Higher Bonding Loads

1.3, Fabrication Techniques (cont.)

oxygen/hydrogen heat exchangers. Both silver and gold have thermal expansion coefficients compatible with copper, and both are compatible with hydrogen and oxygen.

Subsequent bend tests at room temperature lent some validation to the visual metallurgical examination. The copper plated ZrCu stack delaminated and separated after bending as shown in Figure 1.3.1-14. After bending, the gold plated ZrCu stack also showed some signs of delamination (Figure 1.3.1-15). The stacks using silver as the diffusion aid showed no evidence of separation as shown in Figure 1.3.1-16.

As follow on work to the diffusion bonding study undertaken by the NASP program for their heat exchangers (HEX), the SSME program continued the study of solid phase bonding aids. Taking the best (as demonstrated by metalurgical evaluation) solid phase alloy and introducing nickel as a candidate, the diffusion bond study was continued. For the SSME HEX program, additional bonding studies were undertaken and evaluated by tensile testing. Nickel demonstrated higher tensile strength than silver over a temperature range from room temperature (R.T.) to 1000 deg F. In addition, based on the number of specimens and tensile test results, the nickel results were more repeatable.

As the diffusion bonding study was continued by the OTV program, repeating the silver aided bonds was of interest for increased thermal conductivity. A significant amount of work had been undertaken to refine the bonding process. Changes to the bonding parameters of temperature, applied pressure, and time were custom tailored to the stages of the diffusion bond process.

1.3.2   Mechanical Property Results Form Current Bonding Experiments

As the diffusion bonding study was continued by the OTV program, further investigation of ZrCu bonded with silver aids was desired to obtain the increased thermal conductivity properties without sacrificing the tensile strength. Compiling the results of the previous experiments, conducted on the NASP and the SSME HEX, refinements to the overall diffusion bonding process to eliminate void formation, were used to define the bond cycle for the preparation of
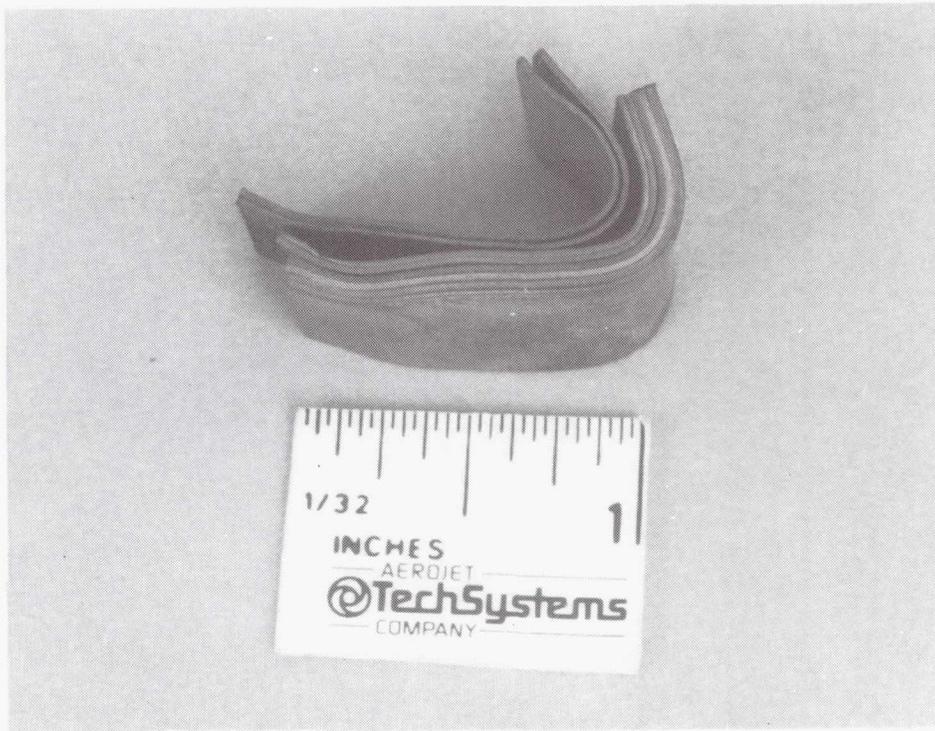
**Figure 1.3.1-14.   Results of Ambient Bend Test on Copper Aided Zirconium Copper**
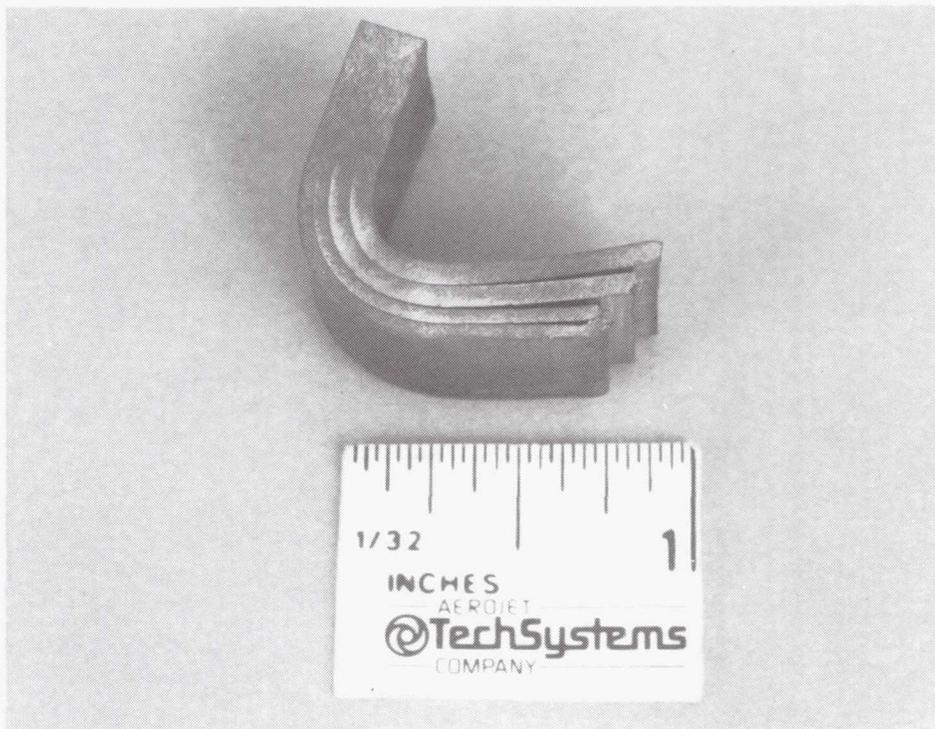
Figure 1.3.1-15.   Results of Ambient Bend Test on Gold Aided Zirconium Copper
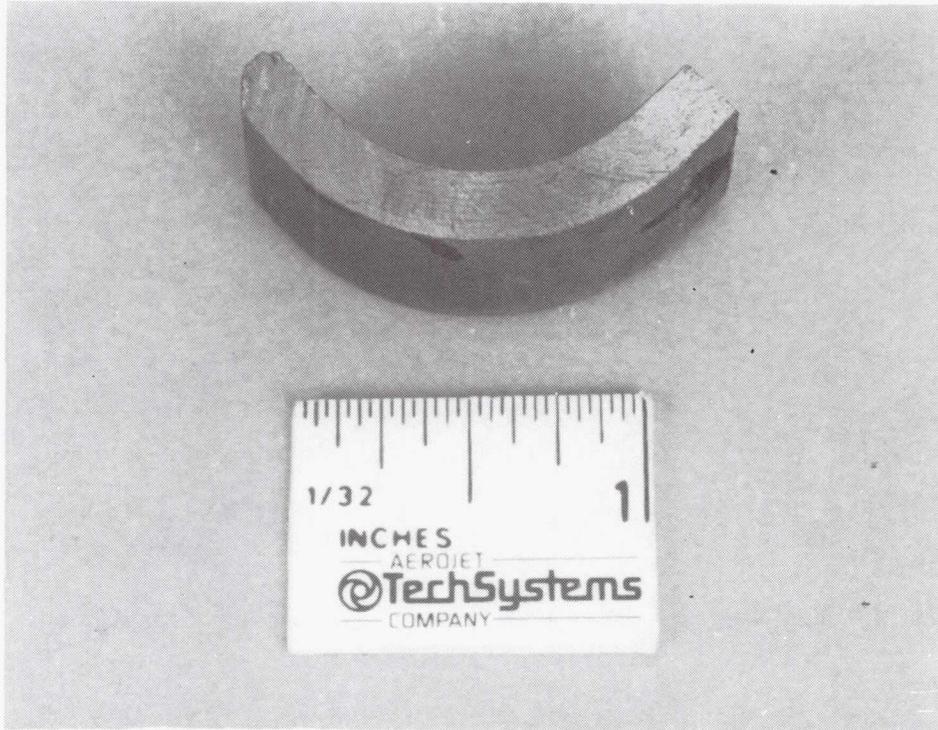
Figure 1.3-1-16. Results of Ambient Bend Test on Silver Aided Zirconium Copper

1.3, Fabrication Techniques (cont.)

the samples for the OTV program. These refinements consisted of modifying the bonding temperature, applied pressure, and bond time to be specifically tailored for each individual stage of the overall diffusion bond process. The diffusion bonding process is considered to take place in two stages outlined below.

1) The first step provides the temperature and pressure required for microscopic plastic deformation of the metal to result in intimate metal-to-metal contact. This overcomes the surface roughness and flatness of the platelets.

2) The second step provides the time for the diffusion to occur thus completing the bond and ultimately eliminating the interface.

Addition post bond processing in a Hot Isostatic Pressing (HIP) furnace assisted the diffusion process by evacuating resultant voids and ensuring intimate contact without gross deformation of the platelet structure.

1.3.2.1   Specimen Preparation

The specimens were prepared and diffusion bonded per Aerojet specifications. A representative bonded stack is shown in Figure 1.3.2-1.

1.3.2.2   Tensile Data

All tensile testing of the materials presented in this section was performed by MetCut Research Associates Inc. in Cincinnati, Ohio. The material was machined into tensile specimens (Figure 1.3.2-2). Extensometers were used in all tests to measure deflections; cross head displacement was simultaneously measured as a verification.

Since all previous diffusion-bond work with silver as an aid was subject only to visual examination of the joint, no reference point of comparison is available for the tensile test results. Visual indication of the presence of voids in the
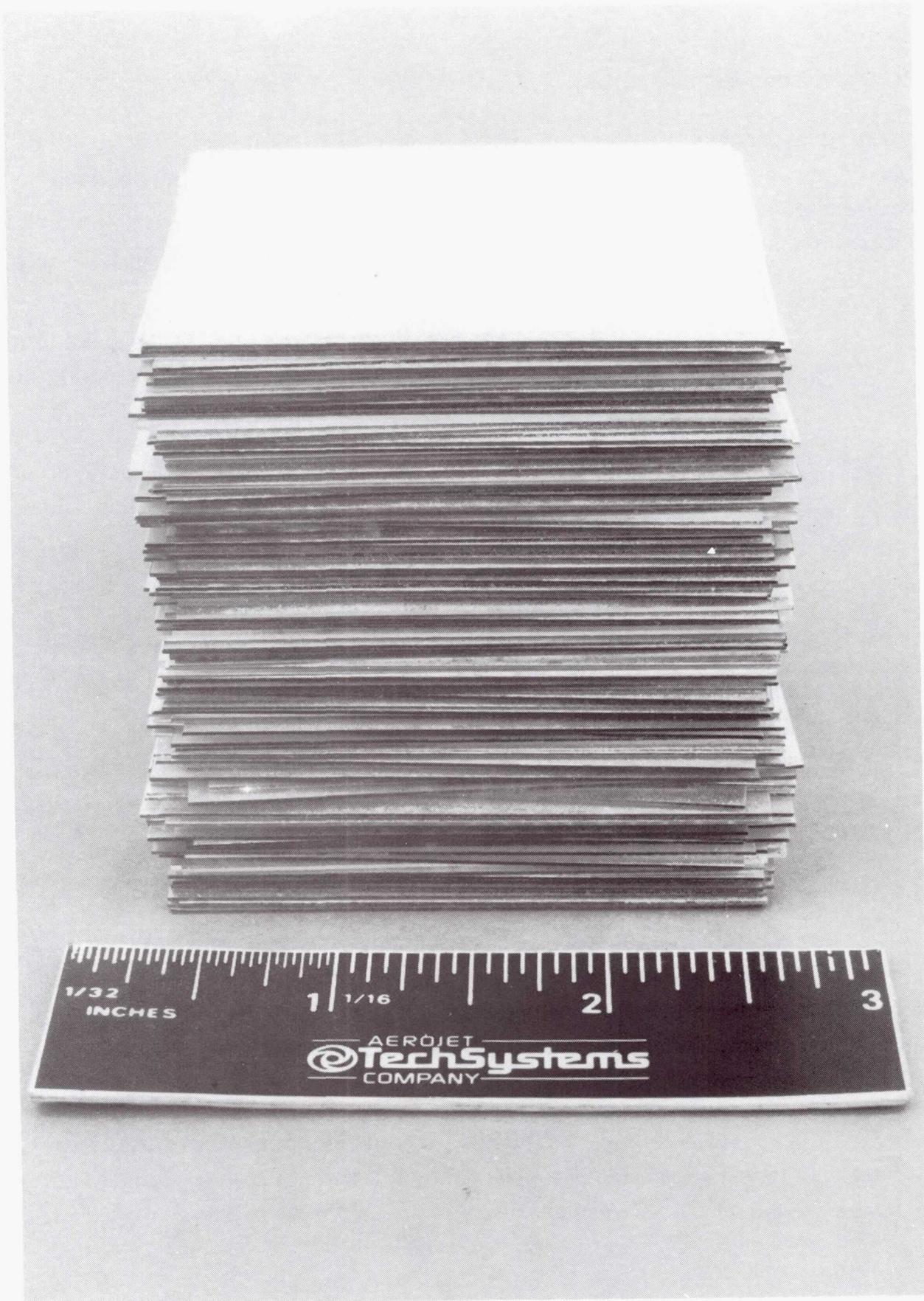
Figure 1.3.2-1. Diffusion Bonded Stack of Zirconium Copper

3/8-16 Thd.

#2 CD & CS
.125/.135 dia.

1/32 x 45° Ch.

.187/.189 dia.

3/16 R.

.370/.372 dia.

1.062

2.250 ± .002

.433

TENSILE SPECIMEN

.188 DIA., 1.062 GAGE LENGTH
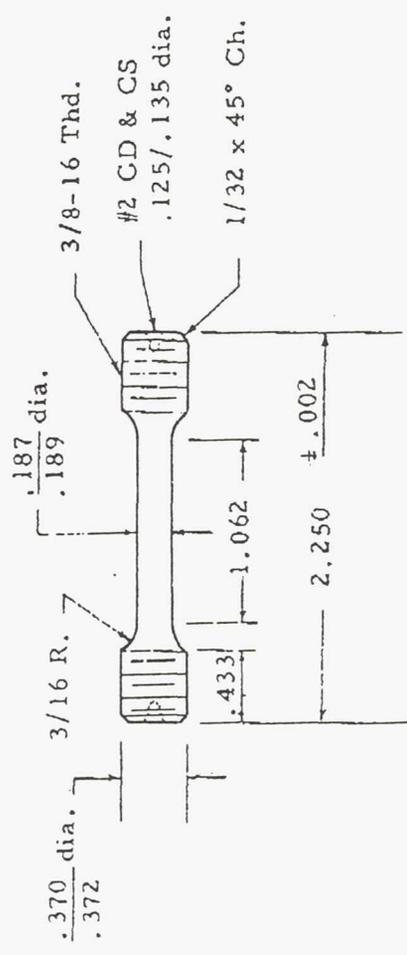
3/8-16 THD.

METCUT RESEARCH ASSOCIATES INC.

CINCINNATI, OHIO 45209

DWG. NO. 711110-1

Figure 1.3.2-2. Tensile Specimen Configuration

1.3, Fabrication Techniques (cont.)

diffusion zones of the earlier specimens empirically suggests a weakness in this zone. The objective of the tensile testing on this program is measure the diffusion bonded parts against the parent metal properties.

Figure 1.3.2-3 plots the tensile strength for the two bonding aids (Ni and Ag) versus the baseline material ZrCu. Slightly lower tensile strength is noted at the elevated temperatures of the diffusion bonded samples. This is most likely due to furnace processing of the diffusion bonded sample.

Nickel is approximately 12% stronger than silver as a diffusion aid at 1000°F. Photographs document the failure mode of the Ni aided tensile specimens (Figure 1.3.2-4) and the Ag aided tensile specimens (Figure 1.3.2-5).

The data for the Ag plated specimens at 1000°F is suspect due to the location of the failure. This location is where one of the extensometers was located and appears in all 3 samples.

1.3.2.3 Thermal Conductivity Test Results

All thermal conductivity testing of materials presented in this report was performed by Southern Research Institute (SRI) of Birmingham, Alabama. This data was taken using the comparative rod apparatus (CRA) method detailed in Appendix A. Specimens used to obtain the ZrCu base metal data came from a single heat (or batch) of bar material. Thermocouples were located in the specimens as depicted in Figure 1.3.2-6.

The measured thermal conductivity data for the ZrCu base metal, and ZrCu bonded with either Ni or Ag, are shown in Tables 1.3.2-I, -II, and -III. Table 1.3.2-IV contains average thermal conductivities obtained from this data, corrected by using the linear curve fit parameters to derive the thermal conductivities as a function of temperature. A plot of the average data from the three data sets, and the linear curve fits for each data set, are presented in Figure 1.3.2-7.
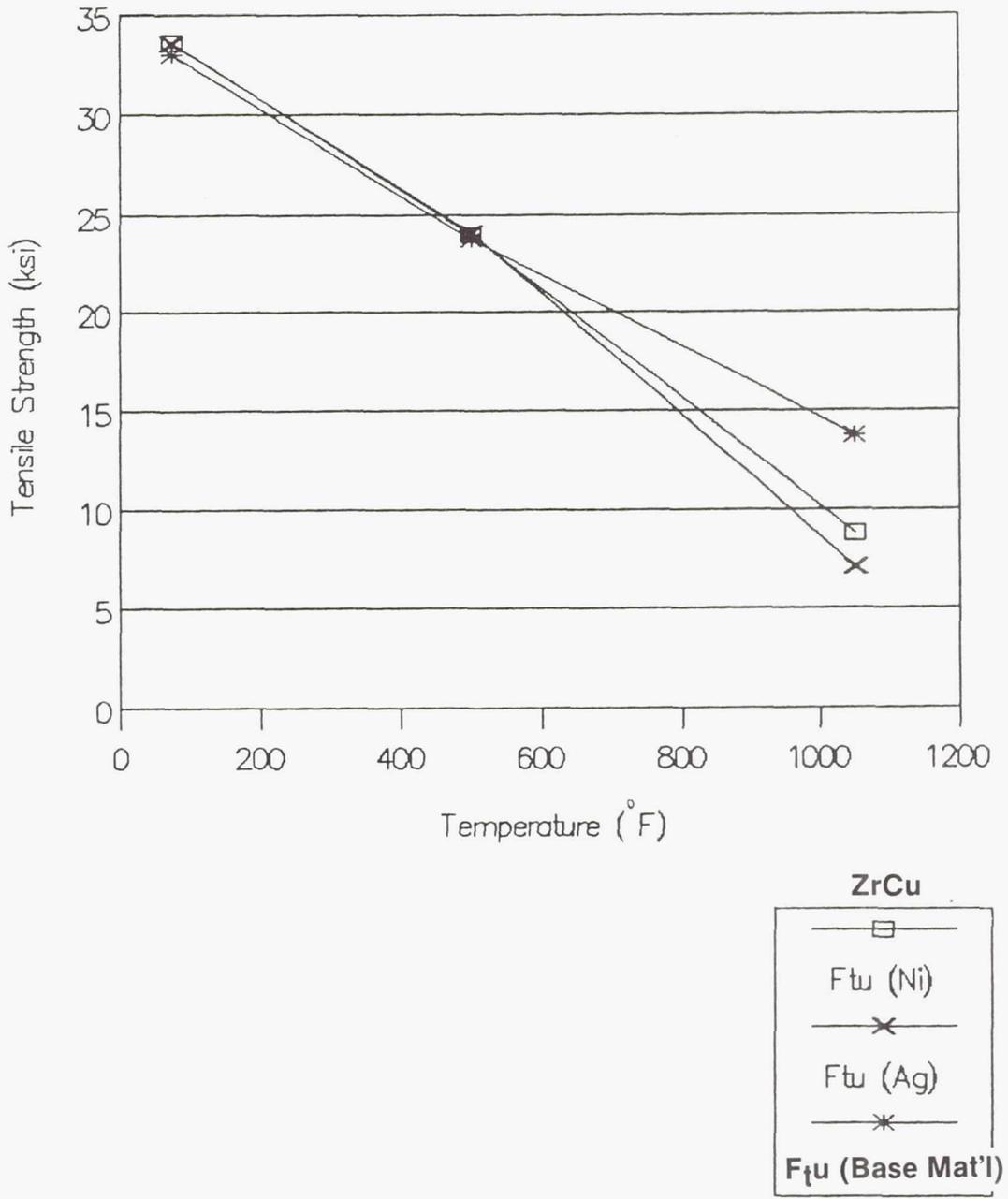
Figure 1.3.2-3. Tensile Test Results

Figure 1.3.2-4. Nickel Aided Tensile Test Specimens
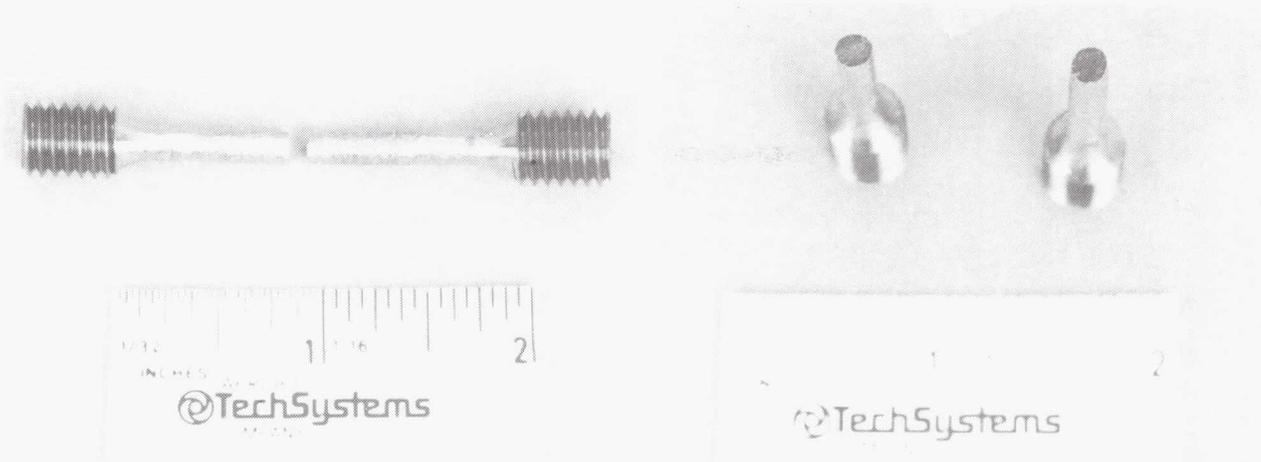
R.T. Tensile Specimens
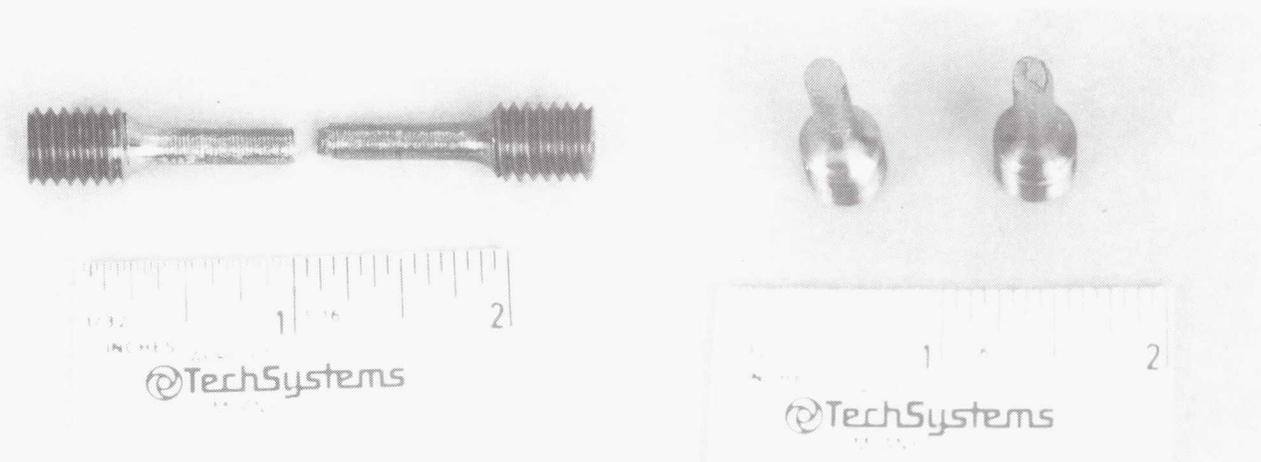
500°F Tensile Specimens
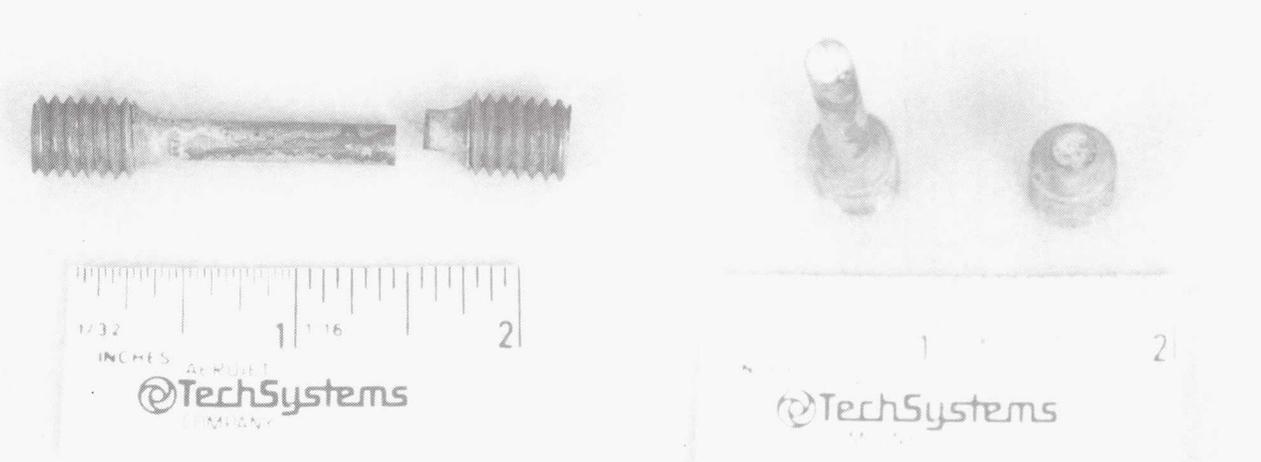
1000°F Tensile Specimens

Figure 1.3.2-5. Silver Aided Tensile Test Specimens

35
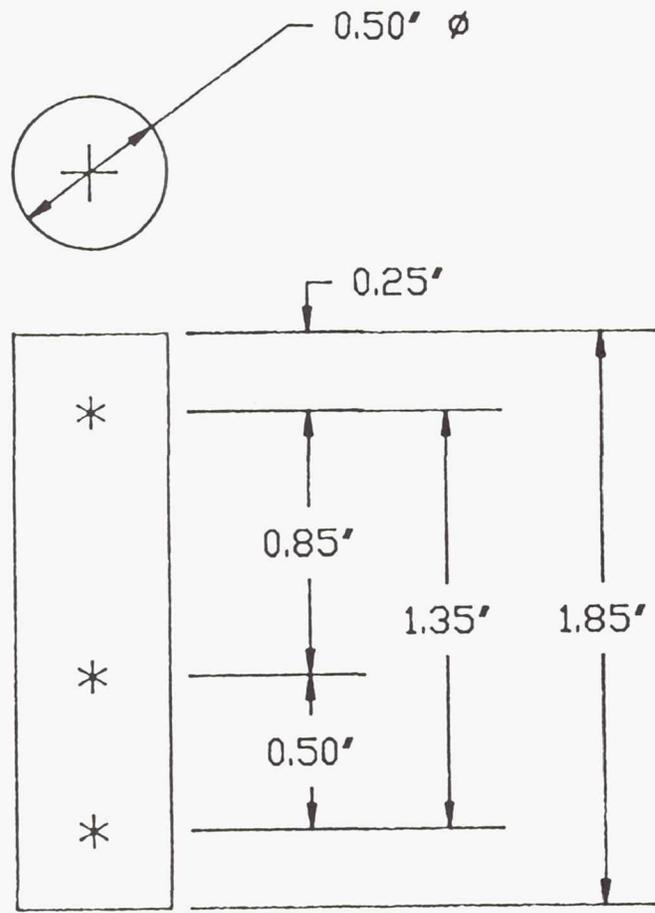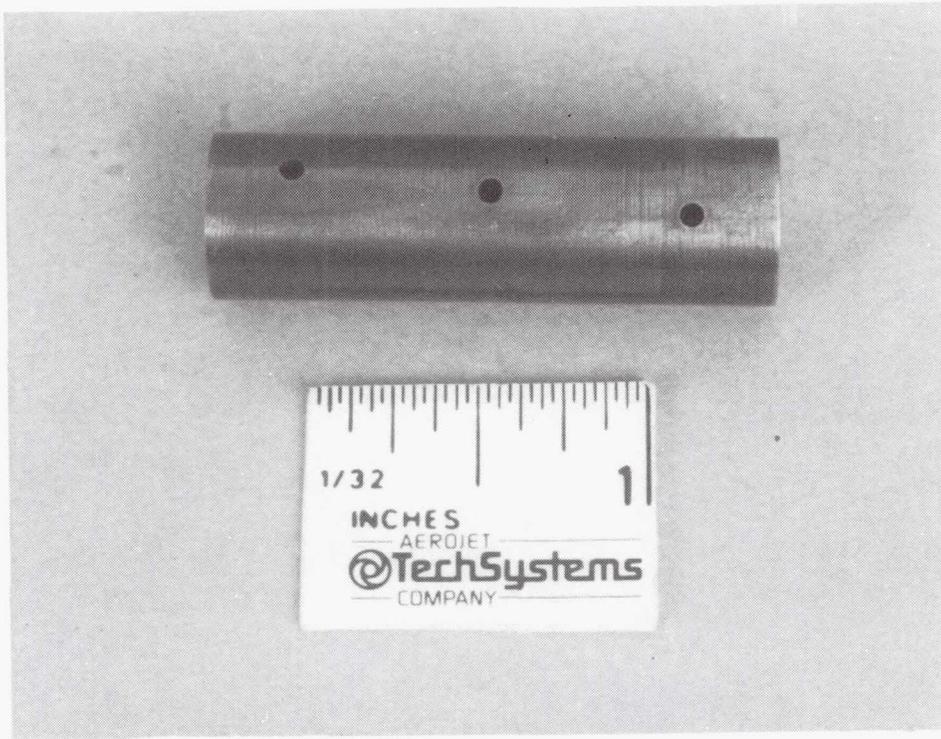
Figure 1.3.2-6. Comparative Rod Apparatus Specimen Description

TABLE 1.3.2-I

THERMAL CONDUCTIVITY DATA FOR ZIRCONIUM COPPER

Test Temp.	Conductivity (k) *	Average k
49	2267	
50	2272	2269.5
177	2414	
176	2423	2418.5
185	2418	
185	2423	2420.5
401	2386	
401	2394	2390
542	2333	
542	2338	2335.5
710	2346	
710	2345	2345.5
815	2405	
817	2408	2406.5
998	2025	
997	2021	2 023.2

* BTU-in/hr-ft2-½F

TABLE 1.3.2-II

THERMAL CONDUCTIVITY DATA FOR NICKEL-AIDED DIFFUSION-BONDED ZIRCONIUM COPPER

Test Temp.	Conductivity (k) *	Average k
130	1937	
130	1938	1937.5
503	1898	
503	1901	1899.5
740	1936	
741	1936	1936
920	1993	
921	1984	1988.5
1260	2007	
1257	2007	2007

*   BTU-in/hr-ft2-F

TABLE 1.3.2-III

THERMAL CONDUCTIVITY DATA FOR SILVER-AIDED DIFFUSION-BONDED ZIRCONIUM COPPER

Test Temp.	Conductivity (k) *	Average k
102	2508	
102	2505	2506.5
434	2406	
434	2393	2399.5
818	2437	
819	2412	2424.5
1272	2350	
1275	2349	2349.5

* BTU-in/hr-ft2-F

TABLE 1.3.2-IV

AVERAGE ZIRCONIUM COPPER DIFFUSION-BONDEDTHERMAL CONDUCTIVITIES *

	AVERAGE DATA POINTS			CORRECTED AVERAGES (Based on linear curve fit data **)		
Temp (F)	Zr-Cu	Zr-Cu w/Ni	Zr-Cu w/Ag	Zr-Cu	Zr-Cu w/Ni	Zr-Cu w/Ag
50	2269			2412.9	1902.7	2488.9
100				2402.9	1906.6	2483.2
102			2507	2402.5	1906.7	2483.0
130		1938		2396.9	1908.9	2479.8
177	2419			2387.5	1912.6	2474.5
185	2420			2385.9	1913.2	2473.6
200				2382.9	1914.4	2471.9
300				2362.9	1922.1	2460.6
400				2343.0	1929.9	2449.3
401	2390			2342.8	1930.0	2449.2
434			2400	2336.2	1932.5	2445.4
500				2323.0	1937.7	2438.0
503		1900		2322.4	1937.9	2437.6
542	2335			2314.6	1940.9	2433.2
600				2303.0	1945.4	2426.7
700				2283.0	1953.2	2415.4
710	2346			2281.0	1954.0	2414.2
740		1936		2275.0	1956.3	2410.8
800				2263.1	1961.0	2404.1
816	2406			2259.9	1962.2	2402.2
818			2424	2259.5	1962.4	2402.0
900				2243.1	1968.7	2392.7
920		1989		2239.1	1970.3	2390.5
998	2023			2223.5	1976.3	2381.7
1000				2223.1	1976.5	2381.4
1100				2203.1	1984.3	2370.1
1200				2183.1	1992.0	2358.8
1259		2007		2171.4	1996.6	2352.2
1273			2350	2168.6	1997.7	2350.6

* BTU-in/hr-ft2-F

** equation parameters

	intercept	slope
Zr-Cu	2422	-0.19977
w/ Ni	1898	+0.07767
w/ Ag	2494	+0.11308

THERMAL CONDUCTIVITY OF BONDED Zr-Cu
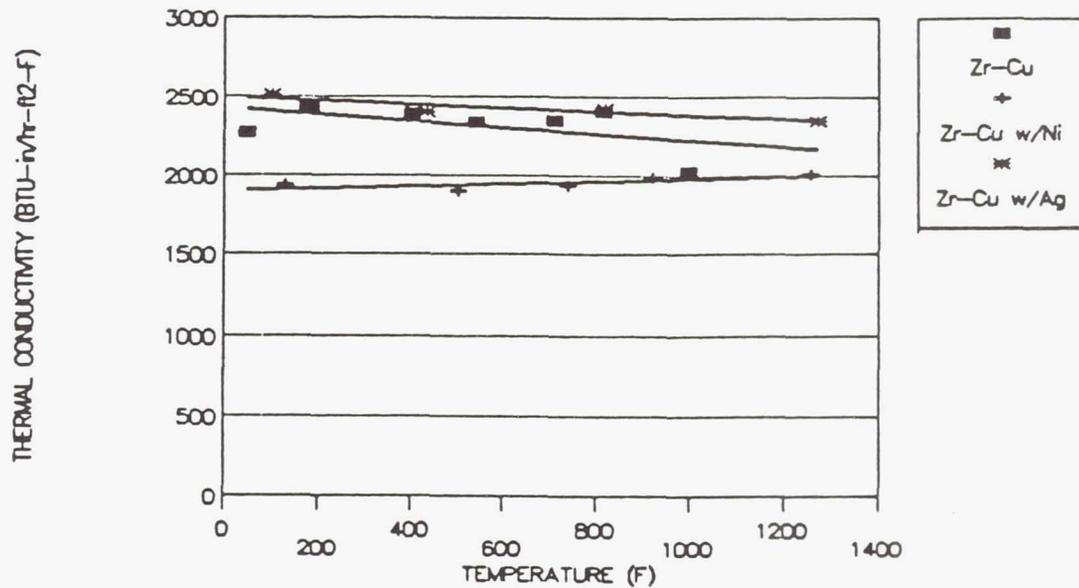
The baseline Zr-Cu data agrees with other sources, Reference 2, in showing a slight decrease in conductivity with increasing temperature. The Ag aided bond data shows no measurable difference from the Zr-Cu data. The Ni aided bond data shows lower conductivity as expected. The effect of the Ni decreases with increasing temperature, characteristic of Cu-Ni alloy thermal conductivity data from Reference 3.

Figure 1.3.2-7. Thermal Conductivity of Bonded Zirconium Copper

1.3, Fabrication Techniques (cont.)

ZrCu Base Metal — Figure 1.3.2-8 shows the thermal conductivity data from the ZrCu base metal specimen plotted with a design allowable curve taken from Reference 4. It can be seen that the test data agrees well with previous estimates of the thermal conductivity of ZrCu, validating the CRA method used in determining thermal conductivity in this alloy system.

It is noted that the 1000°F data point falls significantly below the fitted line; however since neither OFHC, nor design allowable ZrCu curves show any suggestion of thermal conductivity drop-off at this temperature range, it is assumed that this point represents data scatter and does not indicate a major deviation from the fitted curve. Since this data point was obtained at the highest temperature tested, this assumption cannot be verified at this time.

ZrCu w/ Ni Bond Aid — The bulk thermal conductivity (i.e., the average thermal conductivity of a bonded stack) shows a significant reduction. The reduction in thermal conductivity, due to Nickel in solution at the bond lines, is greatest at room temperature and decreases at higher temperatures as shown in Figure 1.3.2-9. These differences represent an average drop in bulk thermal conductivity of approximately 20% at room temperature (80% of ZrCu), and 11% (89% of ZrCu) at 1200 °F. This bulk value is applicable only to bonded stacks with similar thermal cycles and approximately equivalent average platelet thickness. The effect of the bonds increases as the ratio of bond width to unaffected ZrCu platelet thickness increases, as occurs in stacks with a higher average platelet thickness.

ZrCu w/ Ag Bond Aid — The thermal conductivity of Ag aided bonds shows no significant difference from the ZrCu base metal at any test temperature as illustrated in Figure 1.3.2-10. Statistical analysis of the ZrCu and ZrCu w/Ag data cannot distinguish a difference in mean thermal conductivity, based on a 95% confidence interval of the means, and a computed t statistic of -1.944 and a significance level of 0.064. Small differences are therefore attributed to variations in base-metal composition/thermal conductivity and variability in measurement reproducibility.

Zr-Cu TEST DATA vs DESIGN ALLOWABLE
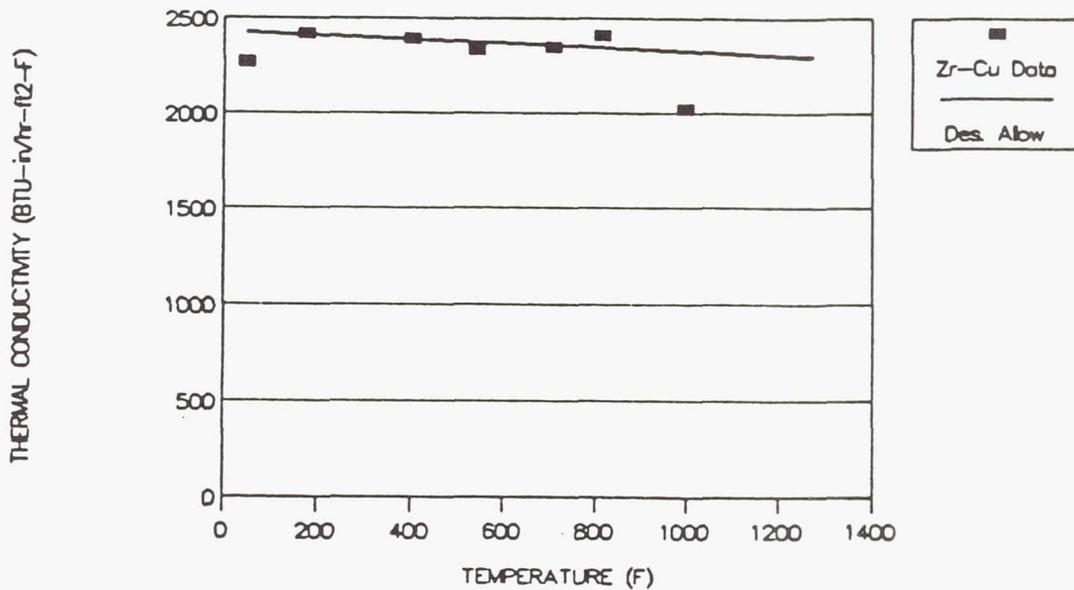
The baseline Zr-Cu data matches the Reference 4 curve closely except for the room temperature and 1000°F data points. Since neither any Zr-Cu data, OFHC Cu data, nor Cu-Ni data shows any suggested deviation from a straight line in this temperature range, it is assumed that these data points represent random variation in the measurements.

Figure 1.3.2-8. Zirconium Copper Test Data Versus Design Allowable

THERMAL CONDUCTIVITY
Zr–Cu vs Zr–Cu w/Ni
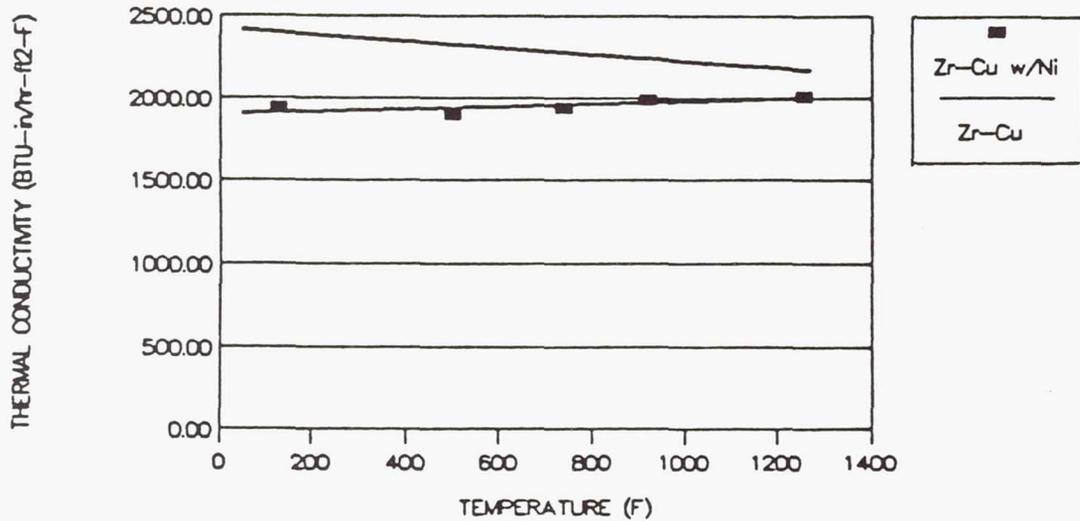
The Ni aided bond data fits a straight line with a slightly posi-
tive slope. The effect of the Ni rich bond zone has a moderate
effect on the bulk thermal conductivity of the stack compared to
the baseline Zr-Cu thermal conductivity.

**Figure 1.3.2-9. Thermal Conductivity of Zirconium Copper Versus Zirconium
Copper With Nickel Aid**

44

THERMAL CONDUCTIVITY

Zr–Cu vs Zr–Cu w/Ag
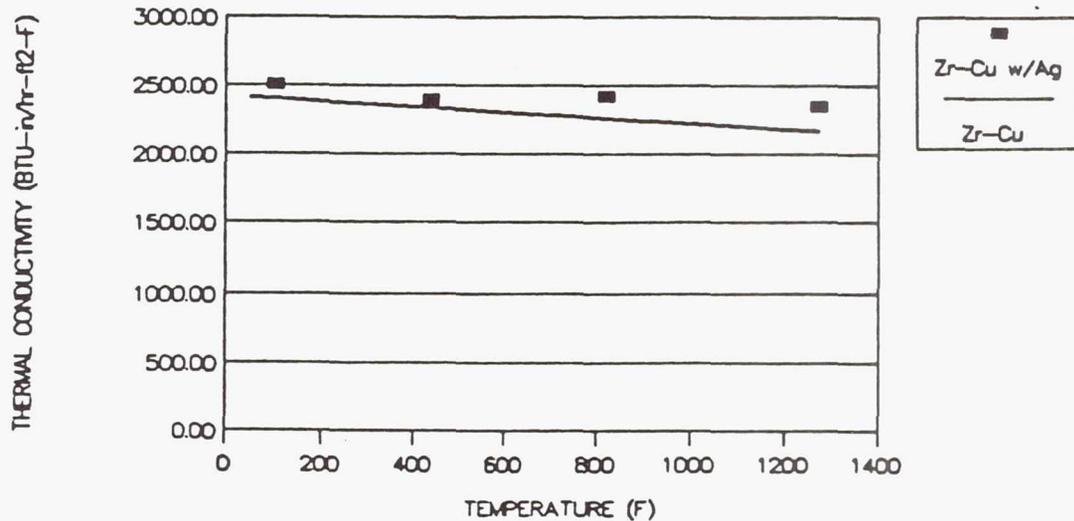
The Ag aided bond data shows a slight deviation above the typical Zr-Cu thermal conductivity. The addition of silver to copper should reduce the average thermal conductivity slightly, therefore this effect is assumed to be due to different lots of Zr-Cu and slight errors in measuring thermal conductivity in high conductivity materials.

Figure 1.3.2-10. Thermal Conductivity of Zirconium Copper Versus Zirconium Copper With Silver Aid

45

1.3, Fabrication Techniques (cont.)

1.3.2.4 Analytical Predictions for Thermal Conductivity

Ni Aided ZrCu — The strength advantages of using nickel as a bonding aid have been well demonstrated in the SSME external heat exchanger program, however, based on reference thermal conductivity data for simple binary CuNi compositions, (Reference 5), a significant drop in thermal conductivity can be expected in the area of the diffusion bonds.

The thermal conductivity of each bond can be calculated by assuming additive thermal resistivity of the base ZrCu and the ZrCuNi bond diffusion zone. Therefore the bulk thermal resistivity of the stack should be represented by:

$$R_{bulk} = R_{zr-cu} + R_{bond} \tag{1}$$

Where R_{bulk} is the thermal resistivity of the bonded stack

R_{zr-cu} is the thermal resistivity of the ZrCu

R_{bond} is the thermal resistivity of the bonds

Solving for the bond thermal resistivity yields:

1.3, Fabrication Techniques (cont.)

$$R_{bond} = R_{bulk} - R_{zr-cu} \tag{2}$$

Since thermal resistivity is inversely related to thermal conductivity by:

$$R = L/k \tag{3}$$

where L is the effective gage length of a material with a thermal conductivity of k.

The thermal resistivity equation can then be re-written in terms of thermal conductivity as:

$$Lbond/kbond = Lcomb/kbulk - Lzr-cu/kzr-cu \tag{4}$$

or solving for k_{bond}

$$kbond = Lbond/(Lcomb/kbulk - Lzr-cu/kzr-cu) \tag{5}$$

1.3, Fabrication Techniques (cont.)

where

k_{bond} = the bond zone thermal conductivity

k_{bulk} = the measured bonded stack thermal conductivity

k_{zr-cu} = the baseline ZrCu thermal conductivity

and

L_{bond} = the measured average bond width

L_{comb} = the average platelet thickness (ignoring the thickness of the applied bonding aid)

L_{zr-cu} = the thickness of the unaffected ZrCu (IE average platelet thickness minus the bond zone width).

The stacking sequence of the Ni aided bonded specimen is a repetition of 2 each 0.008, 4 each 0.010, 4 each 0.012, and 4 each 0.017" platelets, which results in an average platelet thickness (L_{comb}) of .172"/14 = 0.0123". Scanning electron microprobe analysis of several typical Ni aided bonds in the specimen indicates the average Ni aided bond width (L_{bond}) to be 0.0023" thick. The corresponding unaffected ZrCu length (L_{zr-cu}) is then 0.0123" - 0.0023" = 0.010".

The baseline ZrCu thermal conductivity (k_{zr-cu}) is 2410 Btu-in./hr-ft^2-°F at room temperature, 2343 at 400°F, 2263 at 800°F, and 2183 at 1200°F, and the bulk Ni aided ZrCu thermal conductivity (k_{bulk}) is 1904 Btu-in./hr-ft^2-°F at room temperature, 1930 at 400°F, 1961 at 800°F, and 1992 at 1200°F, from the data in Table 1.3.2-IV.

Substituting the appropriate gage lengths and measured thermal properties for both the baseline ZrCu and Ni aided bonds at select temperatures (from the data in Table 1.3.2-IV) into this thermal conductivity equation yields:

47

1.3, Fabrication Techniques (cont.)

$$k_{bond} = 995 \text{ Btu-in./hr-ft}^2\text{-}°F \text{ at room temperature}$$

$$k_{bond} = 1093 \text{ Btu-in./hr-ft}^2\text{-}°F \text{ at } 400°F$$

$$k_{bond} = 1241 \text{ Btu-in./hr-ft}^2\text{-}°F \text{ at } 800°F$$

and

$$k_{bond} = 1443 \text{ Btu-in./hr-ft}^2\text{-}°F \text{ at } 1200°F$$

Verification of these calculations is difficult since there is no literature data available regarding the effects of nickel on the thermal conductivity of Zr-Cu. Existing data on the thermal conductivity of nickel/copper solutions in Reference 5 can be used, however, if the simplifying assumption is made that the zirconium in the alloy (0.10 to 0.20%) has a negligible effect on the alloy's conductivity. It now becomes feasible to convert the calculated bondline thermal conductivity to estimated nickel concentration using the appropriate data from Reference 5, and comparing these results with actual measurements of the nickel content of the bonds. If the above assumption is true, there should be a good correlation between derived and measured nickel contents at all test temperatures.

Figure 1.3.2-11 is a plot of the effects of test temperature on the thermal conductivity of various CuNi concentrations of interest. As expected, nickel content has a major effect of decreasing thermal conductivity. Note that all CuNi curves have positive slopes, as compared to the slightly negative slope of pure copper, and that the dilute Ni concentration curves show the greatest effect of temperature (largest slopes), while a high Ni concentration (20%) shows a relative insensitivity to temperature. As a result, the difference in conductivity between pure copper and the copper/nickel solutions, particularly dilute (<10% nickel concentrations) is not a constant, but rather decreases with increasing temperature.

Figure 1.3.2-12 presents the data shown in Figure 1.3.2-11, rearranged to show thermal conductivity of copper as a function of Ni concentration for various test temperatures. This allows an easier correlation between thermal conductivity and Ni content. The four calculated bondline thermal conductivities of 995, 1093, 1241, and 1443 BTU-in/hr-ft^2-°F vs room temperature, 400°, 800°, and 1200°F respectively, are plotted in Figures 1.3.2-11 and 1.3.2-12. Figure 1.3.2-11 shows the expected reduction in thermal conductivity, however, the slope of thermal

EFFECT OF TEMP. on Cu CONDUCTIVITY
as a FUNCTION of Ni CONTENT
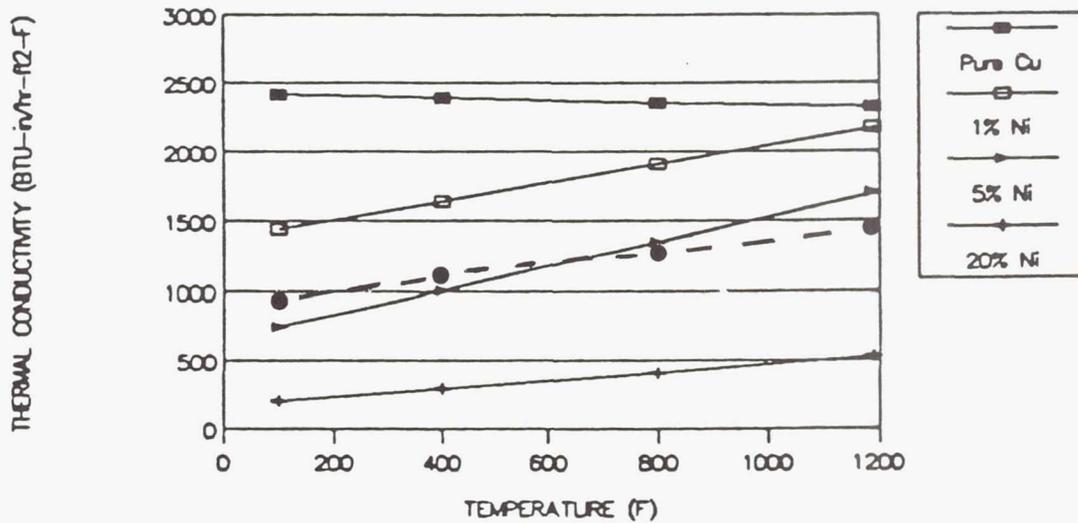
Nickel has a very strong negative effect on the thermal conductivity of copper. Dilute Ni solutions (<5%) show a relative improvement in conductivity at elevated temperatures. High Ni concentrations show less of an improvement with increasing temperature (Reference 5). The dashed line represents calculated bond line thermal conductivity.

Figure 1.3.2-11. **Effect of Temperature on Copper Conductivity as a Function of Nickel Content**

EFFECT OF Ni on Cu CONDUCTIVITY
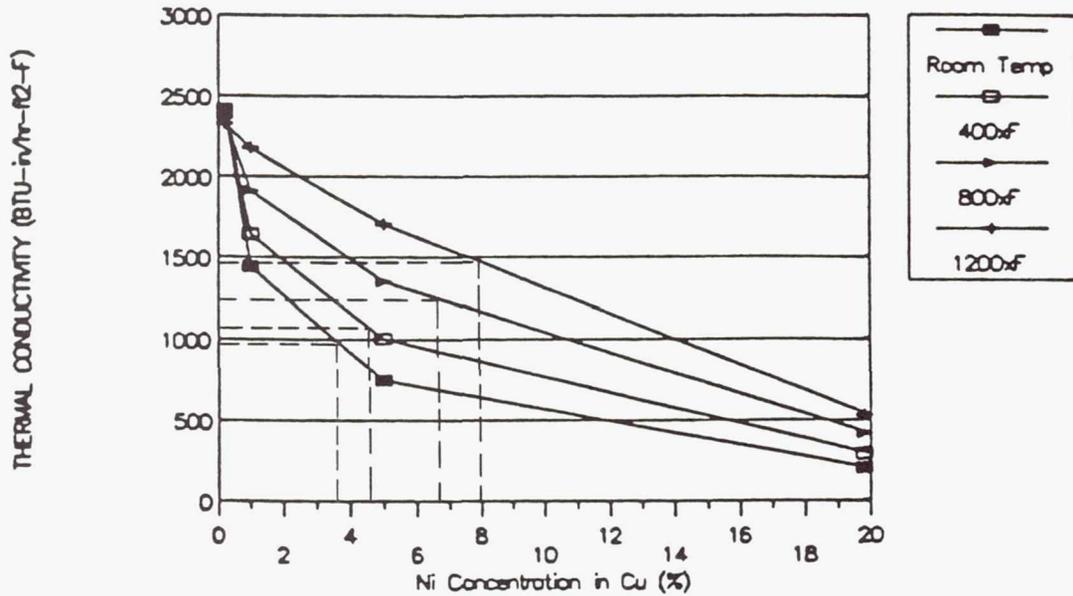
Rearranging the curves from Figure 1.3.2-11 allows thermal conductivity to be determined for a given Ni content. The values of the four calculated bond-line thermal conductivities at four temperatures are represented by the dashed lines above. Note that for the same physical specimen, this data would indicate the Ni concentraton increasing with temperature. Since the same specimen was used to measure thermal conductivity at various temperatures, this would indicate the presence of some other factor with a stronger influence at high temperatures.

**Figure 1.3.2-12. Effect of Nickel on Copper Conductivity**

1.3, Fabrication Techniques (cont.)

conductivity vs temperature appears equivalent to the 20% Ni curve. Figure 1.3.2-12 shows that the apparent Ni content of the bonds increases from 3.6% at room temperature to approximately 8% at 1200°F. This is an obvious discrepancy since all bond stack thermal conductivity measurements were made on the same sample. Since the nickel content of the bonds must be constant, two hypotheses could explain the discrepancy, either the average Ni content is 20% and some factor is increasing the thermal conductivity uniformly at all temperatures, or the average Ni content is closer to 3.5% and some other factor is acting synergistically with the Ni at elevated temperatures to further degrade thermal conductivity.

Microprobe analysis of six typical bond lines from Ni aided specimens shows a maximum residual Ni content at the center of the bond of approximately 6.8%. Assuming a linear concentration gradient from the bond centerline to the edge of the diffusion zone results in a calculated average Ni content in the bond zone of 3.4%, therefore, it would appear that some other factor besides Ni is degrading the thermal conductivity of the bonded stack at elevated temperatures. The most likely factor is the effect of zirconium, originally assumed to be negligible.

The thermal conductivity curve for pure copper shown in Figure 1.3.2-11 is almost identical to the measured curve for ZrCu shown Figure 1.3.2-8, at least up to 800°F and for this reason zirconium was assumed to have a negligible effect on conductivity. However, since the ZrCu thermal conductivity was only measured up to 1000°F, and since the 1000°F data point fell well below the anticipated curve, it is not unreasonable to assume that the thermal conductivity of ZrCu diverges from pure copper at approximately 1000°F due to significant solution of zirconium starting in this temperature range. This effect may be further increased by the effects of nickel in solution. Phase diagrams, Figure 1.3.2-13, show greater solubility for zirconium in nickel than in copper, suggesting that the CuNi alloys may have higher solubility of zirconium than pure copper, and therefore should show more pronounced effects on conductivity at elevated temperatures.

If the assumption that the Cu-Ni bond zone has higher zirconium solubility than pure copper is correct, the effect would be greater in the bonded stack than in the normal ZrCu with no Ni. Using the test data to correct the curves at high temperature results in Figure 1.3.2-14. This curve also converts thermal conductivity into % ZrCu conductivity for simplified application to subsequent calculations of Ni aided bond thermal conductivities.

51

(b)

(a)
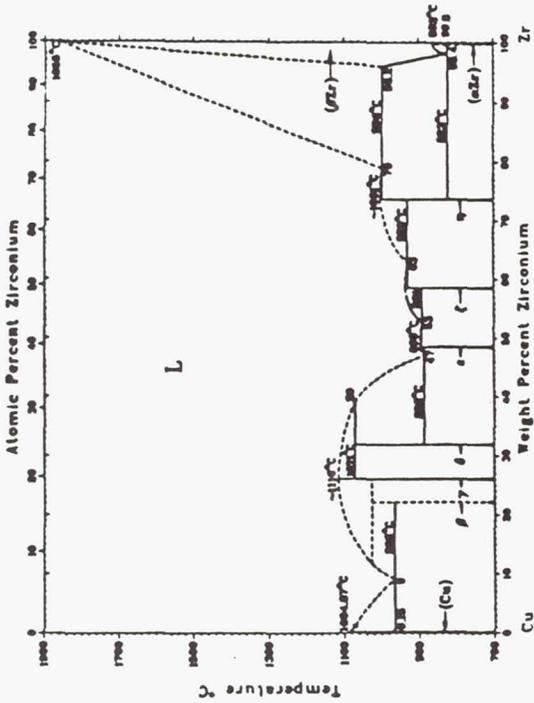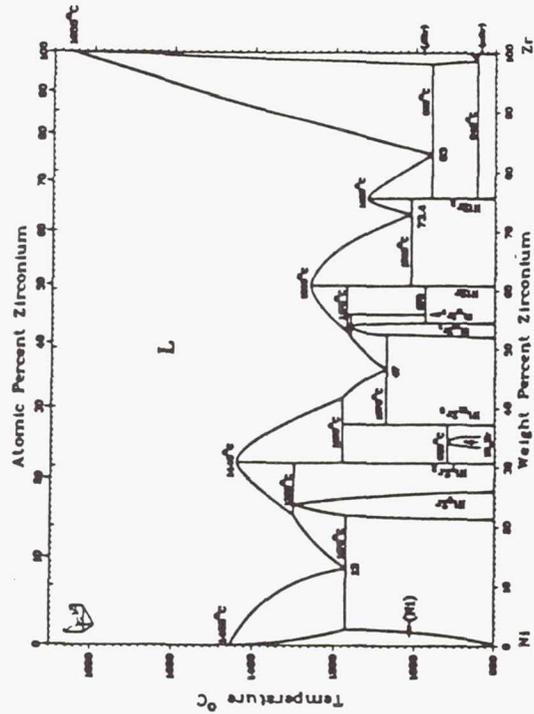
Zirconium has a very low solubility in copper (0.2%) at the solution temperature of Zr-Cu, 1700°F (927°C). The solubility in Ni at the same temperature is estimated to be low, but significantly greater than in Cu. This suggests that Zr should have a higher solubility in Cu-Ni (i.e., bond zone) than in pure Cu.

Figure 1.3.2-13. Solubility of Zirconium in Copper (a) Versus Solubility of Zirconium in Nickel (b)

EFFECT of Ni on Zr–Cu CONDUCTIVITY
Corrected for Zr Solubility in Bond
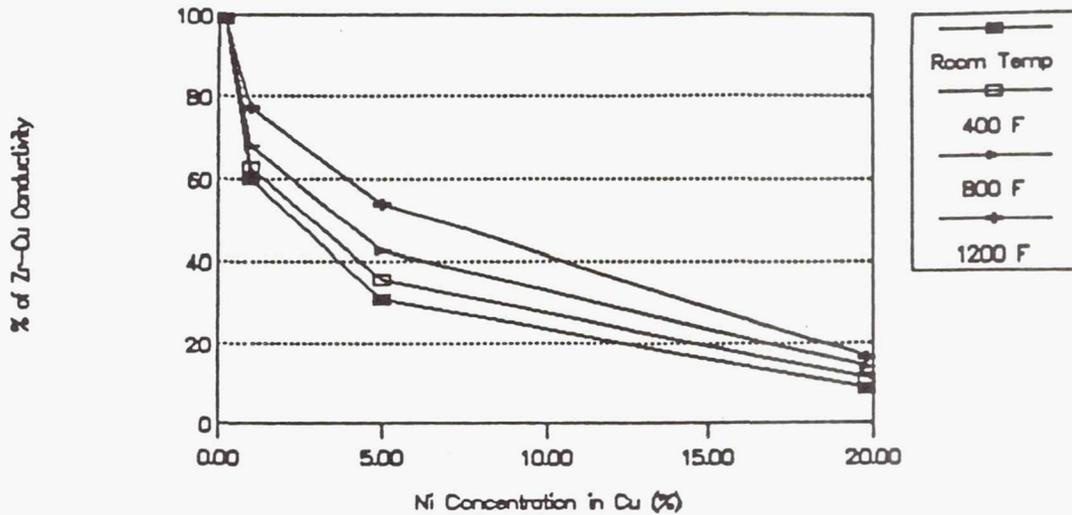
Rearranging the curves in Figure 1.3.2-12 to correct the effects of increased Zr solubility in the Ni rich bond zone results in a downward shift in bond thermal conductivities at temperatures above room temperature. The data has been plotted as % of baseline Zr-Cu thermal conductivity to simplify bond and bulk thermal conductivity calculations per equations (7) and (10).

Figure 1.3.2-14. Effect of Nickel on Zirconium Copper Conductivity Corrected for Zirconium Solubility in Bond

1.3, Fabrication Techniques (cont.)

The above calculations are specifically applicable to Ni aided bonds with the same average platelet thickness, and which have been exposed to thermal cycles resulting in equivalent Ni concentration diffusion gradients to those measured in these bonds. The thermal conductivities of bonds made under different conditions will have significantly different bulk thermal conductivities. These alternate bond condition thermal properties may be estimated by measuring the actual Ni content and diffusion zone width using the SEM/EDX microprobe, determining the average platelet thickness in the stack in question, and using the appropriate thermal conductivity estimated from the curves in Figure 1.3.2-14.

Referring to the additive thermal resistivity equation:

$$R_{bulk} = R_{zr-cu} + R_{bond} \tag{1}$$

Converting this equation to equivalent thermal conductivity terms using equation (3), and solving for k_{bulk}:

$$k_{bulk} = L_{comb} / ((L_{zrcu}/k_{zr-cu}) + (L_{bond}/k_{bond})) \tag{6}$$

Since the corrected Ni vs thermal conductivity curve in Figure 1.3.2-14 is plotted as % ZrCu, $k_{bond} = k_{zr-cu} * \%ZrCu$. Therefore, performing the k_{zrcu} substitution and rearranging (6):

$$k_{bulk} = k_{zrcu} * L_{comb} / ((L_{zrcu}) + (L_{bond}/\%ZrCu)) \tag{7}$$

In order to estimate the bulk thermal conductivity of a new Ni aided bonded stack it will be necessary to know:

1. %ZrCu, the ratio of k_{bond}/k_{zrcu} taken from Figure 1.3.2-14 for the measured average bond Ni concentration.

2. L_{comb}, the <u>average</u> platelet thickness of the stack.

3. L_{bond}, the measured bond width.

1.3, Fabrication Techniques (cont.)

4. $L_{zrcu} = L_{comb} - L_{bond}$.

5. k_{zrcu}, design allowable thermal conductivity @ temperature.

For example, if a bonded stack resulted in a bond zone .001" wide, with an average Ni content of 10%, and an average platelet thickness of .008", the equation parameters would be:

$\%ZrCu = .25$

$L_{comb} = .008"$

$L_{bond} = .001"$

$L_{zrcu} = .008 - .001 = .007$

$k_{zrcu} = 2410$ Btu-in.-hr-ft^2-°F) at room temperature

Therefore, the bulk thermal conductivity should be:

$k_{bulk} = 2410 * .008/(.007+(.001/.25) = 2410 * .72 = 1752$ Btu-in./hr-ft^2-°F

at room temperature

The situation for heat flow parallel to the bond lines is somewhat different. This situation is analogous to an electrical circuit with parallel resistors. In this case, bulk thermal conductivity additive, not thermal resistivity. The bulk thermal conductivity is determined by:

$$kbulk=kbond*(Lbond/Lcomb)+kzrcu*(Lzrcu/Lcomb) \qquad (8)$$

The specimen used to determine the bulk transverse thermal conductivity in would be expected to have a bulk conductivity parallel to the bonds of:

$k_{bulk} = 995*(.0023/.0123) + 2410*(.010/.0123)$

$= 2145$ Btu-in./hr-ft^2-°F at room temperature

1.3, Fabrication Techniques (cont.)

The above assumptions and calculations are reasonable for the CuNi system which is a simple, single phase, 100% solid solution system, Figure 1.3.2-15. Similar calculations and conclusions could be drawn from any such metallurgical system, however, more complex systems containing intermetallics or eutectic phases may be much more complicated.

Ag Aided ZrCu Diffusion - The relatively large affect of Ni of the thermal conductivity of ZrCu lead to the consideration of silver as a bonding aid. Early bond test data showed very good room temperature strength with silver as a bonding aid, however no high temperature tensile data has been generated to date.

The thermal conductivity data shows no measurable affect of silver on the thermal conductivity properties of ZrCu. This result is not unexpected, based on metallurgical phase diagram data available for AgCu, Figure 1.3.2-16, Reference 5. Silver and copper form a simple eutectic which consists of two distinct phases, one copper rich and the other silver rich. At a typical ZrCu aging temperature of 1100 F the copper rich phase contains approximately 3% silver, and the silver rich phase contains approximately 4% copper. Therefore in a Ag aided ZrCu bond stack, three distinct composition zones are present, pure ZrCu, Cu-2%Ag, and Ag-6%Cu. Figure 1.3.2-17 shows the effect of both Ni and Ag on Cu conductivity at room temperature. The anticipated Cu-3%Ag conductivity based on this data would be within 5% of ZrCu, and Ag-4%Cu would be approximately equal to ZrCu because of the higher conductivity of Ag.

Scanning electron microscope (SEM) examination shows a silver rich phase at the bond line which is 75 μ-inches wide. This indicates that the original silver plating thickness was at the high end of the specified thickness range (20-40 μ-in per surface). SEM microprobe data, show the total diffusion zone of Ag into the ZrCu matrix is approximately 50 μ-inches on either side of the Ag rich phase. Therefore, in a 0.020" platelet, the Ag rich phase represents 75 μ-in (or .04% of the platelet thickness), the Cu rich phase represents 50 μ-in (.03% of the thickness), and the ZrCu base metal represents 200000 μ-in (99.93%).

Figure 1.3.2-15. Phase Diagram Showing Single Phase Solid Solution of
Copper and Nickel
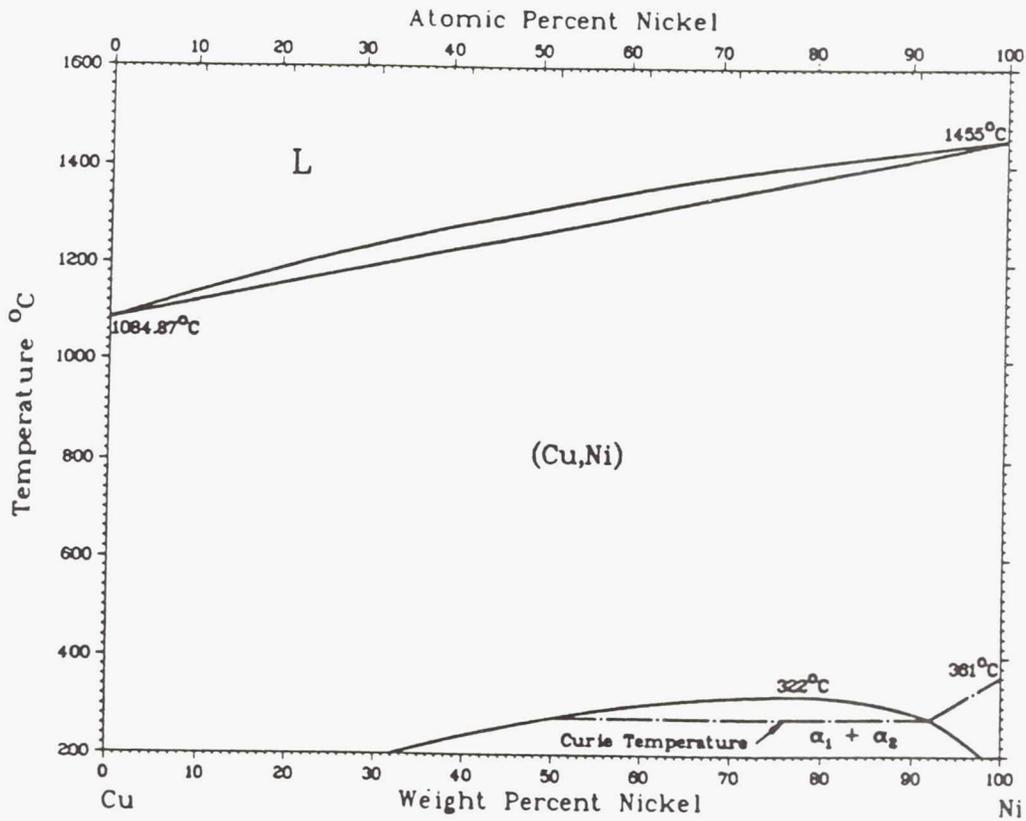
The Cu-Ni phase diagram from Reference 3 show that these two
elements form a simple single phase solid solution system at the
temperature associated with bonding and post-bond heat treat-
ing.

57
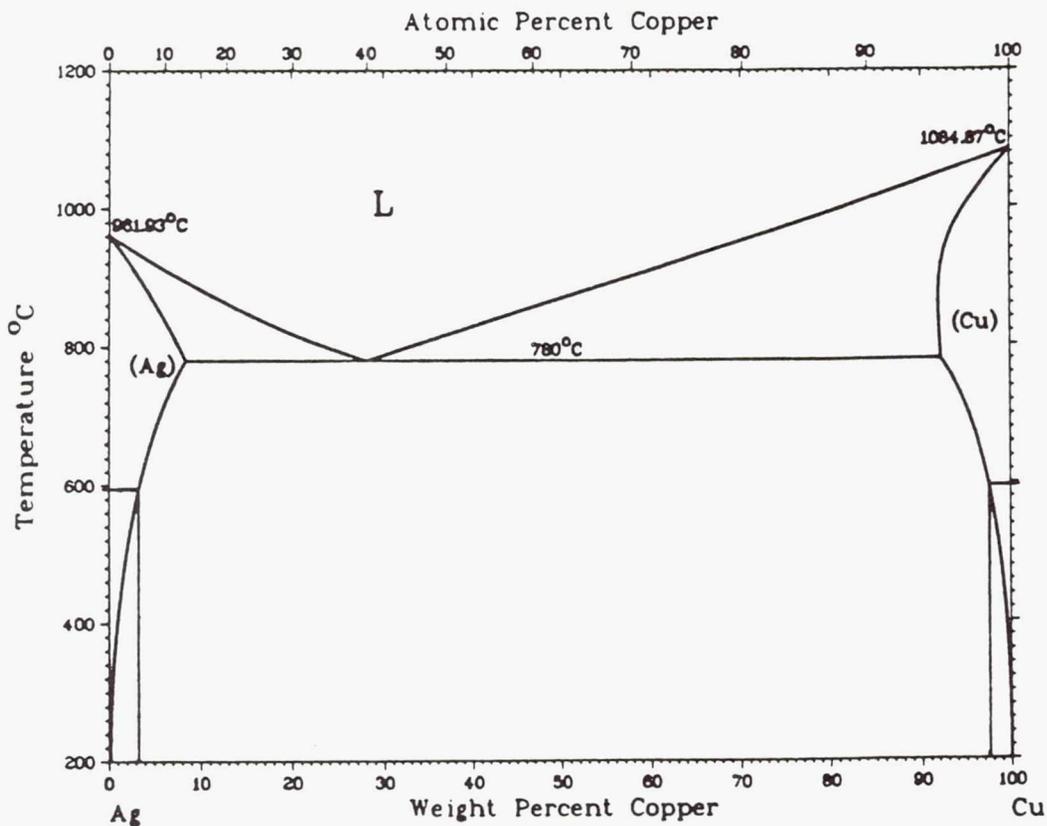
The Cu-Ag phase diagram from Reference 3 shows the limited extent of Cu and Ag solubility at the Zr-Cu aging temperature of 1100°F (593°C).

Figure 1.3.2-16. Phase Diagram Showing Limited Solubility of Copper and Silver

58

Ag and Ni Effects on Cu Conductivity
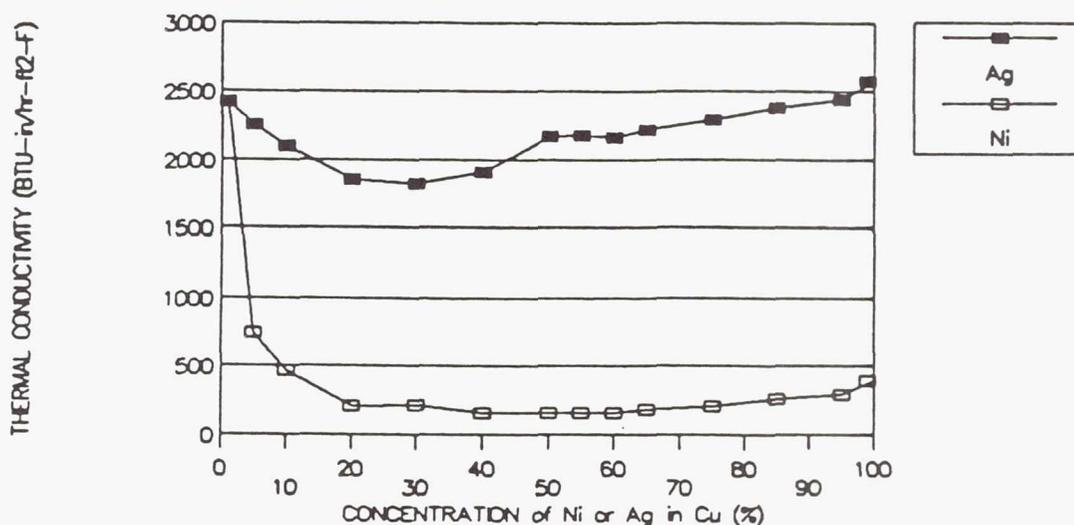
Solid solution alloying generally has a detrimental effect on the thermal conductivity of a pure metal. The effect of Ag on Cu conductivity is moderate at any temperature, because of the limited solid solubility of Ag in Cu, and Cu in Ag, and the high conductivities of the individual elements. Ni, however, shows a much stronger effect, accentuated by the complete solubility of Cu and Ni, and by the much poorer conductivity of Ni.

Figure 1.3.2-17. Silver and Nickel Effects on Copper Conductivity

1.3, Fabrication Techniques (cont.)

As in the case of 100% solid solution systems, the transverse bond thermal conductivity of a stack can be determined by adding the thermal resistivities of the base-metal and the bond. The only significant difference from the CuNi system is in the average solute content of the bond diffusion zone. In the CuNi system, there is a continuous Ni gradient. In the CuAg system, the diffusion zone has two distinct regions, the high Cu and high Ag phases. It is most accurate to assume two bond zones for each joint in the CuAg stack when calculating its thermal conductivity. Therefore, the bulk thermal resistivity of an Ag aided stack could be calculated by:

$$R_{bulk} = R_{bond\,1} + R_{bond\,2} + R_{zrcu} \tag{9}$$

or

$$k_{bulk} = L_{comb} / (L_1/k_1 + L_2/k_2 + L_{zrcu}/k_{zrcu}) \tag{10}$$

where

L_{comb} = the average platelet thickness

L_1 = width of the Ag rich bond phase

k_1 = the thermal conductivity of the Ag rich phase

L_2 = width of the Cu rich bond phase

k_2 = the thermal conductivity of the Cu rich phase

L_{zrcu} = width of the unaffected ZrCu

k_{zrcu} = the thermal conductivity of the unaffected ZrCu

1.3.3 Baffle Fabrication Conclusions

Utilization of the diffusion bonding process is a viable method to obtain required geometries within a homogeneous parent material structure. Recent progress with various solid-state diffusion aids are providing mechanical properties approaching that of the parent material. Silver is the diffusion aid of

choice for the regeneratively cooled baffle structures. Use of silver as a bonding aid for ZrCu has no measurable effect on the bulk thermal conductivity of the ZrCu due to the high thermal conductivity of the dilute AgCu and CuAg solutions. Tensile strength, although showing a slight degradation, is sufficient for structural integrity of the part. Further modifications to the bonding parameters can continue to enhance the strength characteristics of the silver-aided diffusion-bonded ZrCu.

Nickel is the bonding aid currently in use for diffusion bonding of ZrCu components. Use of nickel reduces the bulk thermal conductivity of a bonded ZrCu stack. The extent of the reduction is dependent on the specific bonding parameters and the average platelet thickness of the stack. The bonding parameters used for this study resulted in thermal conductivities of 80% of the base-line properties at room temperature and 89% of the base-line at 1200 deg F. The thermal conductivity of nickel aided bonds does show improvement at elevated temperatures, however, not as much as would be expected solely by the alloying effects of Cu and Ni on thermal conductivity.

2.0 CHANNEL MACHINING STUDY

2.1 MATERIAL SELECTION

Copper alloys that have been evaluated for use as liners in regeneratively cooled combustion chambers include: OFHC Copper, GlidCop (Cu-0.15Al2), ZrCu (Cu-0.15 Zr), NARloy-Z, and NASA-Z (both Cu-3Ag-0.4Zr). Copper is desirable due to its high thermal conductivity. Copper alloys bring increased strength with slightly lower thermal conductivities. As chamber operating pressure differential become higher, use of higher strength alloys is necessary.

Design of chamber liners has used low-cycle-fatigue data for estimating the life of the chamber. Recent Aerojet in-house studies (Ref. 7) suggest that chamber liner performance should not be limited exclusively to strain controlled low-cycle-fatigue data, but should also factor in the dependency upon creep-rupture strength. These analyses indicate that an alumina dispersion strengthened copper alloy (GlidCop) liner would provide a longer life chamber than those utilizing NASA-Z or ZrCu copper alloys.

Dispersion strengthened (DS) copper alloys offer a unique combination of high strength and and thermal conductivity properties. The strengthening results from a uniform dispersion of fine aluminum oxide (Al_2O_3) particles in a pure copper matrix. The Al_2O_3 particles act as barriers to the movement of dislocations. They are stable at elevated temperatures, and help retain much of the room temperature strength of DS copper at or after exposure to such temperatures.

The most effective strengthening is achieved when both the Al_2O_3 particle size and the spacing between the particles are small. Various methods are available, and have been used in the past for making DS copper. These methods include: mechanical mixing, co-precipitation, melting of nitrates, and internal oxidation. Of these methods, the best dispersion has been obtained by the internal oxidation process, and it is the only commercial process in use today to make DS copper (Reference 8). Figure 2.1-1 illustrates the manufacturing process for the present day GlidCop alloy.

```
┌─────────────────┐
│      Melt       │
│     Cu-Al       │
└─────────────────┘
         │
┌─────────────────┐
│    Atomize      │
│   (Powder)      │
└─────────────────┘
         │
┌─────────────────┐
│   Blend with    │
│    Oxidant      │
└─────────────────┘
         │
┌─────────────────┐
│    Internal     │
│    Oxidation    │
└─────────────────┘
         │
┌─────────────────┐
│   Reduction     │
└─────────────────┘
         │
┌─────────────────┐
│  Consolidation  │
│  (Full Density) │
└─────────────────┘
```
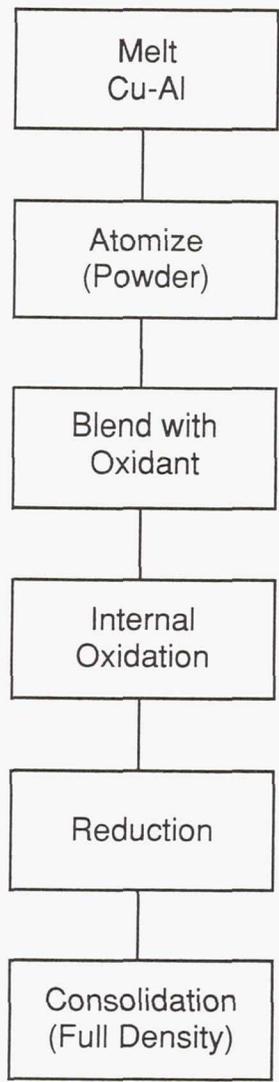
2.4.0.48

Figure 2.1-1. Manufacture of Dispersion Strengthened Copper

2.1, Material Selection (cont.)

Although the copper alloy, GlidCop, was dismissed in earlier evaluations (Ref. 9), the recent processing changes have resulted in superior mechanical properties. Table 2.1-I lists the properties of the various GlidCop alloys compared to OFHC copper. For this study, the Al-15 was selected. Table 2.1-II lists the compositions of the various GlidCop alloys.

Changing the material used for the combustion chamber is dependent on demonstration of the adaptability of the new alloy to the design features of the chamber. Utilization of copper alloys does have a foundation in the use of copper for the basic fabrication processes. However, various constituents in each alloy may cause a slight modification of the fabrication process to provide quality hardware.

Figure 2.1-2 depicts the typical construction of a regeneratively cooled combustion chamber wall. Cooling channels are milled into a nozzle shaped liner. Selection of a new chamber material must first offer demonstration of its machineability and establish the recommended machining parameters. Next, the backside of the coolant channels in the liner is closed by depositing a pressure containing shell over the entire liner. A good bond between the liner and closeout material must be demonstrated to contain high pressure coolant. Chemical compatibility between the propellants and combustion products are required of the selected liner and closeout materials.

The machining studies documented in this report are a continuation of an earlier IR&D program (Reference 12) which investigated machining a long-life channel geometry utilizing state-of-the-art copper alloys NASA-Z and ZrCu.

In support of this IR&D task, analytical work indicated that achieving higher performance within a reduced-size space transportation system required operation at higher chamber pressures. Operation of these engines at higher chamber pressures provides a more difficult task for engine cooling due to the higher heat fluxes encountered. An additional complexity is also encountered at low-thrust-throttled conditions where the amount of propellant available for active cooling is very small relative to the total heat load.

64

TABLE 2.1-I

PHYSICAL PROPERTIES OF DS COPPER AND OF COPPER

Property	C15715	C15760	OF Copper
Melting Point: °C.	1083	1083	1083
Density: at 20°C., Mg/m^3	8.84	8.81	8.94
Electrical Resistivity: at 20°C. $\mu\,\Omega \bullet m$	186	221	171
Electrical Conductivity: at 20°C., Megmho/m	54	45	58
% IACS	92	78	101
Thermal Conductivity: at 20°C., Watt/meter $\bullet$ °K	365	322	391
Coefficient of Thermal Expansion: (20-1000°C.), $\mu\,m/m/°C.$	16.6	16.6	17.7
Modulus of Elasticity: at 20°C., GPa	125	125	115

TABLE 2.1-II

CHEMICAL COMPOSITIONS OF DS COPPER GRADES

Grade Designation		Copper		Aluminum Oxide	
CDA	Manufacturer	Wt. %	Vol. %	Wt. %	Vol. %
C15715	AL-15	99.7	99.3	.3	.7
C15720	AL-20	99.6	99.1	.4	.9
	AL-25	99.5	98.8	.5	1.2
C15760	AL-60	98.9	97.3	1.1	2.7
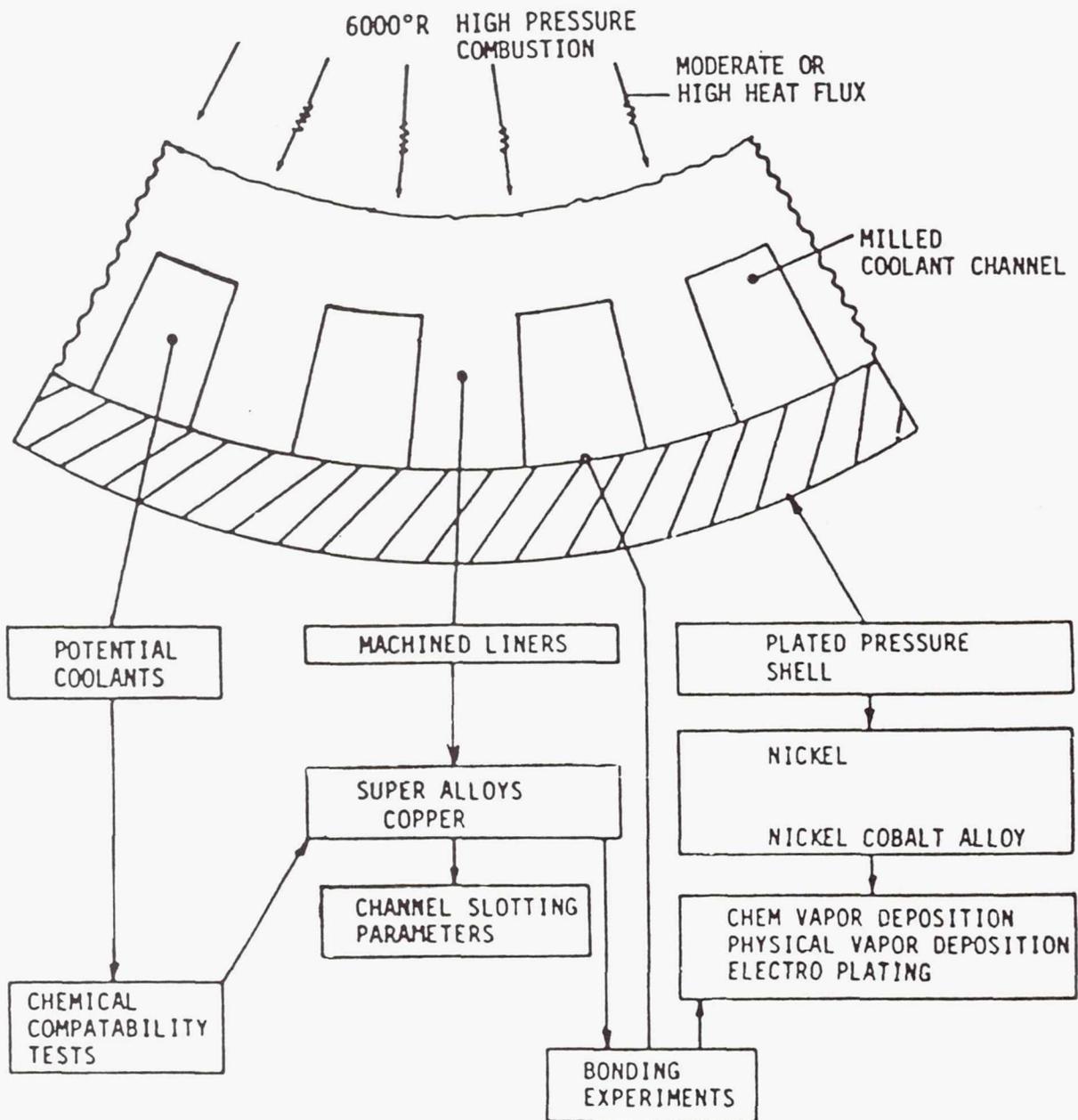
Figure 2.1-2. Typical Construction and Development of a Regeneratively Cooled Combustion Chamber

2.1, Material Selection (cont.)

Computer model analyses were undertaken which indicated that the primary consideration in optimizing the channel configuration for the long-life engines was to minimize channel width. This enabled full advantage of the coolant surface area provided by the land and external wall. In this manner a large heat flux transformation was accomplished. The added fin effect produced by using smaller channels was aided by the increase of coolant heat transfer coefficients on the land and external wall. Because hydrogen heat transfer coefficients increase as the wall temperature decreases, the resulting channel sizes are reduced. Reduction of the gas side wall temperatures gave an added bonus of longer cycle life due to the reduced thermally induced strain. These tradeoffs for the 7.5K thrust level TCA are presented in Figure 2.1-3.

Optimization of the material properties for GlidCop has not been completed for the final TCA analysis. Additional stress analysis to factor in the creep-rupture strength (Figure 2.1-4) gained by using the GlidCop alloy remains. It is important to first address the fabricability of this dispersion hardened alloy and to obtain the strengths of both electro formed (E.F.) closeouts and welded joints prior to finalization of the design and its supporting analysis.

2.2   CHAMBER DESIGN

The 7.5K thrust level regeneratively-cooled chamber profile is shown in Figure 2.2-1. A summary of the channel dimensions is depicted in Table 2.2-I. Several factors increase the difficulty of machining the chamber channels and need to be addressed prior to fabrication of the GlidCop chamber liner. These include:

1) HIGH ASPECT RATIO (CHANNEL DEPTH/WIDTH = 10:1): Channels are deep, varying from a 0.400" depth at the converging section of the barrel to a 0.083" depth at the throat.

   • Higher aspect ratios increase the tendency for channels adjacent to the cutter to "lay-over" during machining. Tendency for channel lay-over is inhibited somewhat by the strengthening effects of the contour curvature.

W_{Chan} = 0.10", Land = .011", 233 Channels   MR = 5, PC = 2075 psia, $\dot{w}_{H_2}$ = 2.6317 lb/s

OTV Throat Study

ΔT_{chan}, $T_{max\ wall}$, $\Delta P/in$, V_{H_2}

Channel Depth @ T_b = 200°R

Max ΔT Across Channel

Max Wall Temp (°F)

Velocity

$\Delta P/in$

y-axis (left): $T_{wall\ max}$ (°F) and $\Delta T_{across\ Channel}$

y-axis (right): $\Delta P/in$ (psia/in) and V_{H_2} (ft/s)

x-axis: Channel Depth (inches)
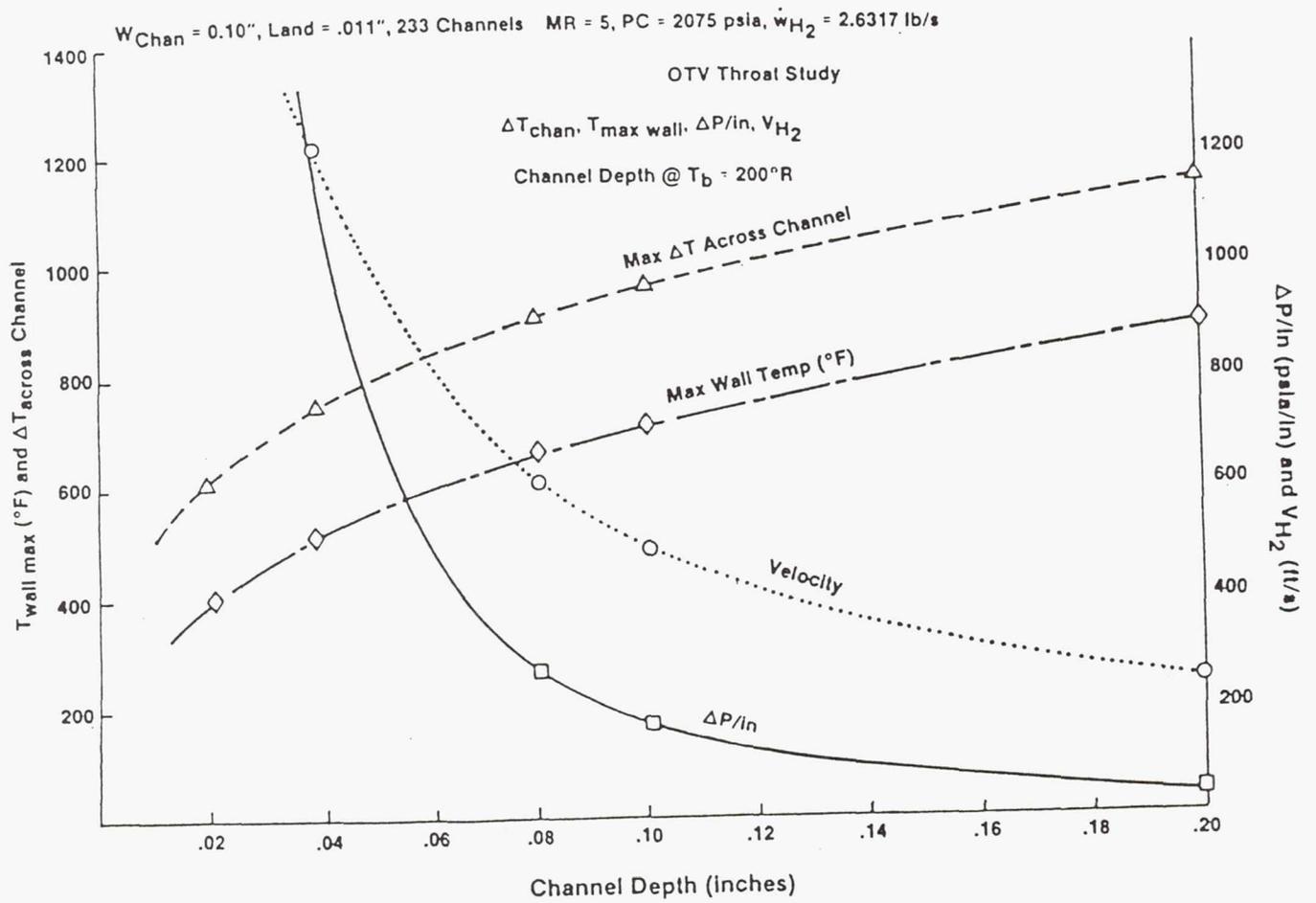
Figure 2.1-3. 7.5K Thrust Level Throat Geometry Tradeoff Study

68
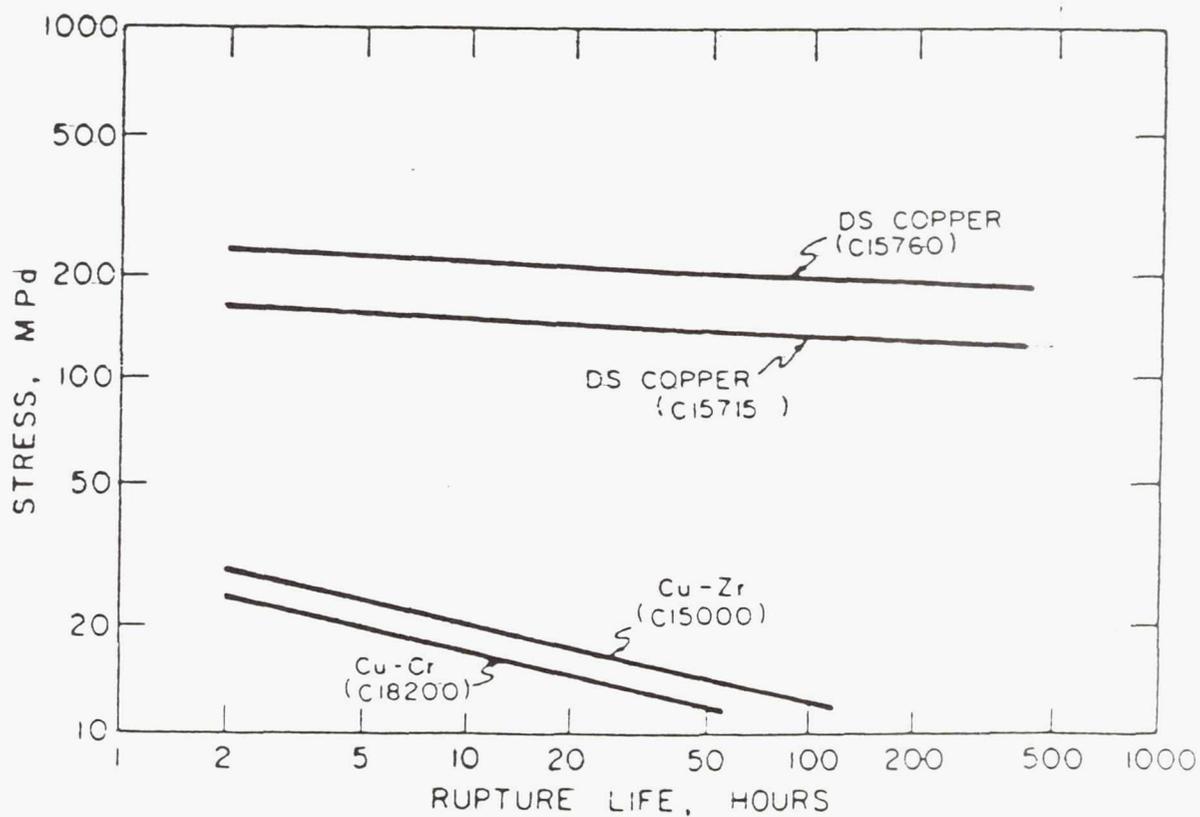
DS COPPER (15760) COLD WORKED 73%
DS COPPER (15715) COLD WORKED 84%

Figure 2.1-4. Stress Rupture Properties of Copper Alloys

69
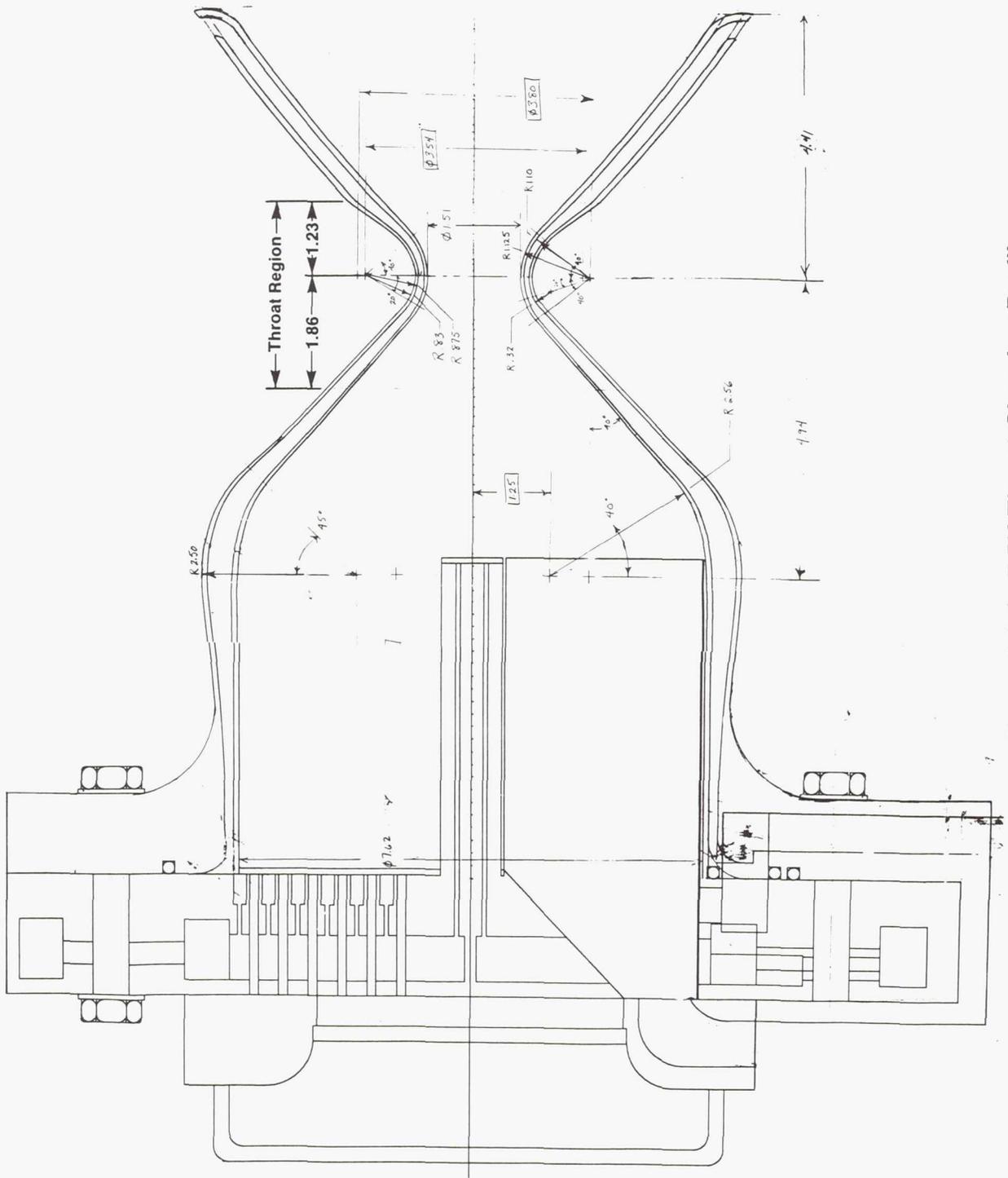
Figure 2.2-1. 7.5K Thrust Chamber Profile

TABLE 2.2-I

SUMMARY - 7.5K TCA REGENERATIVE-COOLED CHAMBER COOLANT-CHANNEL GEOMETRY

POSITION ON CHAMBER	A/AT	DEPTH (IN)	WIDTH (IN)	LAND (IN)	WALL (IN)
AT INJECTOR FACE	25.32	0.105	0.065	0.040	0.060
END OF BAFFLES	25.32	0.400	0.062	0.040	0.0582
MID CONVERGING SECTION	12.20	0.287	0.029	0.040	0.0337
THROAT	1.0	0.083	0.010	0.011	0.0200
AREA RATIO 2	2.01	0.190	0.019	0.011	0.0380
AREA RATIO 4	4.03	0.300	0.030	0.013	0.0600
AREA RATIO 8	8.06	0.300	0.030	0.030	0.0600
AREA RATIO 17	16.90	0.300	0.030	0.056	0.0600
HYDROGEN INLET MANIFOLD	28.0	0.300	0.030	0.080	0.0600

- Deep cuts induce higher blade stress because of the need to use larger blade diameters offset with less arbor support.

2) LENGTH OF CUT: The 7.5K thrust level OTV chamber has an approximate 16.27" total profile length over which to maintain tight tolerances. The most critical "mini" channels in the throat area cover a profile length of approximately 3.8".

   - Longer cuts tend to increase blade wear and the risk of blade failure or breakage.

   - Chamber is at greater risk due to friction generated heat of dull-blade cutting. Possibility increases for distortion of channels and possible cracking, chipping, or breakage of cutters.

3) HIGH CONTRACTION RATIO (CR =25): Contour narrows sharply at the throat, converging and diverging angles equal to 40 degrees.

   - May require cutter blade size reduction in the narrow throat region. Supporting arbor diameter is further reduced to achieve deeper cuts.

   - Thinnest channels must be machined where blade stability will be difficult to maintain.

4) THIN WALL: Gas-side wall thickness varies from a 0.060" maximum at the chamber barrel and nozzle to a 0.020" minimum at the throat.

   - Reduces chamber strength. Chamber can deflect from tool pressure during:

   - Machining of the channels, if I.D. machined first. Use of chamber ID mandril for support of chamber required.

   - Boring of chamber ID, if O.D. and channels are machined first. Use of some type of OD support necessary.

2.0, Channel Machining Study (cont.)

2.3 FABRICATION STUDY

The overall objective for this subtask was to demonstrate the ability to repeat fabrication of the "mini"-channel technology in GlidCop. This targeted the first two items of concern, the aspect ratio of the channel and the length of cut. Prior to fabrication of the chamber, the ability to maneuver the cutting tool through the high contraction-ratio throat and the ability to maintain the thin gas-side wall thickness would need to be demonstrated in a contoured billet. However, the basic cutting parameters needed to be established first.

The ability to fabricate channel and land widths to tolerances of approximately 0.001 inch was verified by measurements made with a toolmaker's microscope. Two groups of channels were made in 1.9 inch diameter barstock. The first group replicated the channels of the 3.0K thrust level engine throat geometry and the second group demonstrated the channels for the 7.5K thrust level chamber throat geometry. These dimensions are summarized in Table 2.3-I.

In support of the fabrication study, a 2.0 inch diameter bar stock of GlidCop Al-15 was ordered from SCM Metal Products in Cleveland, Ohio. The part number assigned by SCM is AL15RAA and that assigned by Aerojet is 1203258. Recommendations from SCM on the machining of GlidCop indicated that due to its higher strength, it should machine more like a steel than a copper. Within the test plan, the initial conditions were reviewed from the ZrCu machining studies and used as input to the machinist for the cutting of the shallow 0.038" cuts. Modifications to these parameters where then used to make the deeper 0.083" cuts. Because the machining of the mini-channels is unique, no reference data for machining similar channels in steel is available for comparison.

The test plan is presented in Table 2.3-II and accompanied by the illustrations in Figure 2.3-1. The desired tolerance to be held on channel and land dimensions was +/- 0.002".

The first step of the test plan (Table 2.3-II) was directed at preparation of the bar stock. Reasons for this are twofold. First, the processing method for GlidCop yields a thin (less than 0.030" radial) skin of OFHC on the surface. For these studies,

TABLE 2.3-I

3.0K TCA Chamber @ Throat			7.5K TCA Chamber @ Throat
Entrance angle	=	40 degrees	40 desgrees
Exit angle	=	15 degrees	15 degrees
Channel Width	=	0.010 inches	0.010 inches
Channel Depth	=	0.038 inches	0.083 inches
Land Width	=	0.011 inches	0.011 inches
Gas Side Wall	=	0.020 inches	0.020 inches
Throat Diameter	=	0.96 inches	1.500 inches

Step Transition
    Barrel & Nozzle
        Channel Width = 0.020 inches
        Channel Depth = 0.100 inches
        Land Width
        Gas Side Wall

        Channel Width
        Channel Depth
        Land Width
        Gas Side Wall

Gradual Transition
    Barrel (-2.41 inch)
        0.025 inches
        0.250 inches
        0.040 inches
        0.0310 inches
    Nozzle (2.41 inch)
        0.030 inches
        0.300 inches
        0.039 inches
        0.060 inches

TABLE 2.3-II

TEST PLAN

1) Clean up 2" diameter GlipCop bar stock to 1.9" diameter.

2) Duplicate geometry of 3.0K design without transition step

3) Repeat Step #2 to a increased depth of 0.083".

4) Demonstrate smooth transition from throat geometry to barrel geometry.

Inspection Requirements

1) Surface finish

2) Land deformation

3) Tolerance, actual held (desired ± .002")

a)

6"

Remove Cu Coating
Clean up O.D.

1.9"

b)

.011

.010 Wide
x .083 Deep

a) Cut 12 Channels
b) Compare Cutting
Charactristics to
those of Zr Cu

c)

.011

.010 Wide
x .083 Deep

a) Cut 12 Channels

d)

.025 Wide
x .25 Deep

.010 Wide
x .083 Deep

.030 Wide
x .3 Deep

a) Cut 6 Channels
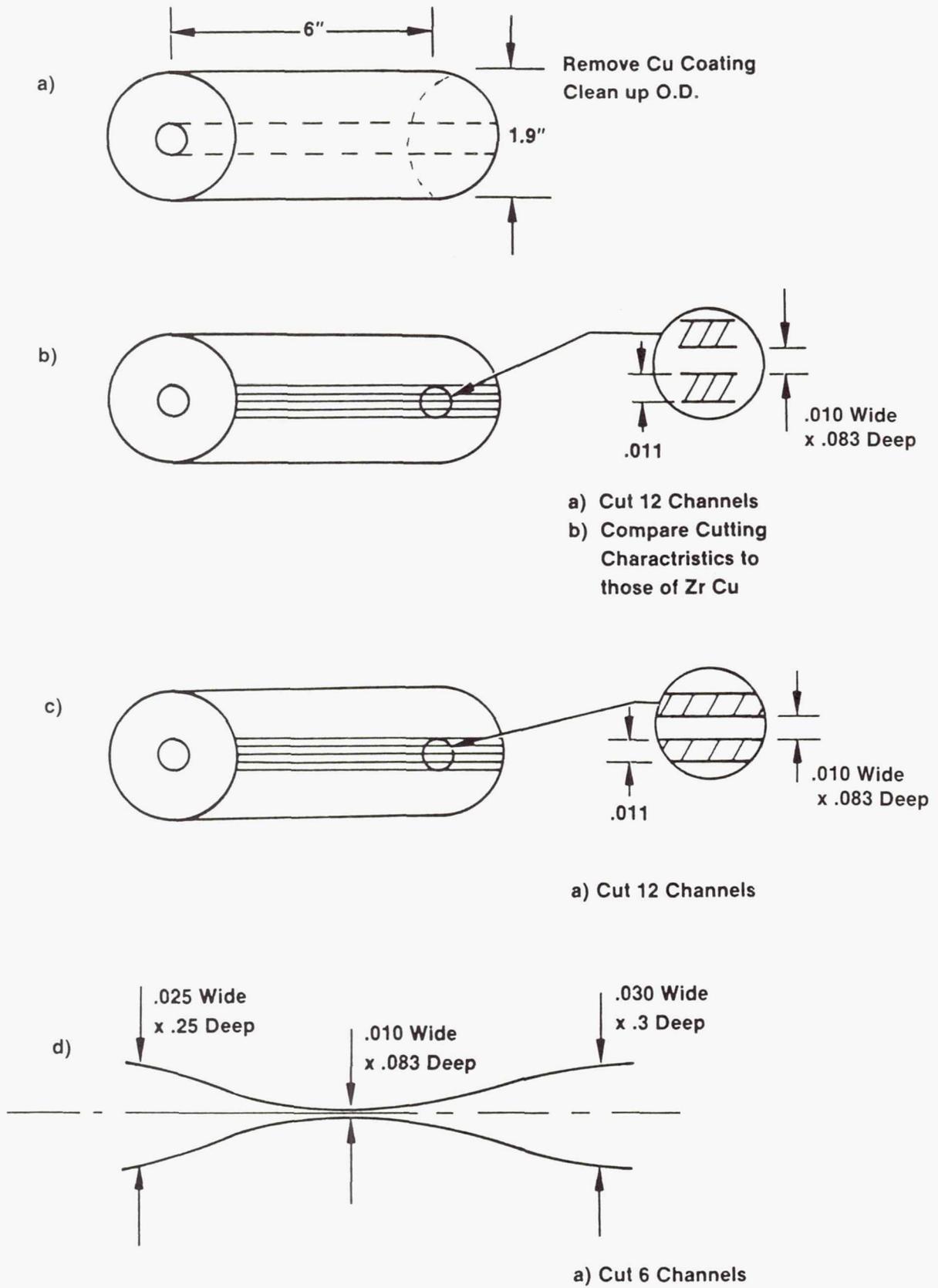
Figure 2.3-1. GlidCop Machining Study Test Plan

76

2.3, FabricationStudy (cont.)

this OFHC copper layer was removed. Secondly, it was desired to have the OD of the barstock equal to the OD dimension of the 7.5K throat diameter (Figure 2.3-1a).

Identification of the variables involved in the understanding of the machineability of the GlidCop alloy include: spindle speed, cutter feed rate, lubrication system, feed direction, cutting tool deflection, rake angle/number of teeth, and material hardness.

1) Spindle speed: The speed was optimized for efficiency of time and quality of cut. Speed was varied from 210 to 325 RPM (55-85 SFPM) for the 0.038" deep cut with a 1" diameter high speed steel cutter and from 325 to 83 RPM (233 - 58 SFPM) for the 0.083" deep cuts with a maximum cutter diameter of 2.75 " high speed steel. This indicated a sharp drop off in speed rate for the increased depth of cut with increased cutter diameter. Earlier work with the ZrCu tried speed in the range of 250 to 335 RPM (65 - 87 SFPM) with better success at the lower rate of 250 RPM. The ZrCu studies were accomplished with a 1" diameter, high speed cutter.

2) Cutter feed rate: Initially, a 0.375 fpm feed rate was evaluated which was rapidly increased to 0.85 to 1.5 fpm for the 0.038" deep channels. A slightly slower rate of 0.75 was judged best for the deeper (0.083") cuts. The earlier work with ZrCu evaluated feed rates of 0.6 to 2.4 ipm (equivalent to 0.05 to 0.2 fpm).

3) Several lubrication and coolant techniques were evaluated. The first used kerosine and proved very difficult to keep the cutting blade clean. Next, brushing oil onto the channels was evaluated. This too failed to adequately clear the chips and keep the cutter clean. The most successful was the use of a mixture of oil and water, commonly referred to as "Spray Mist", directed onto the channel using a 40 psi air source.

4) Two types of peripheral milling were considered as options for slotting: conventional versus climb cutting (see Figure 2.3-2). Both cutting methods were attempted, however conventional cutting produced considerable cutter wobble causing the channel dimensions to fall outside desired tolerances. Climb cutting produced less cutter wobble and gave good results that were within the desired tolerances.

Direction of Cutter Rotation

Key

Hollow Ground Cutter

Shaft

Cutter Support

Work Feed

Work Feed

Conventional or Up Milling

Climb or Down Milling
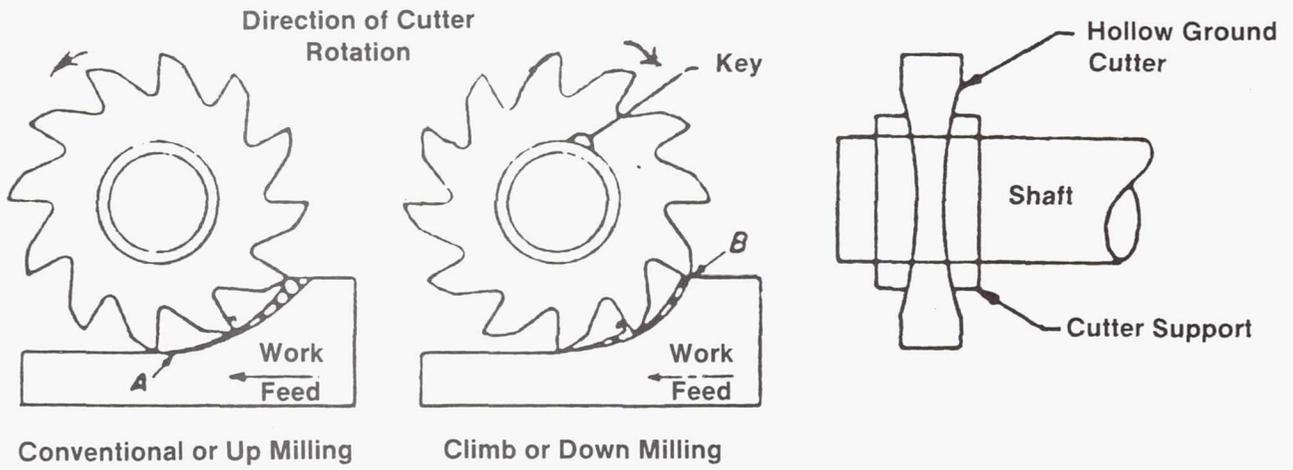
Figure 2.3-2. Conventional Versus Climb Milling

5) Cutting tool deflection: In an effort to minimize the deflection of the cutter due to the force of cutting the channel, an arbor was made to support the cutter. The arbor served to stabilize the blade resulting in more accurate machining and also reduced the cutter tool bending stress. The depth of the channel to be cut established the length of exposed blade on the cutter. This tooling is shown in Figure 2.3-3.

6) Number of teeth/Cutter diameter: For the shallow 0.038" deep cuts, a 1" diameter cutter with 90 teeth was used. For the deeper 0.083" cuts, a 2.75" diameter cutter was used with 70 teeth. This trend is opposite what was observed with the ZrCu studies in which a 1" diameter cutter with 30 to 24 teeth was preferred.

7) Material hardness: The Brinell hardness was measured at an average of 109. This is in the expected range for the heavily cold worked structure of the Glidcop. This compares to a Brinell hardness of 60 for the softer ZrCu used in earlier studies.

Configuration of the cutter tool was also evaluated. A blade was ground to form a hollow-ground blade and used as a cutting comparison with the straight blade. These configurations are illustrated in Figure 2.3-4. The hollow ground blade was found to make sharper cuts and was used in subsequent machining studies.

The methodology utilized in approaching cutting of the channels is documented by Table 2.3-III.

2.3.1 Inspection Results

Figure 2.3-5 shows the bar stock at the completion of the machining studies. Cross sections were taken at the locations noted. Closeup photographs of the channels are presented in Figure 2.3-6 and 2.3-7. After mounting of the sections, photographs and measurements were taken of the channels. Since the channels were machined with varying parameters (Figure 2.3-8), the last two (#11 & 12 and #23 & 24) channels from each group were inspected with a toolmaker's microscope (or Measurescope). This data is presented in Table 2.3-IV for the 0.038" deep channels and Table 2.3-V for the 0.083" deep channels. Expected tolerances of +/- 0.002"

Figure 2.3-3. GlidCop 7.5K TCA Regenerative-Cooled Chamber Channel Fabrication Study — Tooling

Cutter for
0.038''
Channel Depth
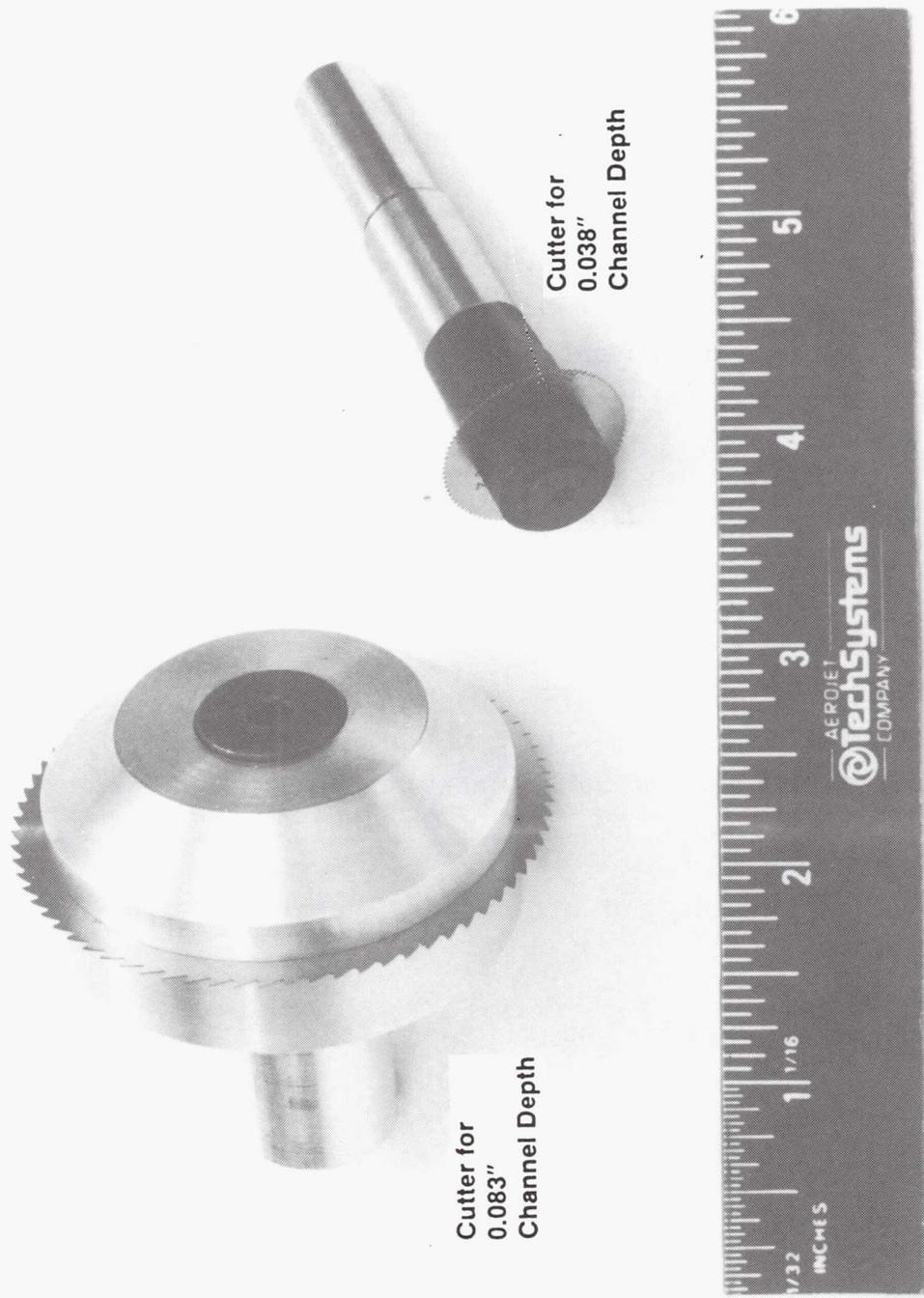
Cutter for
0.083''
Channel Depth

81

a) Hollow Ground — Cutter Support

b) Straight Sided Cutter — Cutter Support

2.4.0.50
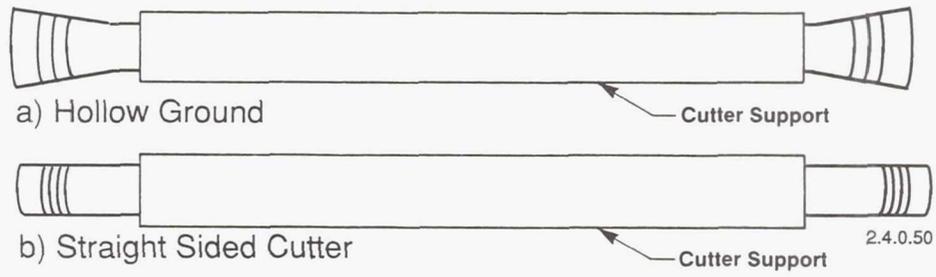
Figure 2.3-4. Cutter Configurations

TABLE 2.3 - III
MACHINIST NOTES

Cut No.	Spindle Speed (RPM)	Feed Rate (fpm)	Type	Spray	Time /channel (min)	Depth of cut (inches)	Type of Mill Cut	Notes
1	210		0.375		16	0.038	Climb	Not bad - cutter plugged at times. 3 teeth were missing at end. Channel increased dimensionally from start to finish.
2	325		0.460	A	13	0.038	Climb	Good - no plugging of teeth.
3	325		0.460	A	13	0.038	Climb	Good
4	325		0.600	A	10	0.038	Climb	Good - slot 0.011
5	325		0.750	A	8	0.038	Climb	Good - slot 0.010
6	325			A	9	0.038		Good
7	325		0.85	A	7	0.038		Good - slot 0.010, land bending not as noticeable
8	325		1.00	A	6	0.038		Good - Burr starting to form on top of slot
9	325			A		0.038		
10	325		0.850	A	8	0.038	Climb	Good - 0.010 slot, cutter becoming dull, land 0.012.
11	325		0.850	A	7	0.038	Climb	
12	325		1.500	A	4	038	Climb	
New Cutter Installed								
13	325			A		0.083	Climb	Cutter broke.
14								Skipped - broken blade in way
15	325		0.17	A	34	0.083		Good - 0.010 slot
16	325		0.200	A	28	0.083		Good - 0.010 slot, 0.001 deflection in adjoining land
Utilized two cut approach								
17	325		0.600	A	10	0.044	Climb	First cut good, fast cutting
17	325		0.400	A	15	0.039		Second cut good - first cut a few tenths bigger - no deflection of adjacent land
18	325			A	11	0.048	Climb	Good
18	325			A	10	0.035		Good
19	325			A		0.050		Good
19	325			A		0.038		Good
20	325			A	12	0.050	Climb	Slot OK
20	325			A	10	0.038		Slot OK - bent adjacent land cutter dull
New cutter								
21	210			A		0.050	Std	Slot no good with std. milling
21	210			A		0.038	Climb	Slot good
22	210			A		0.050	Climb	Good
22	210			A		0.038	Climb	Good
New cutter - 2.75" - 73 teeth								
23	83		0.750	A	12	0.050	Climb	Good
23	83		0.750	A	8	0.038	Climb	Good
24	83		0.860	A	7	0.083	Climb	Good - 0.010 slot
25	83		1.000	A	6	0.083	Climb	Good - 0.010 slot
26	83			A		0.083	Climb	Good - 0.010 slot, no bending of land-coarse teeth work faster

NOTE: A - Oil and water mist with air

82

Figure 2.3-5. GlidCop 7.5K TCA Regenerative-Cooled Chamber Channel Fabrication Study
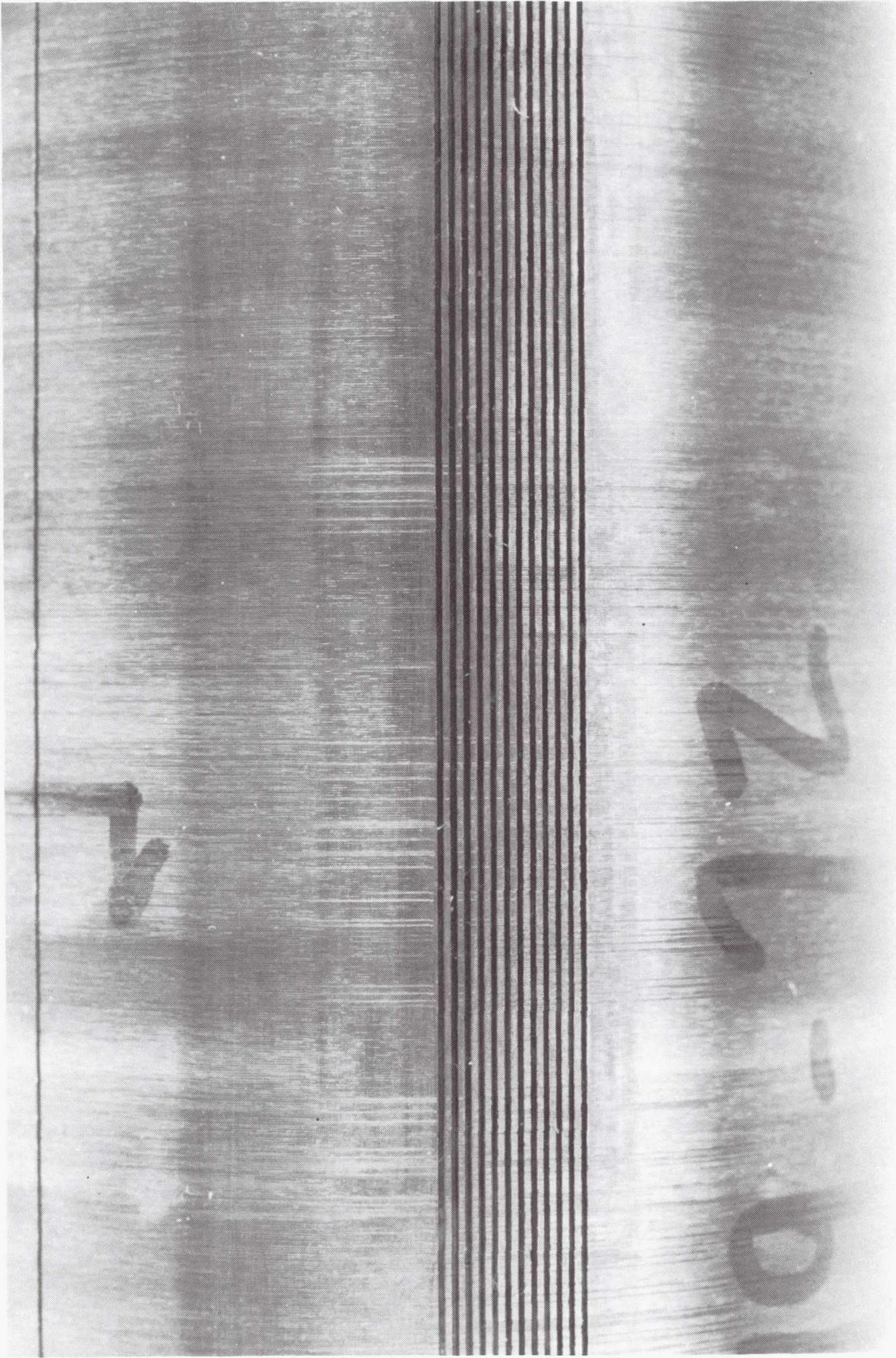
Figure 2.3-6. GlidCop 7.5K TCA Channel Design (0.010" Wide x 0.083" Deep)
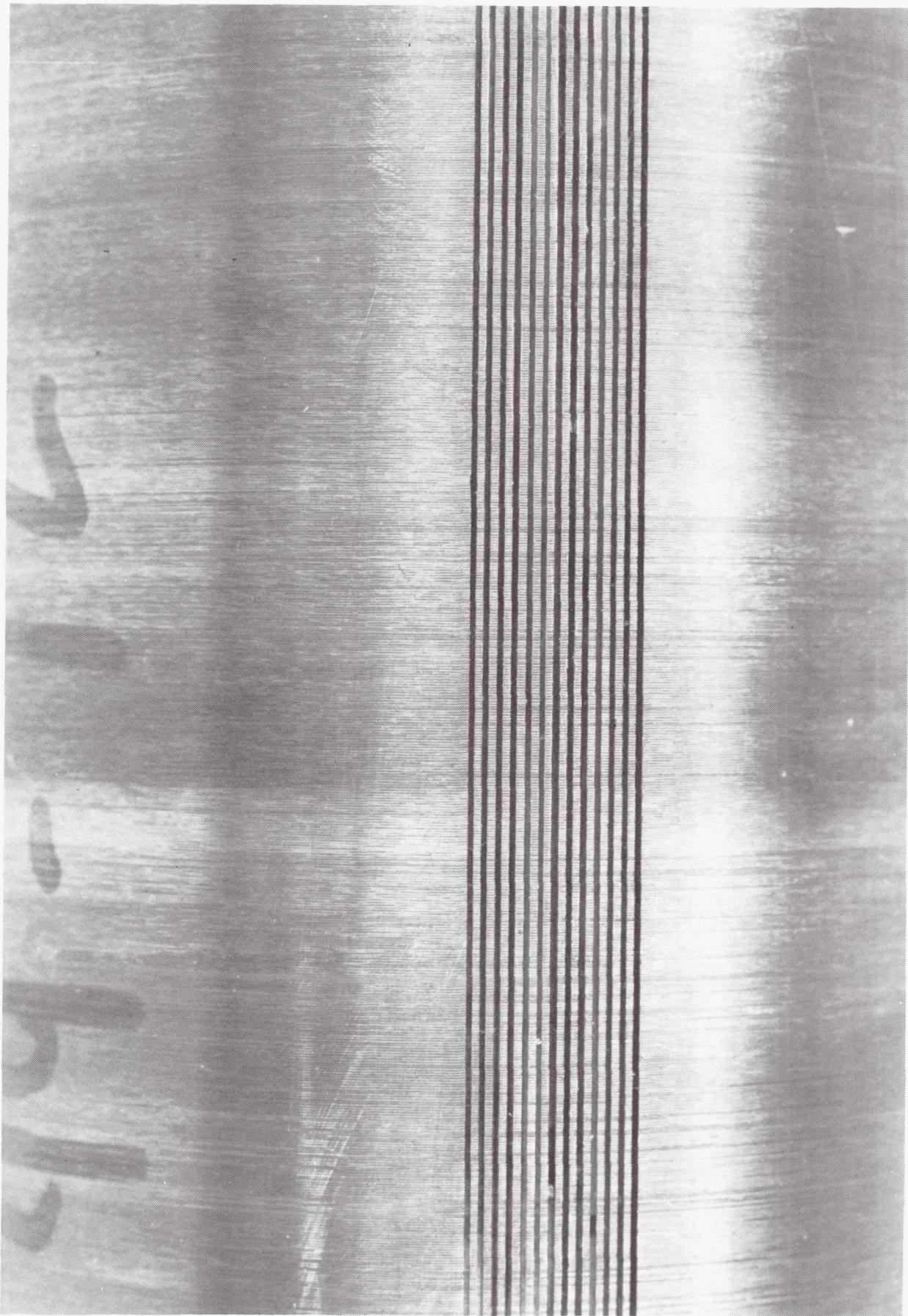
Figure 2.3-7. GlidCop 3.0K TCA Channel Design (0.010" Wide x 0.038" Deep)

1 Cut to
Depth of
0.083"

2 Step Cut:
0.045" Depth
0.038" Depth

1 Cut to
Depth of
0.083"

1
2
3
4
5
6
7
8
9
10
11
12
13

10X Scale
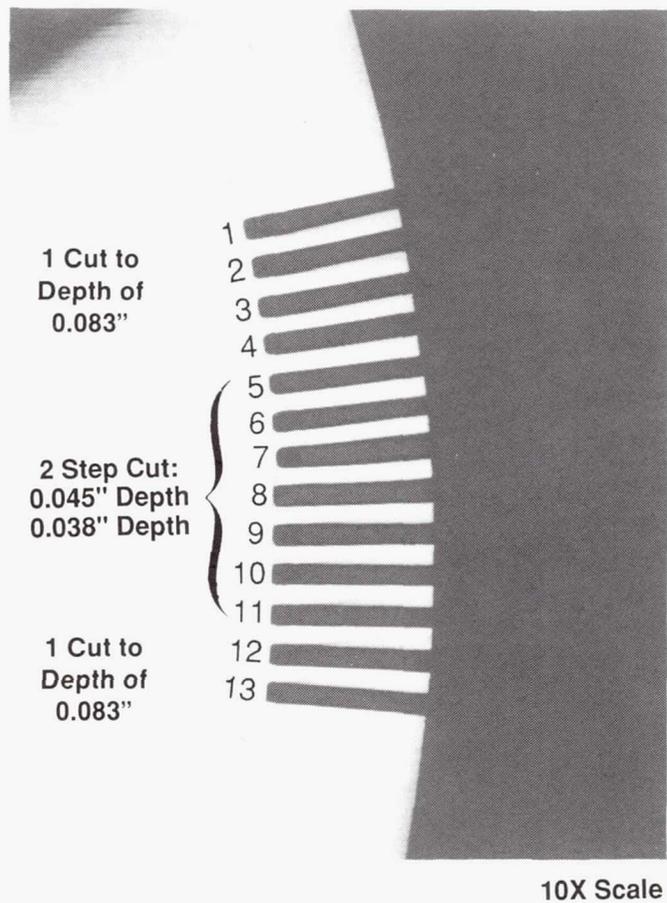
Figure 2.3-8. Cross-Section of 0.083" Deep Channels

TABLE 2.3-IV

GLIDCOP MACHINING STUDIES
0.038″ DEEP CHANNELS

Shallow Channels - GlidCop

	#1		#2		#3
A	.0106	A	.0103	A	.0103
B	.0101	B	.0102	B	.0101
C	.0118	C	.0120	C	.0123
D	.0110	D	.0114	D	.0117
E	.0370	E	.0375	E	.0373
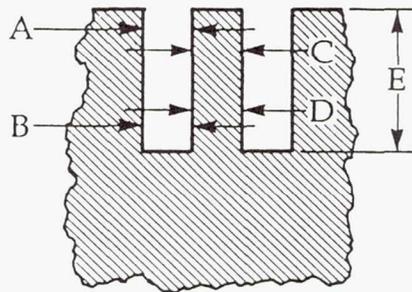
TABLE 2.3-V

GLIDCOP MACHINING STUDY

0.083″ Deep Channels

	#1		#2		#3
A	.0102	A	.0102	A	.0099
B	.0100	B	.0097	B	.0105
C	.0120	C	.0127	C	.0122
D	.0100	D	.0110	D	.0105
E	.0840	E	.0850	E	.0855
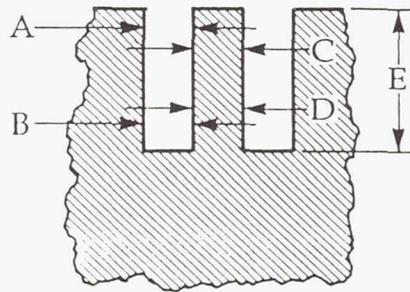
2.3, FabricationStudy (cont.)

were maintained. Key-stoning effects on the land dimensions due to the deep channels are within the allowable tolerance band as illustrated in Figure 2.3-9.

Channel wall roughness was measured at an average of 63 micro inches. This is slightly rougher than the 24 to 42 micro inches recorded at completion of the earlier studies with ZrCu.

2.3.2 Transition of Channels

With the mini channels through the throat area, the channel goes through a transition in cross-sectional area as it moves up into the barrel section. Figure 2.3-10 outlines two approaches to this widening of the channel. The first is a step transition in which the cutter is changed to a thicker blade to cut a wider path. As the two cutter paths (W1 and W2) come together, a step is formed in the flow stream. The 3K thrust level chamber utilized this step machining method with the regeneratively cooled throat section shown in Figure 2.3-11. This is simple to machine, however, a large pressure drop is experienced due to the abrupt transition.

With the higher thrust level engines, a method to blend the channel transitions is desirable. Though this can be achieved with the same cutters used to generate the channels, it would be a time consuming and costly process. Alternate methods of achieving this blend were explored as part of this channel fabrication subtask.

One method would be to use different thickness cutters to machine channels of width W1 and W2. An EDM (Electron Discharge Machining) electrode would be made to burn off the edges from the resulting step. Although it is not cost effective to EDM the entire channel, EDMing the transition portion would not be cost prohibited.

A second method explored was the use of a "fly cutter". The channel transition achieved with this special cutter is shown in Figure 2.3-12. The cutter used in this step is shown in Figure 2.3-13. To use this cutter, the initial channel geometry would be cut into the chamber resulting in a step transition between the two channel widths. The fly cutter would then be used in the transition section to
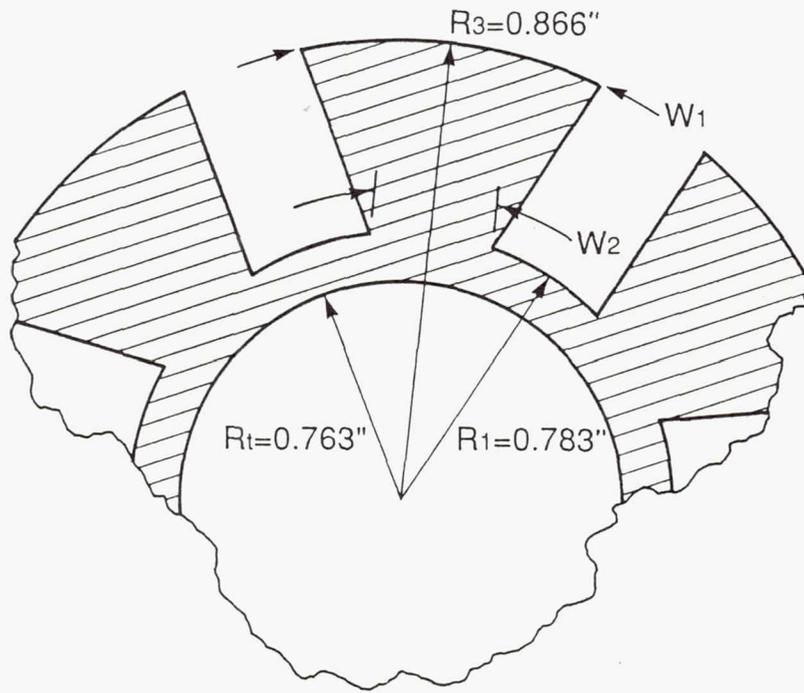
Figure 2.3-9. "Key-Stone" Effect on Channel is Within Channel Tolerance

Step Machining

a)

W₁ ... W₂   (Top View)

D₁ ... D₂   (Side View)

Blended Machining

b)

W₁ ... W₂   (Top View)

D₁ ... D₂   (Side View)

2.4.0.52
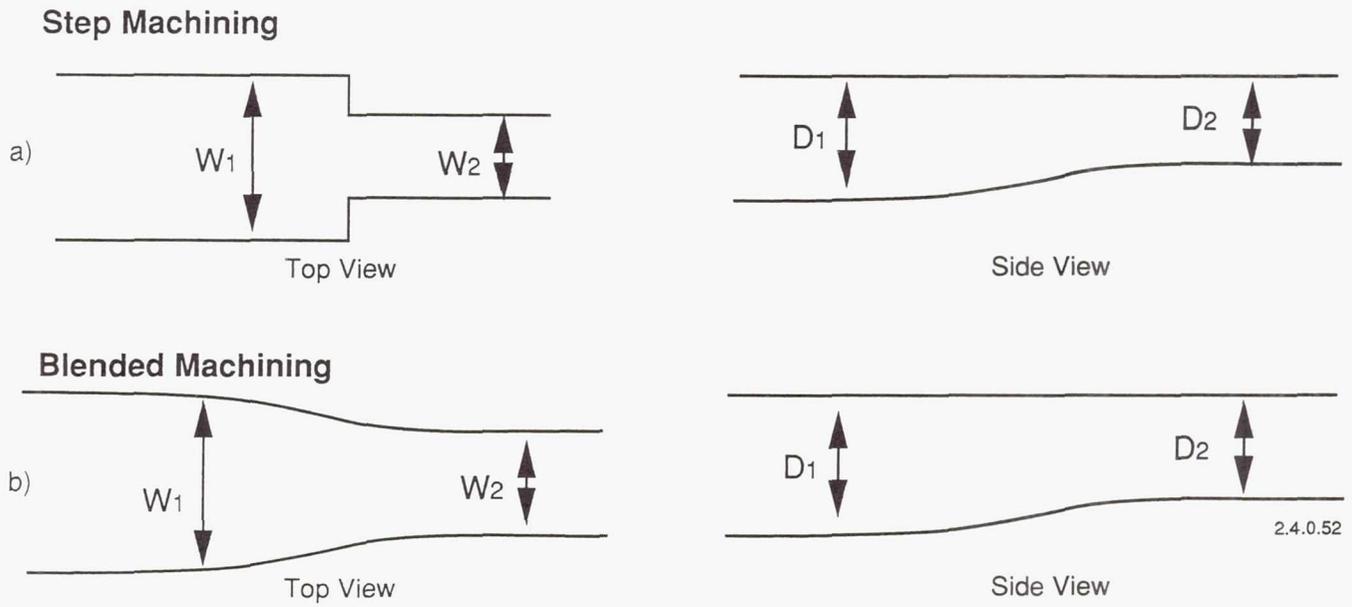
Figure 2.3-10. Channel Transition Methods

91
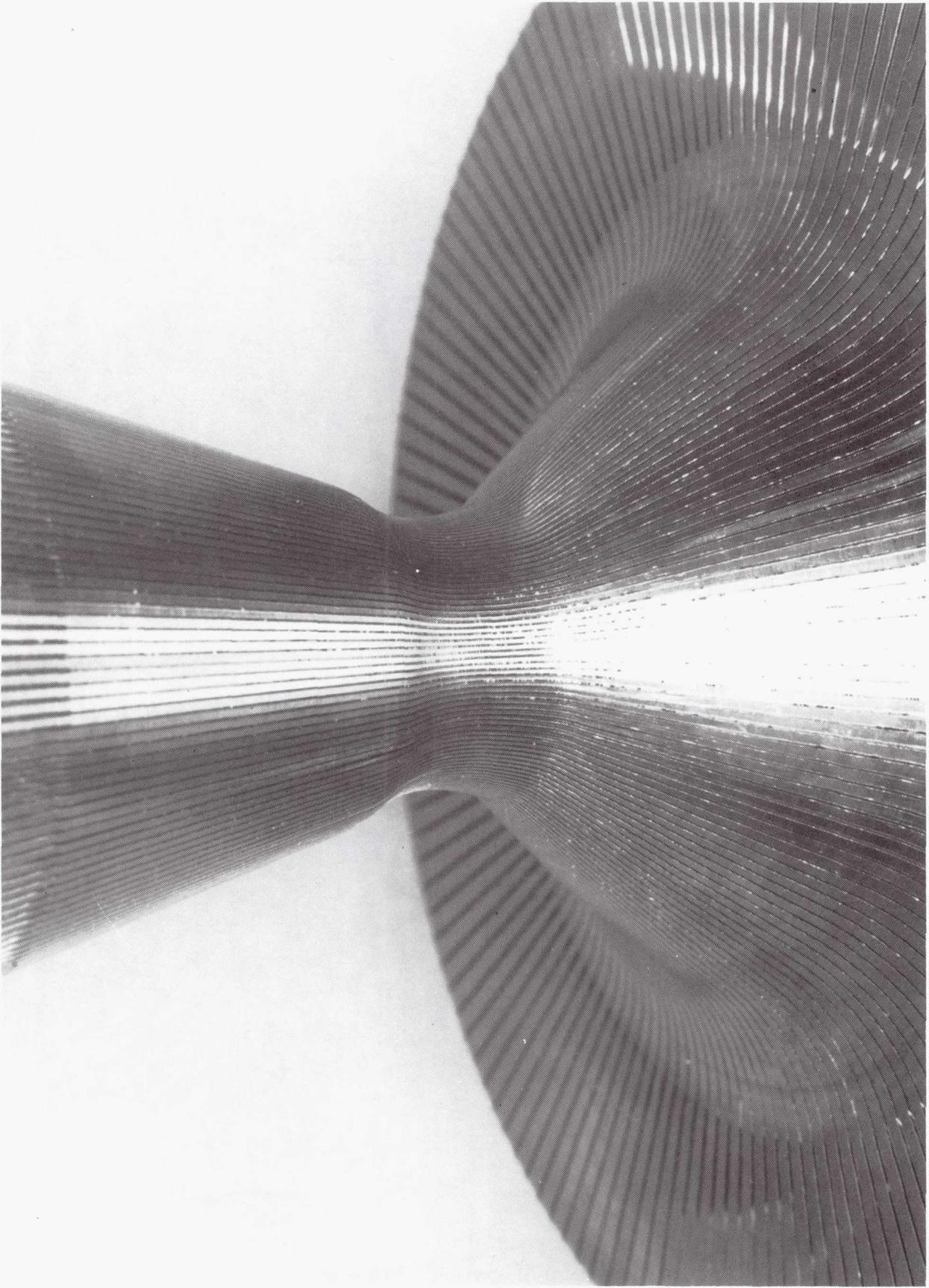
Figure 2.3-11. OTV 3.0K TCA – Cooled Throat Section Illustrating Step Channel Transition
(NAS-Z Copper)
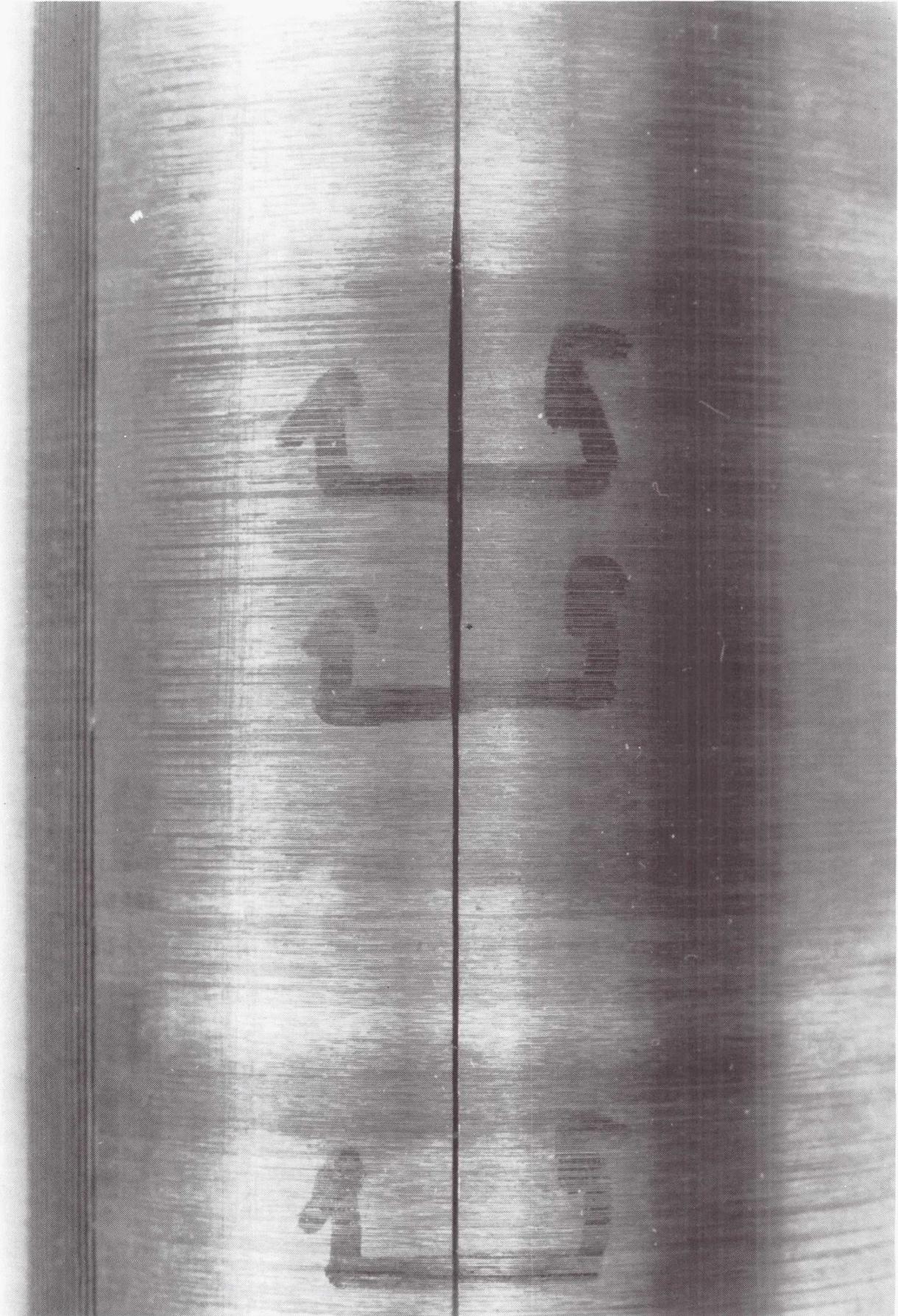
Figure 2.3-12. "Fly-Cutter" Channel Transition (Glid Cop)
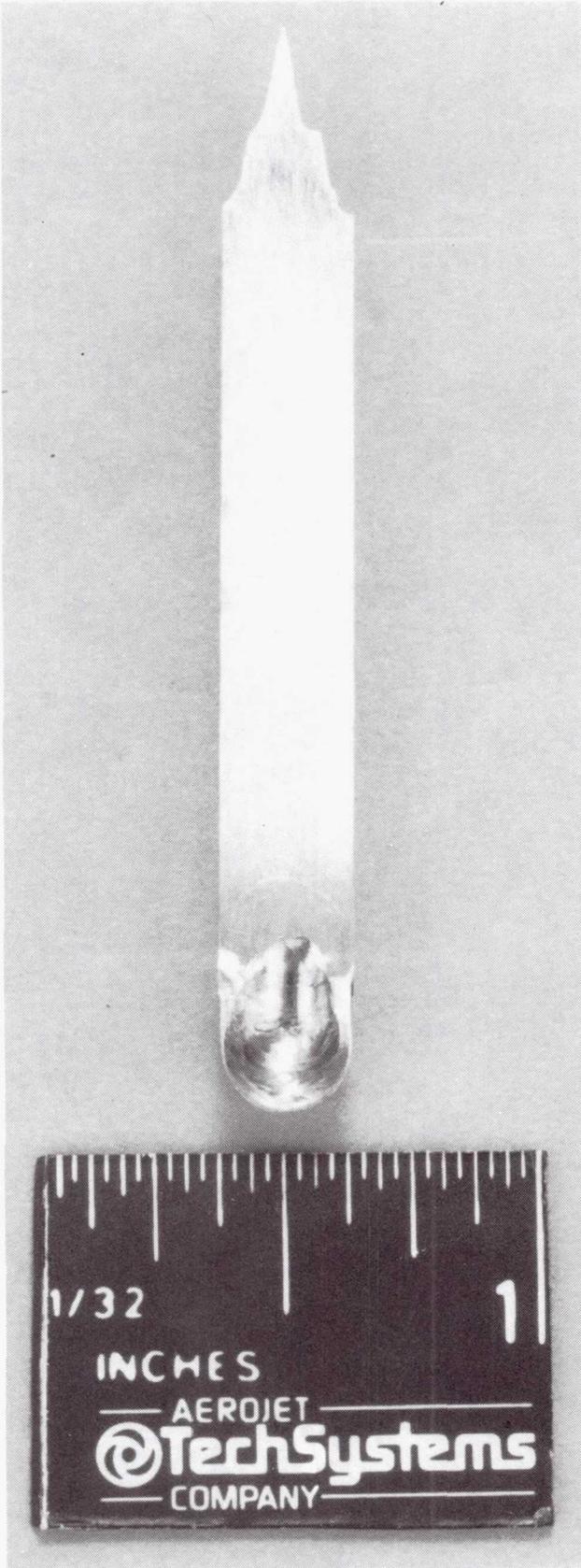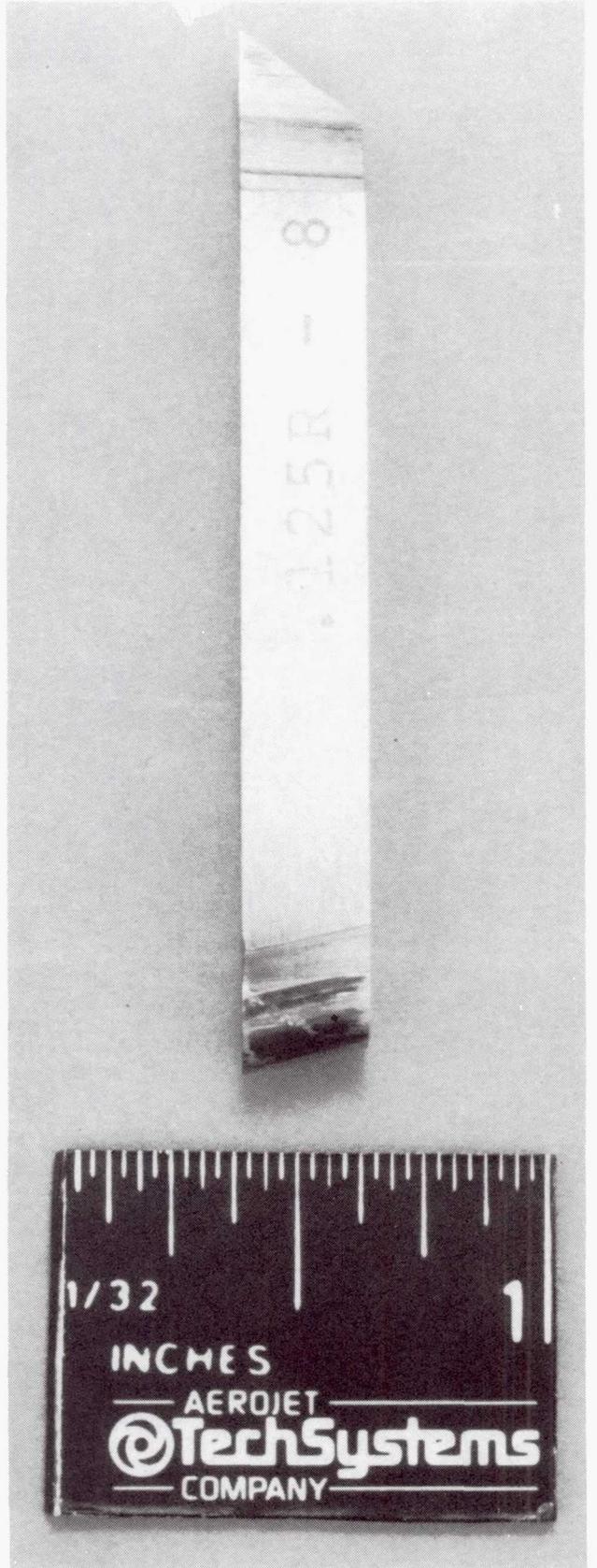
Front View   Side View

Figure 2.3-13. "Fly-Cutter" Tooling

94

2.3, FabricationStudy (cont.)

again remove the sharp edges. Cross sections of the channel are shown in Figure 2.3-14 where (a) shows the initial introduction of the fly cutter into the mini channel and (b) is taken at the point of the maximum desired channel width.

Of the two proposed methods to more smoothly define the channel transitions, only the fly cutter was demonstrated. Technology for the EDM cutting is available. To compare the methods, flow testing would be needed to evaluate the resulting pressure drops due to restriction and surface roughness.

2.4 CHAMBER FABRICATION CONCLUSIONS

Initial findings of machining GlidCop indicate that it should be treated more like a steel than a copper. This along with the cleanliness of the cut, indicate flexibility in machining the high aspect (depth to width) ratio, mini channel geometry for the OTV engine chamber.

This subtask has completed the first phase of material evaluation for regeneratively cooled chambers. Follow on work is needed to complete verification of GlidCop for use in combustion chambers. This work would be part of the final design effort toward a TCA design and would include verification of the:

1)   Ability to weld.

2)   Ability to structurally adhere an electroformed nickel, or nickel alloy closeout.

3)   Ability to machine the contoured "mini" channels.

Samples of both welded GlidCop and electroformed nickel closeouts to GlidCop could readily be obtained as part of a final TCA design task. Tensile specimens of these joints would establish the acceptable design limit properties.

Since mini channels have already been successfully machined to a 6" length on a cylindrical GlidCop specimen, contoured mini channel machineability is best verified with a full-scale, 7.5K thrust level model. Actual chamber geometry will directly address several potential channel-machining problems and will
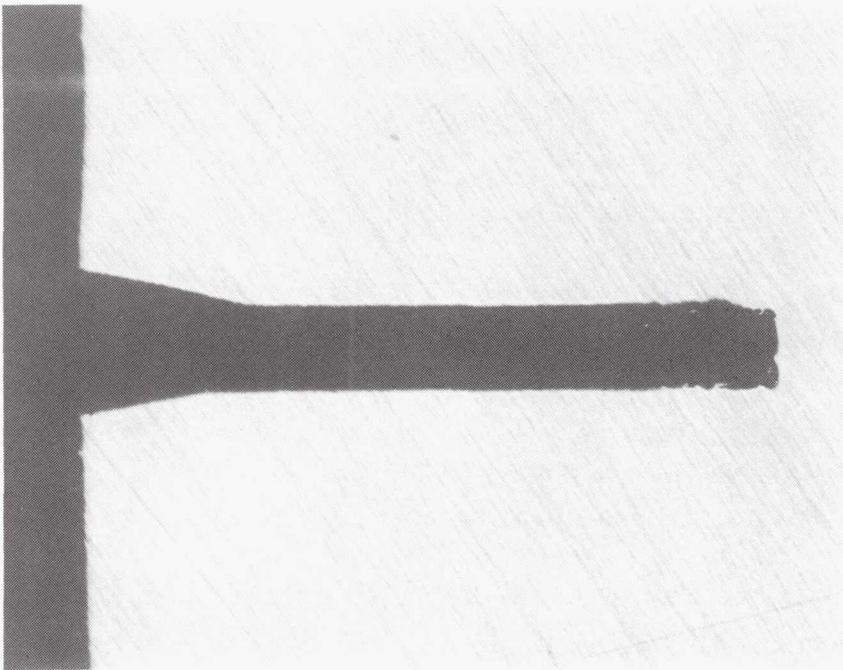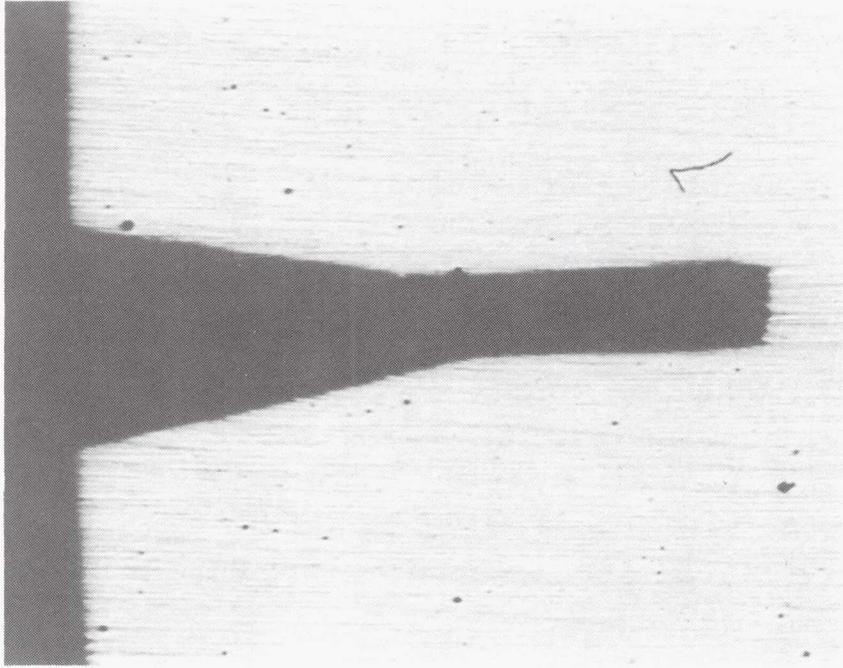
Figure 2.3-14. Cross-Section of Transition Channels Using Fly-Cutter

2.4, Chamber Fabrication Conclusions (cont.)

include the effects of curvature on channel fabrication. Also, since the 7.5K chamber has the smallest throat radius and throat curvature, successful results for the 7.5K thrust level model would imply channel machineability at higher thrust levels. A contoured chamber sample using the dimensions in Figure 2.2-1 should verify the ability to machine contoured mini channels in the GlidCop alloy.

3.0 INJECTOR STUDIES

3.1 INJECTOR DESIGN

The injector design is based on the 'T' triplet premix element, tested as part of the 3K thrust level program (Reference 1). This injector consisted of 2 annular rows of elements, each containing 36 elements, arranged around the center body structure as shown in Figure 3.1-1. The elements were canted at a 20 degree angle as shown in Figure 3.1-2. Thrust rating per element for the 3K injector was 45 lbf for each of the 36 elements in the outer row and 38 lbf for each of the 36 elements in the inner row. Baseline element design for the 7.5K thrust level engine injector utilized the geometry of the 3K outer row elements. As the OTV dual propellant expander cycle engine is scaled up in thrust level, the centerbody structure is replaced with a baffle assembly. The hydrogen cooled baffles provide additional surface area for heat input to the propellant thereby minimizing the regenerative hydrogen cooled chamber length. The 7.5K thrust level injector was designed using a 8 blade baffle geometry, dividing the injector into 8 pie shaped segments containing 168 elements as shown in Figure 3.1-3.

The injector element pattern is contained in a stack of Nickel platelets which are diffusion bonded to the manifold. Figure 3.1-4 illustrates the element design. The fuel passages impinge sideways on the oxidizer stream into a cup area for mixing of the fuel and oxygen prior to injection into the chamber for combustion.

Utilization of platelets for formation of the injector element allows easy customization of each element. Geometries for the 3K thrust level injector were different for the inner and outer row elements. Likewise, for the baffled injector designs, customization of the elements according to the location (i.e. at the wall versus at the center of the pie segment) is easily incorporated.

Results from the 3.0K thrust level TCA testing (Reference 1) were used to finalize the design of the injector element at the 7.5K thrust level. Higher than expected heat flux levels within 0.5 inches of the injector face indicated changes needed to be made to the element to "detune" its performance to provide nominal heat flux levels of 10 BTU/sec in.^{2} in the barrel section.
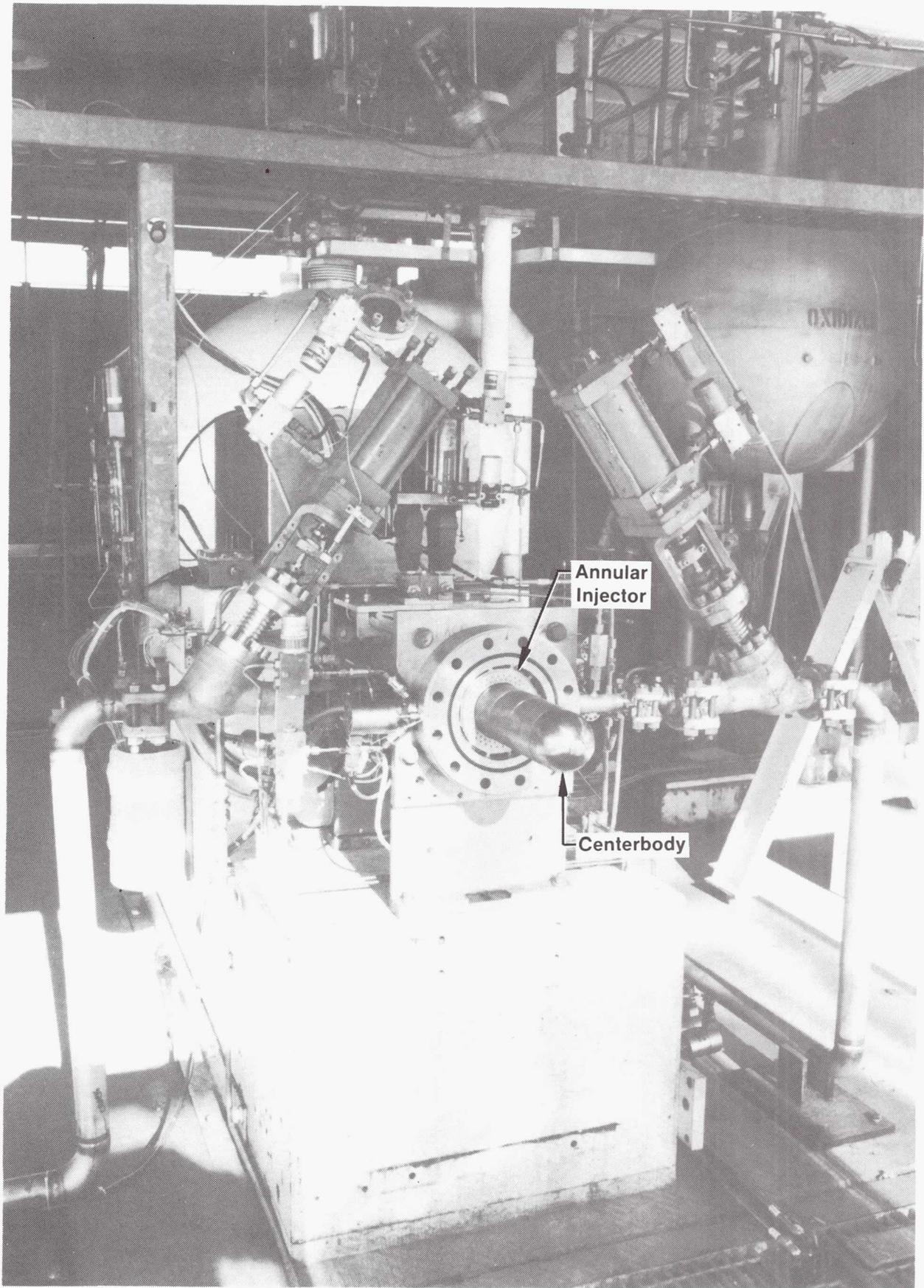
Figure 3.1-1. 3K TCA Injector and Centerbody on Test Stand

20°

36 Elements
Inner Row

36 Elements
Outer Row

36 Places
Cross-Drilled Holes

3K Annular Injector
O.D. = 5.62
I.D. = 4.00
N_E = 72 Elements
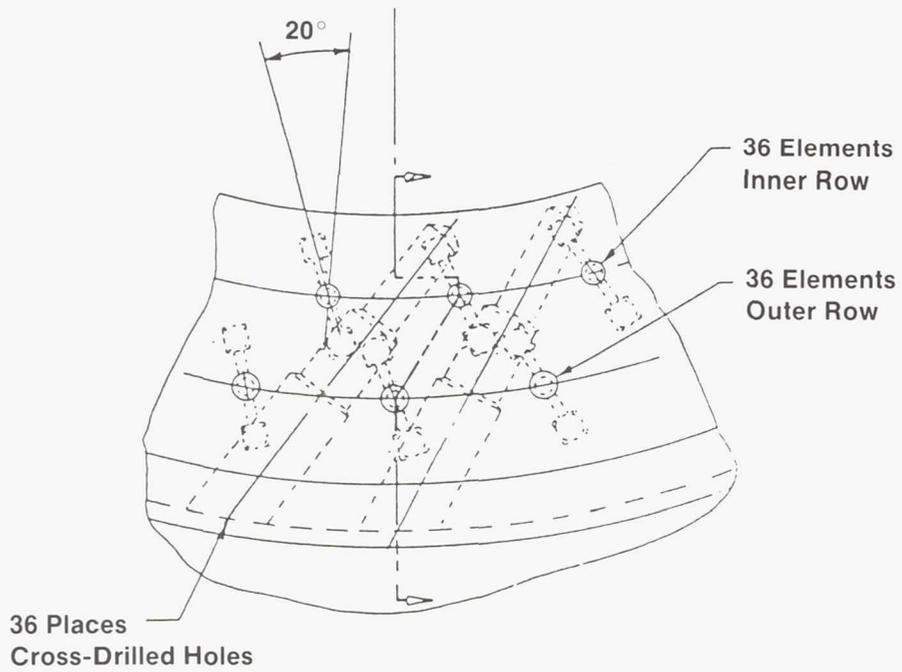
Figure 3.1-2. "I"-Triplet Premix Element Injection Patter

100

(TOP VIEW OF INJECTOR)
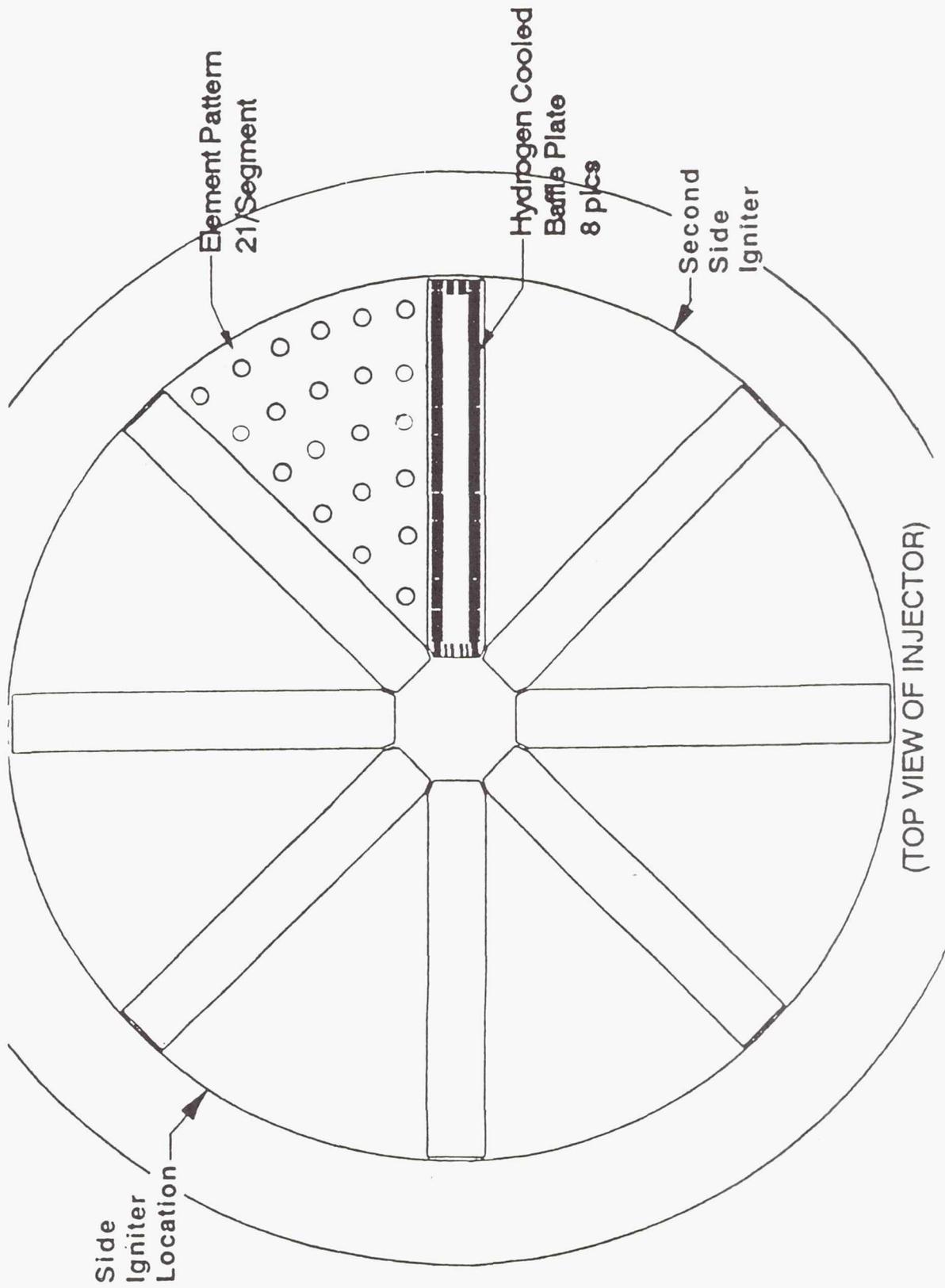
Figure 3.1-3. 7.5K TCA Injector Pattern
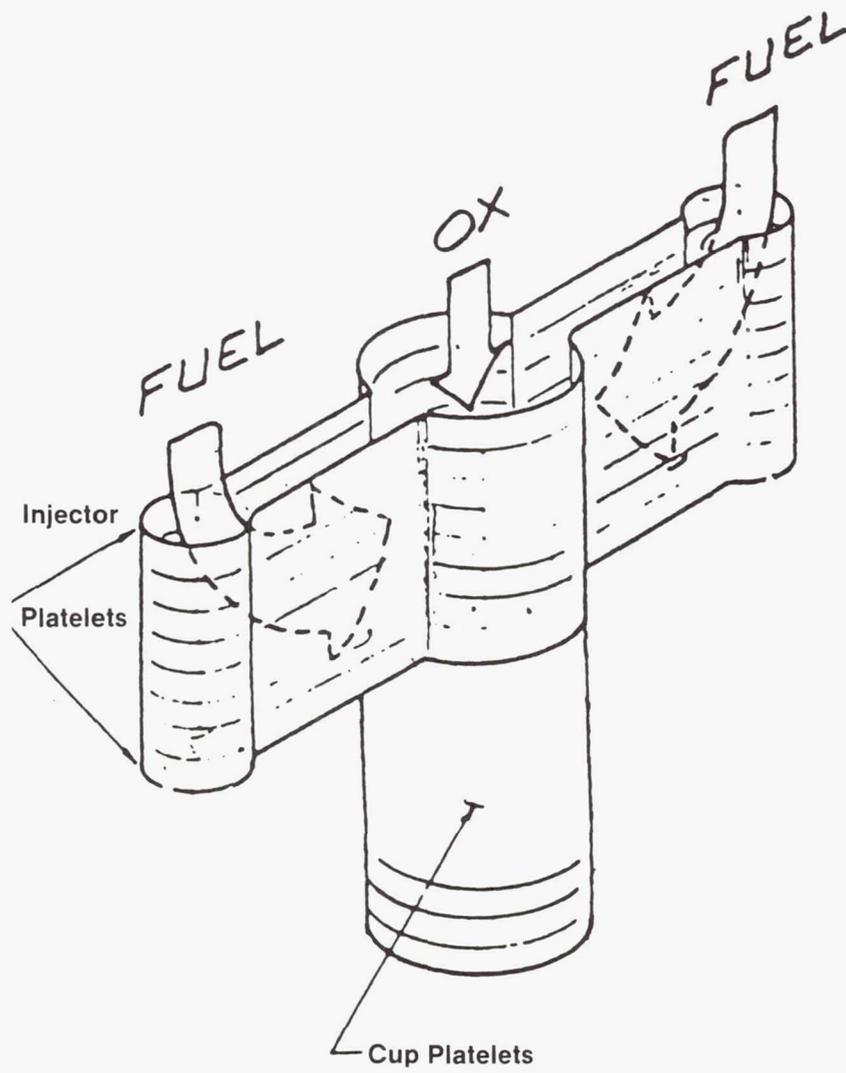
Figure 3.1-4. Cross-Section of the "I"-Triplet Premix Element

3.1, Injector Design (cont.)

For the OTV engine design requirements, the gas-gas 'I' triplet premix element had been chosen to satisfy the high Isp requirements, provide the capability to operate over a wide throttling range (10:1), and enable adequate combustion gas mixing in a relatively short (<10") chamber length.

Verification of the injector and regenerative channel design was achieved with hot fire testing of a heat-sink version of the chamber with only the throat section using hydrogen cooling. During this testing, heat flux information was obtained to characterize the axial profile in the chamber. This information indicated higher than designed heat fluxes occurring within a 1/2 inch axial length from the injector face at the wall of the center body. The fluxes rapidly leveled off after this initial 1/2 inch length to values closely approximating the design goals This can be expected with the 'I' triplet element as shown in Figure 3.1-5. The heat flux associated with the data band are shown tabulated in Figure 3.1-5.

Two approaches were feasible for application of this study to the 7.5K thrust level TCA injector design: 1) Retesting of the existing 3.0K injector with new face plates, or 2) cold flow uni-element testing.

Earlier work at Aerojet had characterized this injector element and defined areas which would increase or decrease the mixing efficiency (References 10 and 11). This characterization of the 'I' triplet injector element showed a wide tolerance range to mixing efficiency variances. At a mixture ratio of 6, mixing efficiencies can be experienced as low as 90% without seriously comprising the element Energy Release Efficiency (ERE) as illustrated in Figure 3.1-6.

To study reorientation or detuning of the injector element, Table 3.1-I lists the approaches and compares the relevant information obtainable. With this information it would have been possible to take a "best guess" approach to designing a new face plate for the existing 3.0K thrust level injector. However, due to the differing geometry between the flat plate baffles of the 7.5K design and the annular configuration of the 3.0K design, extrapolation of the heat flux information would have been difficult.

103

Premix Element Nominal Heat Flux Range vs Axial Dist.		
TC Location (Inches From Inj Face)	ϕ ets/ϕ nom	
	2.5	1.3
0.75	24.2	12.8
2.60	22.4	12.5
4.75	20.2	12.0
7.80	17.1	11.4
10.10	14.8	11.0
11.85	13.1	10.6
13.00	11.9	10.4
ϕ ave	17.7	11.5

Injection Momentum Ratio $\frac{W_o V_o}{W_f V_f}$

Estimated to Nominal Heat Flux at L_{comb} = 1.9 cm (.75 in) — ϕ_{est}/ϕ_{nom}

Figure 3.1-5. Heat Flux Versus Momentum Ratio for Various Injector Elements
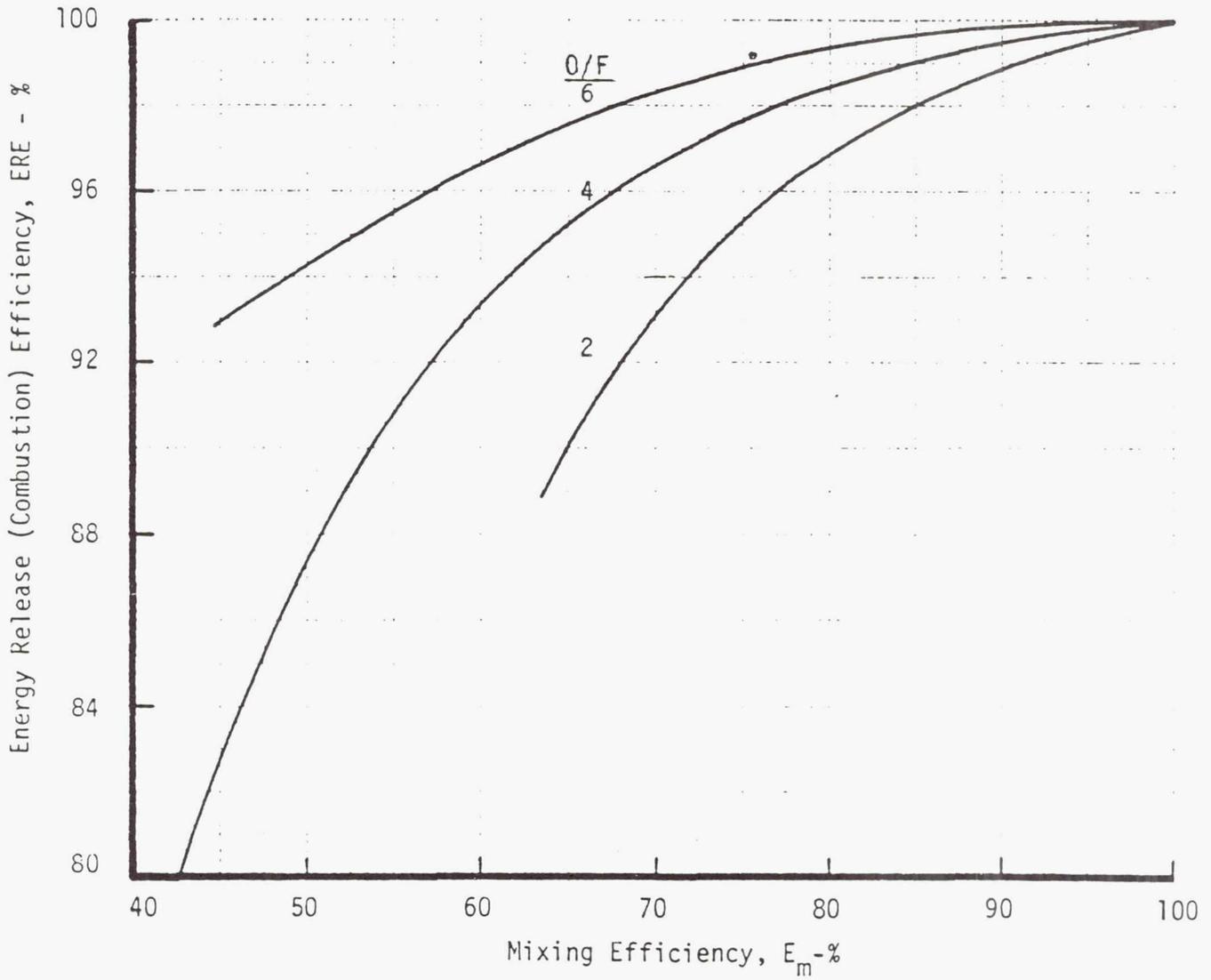
Figure 3.1-6. Empirical Relationship Between Combustion Efficiency and
Mixing Efficiency for Pre-Mix Injector Equipment

105

TABLE 3.1-I

SUMMARY OF DESIGN AND OPERATING EFFECTS ON MIXING EFFICIENCY

E_m Influence

	Coax	Swirler	Increased Shear	Premix	Doublet	Parallel	Triplet
Increasing F/E	D	M	D	D	D	D	D
Increasing A_f/A_o	D	M	D	M	I	NT	M
Increasing L/D	I	I	I	I	I	I	I
Increasing O/F	D	O	D	M	I	I	M
Increasing Prop. Temp.	D	I	D	I	NT	D	NT
Increasing Spacing	NA	NA	NA	NA	M	NT	NA
Increasing Impingement Angle	NA	NA	NA	NA	NT	NA	M
Increasing Orifice Width	NA	NA	NA	M	NT	NT	NT
Increasing Swirl	NA	I	NA	NT	NA	NA	NA

I Indicates increasing Em

D Indicates decreasing Em

M Indicates a maximum or minimum in Em

O Indicates no influence

NT Not tested

NA Not applicable

3.1, Injector Design (cont.)

The benefit of cold flow testing is the ease in which many element geometry changes can be studied in a short time at a minimum cost. However, to fully evaluate the element changes and the resulting changes in heat flux level, hot fire testing at the 2000 PC level would need to be repeated. For the purposes of this study, the uni-element cold flow testing was selected as the most cost effective method of understanding the element.

3.2 POST-HOT FIRE TEST COLD FLOW VERIFICATION

Prior to modifying the 3.0K element geometry for use in the 7.5K injector design, post hot fire cold flow testing of the injector was undertaken to rule out the possibility of flow anomalies which may have caused the high heat fluxes experienced in the hot fire testing. The 3.0K injector is shown in Figure 3.2-1.

Figure 3.2-2 illustrates the approach taken for the cold flow characterization (Kw) check of the injector. Gaseous Nitrogen was used to flow the hydrogen and oxygen circuits separately. Table 3.2-I lists the dates, injector condition, and reason for cold flow test. A summary of the corresponding GN2 cold flow effective cold flow area (CdA) results for each of these dates is tabulated in Table 3.2-II. The first set of cold flow tests on 4/3/85 were conducted prior to a modification to the injector which increased hydrogen face film cooling around the centerbody. This primarily affected the hydrogen CdA of the inner row since the additional face cooling was fed from the inner row manifold. Figure 3.2-3 presents the effective flow area for each element after the first post-test cold flow. Post-test cold flow before and after the back-flushing showed consistent CdA values. A maximum variance of 5% was observed which is acceptable for gas flow.

Element-by-element mixture ratios based on the cold flow CdA's are shown in Figure 3.2-4 and Figure 3.2-5. The slight shift in MR between the 1985 data and the 1988 data is attributed to the increased hydrogen face film cooling to the injector added after the 4/3/85 cold flow. The variances observed in Figures 3.2-4 and 3.2-5 are in an acceptable range for the injector. Supply pressure for the 1985 cold flow was 15.7 psia and that for the 1988 cold flow was 30 psia.
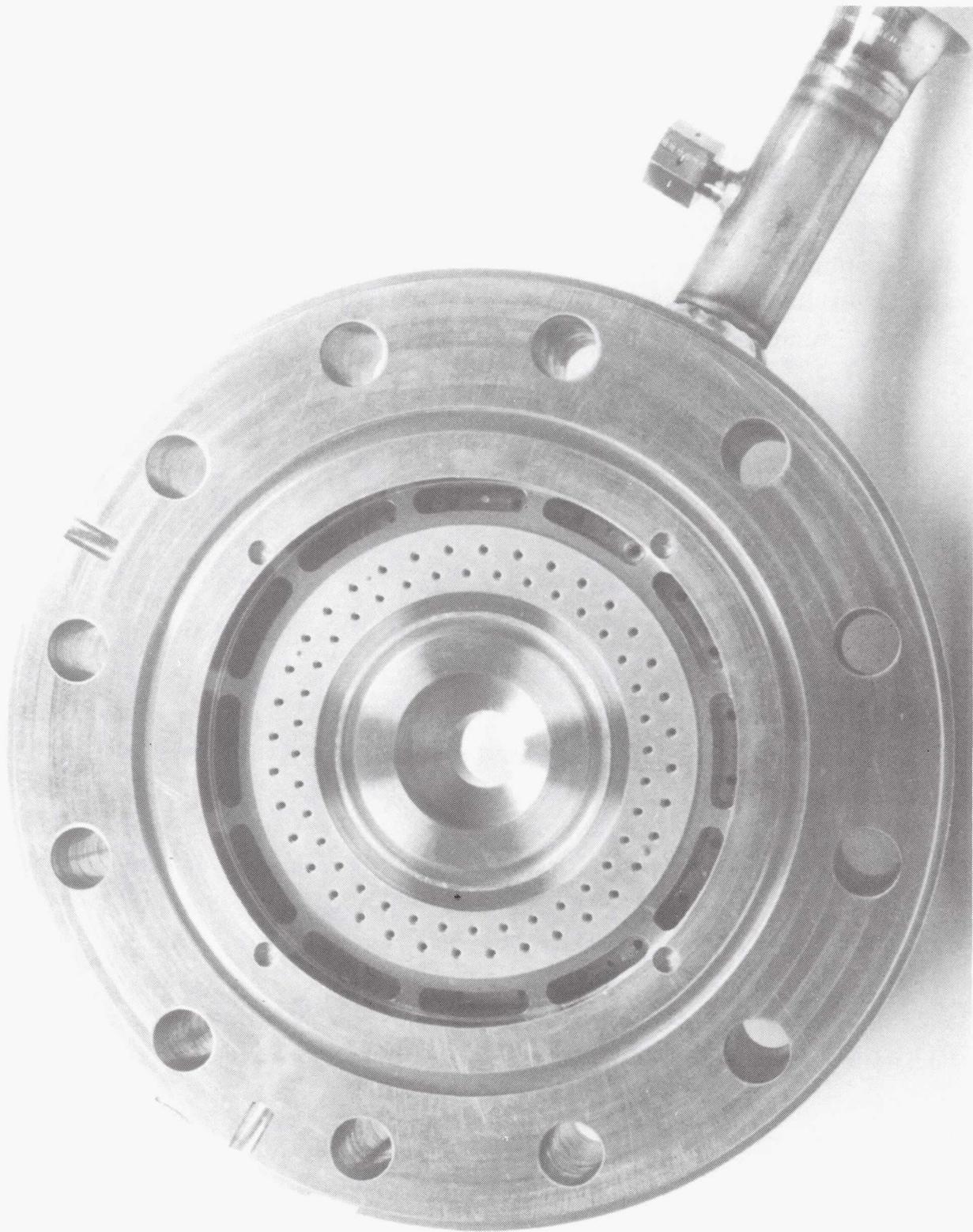
Figure 3.2-1. 3.0K TCA Injector Hardware
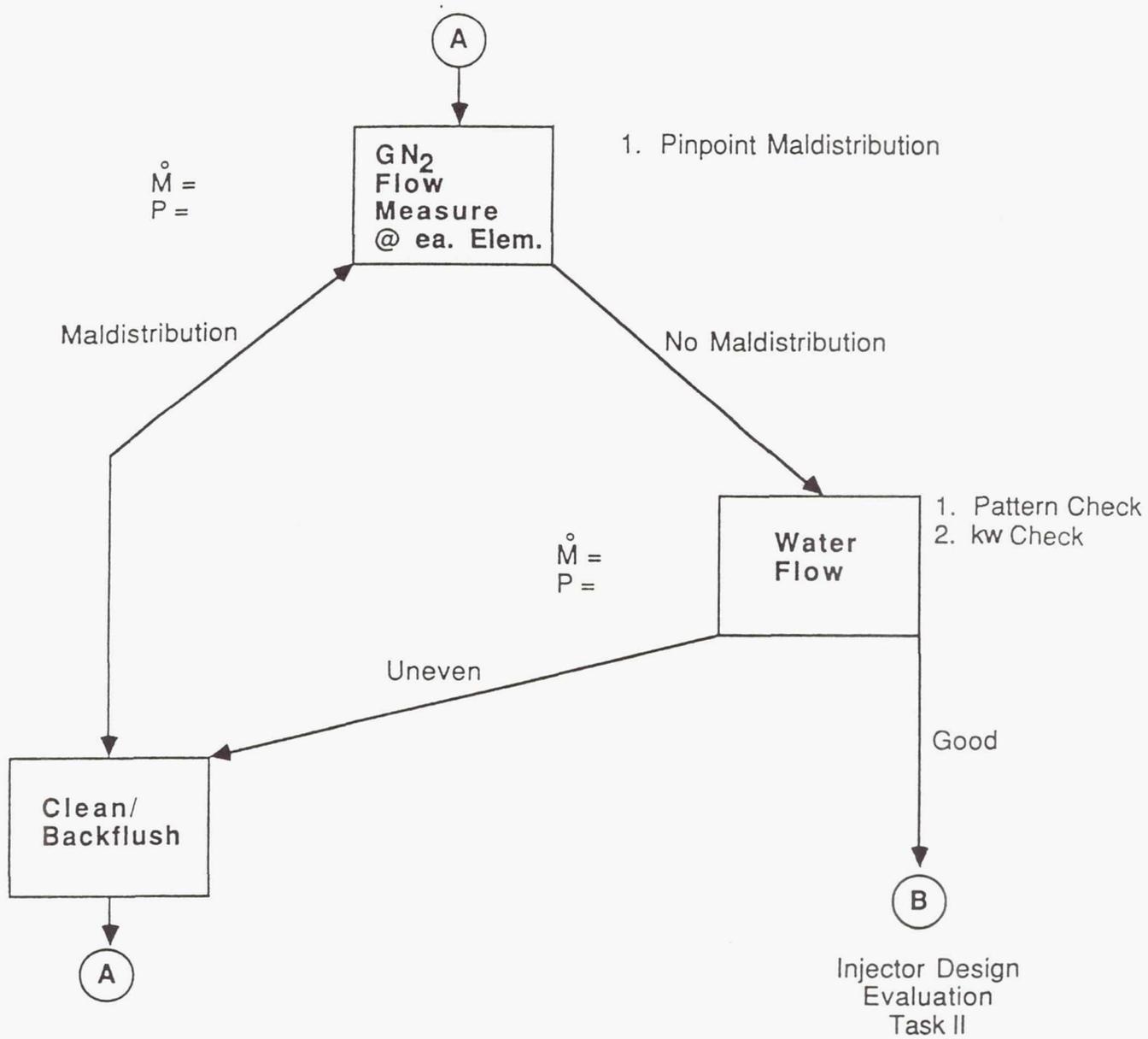
Figure 3.2-2. 3.0K TCA Injector Cold Flow Test Logic

TABLE 3.2-I

3K OTV INJECTOR GN$_2$ COLD FLOW HISTORY

Date	Reason
4/3/85	Pre-fire injector Kw determination (before injector modification)
9/28/88	Post-test cold flow check for possible element mixture ratio bias
10/24/88	Injector backflush to remove possible contaminants
11/4/88	Injector resistance check after backflush

TABLE 3.2-II

SUMMARY OF GN$_2$ COLD FLOW TEST RESULTS

	4/3/85 Cold Flow	9/28/88 Cold Flow	11/4/88 Cold Flow
Fuel Inner Row CDA	0.0561	0.0672	0.0666
Fuel Outer Row CDA	0.0704	0.0857	0.0846
Ox Inner Row CDA	0.0691	0.0690	0.0695
Ox Outer Row CDA	0.0898	0.0778	0.0774
Fuel Injector CDA	0.1265*	0.1529	0.1512
Ox Injector CDA	0.1589	0.1467	0.1469

‾ ‾ ‾ ‾
*H$_2$ face film cooling was increased from 6% to 9.5% after measuring of the C$_D$A
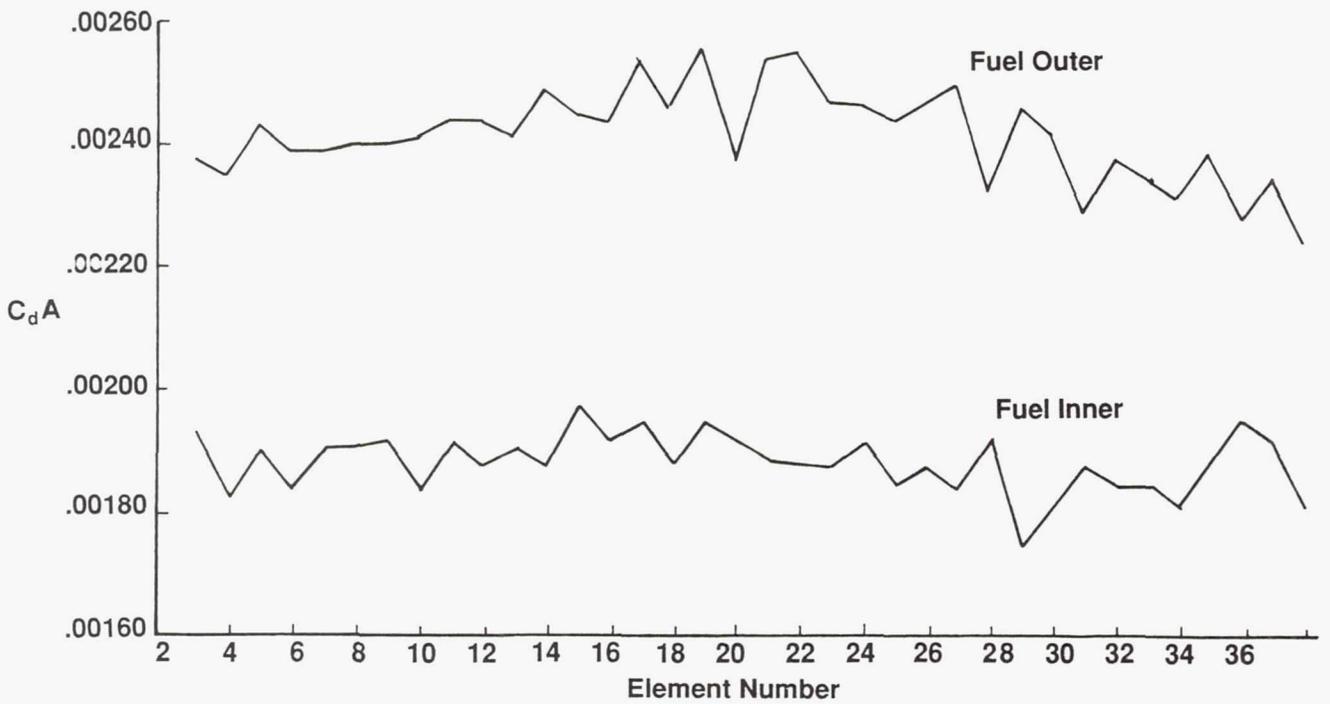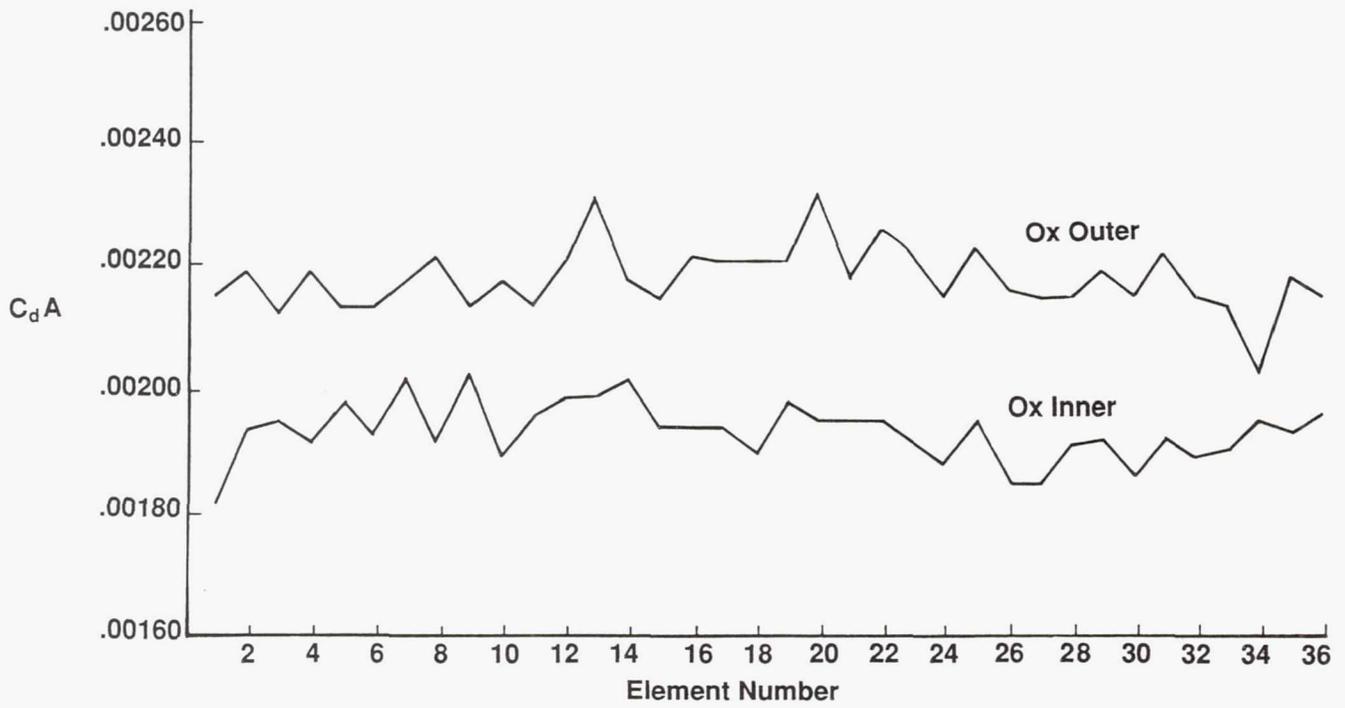
Figure 3.2-3. Element by Element Effective Flow area From 9/88 gN$_2$ Cold Flow

112
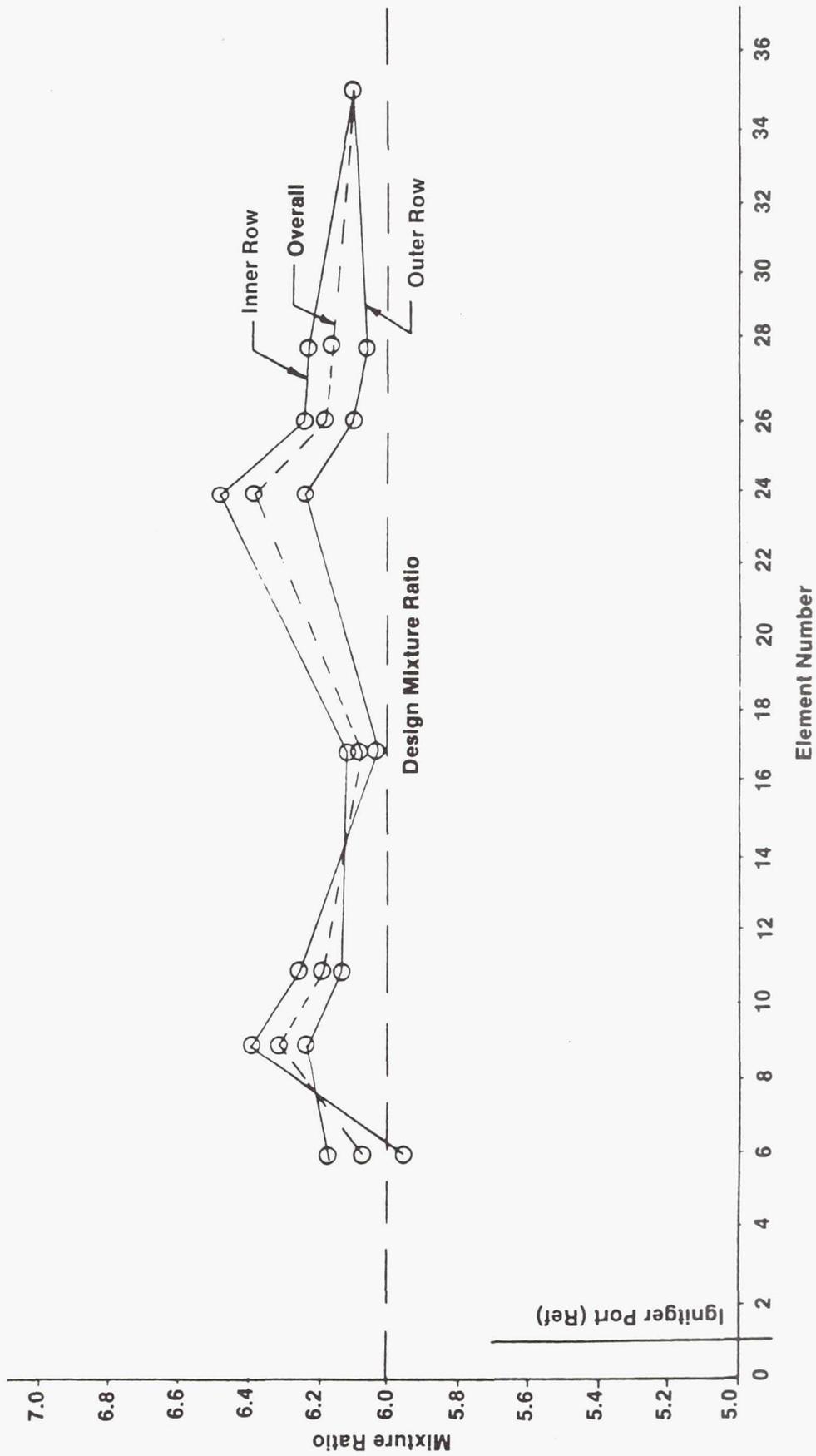
Figure 3.2-4. Pre-Fire Mixture Ratio Distribution for Inlet Pressure of 15.7 psia

113
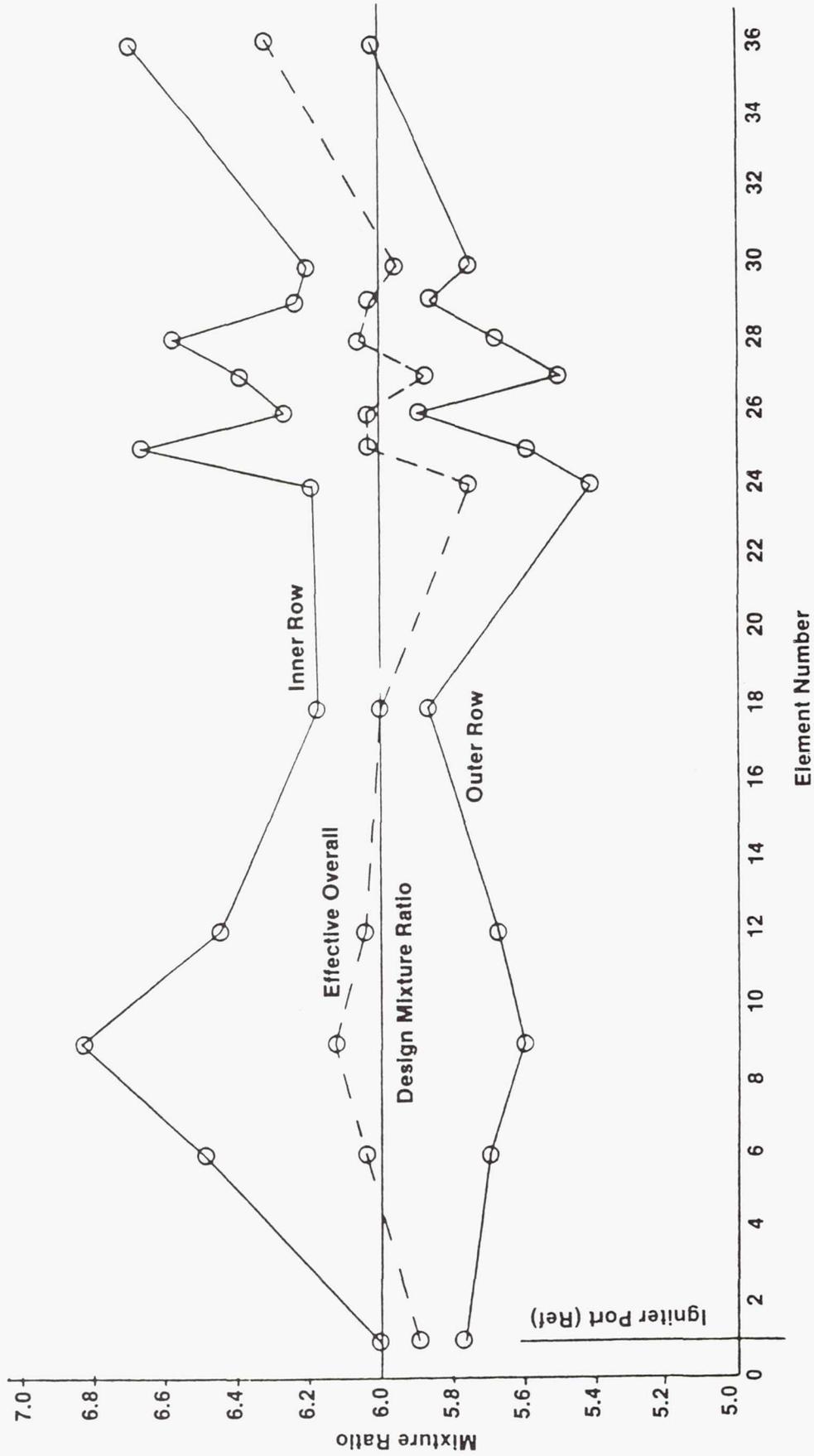
Figure 3.2-5. Post-Fire Mixture Ratio Distribution Too Uniform to Account for High Heat Fluxes

114

3.0, Injector Studies (cont.)

3.3 ELEMENT DESIGN MODIFICATIONS

Since no anomalies were observed in the cold flow injector Kw check, modification of the injector element was initiated. Figure 3.3-1 is an illustration of a segment from the 7.5K thrust level injector design. The zones targeted for customization of the element geometry are marked. Those elements in the center (Zone 4) will remain the same as the 3.0K injector outer row element, and will be referred to as the "Baseline Element". Zones 2 and 3, along the baffle walls, are grouped together since mirroring about the segment center line is the primary difference. This group is referred to as the "Baffle Element". The elements in Zones 1 and 5 are referred to as "Center Elements."

The element geometry was designed by evaluating the fuel and oxidizer normalized momentums. Geometry of the oxidizer element was held constant for all element modifications. Figure 3.3-2 shows the momentum per unit length for the baseline 3K element.

A schematic of the flow through a premix "I" triplet element was shown previously in Figure 3.1-4. A schematic of the C-C and D-D sections for the baseline element is shown in Figure 3.3-3 along with the proposed modifications to these sections. Both sides of the baseline element sections show a narrow flow region in the middle of the platelet stack which is designed to break up the ox stream. The wider upper and lower flow regions are required to wrap around the ox stream to give a fuel rich periphery. The baffle and center element modifications are designed to create a resultant fuel momentum so that there is a more predominantly fuel rich region near the side of the spray fan nearest the chamber wall or baffle. The platelets used in this cold flow study are twice the size of the 3K OTV platelets, and therefore give four times the flow area. These larger platelets produce a larger and easier to visualize spray distribution.

The actual platelet geometries generated are shown in Figures 3.3-4 & -5 for the Baseline Element, Figures 3.3-6 thru -8 for the Center Element Modifications, and Figures 3.3-9 & -10 for the Baffle Element Modifications. In each of these figures, the stacking sequence is given followed by a comparison of the modified

115
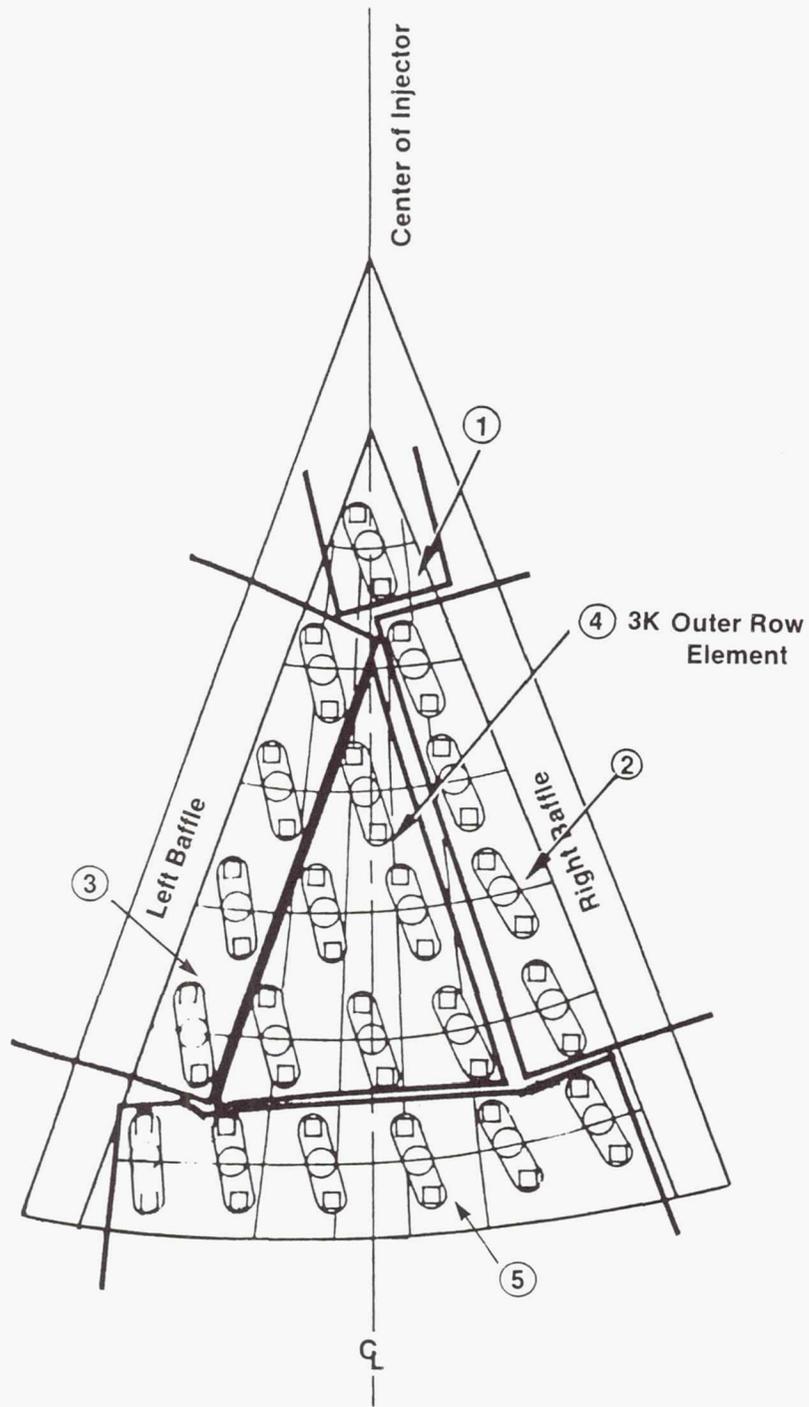
Figure 3.3-1. Segmented Injector Element Zones to Be Modified

116
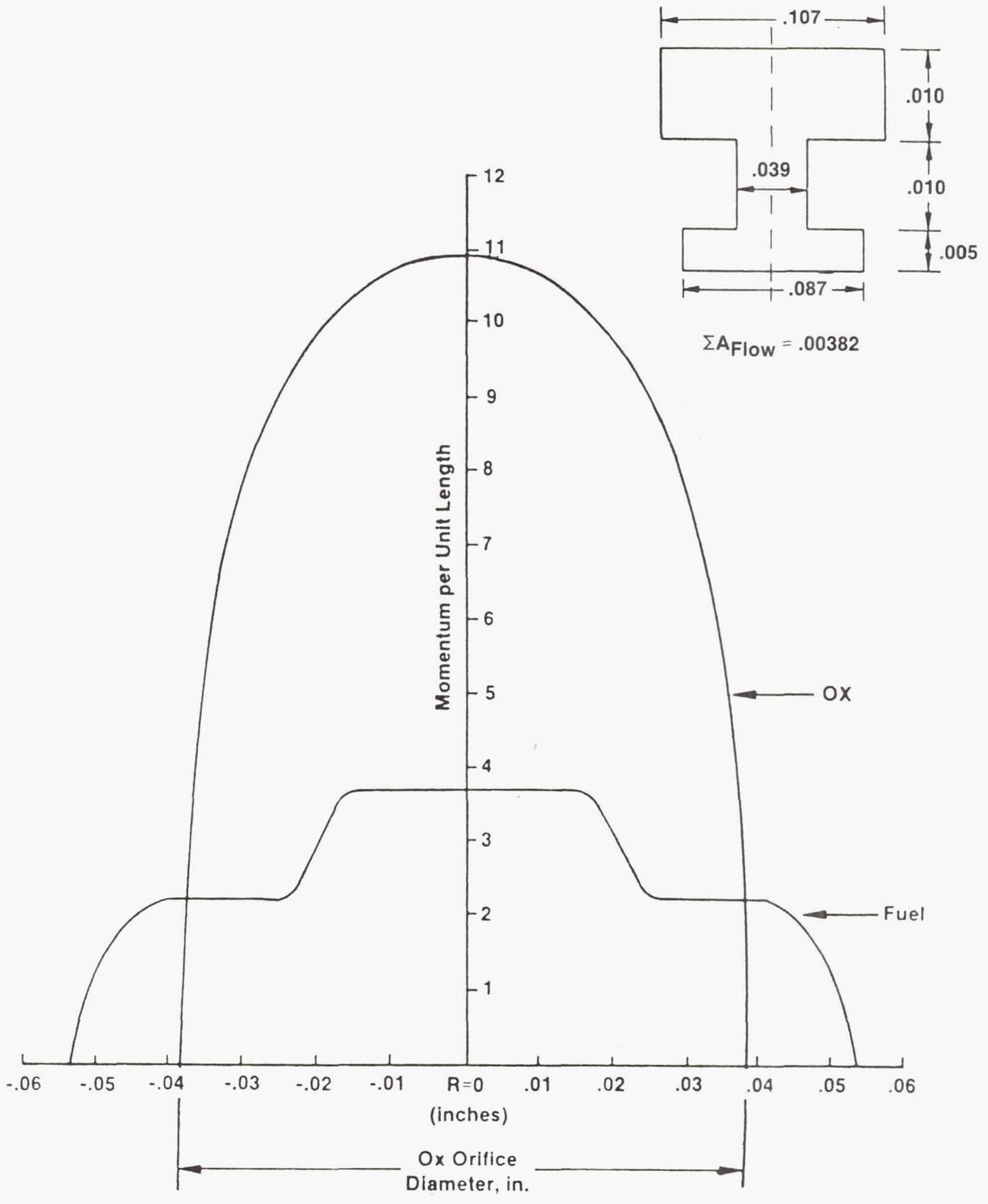
Figure 3.3-2. Momentum Distribution 3.0K Baseline Element
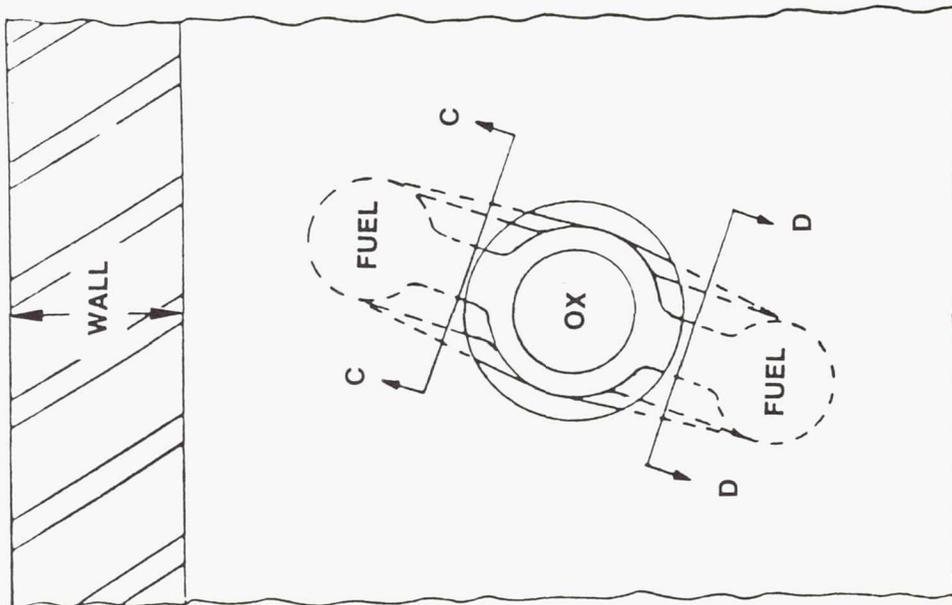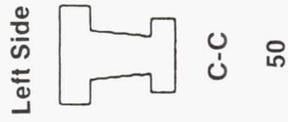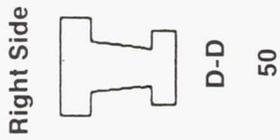
117

Figure 3.3-3. Elements Next to Chamber Wall Will Be Redesigned to Prevent Heat Flux

118

Figure 3.3-4. Stacking Sequence — Baseline Element

Element
Feature
Location
Zone

Loose
Platelets

Baseline Element

A	
No.	Qty
-1	1
-2	2
-4	2
-5	1
-6	4

Cross Section Fuel Circuit*

Section C-C
(Left Side)
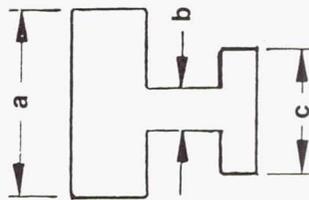
Section D-D
(Right Side)

Mod	a	b	c
A	.214	.078	.173

119
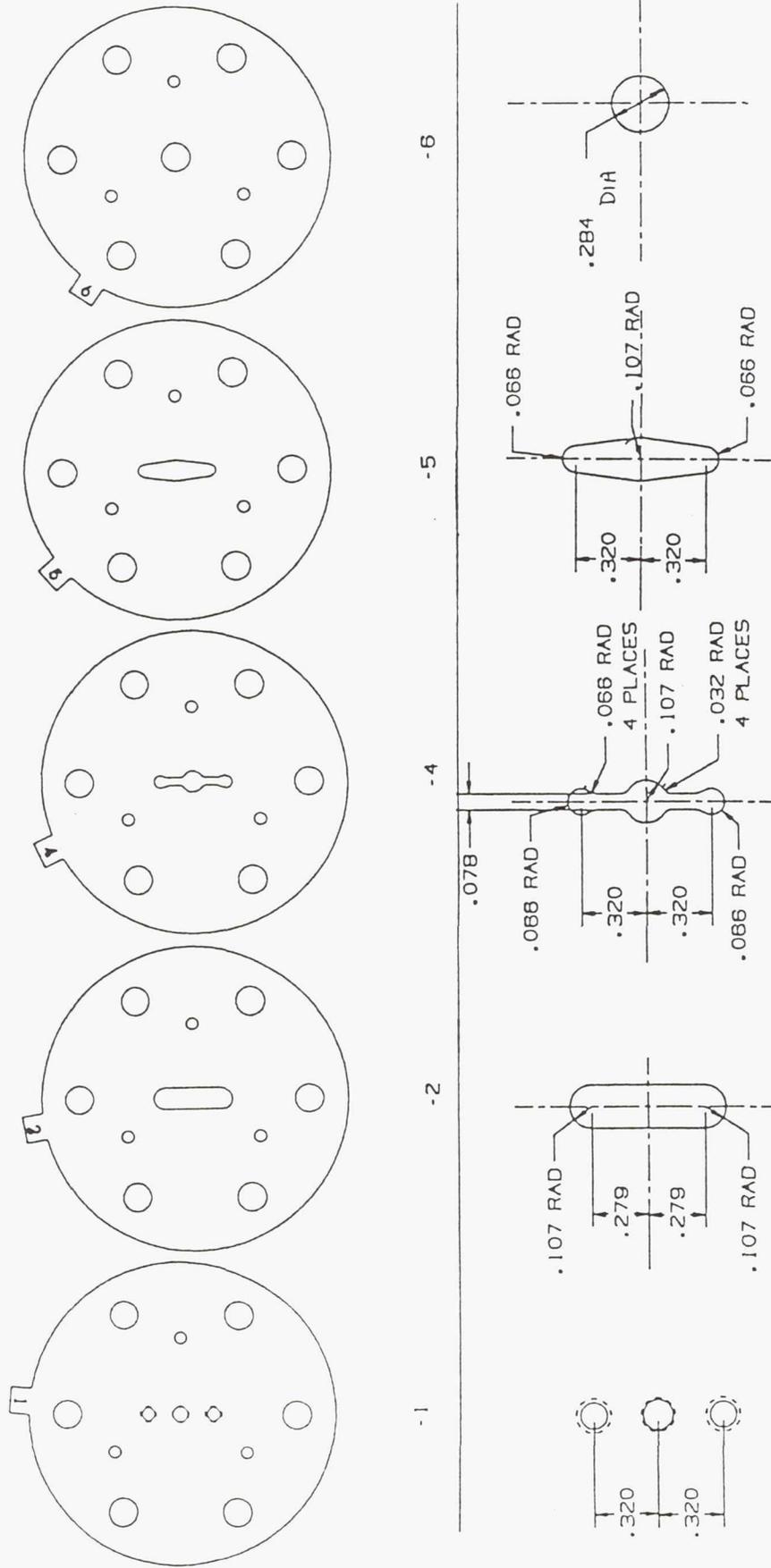
Figure 3.3-5. Baseline Element Platelet Design

120

B		C		D		E	
No.	Qty	No.	Qty	No.	Qty	No	Qty
-1	1	-1	1	-1	1	-1	1
-11	2	-11	2	-16	2	-16	2
-12	2	-12	2	-12	2	-12	2
-11	1	-16	1	-16	1	-11	1
-6	4	-6	4	-6	4	-6	4

Cross Section Fuel Circuit*

Section C-C   Section D-D
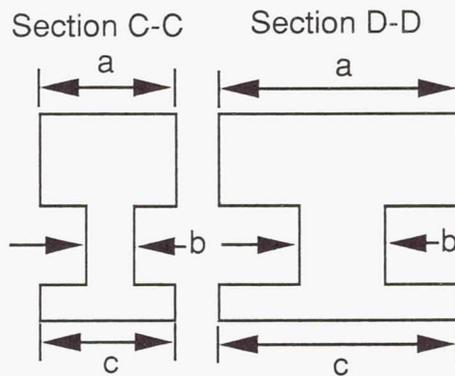
Left Side

Mod	a	b	c
B	.154	.078	.154
C	.154	.078	.1615
D	.1615	.078	.1615
E	.1615	.078	.154

Right Side

Mod	a	b	c
F	.230	.116	.230
G	.230	.116	.230
H	.230	.116	.230
I	.230	.116	.230

2.4.0.53

(Nearest Baffle Corner)

Figure 3.3-6. Stacking Sequence – Center Element Modification
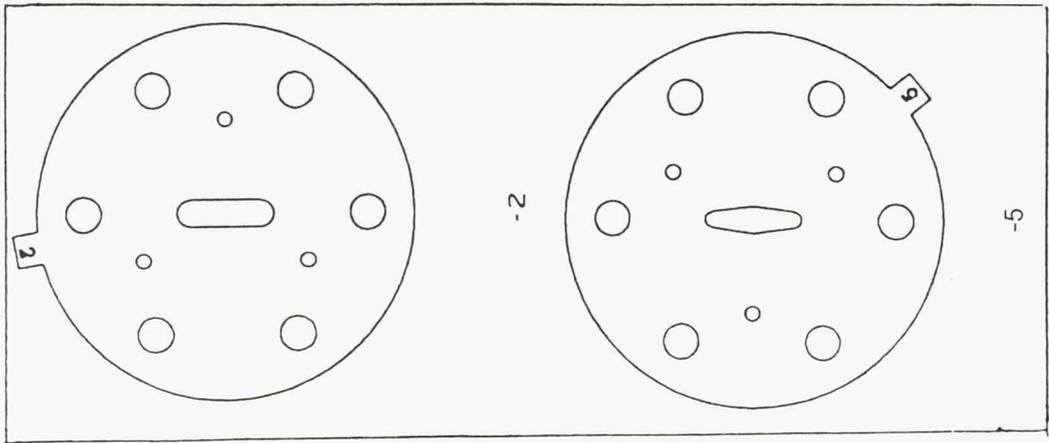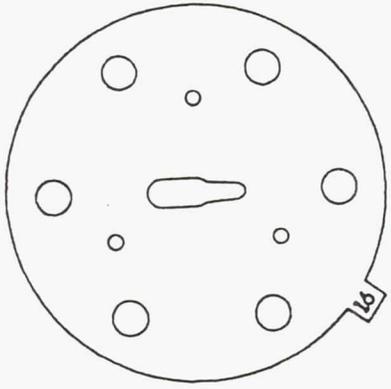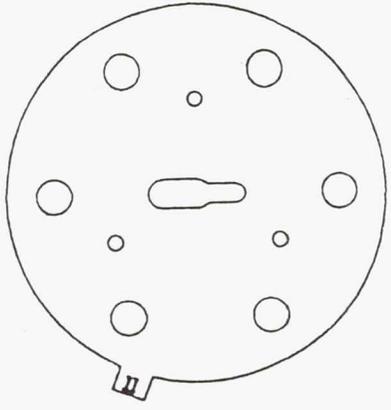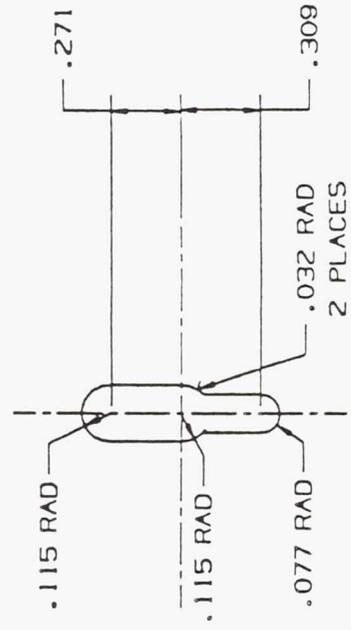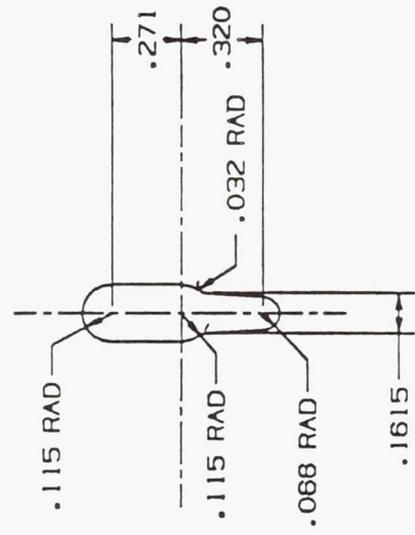
Figure 3.3-7. Center Element Modifications (-16 and -11)

122
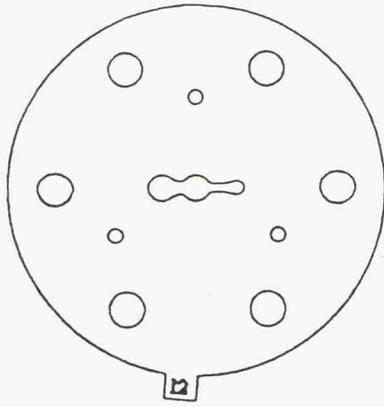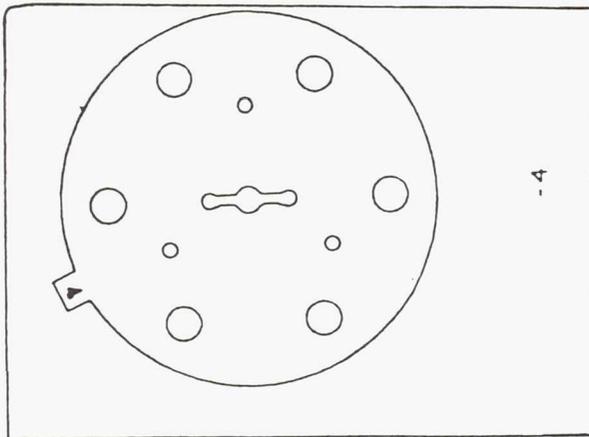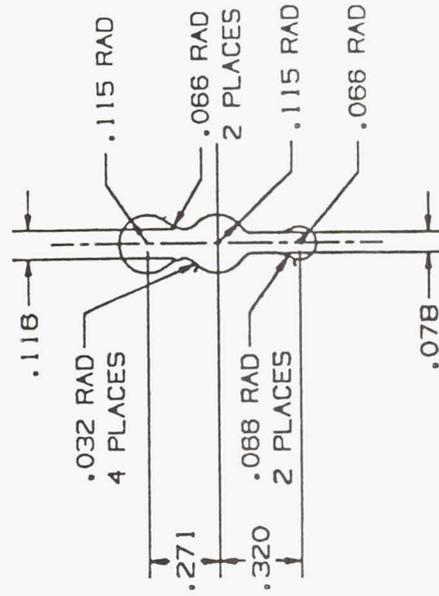
Figure 3.3-8. Center Element Modifications (-12)

123

F

No.	Qty
-1	1
-13	2
-4	2
-13	1
-6	4

G

No.	Qty
-1	1
-13	2
-4	2
-15	1
-6	4

H

No.	Qty
-1	1
-15	2
-4	2
-15	1
-6	4

I

No.	Qty
-1	1
-15	2
-4	2
-13	1
-6	4

Cross Section Fuel Circuit*

Section C-C

Section D-D (Nearest Baffle Wall)

Left Side

Mod	a	b	c
F	.188	.078	.188
G	.188	.078	.177
H	.177	.078	.177
I	.177	.078	.188

Right Side

Mod	a_1/a_2	b	c_1/c_2
F	.115/.107	.078	.115/.107
G	.115/.107	.078	.107/.107
H	.107/.107	.078	.107/.107
I	.107/.107	.078	.115/.107

2.4.0.54

Figure 3.3-9. Stacking Sequence – Baffle Element Modifications
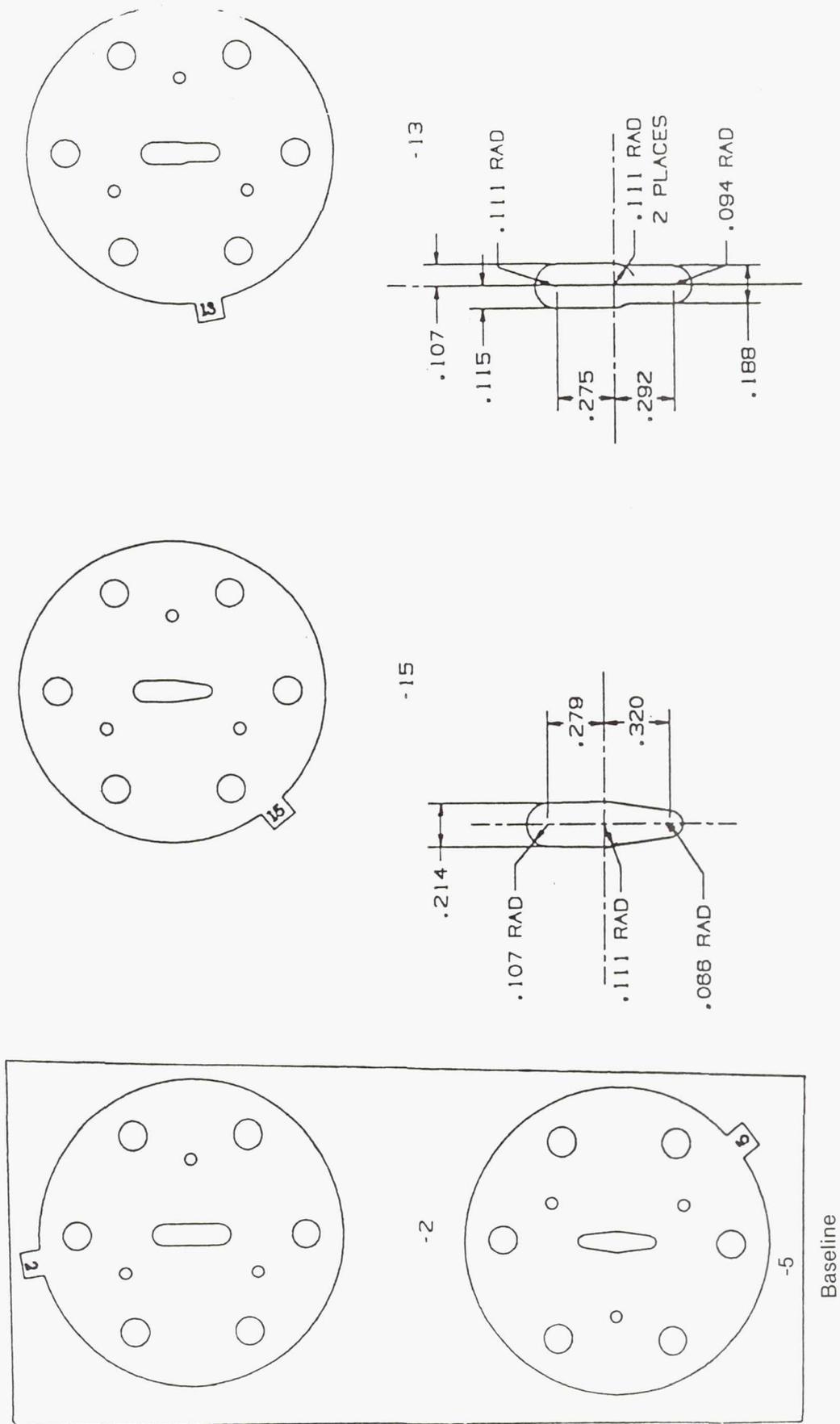
Figure 3.3-10. Baffle Element Modifications (-15 and 13)

125

3.3, Element Design Modifications (cont.)

platelet to the baseline design. Accompanying tables, presented within Figures 3.3-4 thru -10, summarize the corresponding changes in cross sectional flow area for the left and right sides of each fuel circuit.

3.3.1 Uni-Element Cold Flow Test Fixture

Cold flow testing was used to evaluate the element modifications. The uni-element test fixture, shown in Figure 3.3-11, routes fuel & oxidizer simulants to a loose platelet stack that is bolted together. Use of this fixture allows an assortment of geometry changes with a minimum number of platelets. This flow fixture has been used in other uni-element studies at Aerojet to study injector spray mass distributions. To accommodate the element design for this task, new fuel platelets and an oxidizer post were fabricated. Laser cutting of platelets was investigated as a cost saving alternative to chemically milling the element patterns. Results of this fabrication method are discussed in Section 3.4.

3.3.2 Splash Test Setup

Initial splash tests were used as a quick check of the element "footprint" for the different stacking sequences. A schematic of the test stand for the splash tests is shown in Figure 3.3- 12. The actual test stand and data collection center are shown in Figures 3.3-13 & -14, respectively. Photographs of the splash test spray fans are contained in Appendix B. Results of the spray fan data are discussed as they pertain and support the MMRD (or Milkmaid) tests.

Based on the footprint data achieved with the splash tests, subsequent cold flow testing using the "Milkmaid" test stand provided information on the mass flow patterns. Expected pattern variations are presented in Figure 3.3-15.

3.3.2.1 Splash Test Results

The splash tests were run with water as the oxidizer simulant and GN_2 as the fuel simulant. Ambient temperature GN_2 was chosen to simulate the GH_2. Water was chosen for the oxidizer simulant so that one of the flow circuit spray patterns could be visually recorded.

126
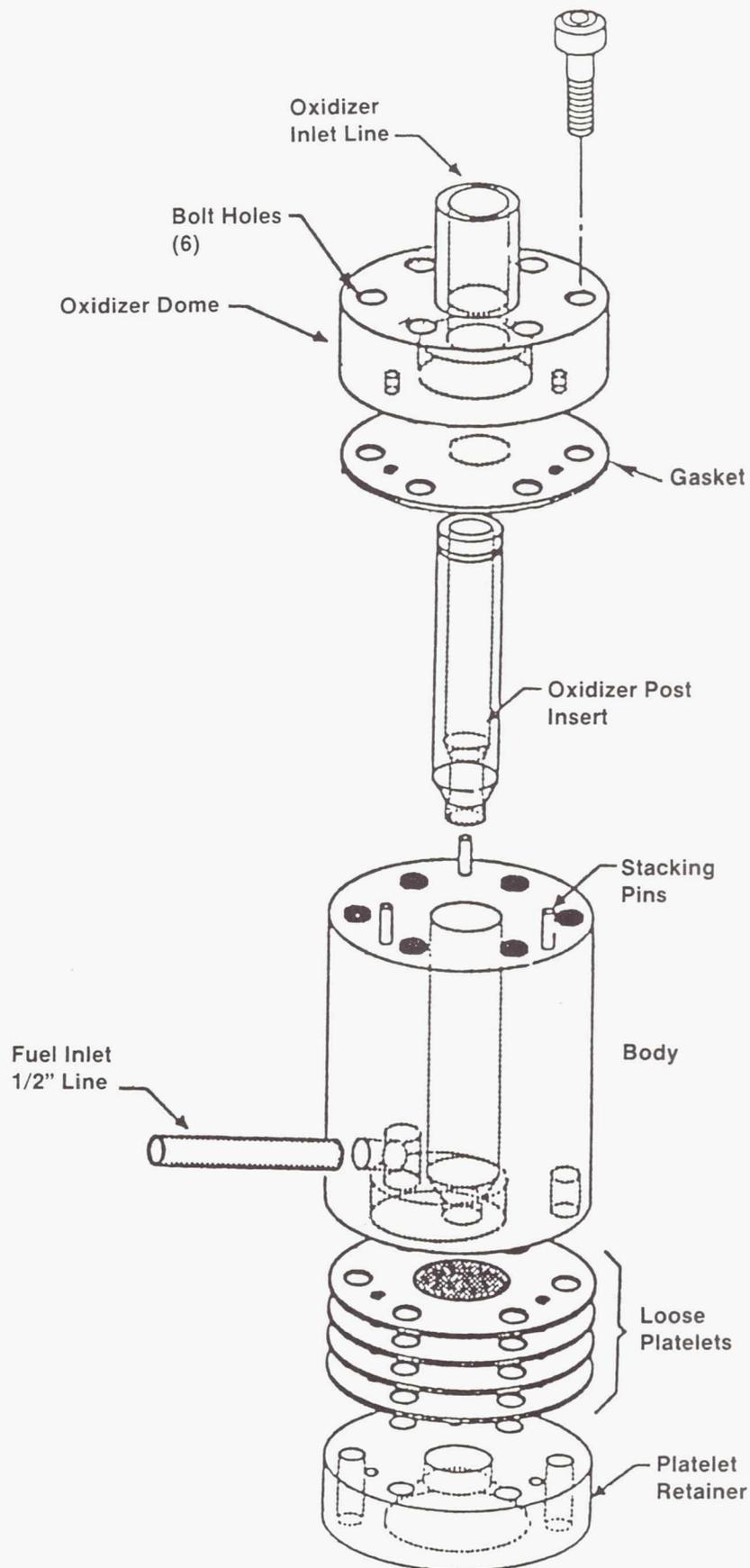
Figure 3.3-11. Uni-Element Test Fixture
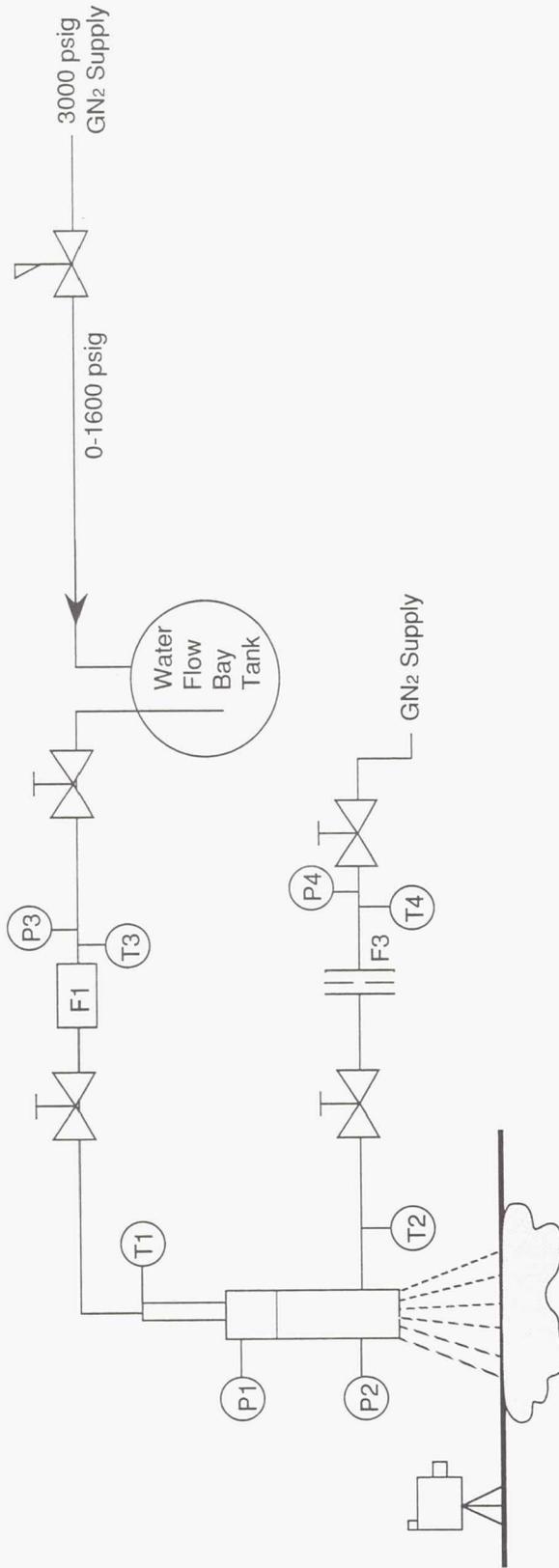
127

Figure 3.3-12 Splash Test Flow Schematic

3000 psig GN₂ Supply

0-1600 psig

Water Flow Bay Tank

GN₂ Supply

P3 T3 F1 T1 P1 P2 T2

P4 T4 F3

II Other Supplies

Polaroid Photographs

I Instrumentation - (Milkmaid Tests)

Designation	Type	Fluid	Range
T1, T2	Thermocouples		0 - 100 deg F
	Pressure Transducers		
P2		GN₂:	0 - 350 psia - Fuel
P1		H₂0:	0 - 250 psia - Ox
F1	Flowmeters	H₂0:	0 - 0.5 lbm/sec
F3	Sonic Venturi	GN₂ Flowrate:	0 - 0.0305 lbm/sec
		GN₂ Velocity:	1147 Fps

1.1.9.48

Figure 3.3-13. Uni-Element Test Stand

129
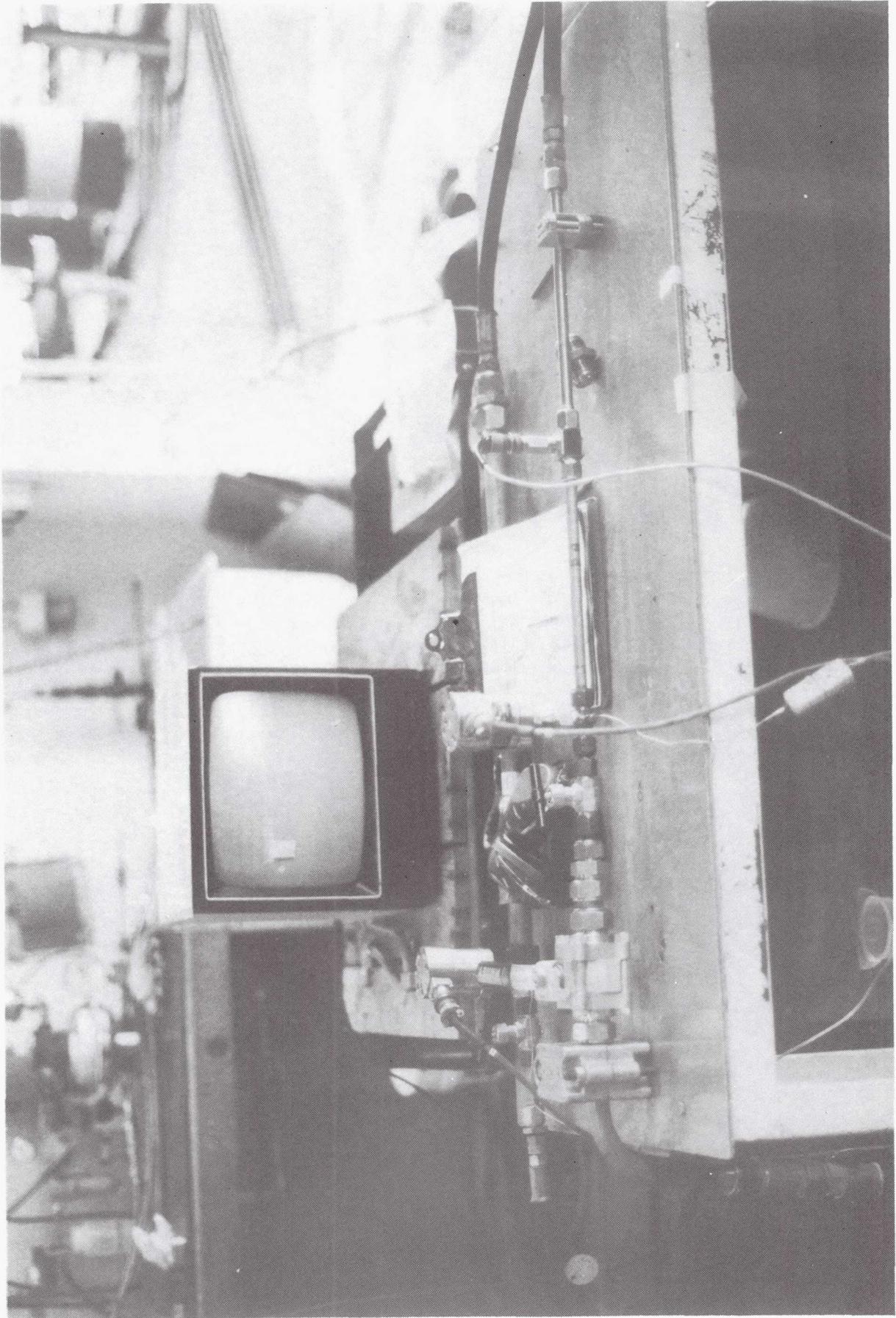
Figure 3.3-14. Uni-Element Test Data Collection Center

3K Element

Ox   Fuel

Center Element And
Wall Element

Wall   Wall

Ox   Fuel

Baffle Element

Baffle   Baffle

Ox   Fuel   2.4.0.49
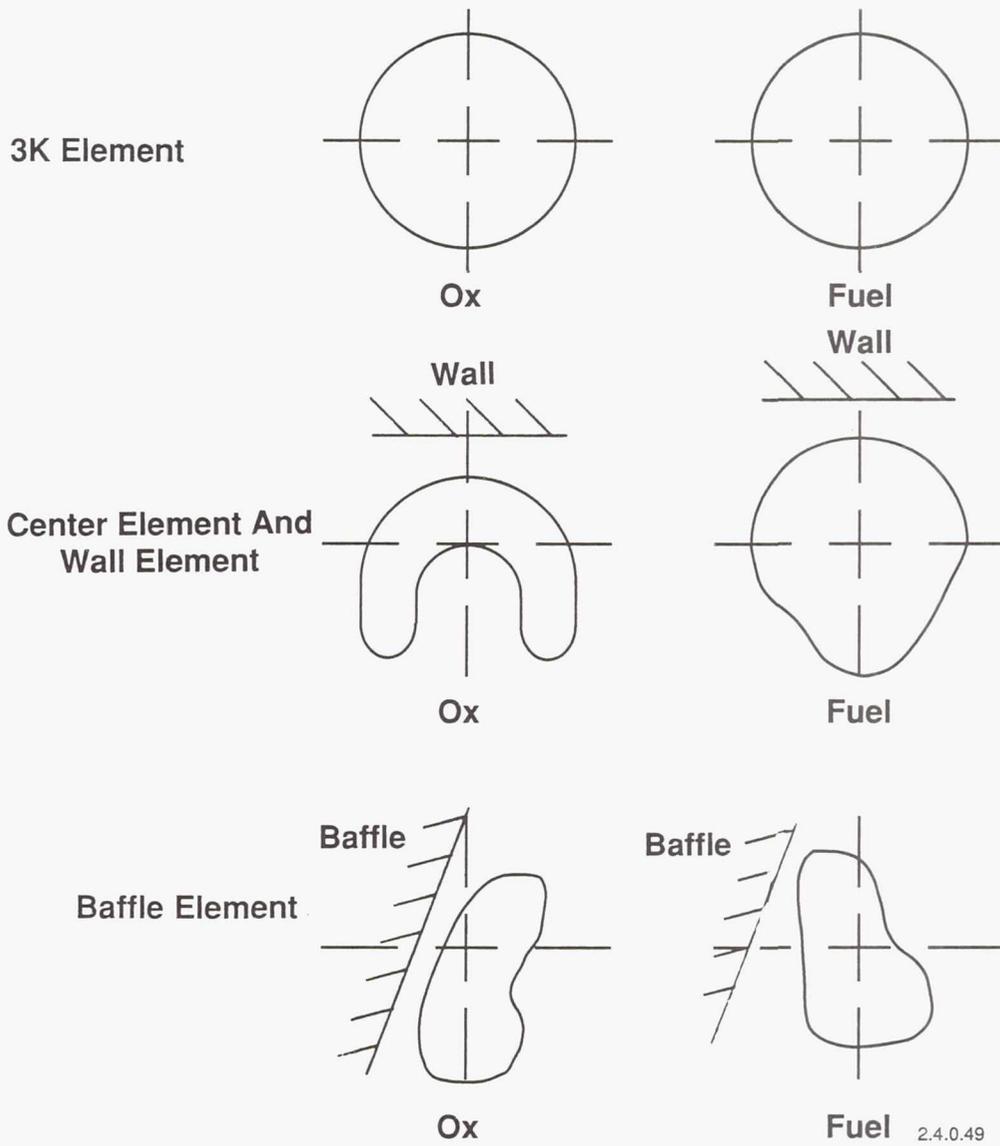
Figure 3.3-15. Predicted Milkmaid Mass Flow Patterns for
Fuel and Oxidizer Elements

131

3.3, Element Design Modifications (cont.)

Each element configuration was tested at four momentum ratios, defined as (wox/wf) * (Vox/Vf). Table 3.3-I summarizes the collected text data. The water flowrates were corrected from the flowmeter reading using a flowmeter calibration curve obtained before the start of the splash tests because of oxygen flow meter inaccuracy at the lowest flow rates. The water flowrates for the low momentum ratio tests of each configuration were calculated using an average element CdA of the three higher momentum ratio tests. The water circuit element effective flow area (CdA) in square inches is obtained by calculation of the pressure drop in circuit:

$$DP = \frac{1}{2}\rho V^2$$

& substituting the relationship of

$$v = \frac{\dot{w}}{\rho A}$$

into the equation provides an effective area relationship as a function of flowrate and pressure drop of

$$C_DA = \frac{\dot{w}}{\sqrt{DP * s.g.}}$$

where: $\dot{w}$ = flowrate in lbm/sec

sg = specific gravity

Dp = injector pressure drop

V = water velocity

ρ = density (lbm/ft^3)

The water velocity in feet per second (fps) was obtained from the mass continuity equation:

$\dot{w} = \rho VA$ where CdA was used for the area resulting:

$V = \dot{w}/\rho*CdA$

TABLE 3.3-I

Date: 3/31/89
File: Sumfin

UNI-ELEMENT TESTING FILE SUMMARY

Uni-Element Testing   Splash Test Summary

Test	T1 Toj (F)	T2 Tij (F)	T3 Tovi (F)	T4 Tfvi (F)	P1 Poj (psia)	P2 Pfj (psia)	P3 Povi (psia)	P4 Pfvi (psia)	Ox Wdot (meas) (lbm/sec)	Fuel Wdot (meas) (lbm/sec)	Oxy Vel (ft/sec)	Fuel Vel (ft/sec)	Momen Ratio	Ox CdA	Fuel CdA
ABAS1	53.0	44.4	57.7	38.4	104.3	142.3	105.2	564.8	0.4057	0.0381	115.3	1119.30	1.10	0.00812	0.0115
ABAS3	57.4	47.2	58.1	40.8	156.9	131.2	159.6	514.8	0.5137	0.0346	145.3	1122.49	1.92	0.00816	0.0114
ABAS5	55.8	46.0	57.7	37.5	204.4	118.7	208.0	464.4	0.5915	0.0313	167.8	1121.16	2.83	0.00813	0.0113
ABAS7	69.6	53.1	58.2	45.2	212.8	91.2	216.9	400.3	0.6212	0.0278	177.7	1129.01	3.52	0.00806	0.0114
BCEN1	65.1	54.6	59.1	55.4	101.9	125.8	103.8	564.4	0.4009	0.0375	113.8	1130.61	1.08	0.00813	0.0129
BCEN3	66.4	55.0	59.0	54.5	155.5	115.9	159.0	515.3	0.5142	0.0342	144.6	1131.04	1.92	0.00821	0.0128
	63.5	55.3	59.0	55.4	206.1	105.1	210.4	464.7	0.5930	0.0310	168.6	1131.38	2.85	0.00812	0.0128
BCEN7	63.9	55.1	59.0	52.5	227.0	93.8	231.5	414.2	0.6207	0.0274	177.5	1131.15	3.55	0.00807	0.0127
CCEN1	63.6	52.4	59.3	45.4	102.9	128.4	104.6	563.8	0.4029	0.0378	114.4	1128.17	1.08	0.00813	0.0127
CCEN3	60.9	53.0	57.7	51.9	154.9	118.9	158.2	516.4	0.5119	0.0343	144.3	1128.84	1.91	0.00819	0.0125
CCEN5	60.2	52.4	57.5	50.3	202.1	107.3	206.4	465.0	0.5859	0.0309	166.8	1128.19	2.80	0.00811	0.0125
CCEN7	60.8	52.6	57.3	49.1	226.4	95.9	230.9	415.0	0.6208	0.0275	177.3	1128.42	3.54	0.00808	0.0124
DCEN1	61.7	53.2	58.8	53.9	102.2	128.1	103.8	564.6	0.4009	0.0375	113.9	1129.12	1.08	0.00812	0.0127
DCEN3	61.7	53.2	58.6	52.7	157.6	120.2	161.0	514.8	0.5163	0.0342	145.6	1129.10	1.95	0.00818	0.0123
DCEN5	61.5	53.2	58.4	51.6	203.3	109.0	207.7	465.0	0.5877	0.0309	167.3	1129.04	2.82	0.00810	0.0123
DCEN7	60.0	53.9	58.6	50.3	212.8	82.9	217.3	400.5	0.6219	0.0277	177.7	1129.88	3.53	0.00807	0.0123
ECEN1	60.2	53.5	59.0	54.4	102.3	125.5	103.9	565.2	0.4011	0.0376	114.0	1129.44	1.08	0.00812	0.0130
ECEN3	61.8	53.8	59.0	53.0	156.0	118.8	159.3	515.6	0.5134	0.0342	144.8	1129.68	1.92	0.00818	0.0125
ECEN5	61.9	54.4	59.0	52.1	205.5	107.9	210.0	464.9	0.5933	0.0308	168.3	1130.36	2.86	0.00813	0.0124
ECEN7	62.7	54.5	58.8	50.9	232.5	95.7	237.0	411.9	0.6262	0.0273	179.8	1130.49	3.65	0.00804	0.0124
FBAF1	68.1	55.5	58.8	53.4	102.2	105.3	103.8	566.6	0.3997	0.0377	113.9	1131.59	1.07	0.00809	0.0155
FBAF3	63.0	54.7	59.0	53.9	156.8	98.0	159.8	515.4	0.5139	0.0342	145.2	1130.67	1.93	0.00817	0.0151
FBAF5	64.3	54.8	58.9	52.1	199.9	89.6	203.8	466.1	0.5805	0.0309	165.8	1130.87	2.75	0.00808	0.0150
FBAF7	68.0	56.0	59.0	47.9	231.0	89.0	235.3	414.6	0.6240	0.0275	179.2	1132.17	3.59	0.00804	0.0134
GBAF1	66.3	55.9	59.3	57.1	102.1	134.4	103.6	564.7	0.4004	0.0374	113.9	1132.04	1.08	0.00811	0.0121
GBAF3	67.9	56.2	59.1	55.9	155.6	124.4	158.6	514.3	0.5123	0.0341	144.6	1132.41	1.92	0.00817	0.0119
GBAF5	70.7	54.6	59.3	47.0	199.8	114.9	203.9	465.6	0.5824	0.0310	165.8	1130.56	2.75	0.00811	0.0117
GBAF7	69.4	53.2	59.1	43.4	232.2	103.0	236.6	415.1	0.6272	0.0277	179.7	1129.05	3.60	0.00805	0.0117
HBAF1	70.0	51.3	59.7	44.0	102.9	144.8	103.7	564.4	0.4018	0.0379	114.4	1126.96	1.08	0.00810	0.0113
HBAF3	70.5	50.7	59.3	41.7	155.3	133.0	158.3	515.5	0.5103	0.0346	144.5	1126.30	1.89	0.00815	0.0112
HBAF5	70.1	54.1	59.4	45.6	202.6	120.2	206.7	465.1	0.5863	0.0311	167.0	1130.05	2.79	0.00810	0.0112
HBAF7	72.3	54.1	59.3	43.9	225.8	107.3	230.5	414.9	0.6183	0.0277	177.0	1130.06	3.50	0.00806	0.0112
IBAF1	59.5	43.6	57.2	37.0	104.9	143.7	105.8	564.6	0.4065	0.0382	115.7	1118.44	1.10	0.00811	0.0114
IBAF3	53.0	42.0	57.2	32.9	157.3	135.5	160.0	515.4	0.5138	0.0349	145.5	1116.66	1.92	0.00815	0.0110
IBAF5	53.3	44.3	57.0	34.8	201.2	120.4	205.0	465.4	0.5865	0.0314	166.4	1119.27	2.78	0.00812	0.0112
IBAF7	52.7	43.5	57.0	31.8	231.7	108.1	235.7	415.1	0.6261	0.0280	179.5	1118.38	3.59	0.00805	0.0111

3.3, Element Design Modifications (cont.)

The GN$_2$ flowrate was found from the sonic orifice calibration chart. The fuel element CdA is calculated using the sonic compressible flow equation listed below:

$$CdA = \frac{w}{(Pin^* \sqrt{((g^*\gamma/R^*T)^*(2/\gamma+1)\wedge(\gamma+1/\gamma-1))}}$$

and the GN$_2$ gas velocity was found with the gas sonic velocity equation listed below:,

$$V = \sqrt{(\gamma^*g^*R^*T/MW}$$

where $\dot{w}$ = fuel flow rate (lbm/sec)
            Cd = empirical discharge coefficient
            A ,= injection flow area (in.^{2})
            g = 32.17 (ft lbm/lbf sec^2)
            R = 1545 ft lbf/lbm deg R
            MW = molecular weight
            T = temperature (deg R)
            γ = ratio of specific heats
            Pin   = inlet pressure (psia)

Each splash test was recorded by Polaroid photographs and 35mm photographs from 4 views: two side views 90 deg apart, and the two corresponding top views (also 90 deg apart). The pictures (Appendix B) show that the spray fan produced by the pre-mix impingement of the fuel on the oxidizer is similar to a conventional triplet pattern.

Measurement of the water (oxidizer circuit) spray fan cone angles from the Polaroid photographs showed a distinct relationship with momentum ratio and element type. The spray cone half angles appeared to decrease in groups in the following order: baseline, baffle elements, and center elements, as shown in Figure 3.3-16. The decrease in spray cone angle with increased momentum ratio occurs due to an increased vertical oxidizer momentum combined with a reduced sidewise fuel momentum. This relationship diminished progressively from the
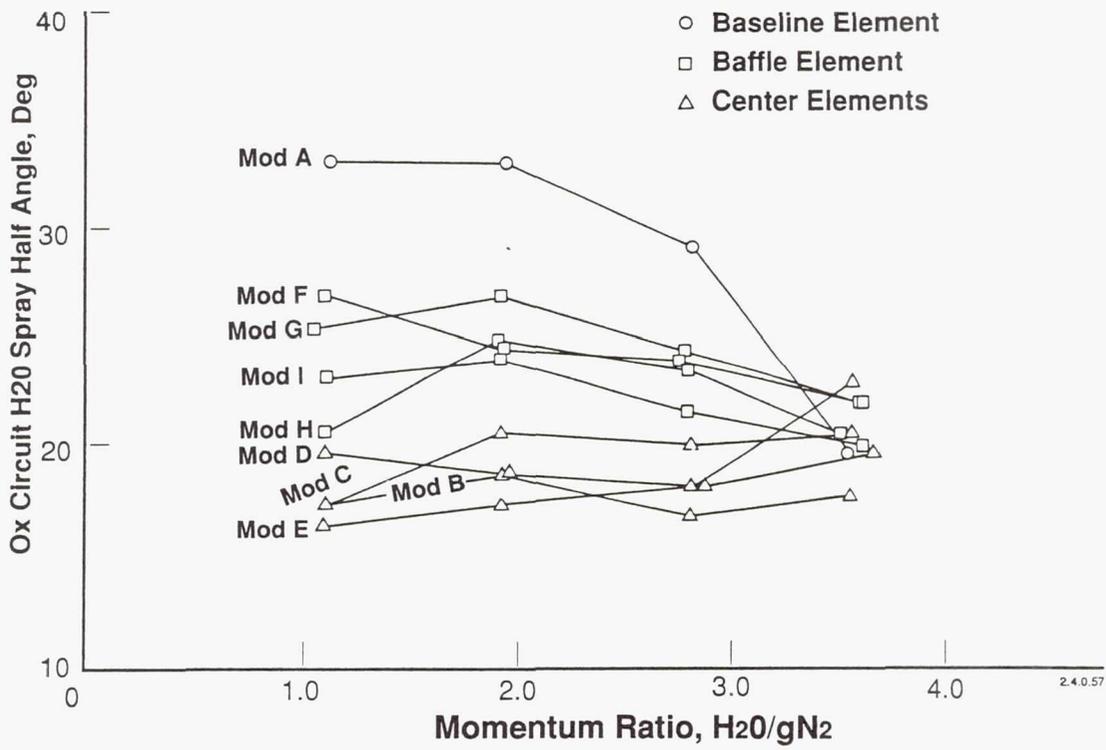
Figure 3.3-16. Effect of Momentum Ratio on Spray Cone Angle

135

baseline element to the center element, which appeared to not have a distinct relationship between cone angle and momentum ratio. This effect may be due to the efficiency of the modified fuel element in surrounding the oxidizer stream as opposed to breaking up the oxidizer stream, as is the case for the baseline element.

The baffle and center element geometries were designed so that all the fuel elements when incorporated into an injector would receive equal flow. This required each of the baffle and center elements to have overall fuel CdA's equal to the baseline element CdA. The water and GN2 CdA's from the splash tests are plotted versus momentum ratio in Figure 3.3-17. The water circuit shows a very consistent CdA of 0.0081 +/- 0.001, which was expected since no modification was made to the oxidizer circuit. Figure 3.3-17 shows that increasing momentum ratio has a negligible effect on CdA when both circuits are flowed together. As shown in Figure 3.3-18 the fuel circuits of the modified elements are all within 15% of the baseline fuel CdA except for the F modification of the Baffle Element (FBAF) configuration. The anomalous data for FBAF is attributed to either a leak caused by under torquing the platelet stack onto the cold flow assembly, or malfunction of one of the pressure measuring devices.

3.3.3 Selected Element Configurations for the Mass & Mixture Ratio Distribution (MMRD) Tests

One element configuration from each of the baseline, baffle, and center element configurations was selected for testing on the Mass and Mixture Ratio Distribution (MMRD) or "Milkmaid" test apparatus. The baseline element was tested as a basis of comparison for the modified elements. The selection of the H modification of the Baffle element (HBAF) and the E modification of the center element (ECEN) used in the milkmaid tests was based solely on the appearance of the spray fan in the Polaroid pictures.

The shape of the spray fans for both the H modification to the baffle element (HBAF) and the E modification to the Center element (ECEN) appeared to be most "different" from the baseline element spray fan. Cross-sections of the selected elements are presented in Figure 3.3-19.
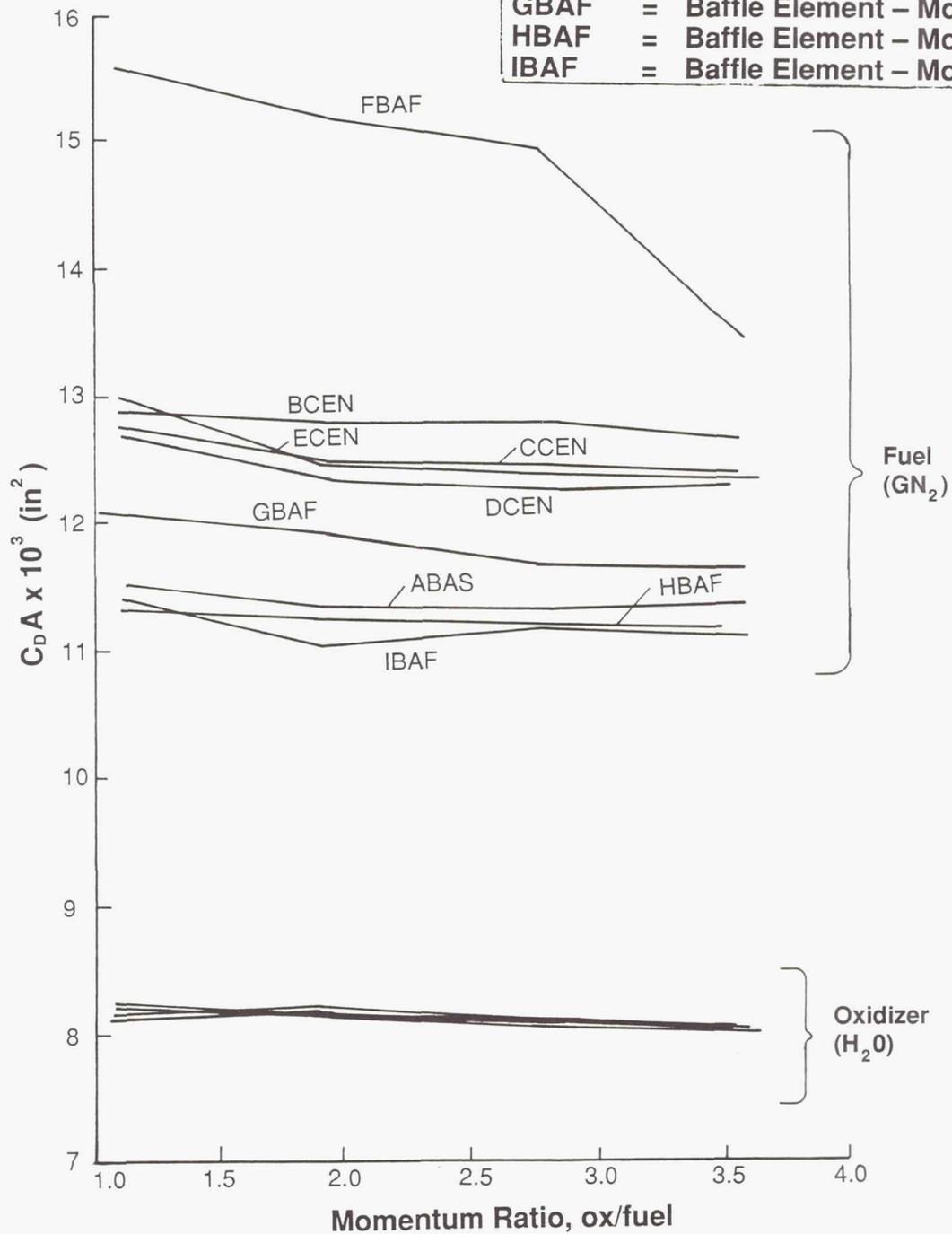
Figure 3.3-17. Effect of Momentum Ratio on Element Effective Flow Area (From Splash Test Data)
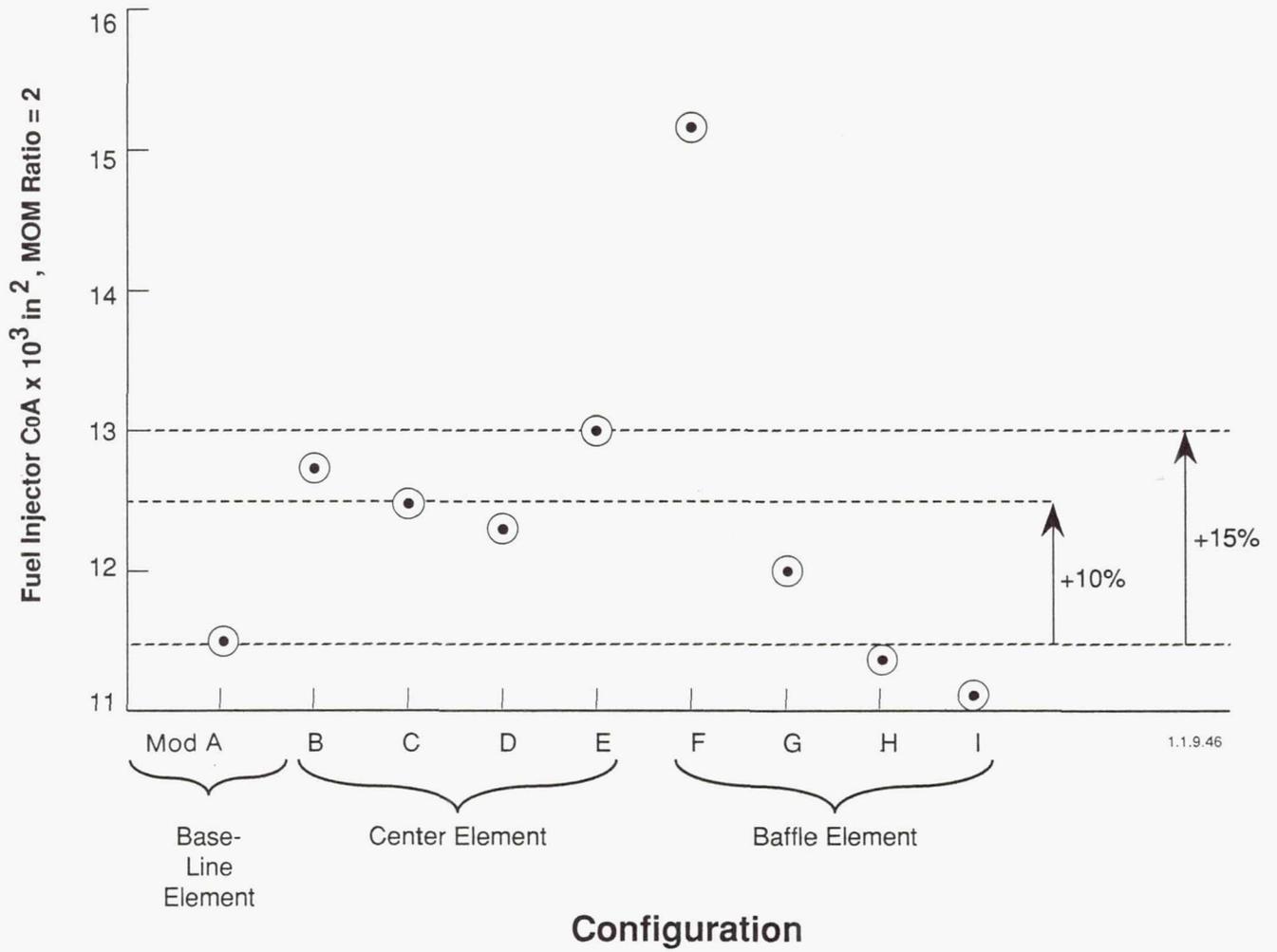
Figure 3.3-18. Fuel Element Flow Area Consistency
(From Splash Test Data)

138
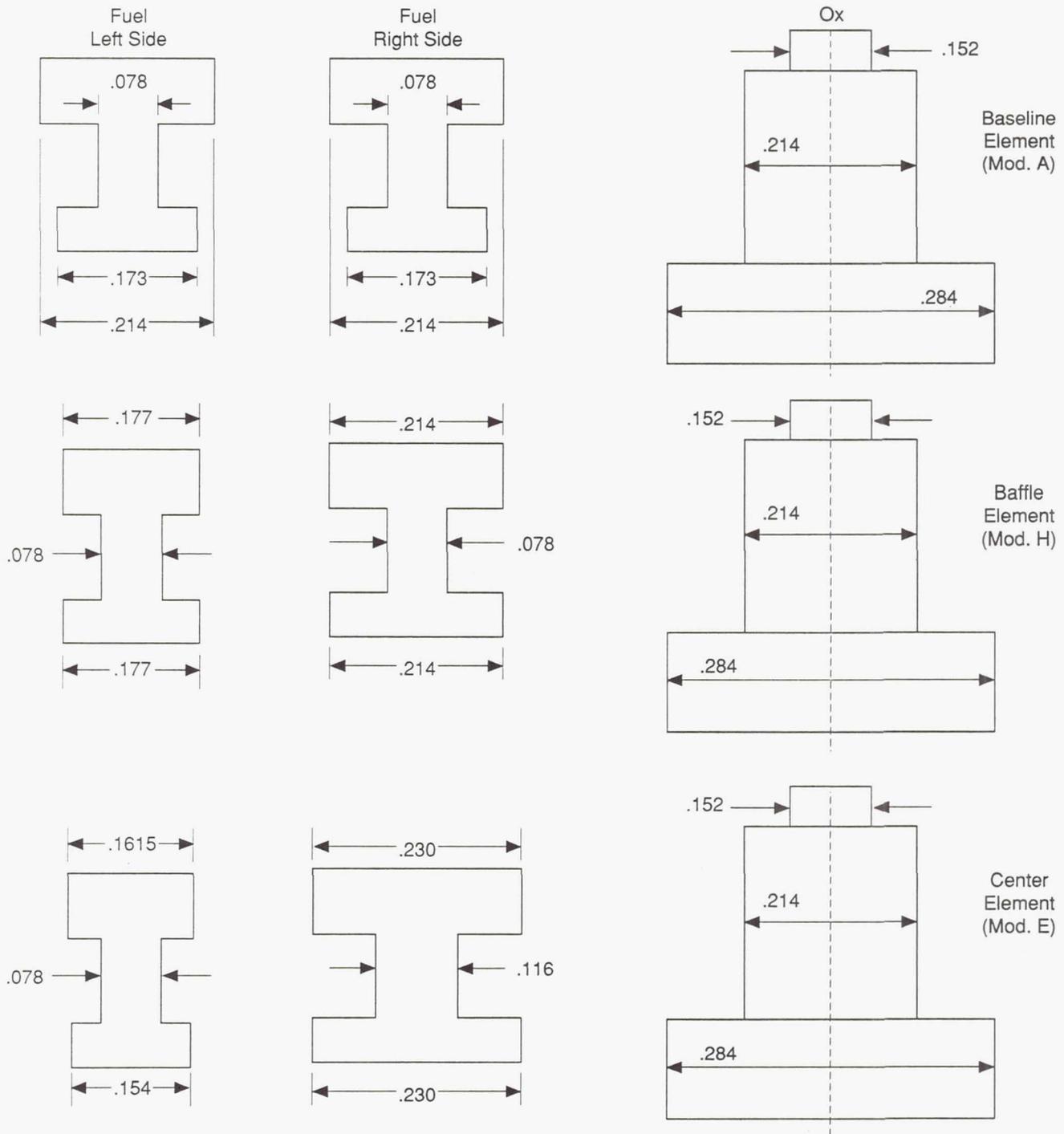
Figure 3.3-19. Cross Section of Selected Elements for Milkmaid Testing

139

3.3, Element Design Modifications (cont.)

3.3.3.1   MMRD Test Results

A schematic of the milkmaid set-up is shown in Figure 3.3-20. The actual milkmaid assembly is shown in Figure 3.3-21 and a closeup of the flow fixture above the collection grid is shown in Figure 3.3-22.

Table 3.3-II summarizes the test data obtained from the three milkmaid tests. The run durations were approximately 26 seconds, and the stock sugar concentration for the fuel circuit was approximately 30% by weight. The milkmaid collection plate was located 5.75 inches from the platelet face, and the element orientation relative to the collection grid is shown in Figure 3.3-23. In this orientation, the smaller cross sectional flow area was on the left of the oxidizer circuit and the larger cross sectional flow area was to the right.

3.3, Element Design Modifications (cont.)

Reduction of the test data from the Milkmaid tests utilized the methodology presented in Figure 3.3-24. Computer program listings for Sugar and FD0073 are presented in Appendix C. Program FD0073 was used to generate the mass and mixture ratio contours for the tests, as shown in Figures 3.3-25 and -26. All the mass contour plots have the same contour levels for ease in comparison. All flowrates were normalized to the actual collected total oxidizer and fuel flowrates since the collection efficiency of the milkmaid apparatus is never quite 100%.

The oxidizer mass contours in Figure 3.3-25 show only a slight response to the changes in the fuel momentum. The oxidizer mass contours have a large central ox-rich core area, represented by the large open area in the center of the oxidizer contour maps. This high oxidizer concentration in the center of the spray fan was also visually evident in the splash tests.

The fuel mass contours in this same figure, however, showed a distinct difference when going from the baseline to the baffle and to the center modifications. The center element configuration showed the most significant change with a large fuel-rich region near the bottom right side of the collection plate. The
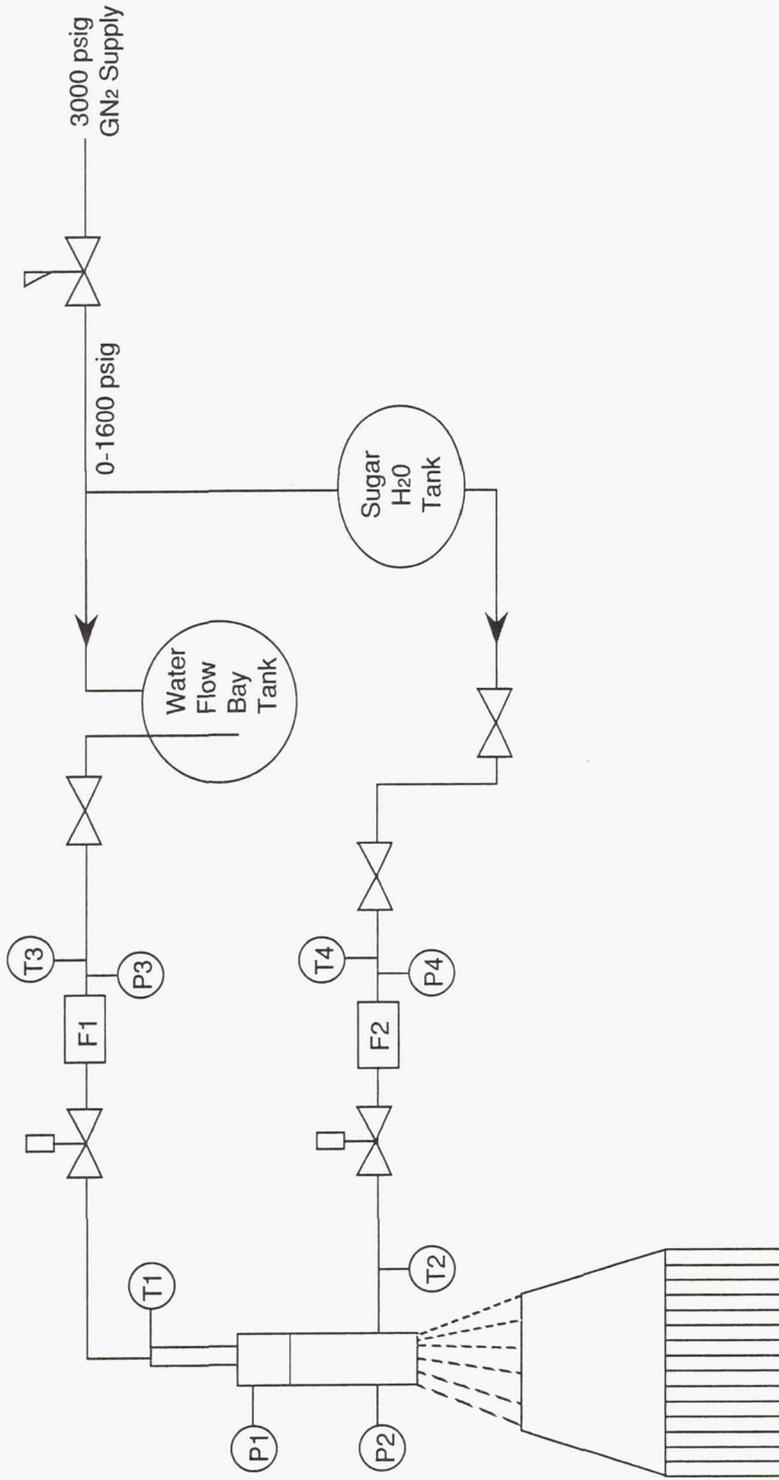
3000 psig GN₂ Supply

0-1600 psig

Sugar H₂0 Tank

Water Flow Bay Tank

T3 P3 F1 T1 P1

T4 P4 F2 T2 P2

1.1.9.47

I Instrumentation - (Milkmaid Tests)

Designation	Type	Fluid	Range
T1, T2	Thermocouples		0 - 100 deg F
	Pressure Transducers		
P1		H₂0:	0 - 250 psia - Ox
P2		Sugar H₂0:	0 - 200 psia - Fuel
F1		H₂0:	0 - 0.5 lbm/sec - Ox
F2		Sugar H₂0:	0 - 0.5 lbm/sec - Fuel

II Other Supplies

Sucrose Solution Concentration = 30%

Stop Watch

Figure 3.3-20. Milkmaid Test Flow Schematic

141
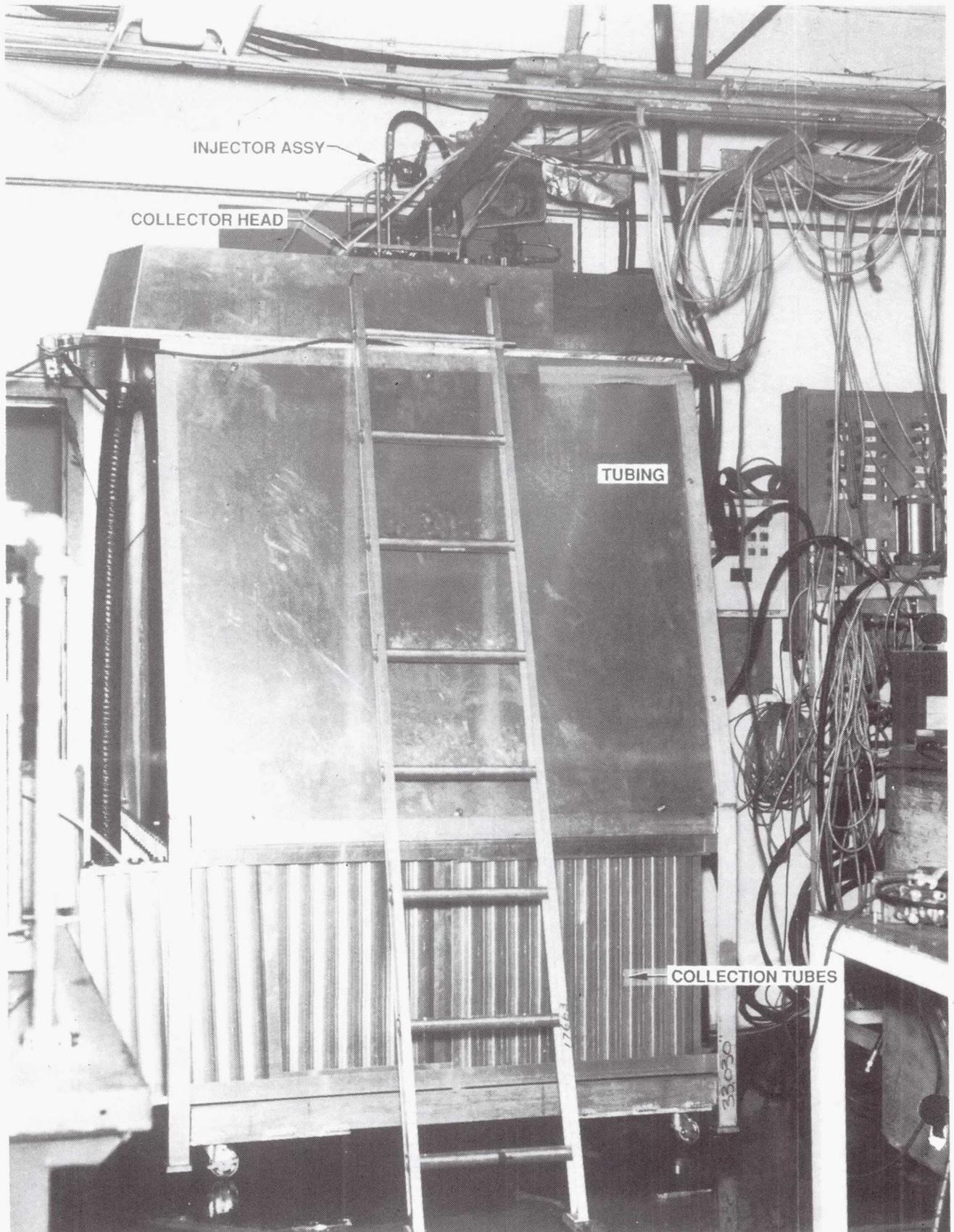
Figure 3.3-21. Milkmaid Test Facility for Injector Cold Flow Tests
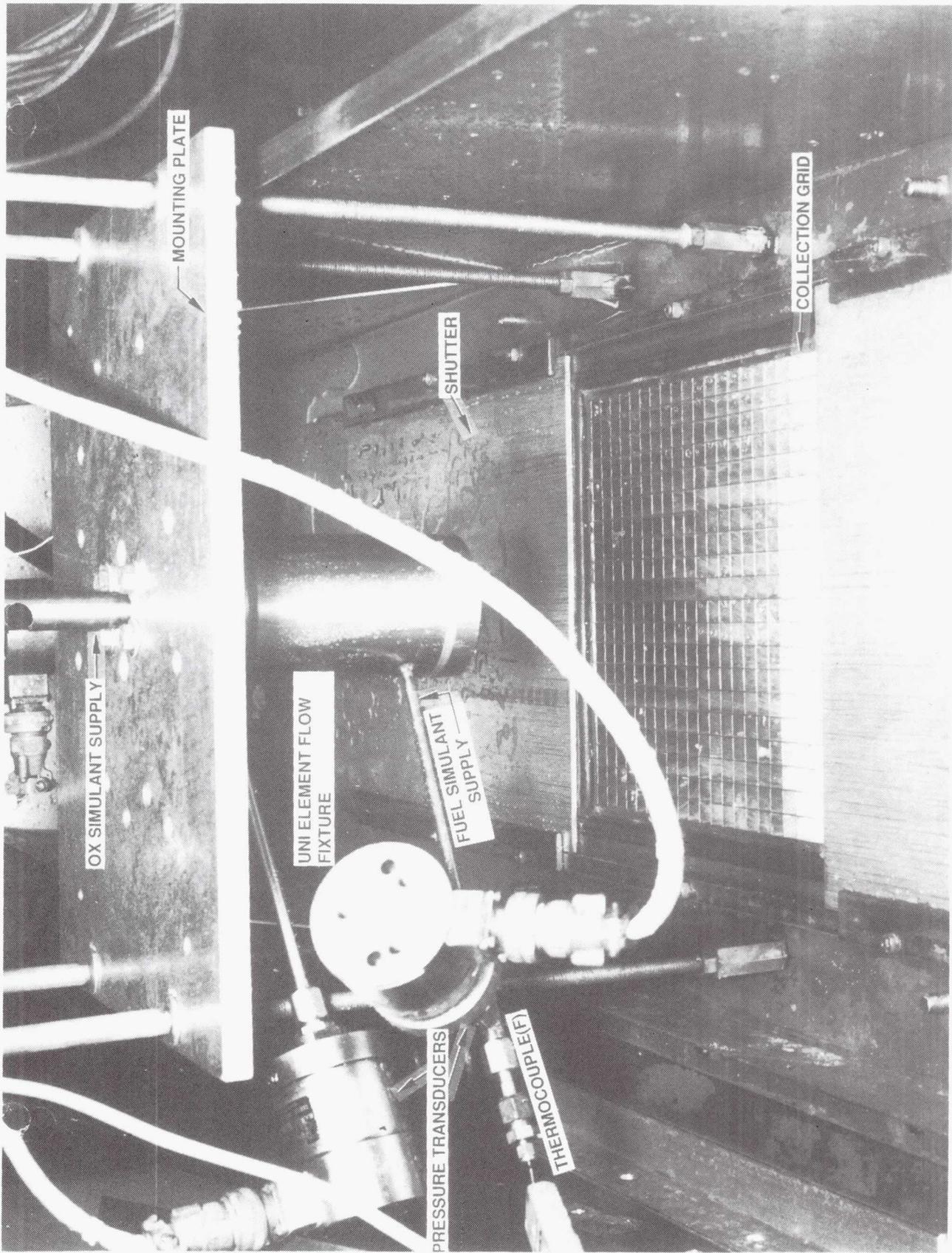
Figure 3.3-22. Uni-Element Flow Fixture Mounted Above the Milkmaid Collection Grid

Labels in figure: MOUNTING PLATE, COLLECTION GRID, SHUTTER, OX SIMULANT SUPPLY, UNI ELEMENT FLOW FIXTURE, FUEL SIMULANT SUPPLY, PRESSURE TRANSDUCERS, THERMOCOUPLE(F)

TABLE 3.3-II

OTV UNI-ELEMENT COLD FLOW MILKMAID TEST SUMMARY

Ox Circuit - H2O
Fuel Circuit - Sugar H2O

Collection Height = 5.75 in.

Test	POFM (psia)	PFFM (psia)	POJ (psia)	PFJ (psia)	FMO lbH2O/s	FMF lbH2O/s	Sg_F	W_{ox} (lbm/sec)	$\dot{W}_F$ (lbm/sec)	KWOJ	KWFJ	C_DA_{OX} (in.²)	C_DA_F (in.²)	VOX (ft/sec)	V_F (ft/sec)	$\dfrac{\dot{W}_{ox}}{\dot{W}_f}$	$\dfrac{\dot{W}_{ox}\,V_{ox}}{\dot{W}_f\,V_f}$ (momentum ratio)
BASMM	262.8	132.5	252.4	122.5	0.767	0.526	1.1217	0.645	0.497	0.0406	0.0424	0.00769	0.00803	193.5	127.3	1.30	1.98
HBAFMM	264.6	131.7	253.2	122.1	0.767	0.511	1.1236	0.645	0.484	0.0405	0.0413	0.00768	0.00783	193.8	126.9	1.33	2.03
ECENMM	256.2	131.8	245.6	120.2	0.756	0.585	1.1236	0.636	0.554	0.0406	0.0477	0.00769	0.00903	190.9	126.0	1.15	1.74

LEGEND

POFM	= pressure upstream of ox flowmeter
PFFM	= pressure upstream of fuel flowmeter
POJ	= oxidizer manifold pressure
PFJ	= fuel manifold pressure
Fmo	= ox flow meter
FmF	= ox fuel flow meter
SgF	= specific gravity fuel simulant
kWOJ	= injector element admittance, ox circuit
kWFJ	= injector element admittance, fuel circuit
CDAOX	= effective flow Area
CDAF	= effective flow area, fuel
VOX	= velocity, ox circuit
VF	= velocity, fuel circuit
$\dot{W}_{ox}/\dot{W}_f$	= flow rate ratio
Ẇox	= flow rate, OX circuit
$\dot{W}_f$	= flow rate, fuel circuit
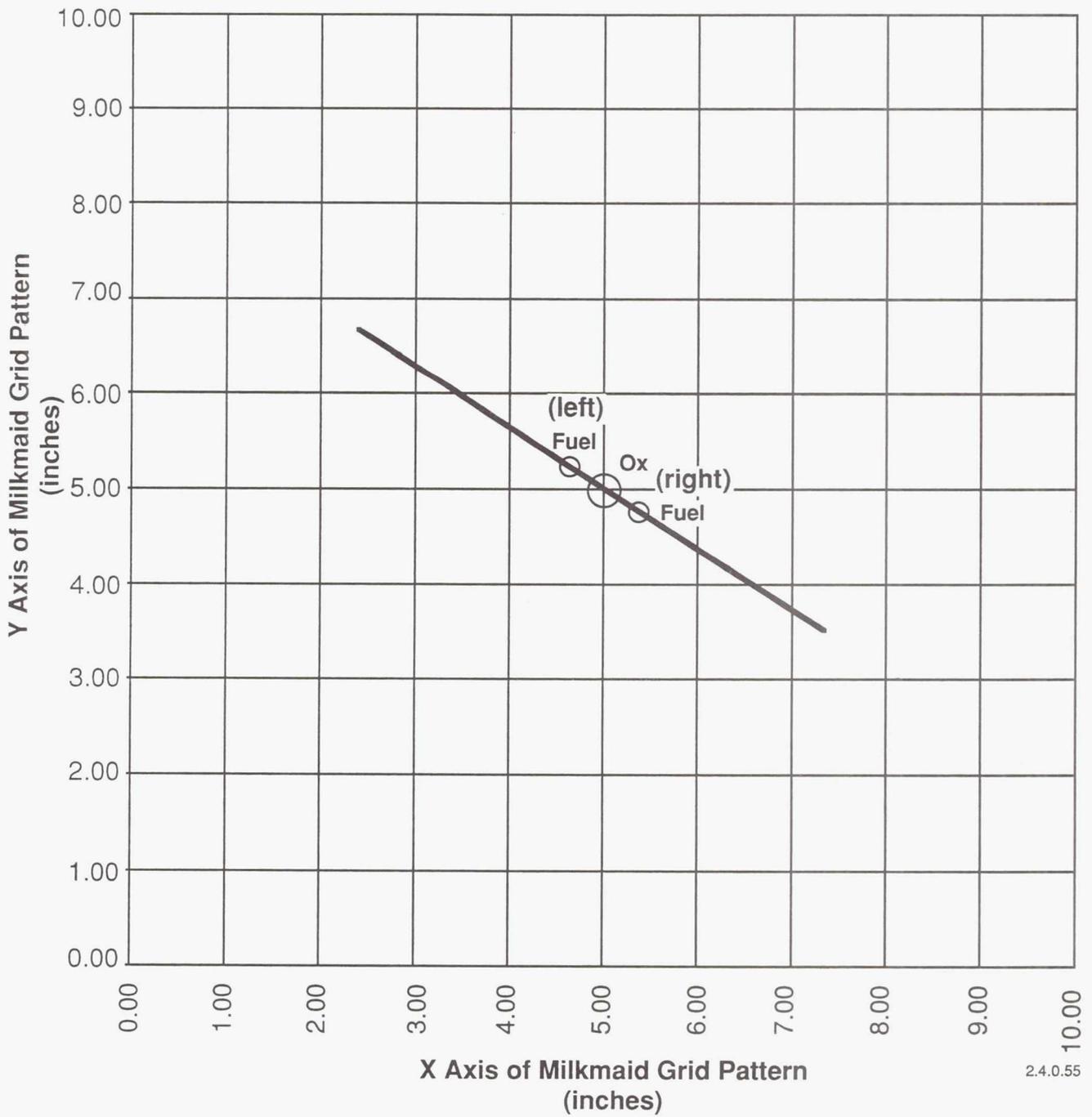
Figure 3.3-23. Element Orientation About the Milkmaid Collection Grid

2.4.0.55

145
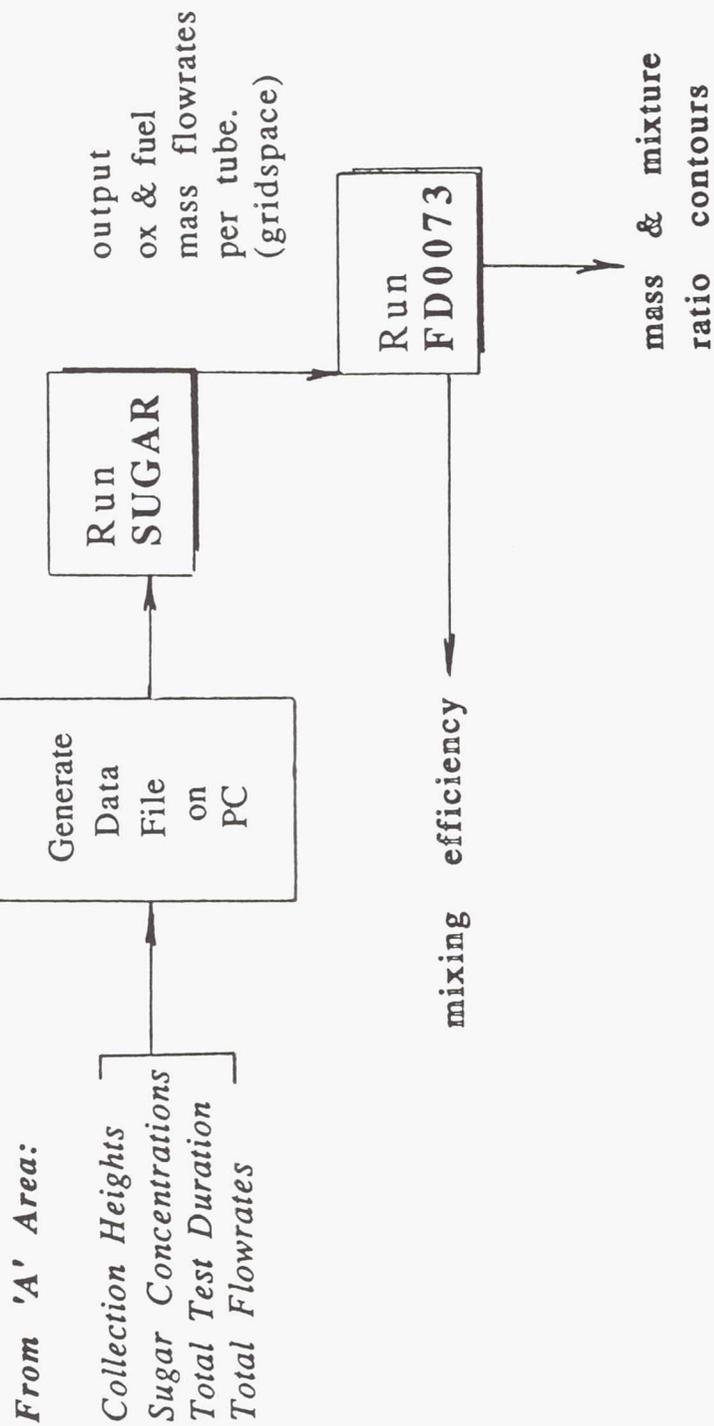
Figure 3.3-24. Milkmaid Data Analysis Logic
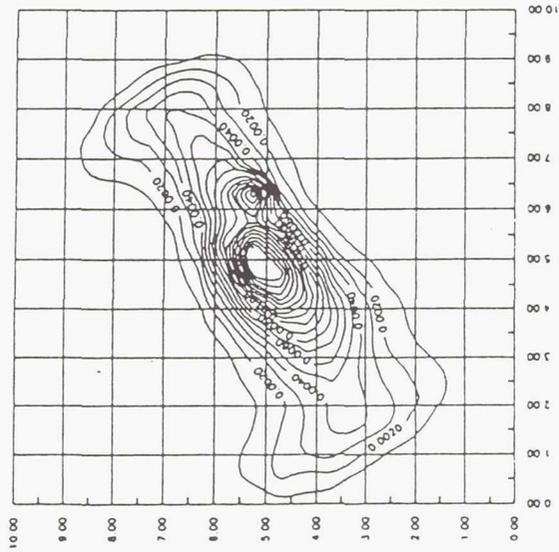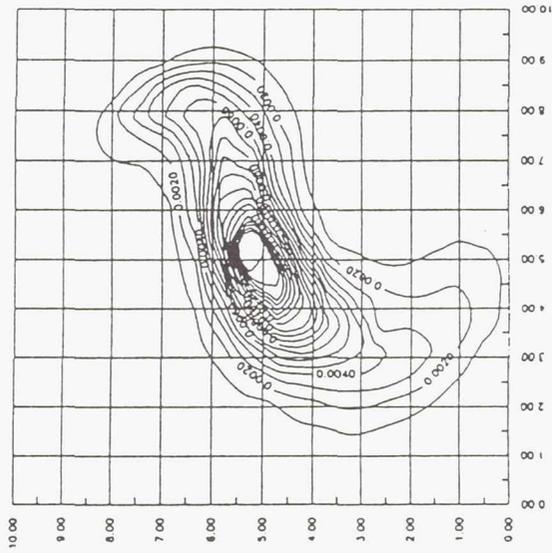
From 'A' Area:

Collection Heights
Sugar Concentrations
Total Test Duration
Total Flowrates

Generate
Data
File
on
PC

Run
SUGAR

output
ox & fuel
mass flowrates
per tube.
(gridspace)

Run
FD0073

mixing efficiency

mass & mixture
ratio contours
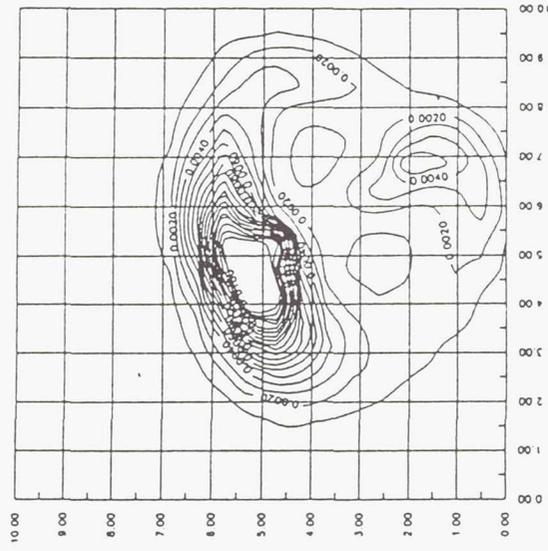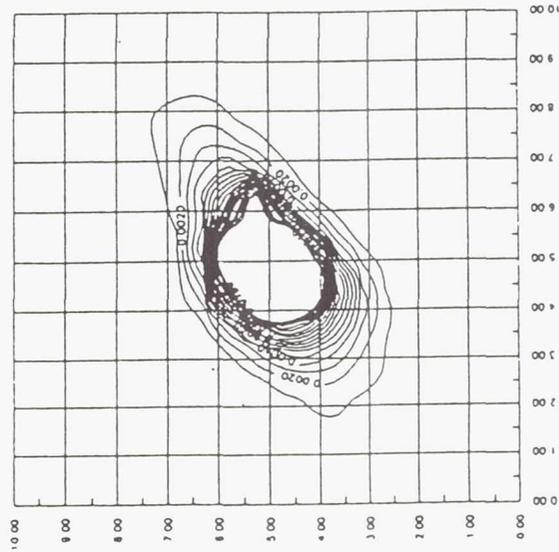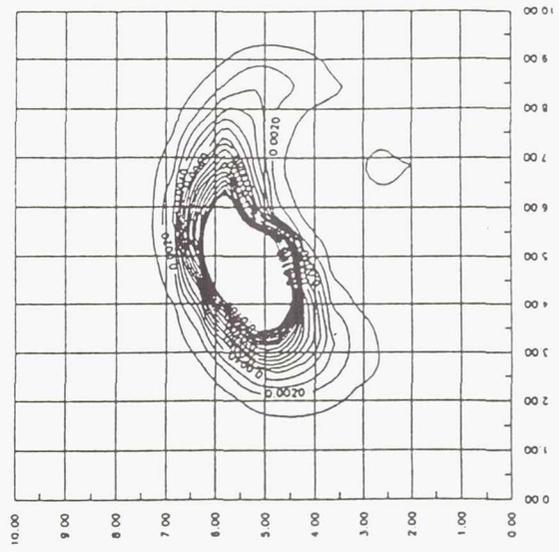
Figure 3.3-25. Oxygen and Fuel Circuit Mass Distribution

147

Figure 3.3-26. Element Total Flowrate & Mixture Ratio Distribution

148

3.3, Element Design Modifications (cont.)

baffle element showed a similar fuel-rich region, but not to the extent shown by the center element.

The mixture ratio contour plots in Figure 3.3-26 show the baseline element has a very oxidizer rich core, but the center element on the other hand has a much more benign central core.

Figures 3.3-27 and -28 give topographical views of the previous two figures, and act mainly as a visualization aid.

The reduced data from the FD0073 computer program for the milkmaid tests is summarized in Table 3.3-III. The oxidizer and fuel flowrates shown in this table are in pounds of simulant per second, not pounds of propellant, which accounts for the extremely low injected mixture ratio. The OTV operating mixture ratio is 6.0. For the cold flow study, it was more important to match the O2/H2 momentum ratio than to match the operating mixture ratio.

The collection efficiencies represent the total mass collected in the collection tubes as a percent of the total injected mass. Em, the mixing parameter, is calculated in computer program FD0073. The mixing parameter Em is used in the two-stream-tube method of calculating mixing efficiency. The range of two stream-tube Em values shown in this table is in the normal range for triplet elements. The two stream tube Em is indicative of the mixing performance efficiency and peripheral thermal compatibility characteristic.

The two-stream-tube mixing parameter, Em, is plotted in Figure 3.3-29 as a function of the oxidizer circuit water spray cone half angle from the splash tests for the element configurations used in the milkmaid tests. This figure shows the mixing efficiency is inversely proportional to the oxidizer spray cone angle. A higher mixing efficiency element confirmation normally implies a more uniform spray mixture ratio, which was evident when comparing the mixture ratio contours.
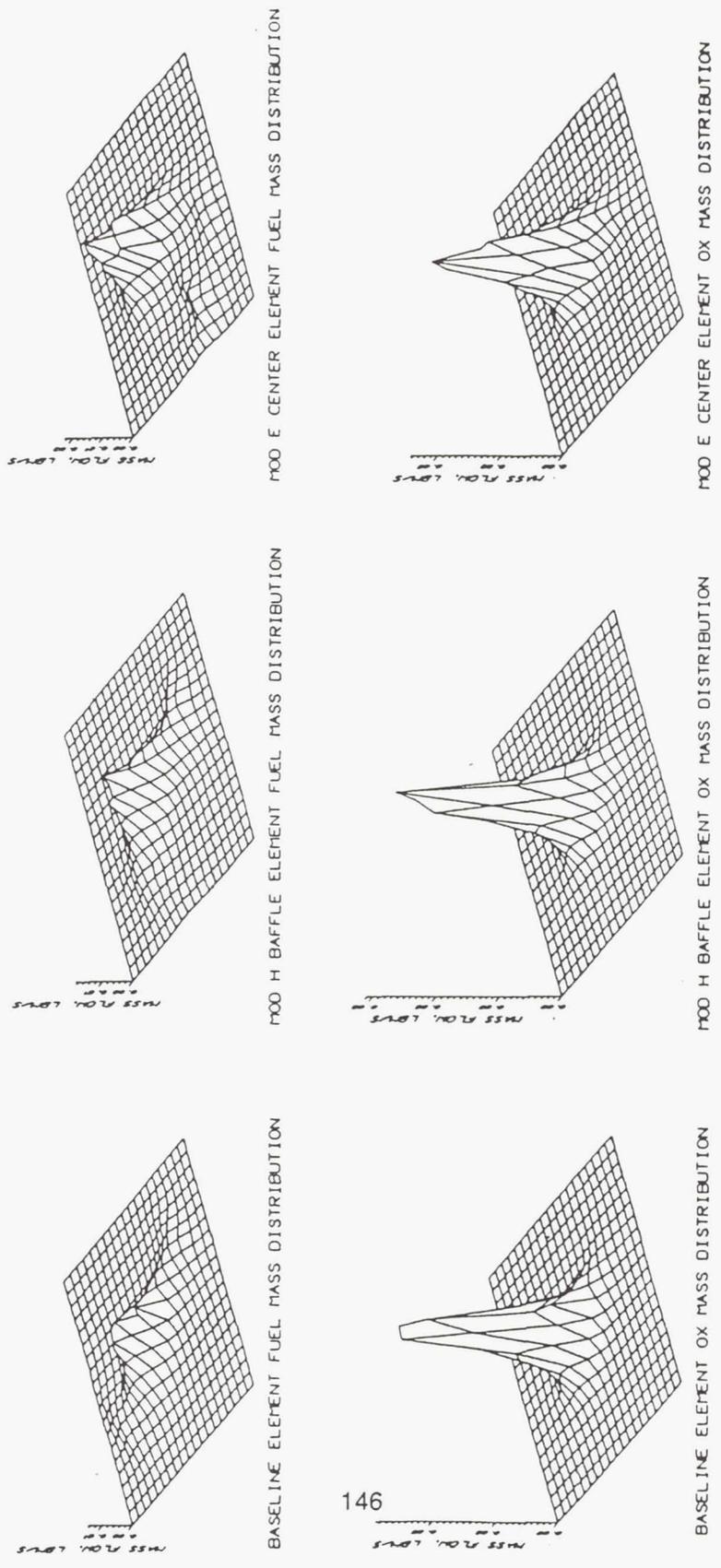
Figure 3.3-27. Topographical View of the Fuel and Oxidizer Mass Distribution

146

150

MOO E CENTER ELEMENT TOTAL MASS DISTRIBUTION
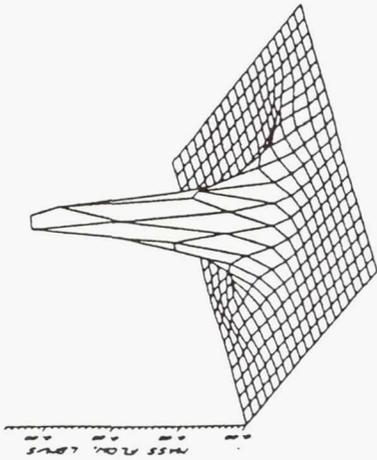
MOO E CENTER ELEMENT MIXTURE RATIO DISTRIBUTION
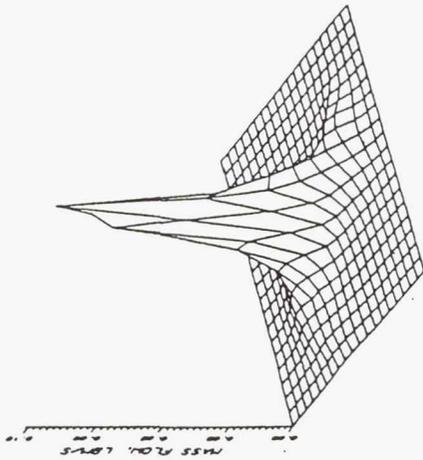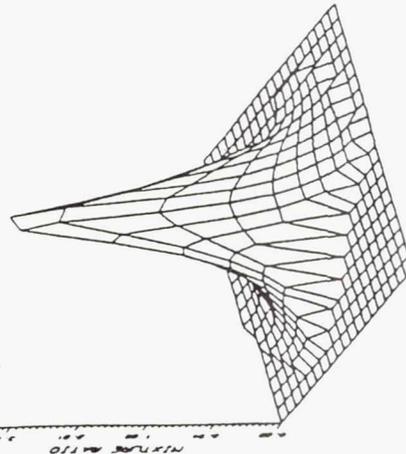
MOO H BAFFLE ELEMENT TOTAL MASS DISTRIBUTION
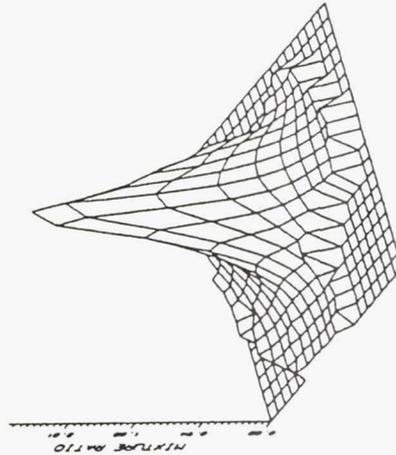
MOO H BAFFLE ELEMENT MIXTURE RATIO DISTRIBUTION

BASELINE ELEMENT TOTAL MASS DISTRIBUTION

BASELINE ELEMENT MIXTURE RATIO DISTRIBUTION

Figure 3.3-28. Topographical View of the Element Mixture Ratio Distribution

147

151

TABLE 3.3-III

OTV ENGINE TECHNOLOGY PROGRAM TASK C.4
SUBTASK IV: INJECTOR STUDIES - UNIELEMENT COLD FLOW

	Milkmaid Results For Baseline Element	Milkmaid Results for Baffle Element Mod H	Milkmaid Results for Center Element Mod E
Collector Size	10.00 in.	10.00 in.	10.00 in.
Total Oxidizer Flowrate	0.645 lb/sec	0.645 lb/sec	0.636 lb/sec
Total Fuel Flowrate	0.497 lb/sec	0.484 lb/sec	0.554 lb/sec
Injected Mixture Ratio	1.30	1.33	1.15
Effective Oxidizer Orifice Area	0.0077 sq in.	0.0077 sq in.	0.0077 sq in.
Effective Fuel Orifice Area	0.0080 sq in.	0.0078 sq in.	0.0090 sq in.
Oxidizer Velocity	193.56 ft/sec	193.81 ft/sec	190.86 ft/sec
Fuel Velocity	127.34 ft/sec	126.96 ft/sec	126.01 ft/sec
Momentum Ratio	1.9726	2.0343	1.7388
Rupe Number	0.332	0.327	0.347
Oxidizer Collection Efficiency	93.45 Percent	96.81 Percent	95.08 Percent
Fuel Collection Efficiency	87.15 Percent	85.98 Percent	86.49 Percent
Overall Collection Efficiency	90.71 Percent	92.17 Percent	91.08 Percent
Collected Mixture Ratio	1.39	1.50	1.26
Normalized Mixture Ratio	1.30	1.33	1.15
Mixing Parameter	.6347	.6636	.7543

Figure 3.3-29. Oxidizer Circuit Spray Half Angle Versus Mixing Parameter (Em)

153

3.3, Element Design Modifications (cont.)

3.3.4   Conclusions

The purpose of this study was to see if slight modifications to the fuel flow cross-section of an 'I' triplet premix element would enhance the wall compatibility by providing fuel-rich regions around the periphery of the spray fan.

The results of the splash test and milkmaid tests documented herein prove that this program was successful. The baffle element and center element modifications both reduced the ox-rich regions of the thermal boundaries and gave increased fuel-rich regions along with increased mixing efficiencies due to the more uniform mixture ratios in the spray fan. These element modifications are also beneficial since the CdA of the modified elements are within 15% of the baseline element CdA and therefore will receive about the same flow per element when incorporated into a full scale injector.

The next phase in evaluation of the 'I' triplet element and modifications would be hot fire testing. The recommended element configurations for the hot fire tests are HBAF, ECEN, and ABAS since cold flow data is now available for these configurations.

3.0, Injector Studies (cont.)

3.4 INJECTOR FABRICATION STUDIES

3.4.1 Injector Material Selection

The injector design for the 7.5K thrust level engine is illustrated in Figure 3.4.1-1. The major components consist of the injector fuel manifold, injector oxidizer manifold, injector face, and baffle assemblies. Weight reduction in the OTV TCA can be most significantly achieved by optimizing injector manifold materials for specific strength (strength/density). Additional constraints on injector material selection include environmental (O_2, H_2) compatibility for manifolding, and thermal conductivity for the face. Table 3.4.1-I summarizes the candidate materials along with the selection parameters.

Since the three major components (manifolds and face) are intimately fabricated (diffusion bonded, brazed, or welded), there must be a general compatibility between each of these component materials. This includes not only metallurgical compatibility but also a reasonable match in thermal expansion coefficients. If the injector face is considered the most extreme environment, selection of this component material will strongly influence the selection of materials for the oxygen and hydrogen manifolds. Selection of an injector face material limits O_2 and H_2 manifold material selections. Therefore the overall weight reduction achievable must be judged by the specific combinations of compatible materials.

3.4.1.1 Injector Face Material Options

Thermal conductivity properties of furnace processed hardware normally show degradation with solid solution alloying. Thus the first choice for an injector face would be a pure metal such as nickel or copper. The material selected for the face also has to be available in the form of platelet stock to facilate use of platelet fabrication. Processing methods for the selected material must be demonstrated for achieving high efficiency diffusion bond joints (i.e. leak tight). Joining of the face to the fuel manifold decrees a reasonable match ($\pm 5\%$) in expansion coefficients between the face and fuel manifold materials.
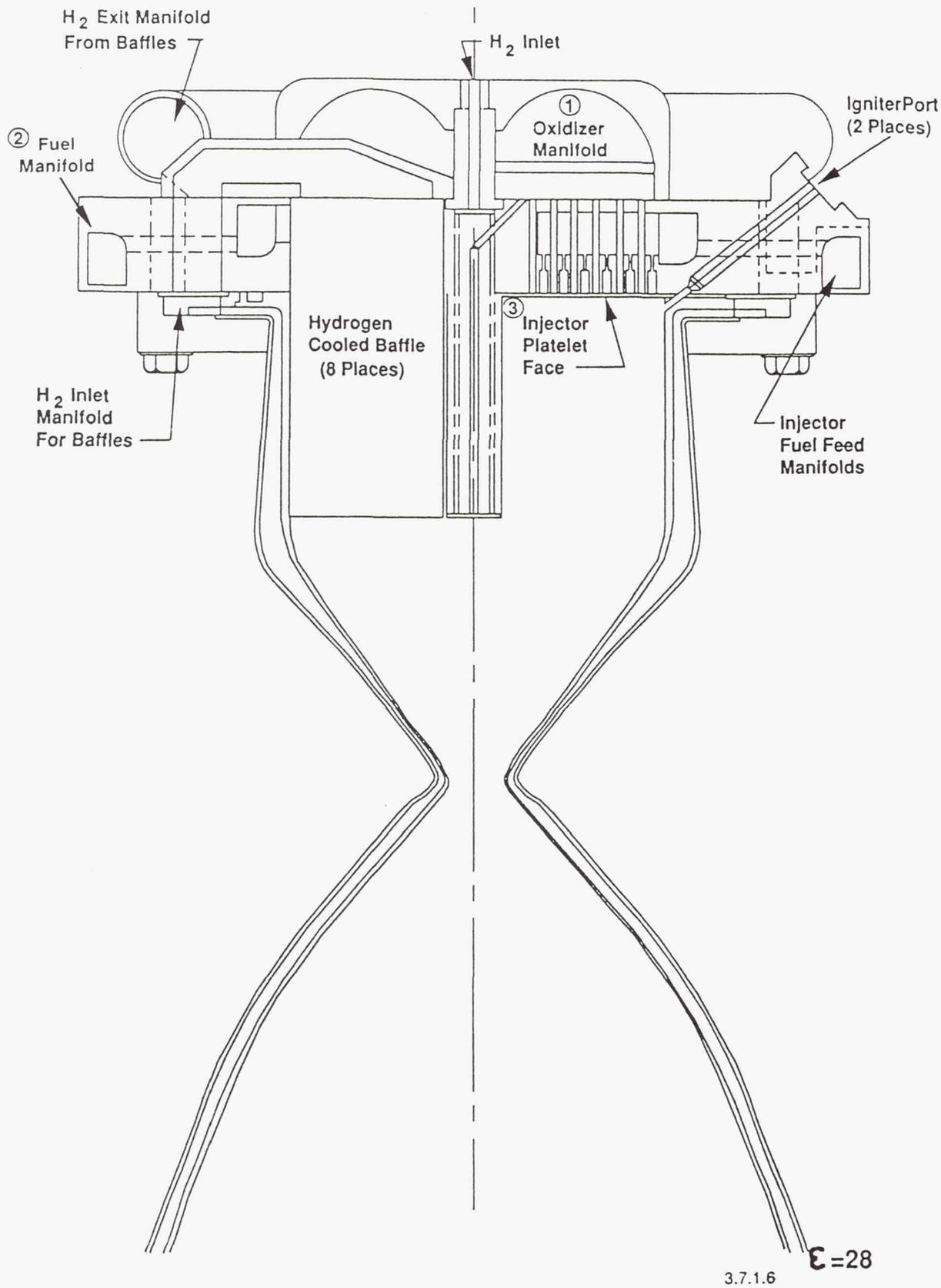
Figure 3.4.1-1. 7.5K Thrust Chamber Assembly — Injector Concept

156

TABLE 3.4.1-I

OTV INJECTOR MATERIAL CANDIDATES

Alloy	Fty @ RT (ksi)	Density (lb/in3)	Specific Strength (Ftu/Density)	CTE (/°F × E-6)	H$_2$ Compat.^ (Ftu H$_2$/Ftu He) (Highest Number Denotes Best Compatibility)	O$_2$ Compat**. Burn Factor	Diffusion Bonding Risk
Iron Alloys							
A-286	100	0.286	350	9.8	0.97	.182	Med
CRES 22-13-5	86	0.285	302	10.3	0.9*	.137	Med
Incology 802	44	0.287	153	10.1	0.99	.347	Med
Incology 909	150	0.296	507	9.8	1	.213	Med
CRES 347	30	0.290	103	10.3	0.91	.147	Low
Cobalt Alloys							
Haynes 188	68	0.330	206	8	0.92	.191	High
J-1650	116	0.320	363	7.5*	0.9*	.183	High
V-36	83	0.303	274	7.5*	0.9*	.224	High
Nickel Alloys							
Inconel 718	150	0.296	507	8.8	0.46	.132	Low
Inconel 625	55	0.305	180	8.8	0.76	.126	Med
Ni 200	15	0.321	47	8.5	0.7*	1.17	Low
Monel 400	25	0.319	78	9.1	0.65	.439	Med
Other Alloys							
Zr-Cu	35	0.323	108	9.8	1	12.1	Low

^ 1.0 = No Effect
* = Estimated
** Reference 14

157

Nickel Face Plate — The material selection for the 3K thrust level injector utilized pure nickel (Ni 200 or 201) as the face material. This alloy has moderate thermal conductivity ($\approx$40 Btu-in/hr-ft^2-°F) and has been successfully diffusion bonded (to itself and 3xx series stainless steel). An expansion coefficient (70 to 1000°F) of 8.5 x 10^{-6} in/in/°F matches well with most nickel and cobalt base alloys, particularly Haynes 188, Hastelloy X, Monel K-500, Inconel 625, and Inconel 718. Diffusion bonding is generally accomplished by using an electroless Ni strike as a bonding aid.

Although Ni 200, 201, and 270 are severely embrittled by hydrogen at room temperature, this effect is not observed at temperatures above approximately 900°F. Therefore Ni is a viable candidate for the injector face.

Copper Face Plate — OFHC copper and the ZrCu alloy have been diffusion bonded (to themselves and Zr Cu to 3xx stainless steel). Although the ZrCu is a solution hardened alloy, its significantly higher strength with little reduction in thermal conductivity ($\approx$170 Btu-in/hr-ft^2-°F), makes it a viable candidate. The thermal expansion coefficient (70 to 1000°F) of 10.75 x 10^{-6} in/in/°F matches with most austenitic stainless steel alloys such as CRES 347 and 304L, and CRES 22-13-5, and iron base superalloys such as N-155, A286, Incoloy 800, and Incoloy 909. A nickel strike is normally used as a bonding aid. As recently demonstrated on this program (Section 1.3) silver has also shown recent promise as a bonding aid.

Molybdenum Face Plate — Commercially pure molybdenum has been bonded to itself for a number of high temperature applications. The high thermal conductivity of this alloy ($\approx$80 Btu-in/hr-ft^2-°F) makes it potentially attractive as an injector face material. Although moly has a very low expansion coefficient (70 to 1000°F) of 3 x 10^{-6} in/in/°F which is lower than most other structural alloys. The diffusion bonding process has been shown to cause a recrystallization of molybdenum resulting in a brittle microstructure. Molybdenum would therefore be a poor choice for this application.

3.4, Injector Fabrication Studies (cont.)

Aluminum Face Plate — Aluminum and its alloys have high thermal conductivity properties, but the melting point ($\approx$900° to 1200°F) limits its usage.

Titanium Face Plate — Although Titanium and its alloys have very high specific strength properties, the thermal conductivity ($\approx$4 to 10 Btu-in/hr-ft^2-°F)is poor. Titanium is also incompatible with high temperature oxygen and hydrogen, and making it unusable in this application.

3.4.1.2 Hydrogen Manifold Material Options

The hydrogen manifold offers the greatest opportunity for reducing the OTV TCA weight through high specific strength materials. The environmental condition most affecting material selection for this component is, of course, high pressure (2300 to 2545 psi) gaseous hydrogen at 300 to 500°F. General classes of structural alloys suitable to this environment include austenitic iron base alloys and cobalt alloys. Nickel base alloys also may be utilized, but show a wide variability to Hydrogen Embrittlement Environment (HEE), and therefore are generally inferior to those mentioned above.

The criteria used to rank alloys to HEE is the ratio of notched tensile strength in He to notched strength in H_2. This criteria does not serve to judge the suitability of an alloy for a given application since it does not consider life properties (fatigue and creep) and does not apply to conditions where the effective stress is below the yield strength of the alloy, however it does appear to distinguish families of alloys which may be degraded by H_2.

The requirement for directly attaching the platelet injector face to the H_2 manifold places additional constraints on the material selection for this component. The ability to directly diffusion bond the platelets to the manifold requires a reasonable match in thermal expansion coefficients with the injector face material. Consideration is also given to brazing and weldability, including the effects of braze thermal cycles and final heat treatments.

159

3.4, Injector Fabrication Studies (cont.)

Austenitic Iron Base Alloys — Alloys considered in this group are A-286, CRES 22-13-5 (Nitronic 50), Incoloy 800, 802, and Incoloy 900, 903, 909. The 300 series stainless steels are also contained in this group but offer little in the way of high specific strength and are included for comparison purposes. Design allowable

tensile properties, thermal expansion coefficients, and densities are presented in Table 3.4.1-I.

Diffusion bonding of these alloys at Aerojet has been limited to the CRES 300 series. CRES 22-13-5 is a solid solution alloy, similar in metallurgy to CRES 347, and therefore should not pose any major bonding problems. It may be anticipated that bonding difficulties will increase with increasing aluminum and titanium contents. This is due to the high oxygen affinity of these elements which results in preferential surface oxidation during high temperature processing (i.e. diffusion bonding or brazing). Recent success at diffusion bonding of Inconel 718 show that it is possible to overcome the aluminum and titanium constituents for high quality diffusion bond joints. The most common solution to allow brazing of these alloys is to nickel plate the surface to provide a diffusion barrier. Such an approach should also be beneficial to diffusion bonding. Incoloy 800 alloys, Incoloy 900 alloys, and A-286 represent increasing potential risks in diffusion bonding development, but it is not anticipated that they represent impossible obstacles to bonding based on the results of the Inconel 718 bonding.

Cobalt Base Alloys — Typical wrought cobalt alloys include Haynes 188, J-1650, and V-36. WI 52 is a casting alloy with a reasonable compromise between strength and ductility. These alloys are typically used in gas turbines under hot, oxidizing conditions. HEE data on Haynes 188 shows it to be only slightly affected by gaseous hydrogen, and it is assumed that the other cobalt alloys will be equally suitable in the OTV H_2 environment. Properties for these alloys are given in Table 3.4.1-I. To date at Aerojet there has been no attempt at diffusion bonding of cobalt base alloys, therefore all alloys of the class present an unknown risk in diffusion bonding.

3.4, Injector Fabrication Studies (cont.)

3.4.1.3 Oxygen Manifold Materials Options

The possibilities of weight reduction in the oxygen manifold are limited by the effects of the high pressure oxygen on structural alloys. Oxygen inlet temperatures of 340°F should not pose an oxidation problem for the structural materials under consideration, even at high pressure (2660 psi), however the potential for metal ignition and combustion must be addressed in the materials selection. The risk of metal ignition and combustion are very difficult to assess in a specific application. Some metals, notably titanium and aluminum, ignite so readily in oxygen that they are never seriously considered for this type of service. Other alloys, such as the 300 series stainless steels, are frequently used in high pressure oxygen systems but have been shown to burn completely if ignited by some external source. This external source may be a severe rub condition or impact of a combustible material (aluminum chip) or some other condition which increases the local temperature and/or breaks up the protective chromium oxide on the alloy. Although the velocities in the injector manifold are low, so as not to lend itself toward particle impact consideration, this is the basis for available oxygen compatibility information.

The specific probability of ignition of a metal cannot be calculated, but it is possible to rank materials as to ignition susceptibility by the use of a calculated "burn factor". This factor is defined as the ratio of the heat of oxidation of each of the constituents of the alloy, and the thermal diffusivity (thermal conductivity / density * specific heat) of the alloy. Table 3.4.1.-I shows a ranked list of some candidate structural alloys listed by increasing burn factor. Experience, and ignition tests performed at NASA's White Sands Testing Facility (Reference 14), have determined that a burn factor greater than 2500 represents a significant risk of metal combustion. Table 3.4.1-II, taken from the Metals Test Program Test Report, TR-477-001, to the ASTM G-4 Committee, shows a promoted combustion ranking of selected metals. This ranking, based on self-extinguishing oxygen pressure (i.e. the pressure below which combustion of the alloy is not self-sustaining), shows that most structural alloys will burn at pressures greater than 1000 psi. Plotting this ranking vs burn factor, Figure 3.4.1-2, suggests that alloys with a burn factor less than 2300 should not

TABLE 3.4.1-II

RANKING OF METALS TESTED IN THE PROMOTED COMBUSTION TEST BASED ON THE SELF-EXTINGUISHING PRESSURE

Material	Self-Extinguishing Pressure	
	MPa	(psig)
Copper 102	55.1^{ab}	(8000)
Monel 400	55.1^{ab}	(8000)
Nickel 200	55.1^{ab}	(8000)
Tin Bronze	48.3^{a}	(7000)
Yellow Brass	48.3^{a}	(7000)
Red Brass	48.3^{a}	(7000)
Inconel 600	6.9	(1000)
Inconel 625	6.9	(1000)
Stellite 6B	6.9	(1000)
Incoloy 800	3.5	(500)
Inconel 718	3.5^{b}	(500)
304 Stainless Steel	3.5^{b}	(500)
316 Stainless Steel	3.5^{b}	(500)
Colmonoy Alloy No. 70	3.5	(500)
Ductile Cast Iron	<3.5	(<500)
Nitronic 60	<3.5	(<500)
9% Nickel Steel	<3.5	(<500)
Aluminum Bronze	<3.5	(<500)
6061 Aluminum	$<1.7^{b}$	(<250)

[a] Highest pressure tested.
[b] Data from Benz, Shaw, and Homa (1986).

162

Burn Factor vs. Oxygen Pressure

No Burn
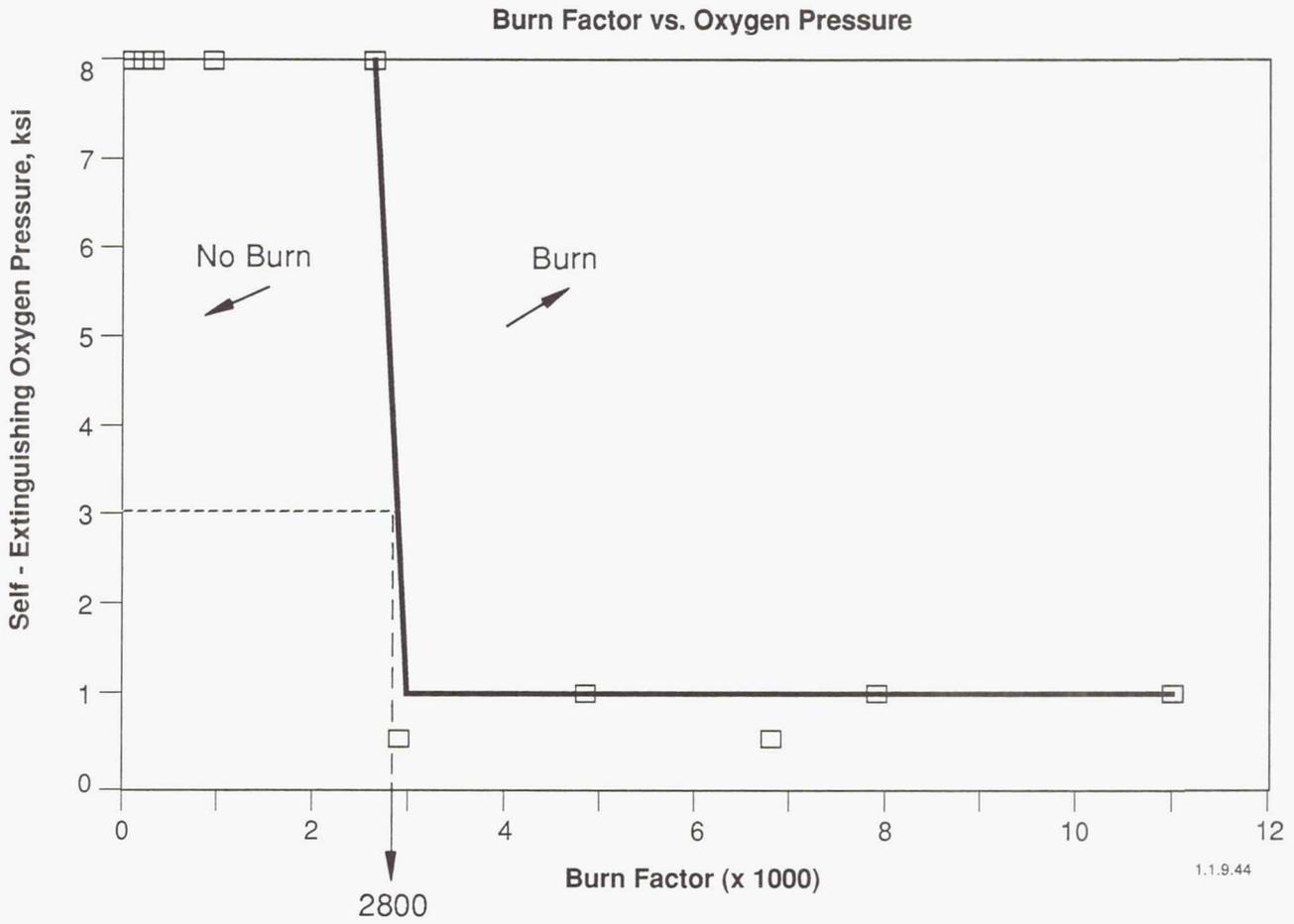
Burn

2800

**Recommended Material Selection for OTV Engine Operation
Has a Burn Factor of <2800**

Figure 3.4-1.2. Oxygen Burn Factor – Combustion Correlation

163

burn at oxygen pressures less than 3000 psi. The transition from safe to susceptible alloys is extremely sharp, indicating that for a conservative design it is desirable to use only alloys proven to be safe at the operating pressure.

The strongest structural alloy meeting this criteria is Monel 400. This alloy, a non-heat treatable solid solution alloy, has mechanical properties similar to the 300 series stainless steels, and should have comparable fabrication characteristics (including diffusion bonding). Monel K-500, a derivative Monel alloy, is

heat treatable and considerably stronger than Monel 400, but is at risk of combustion at 3000 psi oxygen even though the burn factor is less than half that of 300 series stainless steels. All other normal structural alloys, whether iron or nickel base, have a major risk of ignition and combustion in high pressure oxygen service.

3.4.1.4 Optimized Alloy Selections

The three major components of the OTV injector (face, H2 manifold, and O2 manifold) have three distinct criteria for optimization. Selection of each materials for these components requires some compromise in order to permit fabrication of a monolithic structure by diffusion bonding, brazing, or welding. If the injector face is considered to be the most critical selection, choice of hydrogen and oxygen manifolds is limited by that initial face selection, based primarily on thermal expansion coefficients.

ZrCu Injector Face Options — A ZrCu platelet injector face plate offers the greatest opportunity for reducing the weight of the OTV injector. The high thermal of conductivity ZrCu recommends it for face plate applications in any H_2-O_2 engine design, and additional, the good coefficient of thermal expansion match with material suitable in both hydrogen and oxygen service, allows for either diffusion bonding or brazing assembly of the injector, providing an efficient, minimal weight design.

Examination of the list of hydrogen manifold candidates suggests that Incoloy 909 offers an excellent coefficient of thermal expansion match with

3.4, Injector Fabrication Studies (cont.)

ZrCu, and offers the highest specific strength of the hydrogen compatible materials. CRES A-286 and CRES 22-13-5 offer possible alternatives.

The low risk material choices for the oxygen manifold are limited. Monel 400 (Reference 14) offers the highest specific strength of the candidate materials, and should be the first material of choice. Incoloy 802 offers a somewhat higher specific strength, but is marginal from an oxygen environment combustion stand point.

Ni 200 Injector Face Options — Ni 200 platelet injector face plates have already been demonstrated for the OTV engine, however the options for a low risk, low weight injector assembly are limited.

The cobalt base alloys offer the closest coefficient of thermal expansion (CTE) match with acceptable HEE resistance. Haynes 188 has the lowest specific strength of the alloys considered and meets the 95% Ni CTE acceptance requirement. J-1650 provides the highest specific strength, but data on this alloy is limited. Therefore, Haynes 188 would appear to be the alloy of choice. Experience in diffusion bonding and brazing this alloy has been limited, due to the aluminum, titanium, and refractory metal alloying.

As in the case of the ZrCu injector face assembly, the oxygen compatible material options are limited. Monel 400 again provides a reasonable CTE match. Development of diffusion bonding and/or brazing parameters should be no more difficult than in the ZrCu face assembly.

3.4.1.5 Conclusions

The opportunities for weight reduction in the OTV injector body can best be realized by changing construction of the Nickel manifold and platelet face assembly to a ZrCu platelet injector face, diffusion bonded to a forged Incoloy 909 hydrogen manifold, and brazing or diffusion bonding these components to a wrought Monel 400 oxygen manifold. Some fabrication development should be anticipated, however the technology is not greatly extended past our current

3.4, Injector Fabrication Studies (cont.)

database, and useful weight reductions could be anticipated. The exact extent of the weight savings will require an explicit design and detailed stress calculations.

3.4.2 Platelet Fabrication Methods

3.4.2.1 Laser Cutting of Platelets

Generation of the platelets for the uni-element test fixture evaluated alternate methods of platelet fabrication. Two methods of platelet fabrication were evaluated, 1) standard chemical etching, and 2) laser cutting. Laser cutting was selected based on the relative cost and the supporting worder under the 1984 IR&D Project No. LPS 84-20, "Alternate platelet Fabrication". This work was expanded in 1987 & 1988 by L. Schoenman & J. Franklin and documented in Aerojet memo #9990:R&T:2389.

Uni-element platelets for the OTV test plan were designed at 2X scale in stainless steel platelets of 0.010 and 0.032" thickness. Acceptable tolerances of +/- 0.002" were selected based on current laser technology and performance requirements.

The above referenced memo reported demonstration of laser cutting for various geometries in stainless steel platelets ranging in thickness from 0.015 to 0.3 inches. This work had been performed primarily with Yttria Alumina Garnet (YAG) lasers. No indication of the tolerances realized from this work was noted.

3.4.2.2 Evaluation Criteria

Features of interest in evaluating Chemically Etched versus Laser Cut include:

1. Tolerances
2. Maximum/Minimum Thickness of Material
3. Surface Finish
4. Capability of using IGES formatted CAD tape

166

3.4, Injector Fabrication Studies (cont.)

3.4.2.3 Discussion

Tolerances for chemically etched platelets were quoted as a percentage (~10% to 15%) of the material thickness. Thus for the 0.010" thick platelets of interest this would correspond to a range of +/- 0.001 to 0.0015" , whereas the thicker (0.032") platelets would be held within +/- 0.003 to 0.0035". Tolerances quoted for the laser cut platelets indicated that they were thickness independent and could be easily guaranteed at +/-0.005 to +/-0.002. Laser Tech was the only company which felt comfortable quoting +/- 0.001" tolerance.

Within the confines of chemically etched platelets, thinner stock is generally more acceptable up to a maximum thickness of 0.030". Laser cutting is generally aimed at thicker materials. Generally 0.010" thick stock was the thinnest vendors wished to work with.

Obtaining fine surface finishes with chemical etching is only dependant on the quality of the platelet stock. With laser cutting of platelets, the process leaves residual material (dross) on the exit surface. These is a great variation in the amount of dross formed dependant on 1) use of high pressure O_2 or N_2 air &/or mist assistance, and 2) the thickness of the material being cut. The dross is not fastly anchored and is easily removed using 600 grit emery cloth. Other recommendations for removing the dross chemically included acid bath (pickle) or electropolishing.

Evaluating the transferability of Aerojet CAD tapes was not fruitful. Only one company contacted, H.D.E, would have accepted our tapes if put into their format. Due to the simplicity of the drawings, and the need to alter the outline by either a chemical etching or a laser cutting factor most vendors declined to accept our tapes and chose to work from the drawings. An underlying factor seemed to be the lack of CAD equipment among the Laser houses. Although not stated as such in the initial screening process, it would appear that most places sent the drawings to outside companies for digitizing and post-processing.

3.4, Injector Fabrication Studies (cont.)

3.4.2.4   Aerojet Inspection Results.

Upon receipt at Aerojet, the platelets were inspected using the Optical Gaging Products (OGP) visual compator device in the platelet shop. The platelets were inspected, dash number up using bottom lighting. It was noted that inspection of the as cut platelets was difficult due to the dross (or slag) along the inside edges. Irregular and erratic readings were taken at times. Assuming a satisfactory method of removing this layer of dross is proven, the platelets should be cleaned prior to inspection.

Summarization of the inspection data is broken into three groups of information. Dimensions for the large holes (0.281" dia bolt holes) are presented in Table 3.4.2-I for EB Tec and Table 3.4.2-II for Laser Tech. Inspection data for the small holes (0.121" dia alignment pin holes) are presented in Table 3.4.2-III for EB Tec and Table 3.4.2-IV for Laser Tech. Ability to repeat geometries can be accessed by a review of this data.

The important inspection data, that of the features, is presented in Table 3.4.2-V for EB Tec and Table 3.4.2-VI for Laser Tech.

The platelets generated from Laser Tech using a CO2 laser were well within the requested tolerance of +/- 0.002". Those from EB Tec were found to be very sloppy. Hole diameters were visibly out of round, and very few platelets were within the requested tolerance band.

3.4.2.5   Laser Parameters:

Laser Tech prepared their set of platelets using a Lumonics Company Futon 500 watt CO_2 laser. The nozzle is adjustable between a 0.060 to 0.010" diameter. An oxygen assist is utilized and ranges from pressures of 20 to 60 psia. For our job, this machine was run at 25 watts, in a pulsed mode at a 20% duty cycle. A 3.5 focal point lens was used. The material cut was stainless steel series 302.

TABLE 3.4.2-I

INSPECTION DATA FOR YAG LASER CUT PLATELETS - BOLT HOLE DIAMETERS

Vendor - EB Tec
Laser - YAG
Bolt Hole Inspection Summary
Nominal Dimension - 0.281" Bolt Hole Dia
                 - 1.123" Bolt Circle Dia

	Measured Dimensions			Deviation from Nominal Dimensions		
Dash Number	Feature Diameter (inches)	Feature Locating Radius (inches)	Angular Location (degrees)	Feature Diameter (inches)	Feature Locating Radius (inches)	Angular Location (degrees)
-1	0.28220	1.12481	89.98334	-0.0012	-0.0018	0.0167
	0.28378	1.12420	149.96846	-0.0028	-0.0012	0.0315
	0.27973	1.12633	209.97964	0.0013	-0.0033	0.0204
	0.28308	1.12461	269.95505	-0.0021	-0.0018	0.0449
	0.28451	1.12370	329.99490	-0.0035	-0.0007	0.0051
	0.27979	1.12450	30.00353	0.0012	-0.0015	-0.0035
-2	0.28590	1.12420	89.98493	-0.0049	-0.0012	0.0151
	0.28626	1.12580	150.04719	-0.0053	-0.0028	-0.0472
	0.28634	1.12739	209.88873	-0.0053	-0.0044	0.1113
	0.28470	1.12573	269.95908	-0.0037	-0.0027	0.0409
	0.28716	1.12503	330.03567	-0.0062	-0.0020	-0.0357
	0.28396	1.12665	29.95821	-0.0030	-0.0036	0.0418
-4	0.28618	1.12507	89.93457	-0.0052	-0.0021	0.0654
	0.28568	1.12534	149.98048	-0.0047	-0.0023	0.0195
	0.28387	1.12565	209.94629	-0.0029	-0.0027	0.0537
	0.28480	1.12540	269.89754	-0.0038	-0.0024	0.1025
	0.28695	1.12533	329.95556	-0.0059	-0.0023	0.0444
	0.28335	1.12610	29.92916	-0.0023	-0.0031	0.0708
-5	0.28722	1.12627	90.03209	-0.0062	-0.0033	-0.0321
	0.28748	1.12721	150.04795	-0.0065	-0.0042	-0.0479
	0.28402	1.12689	209.93766	-0.0030	-0.0039	0.0623
	0.28649	1.12556	269.91951	-0.0055	-0.0026	0.0805
	0.28656	1.12303	329.98579	-0.0056	-0.0000	0.0142
	0.28485	1.12602	30.05088	-0.0038	-0.0030	-0.0509
-6	0.28654	1.12509	90.00181	-0.0055	-0.0021	-0.0018
	0.28455	1.12458	149.98285	-0.0035	-0.0016	0.0171
	0.28364	1.12461	209.94570	-0.0026	-0.0016	0.0543
	0.28765	1.12397	269.95019	-0.0066	-0.0010	0.0498
	0.28597	1.12560	329.99892	-0.0050	-0.0026	0.0011
	0.28263	1.12452	29.99400	-0.0016	-0.0015	0.0060
-11	0.28507	1.12616	90.01556	-0.0041	-0.0032	-0.0156
	0.28583	1.12618	150.01145	-0.0048	-0.0032	-0.0114
	0.28551	1.12708	209.88036	-0.0045	-0.0041	0.1196
	0.28453	1.12313	269.89953	-0.0035	-0.0001	0.1005
	0.28641	1.12396	330.02112	-0.0054	-0.0010	-0.0211
	0.28233	1.12363	29.97767	-0.0013	-0.0006	0.0223
-12	0.28618	1.12549	90.00079	-0.0052	-0.0025	-0.0008
	0.28626	1.12584	150.01423	-0.0053	-0.0028	-0.0142
	0.28232	1.12618	210.02472	-0.0013	-0.0032	-0.0247
	0.28560	1.12652	269.97863	-0.0046	-0.0035	0.0214
	0.28653	1.12361	330.01792	-0.0055	-0.0006	-0.0179
	0.28521	1.12559	30.07054	-0.0042	-0.0026	-0.0705
-13	0.28791	1.12616	90.04315	-0.0069	-0.0032	-0.0431
	0.28786	1.12642	150.02645	-0.0069	-0.0034	-0.0265
	0.28392	1.12628	210.00901	-0.0029	-0.0033	-0.0090
	0.28513	1.12700	269.92680	-0.0041	-0.0040	0.0732
	0.28707	1.12497	329.96721	-0.0061	-0.0020	0.0328
	0.28612	1.12573	30.07196	-0.0051	-0.0027	-0.0720
-15	0.28552	1.12594	89.98602	-0.0045	-0.0029	0.0140
	0.28885	1.12545	150.02357	-0.0078	-0.0025	-0.0236
	0.28590	1.12566	209.95975	-0.0049	-0.0027	0.0402
	0.28611	1.12518	269.96962	-0.0051	-0.0022	0.0304
	0.28640	1.12429	330.02114	-0.0054	-0.0013	-0.0211
	0.28292	1.12453	30.00892	-0.0019	-0.0015	-0.0089
-16	0.28545	1.12504	89.96340	-0.0044	-0.0020	0.0366
	0.28731	1.12643	149.98636	-0.0063	-0.0034	0.0136
	0.28549	1.12732	209.93353	-0.0045	-0.0043	0.0665
	0.28486	1.12535	289.95189	-0.0039	-0.0024	0.0483
	0.28744	1.12437	330.00007	-0.0064	-0.0014	-0.0001
	0.28311	1.12538	29.97469	-0.0021	-0.0024	0.0253
			Average:	-0.0036	-0.0020	0.0154

TABLE 3.4.2-II

INSPECTION DATA FOR CO2 LASER CUT PLATELETS- BOLT HOLE DIAMETERS

```
Vendor - Laser Tech
Laser  - CO2
Bolt Hole Inspection Summary
Nominal Dimension - 0.281" Bolt Hole Dia
                  - 1.123" Bolt Circle Dia
```

	Measured Dimensions			Deviation from Nominal Dimensions		
Dash Number	Feature Diameter (inches)	Feature Locating Radius (inches)	Angular Location (degrees)	Feature Diameter (inches)	Feature Locating Radius (inches)	Angular Location (degrees)
-1	0.27989	1.12502	90.03423	0.0011	-0.0020	-0.0342
	0.27894	1.12495	150.01192	0.0021	-0.0019	-0.0119
	0.28006	1.12499	210.04502	0.0009	-0.0020	-0.0450
	0.28004	1.12588	269.99995	0.0010	-0.0029	0.0000
	0.27857	1.12455	329.98349	0.0024	-0.0015	0.0165
	0.28034	1.12532	30.0031	0.0007	-0.0023	-0.0031
-2	0.28095	1.12512	90.02151	0.0001	-0.0021	-0.0215
	0.28121	1.12518	150.0287	-0.0002	-0.0022	-0.0287
	0.28095	1.12581	210.00372	0.0001	-0.0028	-0.0037
	0.28054	1.12544	270.0065	0.0005	-0.0024	-0.0065
	0.28266	1.12477	329.97872	-0.0017	-0.0018	0.0213
	0.2809	1.12425	29.994	0.0001	-0.0012	0.0060
-4	0.28089	1.12542	90.01391	0.0001	-0.0024	-0.0139
	0.28004	1.12508	150.03094	0.0010	-0.0021	-0.0309
	0.28032	1.12502	210.04063	0.0007	-0.0020	-0.0406
	0.28128	1.12557	270.04657	-0.0003	-0.0026	-0.0466
	0.28106	1.12582	330.02154	-0.0001	-0.0028	-0.0215
	0.28092	1.12531	30.01603	0.0001	-0.0023	-0.0160
-5	0.28003	1.12526	89.99871	0.0010	-0.0023	0.0013
	0.27971	1.12548	149.98921	0.0013	-0.0025	0.0108
	0.28054	1.12528	210.01331	0.0005	-0.0023	-0.0133
	0.28102	1.12487	270.01125	-0.0000	-0.0019	-0.0113
	0.28123	1.12537	330.02774	-0.0002	-0.0024	-0.0277
	0.28191	1.12551	30.0115	-0.0009	-0.0025	-0.0115
-6	0.27981	1.12527	90.00919	0.0012	-0.0023	-0.0092
	0.27872	1.12242	149.92188	0.0023	0.0006	0.0781
	0.27963	1.12418	209.9859	0.0014	-0.0012	0.0141
	0.28177	1.12527	270.01322	-0.0008	-0.0023	-0.0132
	0.28033	1.12539	330.03679	0.0007	-0.0024	-0.0368
	0.2813	1.12501	30.01392	-0.0003	-0.0020	-0.0139
-11	0.28064	1.1251	89.99332	0.0004	-0.0021	0.0067
	0.28008	1.12451	149.98637	0.0009	-0.0015	0.0136
	0.27998	1.12537	210.02798	0.0010	-0.0024	-0.0280
	0.28051	1.12444	270.00785	0.0005	-0.0014	-0.0079
	0.28124	1.12559	330.03584	-0.0002	-0.0026	-0.0358
	0.28075	1.12489	30.00895	0.0003	-0.0019	-0.0089
-12	0.28009	1.12532	90.00209	0.0009	-0.0023	-0.0021
	0.27986	1.12537	149.9867	0.0011	-0.0024	0.0133
	0.28102	1.12513	210.02788	-0.0000	-0.0021	-0.0279
	0.27956	1.12472	269.99903	0.0014	-0.0017	0.0010
	0.28145	1.12154	330.03256	-0.0004	0.0015	-0.0326
	0.28142	1.12549	30.02471	-0.0004	-0.0025	-0.0247
-13	0.28067	1.12496	89.98281	0.0003	-0.0020	0.0172
	0.2814	1.12464	149.99186	-0.0004	-0.0016	0.0081
	0.28062	1.12539	209.9988	0.0004	-0.0024	0.0012
	0.28018	1.12598	269.98348	0.0008	-0.0030	0.0165
	0.28018	1.12425	329.95163	0.0008	-0.0012	0.0484
	0.28056	1.12487	30.01163	0.0004	-0.0019	-0.0116
-15	0.28144	1.12479	90.01319	-0.0004	-0.0018	-0.0132
	0.28001	1.12531	149.97519	0.0010	-0.0023	0.0248
	0.27957	1.12555	209.98153	0.0014	-0.0026	0.0185
	0.28051	1.12518	269.95801	0.0005	-0.0022	0.0420
	0.28005	1.12452	329.98505	0.0010	-0.0015	0.0149
	0.28068	1.12441	30.00929	0.0003	-0.0014	-0.0093
-16	0.28093	1.12519	89.96843	0.0001	-0.0022	0.0316
	0.27824	1.12559	149.96543	0.0028	-0.0026	0.0346
	0.2795	1.12699	209.94813	0.0015	-0.0040	0.0519
	0.28018	1.1241	269.94216	0.0008	-0.0011	0.0578
	0.27982	1.12421	329.9441	0.0012	-0.0012	0.0559
	0.28041	1.1235	30.02851	0.0006	-0.0005	-0.0285
			Average	0.0005	-0.0020	-0.0009

TABLE 3.4.2-III

INSPECTION DATA FOR YAG LASER CUT PLATELETS - ALIGNMENT PIN HOLE DIAMETERS

Vendor - EB Tec
Laser - YAG
Alignment Pin Hole Inspection Summary
Nominal Dimension - 0.121" Alignment Pin Hole Dia
               - 0.75" Alignment Pin Circle Dia

	Measured Dimensions			Deviation from Nominal Dimensions		
Dash Number	Feature Diameter (inches)	Feature Locating Radius (inches)	Angular Location (degrees)	Feature Diameter (inches)	Feature Locating Radius (inches)	Angular Location (degrees)
-1	0.12126	0.74981	359.97988	-0.0003	0.0002	0.0201
	0.12207	0.75071	120.01204	-0.0011	-0.0007	-0.0120
	0.12160	0.75046	239.90395	-0.0006	-0.0005	0.0980
-2	0.12436			-0.0034		
	0.12514	0.74157	121.21327	-0.0041	0.0084	-1.2133
	0.12550	0.75059	239.93955	-0.0045	-0.0006	0.0605
-4	0.12529			-0.0043		
	0.12429	0.75888	118.74961	-0.0033	-0.0089	1.2504
	0.12450	0.75070	239.92052	-0.0035	-0.0007	0.0795
-5	0.12405	0.75021	0.00367	-0.0030	-0.0002	-0.0037
	0.12488	0.75069	120.04874	-0.0039	-0.0007	-0.0487
	0.12464	0.75088	239.87773	-0.0036	-0.0009	0.1223
-6	0.12396			-0.0030		
	0.12458	0.75470	119.40128	-0.0036	-0.0047	0.5987
	0.12439	0.75040	239.97136	-0.0034	-0.0004	0.0286
-11	0.12483			-0.0038		
	0.12460	0.75759	119.07210	-0.0036	-0.0076	0.9279
	0.12524	0.75008	239.80569	-0.0042	-0.0001	0.1943
-12	0.12403			-0.0030		
	0.12553	0.75245	119.72296	-0.0045	-0.0024	0.2770
	0.12501	0.75063	239.97045	-0.0040	-0.0006	0.0296
-13	0.12558			-0.0046		
	0.12593	0.77183	117.25133	-0.0049	-0.0218	2.7487
	0.12498	0.75160	239.94903	-0.0040	-0.0016	0.0510
-15	0.12531			-0.0043		
	0.12741	0.73495	122.08820	-0.0064	0.0151	-2.0882
	0.12655	0.74972	239.92062	-0.0055	0.0003	0.0794
-16	0.12519			-0.0042		
	0.12562	0.66348	133.52105	-0.0046	0.0865	-13.5211
	0.12550	0.75045	239.86765	-0.0045	-0.0004	0.1324
			Average	-0.0037	0.0019	-0.3397

TABLE 3.4.2-IV

INSPECTION DATA FOR CO2 LASER CUT PLATELETS - ALIGNMENT PIN HOLE DIAMETERS

```
Vendor - Laser Tech
Laser  - CO2
Alignment Pin Hole Inspection Summary
Nominal Dimension - 0.121" Alignment Pin Hole Dia
                  - 0.75" Alignment Pin Circle Dia
```

	Measured Dimensions			Deviation from Nominal Dimensions		
Dash Number	Feature Diameter (inches)	Feature Locating Radius (inches)	Angular Location (degrees)	Feature Diameter (inches)	Feature Locating Radius (inches)	Angular Location (degrees)
-1	0.11981	0.74981	359.99549	0.0012	0.0002	0.0045
	0.11992	0.74998	119.98553	0.0011	0.0000	0.0145
	0.12007	0.75046	240.04344	0.0009	-0.0005	-0.0434
-2	0.12143	0.74988	0.01665	-0.0004	0.0001	-0.0167
	0.12182	0.75009	120.01109	-0.0006	-0.0001	-0.0111
	0.12088	0.75078	240.00082	0.0001	-0.0008	-0.0008
-4	0.12121	0.74997	359.99717	-0.0002	0.0000	0.0028
	0.12071	0.74991	119.99223	0.0003	0.0001	0.0078
	0.12104	0.74984	240.04426	-0.0000	0.0002	-0.0443
-5	0.12112	0.75010	359.98722	-0.0001	-0.0001	0.0128
	0.12112	0.75024	120.01192	-0.0001	-0.0002	-0.0119
	0.12081	0.75037	239.99887	0.0002	-0.0004	0.0011
-6	0.12110	0.74988	359.99511	-0.0001	0.0001	0.0049
	0.12036	0.75011	119.99359	0.0006	-0.0001	0.0064
	0.12085	0.75001	239.96159	0.0001	-0.0000	0.0384
-11	0.12110	0.75018	0.00188	-0.0001	-0.0002	-0.0019
	0.12033	0.74983	120.00300	0.0007	0.0002	-0.0030
	0.12086	0.75033	240.01223	0.0001	-0.0003	-0.0122
-12	0.12100	0.75010	0.00329	0.0000	-0.0001	-0.0033
	0.12079	0.75059	120.03604	0.0002	-0.0006	-0.0360
	0.12052	0.75024	240.03785	0.0005	-0.0002	-0.0378
-13	0.12057	0.74990	0.00282	0.0004	0.0001	-0.0028
	0.12085	0.74953	119.97823	0.0001	0.0005	0.0218
	0.12086	0.75061	239.97248	0.0001	-0.0006	0.0275
-15	0.12135	0.74995	0.00009	-0.0004	0.0000	-0.0001
	0.12081	0.75063	120.02241	0.0002	-0.0008	-0.0224
	0.12078	0.75016	239.92408	0.0002	-0.0002	0.0759
-16	0.12140			-0.0004	0.7500	0.0000
	0.11959	0.77300	117.21328	0.0014	-0.0230	2.7867
	0.12078	0.75062	239.83833	0.0002	-0.0006	0.1617
			Average	0.0002	0.0241	0.0912

TABLE 3.4.2-V

INSPECTION DATA FOR YAG LASER CUT PLATELETS - CRITICAL FEATURE DIMENSIONS

Vendor - EB Tec
Laser - YAG

Feature Size
Inspection Summary

Dash Number	Dimension Type	Nominal Dimensions Feature Diameter (inches)	Nominal Dimensions Feature Locating Radius (inches)	Measured Dimensions Feature Diameter (inches)	Measured Dimensions Feature Locating Radius (inches)	Deviation from Nominal Dimens Feature Diameter (inches)	Deviation from Nominal Dimens Feature Locating Radius (inches)
-1	Diameter	0.132	0.320	0.13235	0.32039	-0.0003	-0.0004
	Diameter	0.152	0.000	0.15294	0.00071	-0.0009	-0.0007
	Diameter	0.132	0.320	0.13354	0.31952	-0.0015	0.0005
-2	Radius	0.107	0.279	0.10913	0.27810	-0.0021	0.0009
	Radius	0.107	0.279	0.10951	0.27876	-0.0025	0.0002
-4	Radius	0.066	0.320	0.06810	0.31929	-0.0021	0.0007
	Radius	0.107	0.000	0.11055	0.00418	-0.0035	-0.0042
	Radius	0.107	0.000	0.10904	0.00096	-0.0020	-0.0010
	Radius	0.066	0.320	0.06837	0.32015	-0.0024	-0.0001
	Width	0.078		0.08199		-0.0040	
	Width	0.078		0.08243		-0.0044	
-5	Radius	0.066	0.320	0.06787	0.31951	-0.0019	0.0005
	Radius	0.066	0.320	0.07236	0.31619	-0.0064	0.0038
	Width	0.214		0.22077		-0.0068	
-6	Diameter	0.284		0.30832		-0.0243	
-11	Radius	0.115	0.271	0.11680	0.27097	-0.0018	0.0000
	Radius	0.077	0.309	0.07858	0.30825	-0.0016	0.0007
	Radius	0.115	0.000	0.11477	0.00366	0.0002	-0.0037
	Radius	0.115	0.000	0.14388	0.02931	-0.0289	-0.0293
-12	Radius	0.115	0.271	0.11564	0.27214	-0.0006	-0.0011
	Radius	0.115	0.009	0.12010	0.00461	-0.0051	0.0044
	Radius	0.115	0.000	0.10696	0.16953	0.0080	-0.1695
	Radius	0.066	0.320	0.06879	0.31838	-0.0028	0.0016
	Width	0.078		0.08135		-0.0034	
	Width	0.116		0.11946		-0.0035	
-13	Radius	0.111	0.275	0.11204	0.27714	-0.0010	-0.0021
	Radius	0.094	0.292	0.09523	0.29282	-0.0012	-0.0008
	Width	0.188		0.19316		-0.0052	
	Width	0.115		0.11935		-0.0043	
-15	Radius	0.107	0.279	0.11726	0.27218	-0.0103	0.0068
	Radius	0.066	0.032	0.07152	0.32055	-0.0055	-0.2885
-16	Radius	0.115	0.271	0.11502	0.27328	-0.0000	-0.0023
	Radius	0.066	0.320	0.06822	0.31978	-0.0022	0.0002
					Average	-0.0037	-0.0134

TABLE 3.4.2-VI

INSPECTION DATA FOR CO2 LASER CUT PLATELETS - CRITICAL FEATURE DIMENSIONS

Vendor - Laser Tech
Laser - CO2

Feature Size
Inspection Summary

Dash Number	Dimension Type	Nominal Dimensions Feature Diameter (inches)	Nominal Dimensions Locating Radius (inches)	Measured Dimensions Feature Diameter (inches)	Measured Dimensions Locating Radius (inches)	Deviation from Nominal Dimension Feature Diameter (inches)	Deviation from Nominal Dimension Locating Radius (inches)
-1	Diameter	0.132	0.320	0.13120	0.31996	0.0008	0.0000
	Diameter	0.152	0.000	0.15106	0.00023	0.0009	-0.0002
	Diameter	0.132	0.320	0.13065	0.32005	0.0014	-0.0000
-2	Radius	0.107	0.279	0.10779	0.27793	-0.0008	0.0011
	Radius	0.107	0.279	0.10739	0.27866	-0.0004	0.0003
-4	Radius	0.066	0.320	0.06533	0.31937	0.0007	0.0006
	Radius	0.107	0.000	0.10772	0.00104	-0.0007	-0.0010
	Radius	0.107	0.000	0.10682	0.00073	0.0002	-0.0007
	Radius	0.066	0.320	0.06597	0.32056	0.0000	-0.0006
	Width	0.078		0.07774		0.0003	
	Width	0.078		0.07828		-0.0003	
-5	Radius	0.066	0.320	0.06643	0.32026	-0.0004	-0.0003
	Radius	0.066	0.320	0.06612	0.32014	-0.0001	-0.0001
	Width	0.214		0.21281		0.0012	
-6	Diameter	0.284		0.28376	0.00011	0.0002	-0.0001
-11	Radius	0.115	0.271	0.11472	0.27080	0.0003	0.0002
	Radius	0.077	0.309	0.07812	0.30537	-0.0011	0.0036
	Radius	0.115	0.000	0.06404	0.05106	0.0510	-0.0511
	Radius	0.115	0.000	0.14589	0.03089	-0.0309	-0.0309
-12	Radius	0.115	0.271	0.11431	0.27104	0.0007	-0.0000
	Radius	0.115	0.009	0.11593	0.00101	-0.0009	0.0080
	Radius	0.115	0.000	0.11438	0.00033	0.0006	-0.0003
	Radius	0.066	0.320	0.06593	0.32026	0.0001	-0.0003
	Width	0.078		0.07766		0.0003	
	Width	0.116		0.11457		0.0014	
-13	Radius	0.111	0.275	0.10994	0.27667	0.0011	-0.0017
	Radius	0.094	0.292	0.09324	0.29331	0.0008	-0.0013
	Width	0.188		0.18765		0.0003	
	Width	0.115		0.11513		-0.0001	
-15	Radius	0.107	0.279	0.10623	0.28018	0.0008	-0.0012
	Radius	0.066	0.032	0.06594	0.31982	0.0001	-0.2878
-16	Radius	0.115	0.271	0.11571	0.26957	-0.0007	0.0014
	Radius	0.066	0.320	0.06611	0.31939	-0.0001	0.0006
					Average	0.0007	-0.0095

3.4, Injector Fabrication Studies (cont.)

EB Tec prepared their set of platelets utilizing a Raytheon 400 watt YAG laser. The nominal beam diameter is 0.018" diameter, which can be adjusted down to 0.005" diameter. A oxygen assist was utilized at 60 psi. The stainless steel series utilized is unknown.

3.4.2.6 Platelet Cleanup Methods

To remove the dross, 3 methods were explored: 1) 600 grit emery cloth followed by water flow, 2) electropolishing, and 3) acid etch (pickle). The -11 geometry platelets were used for the evaluation of the cleaning methods. A control platelet from each vendor was also viewed under the SEM for comparison. These are shown in Figures 3.4.2-1 and 3.4.2-2. Figure 3.4.2-1 illustrates the geometry of the element feature with SEM's of the platelet sides where the laser beam entered and exited (300X magnification). Figure 3.4.2-2 shows the exit surface of the two as-received platelets at 120X magnification.

Figure 3.4.2-3 presents the exit surface of the platelets after dross removal. The chemical cleaning methods tried were a rough first cut at solution, temperature, and time. Promise is shown by these methods and remaining dross could be removed by optimization of either time exposed to the solution or exposure at increased temperature. For this initial try, the acid etch (pickle) yielded the best results in terms of removing the dross without severely attacking the base metal.

Method #1 (Figure 3.4.2-3c):

Emery cloth (600 grit) was used to remove the dross from the mating surfaces of the platelets. The platelets were taped to the bottom plate of the test fixture and dry lapped in a 'figure 8' pattern. The platelets were stacked loose on the flow fixture and bolted together. Subsequent flow testing then removed the dross on the inside walls of the element feature. Inlet pressure for the fuel side was set at 117 psi with gaseous nitrogen flow. Inlet pressure on the oxygen circuit was set at 248 psi with water flow.
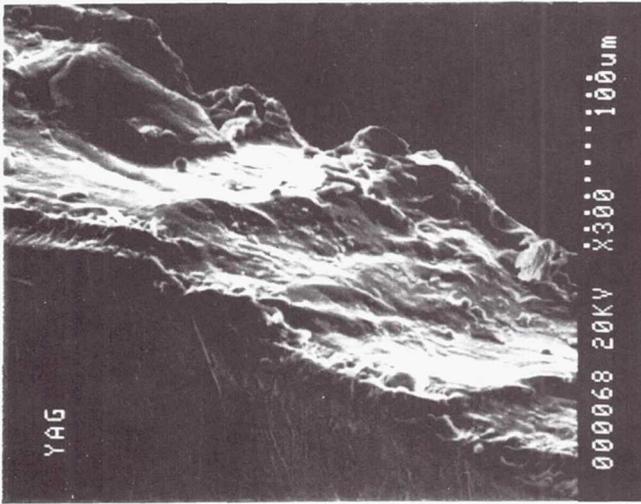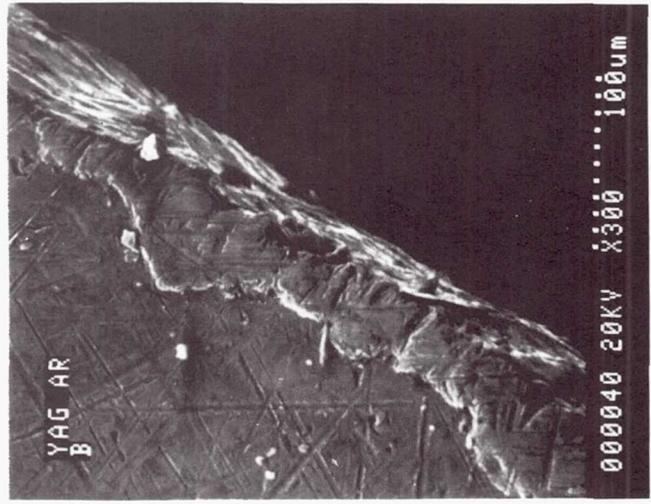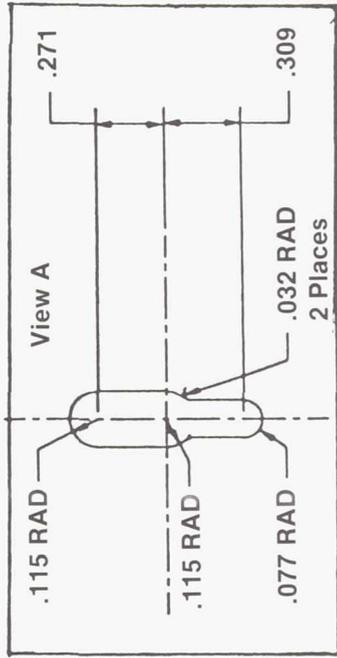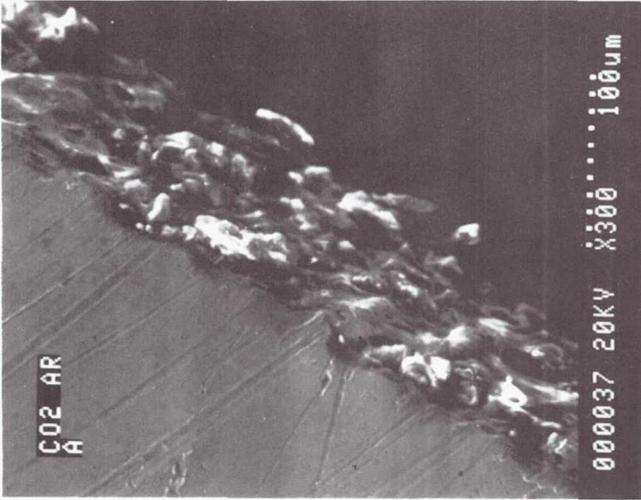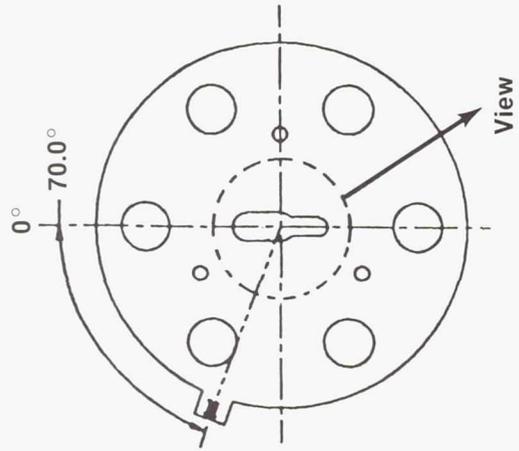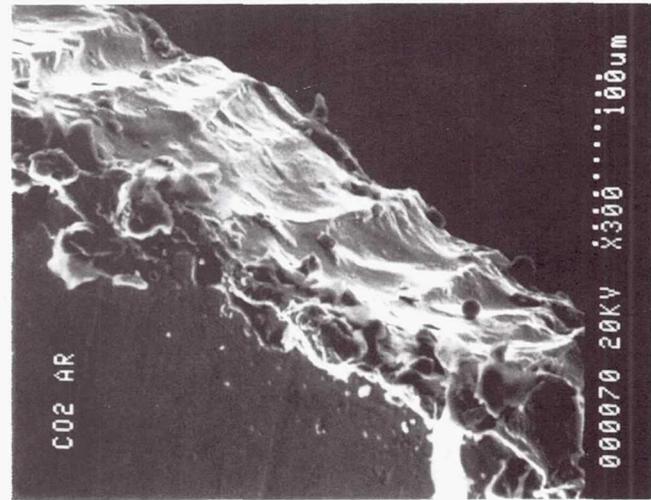
Figure 3.4.2-1. Comparison of Laser Cut Platelets — Laser Beam Entrance and Exit Surfaces

176
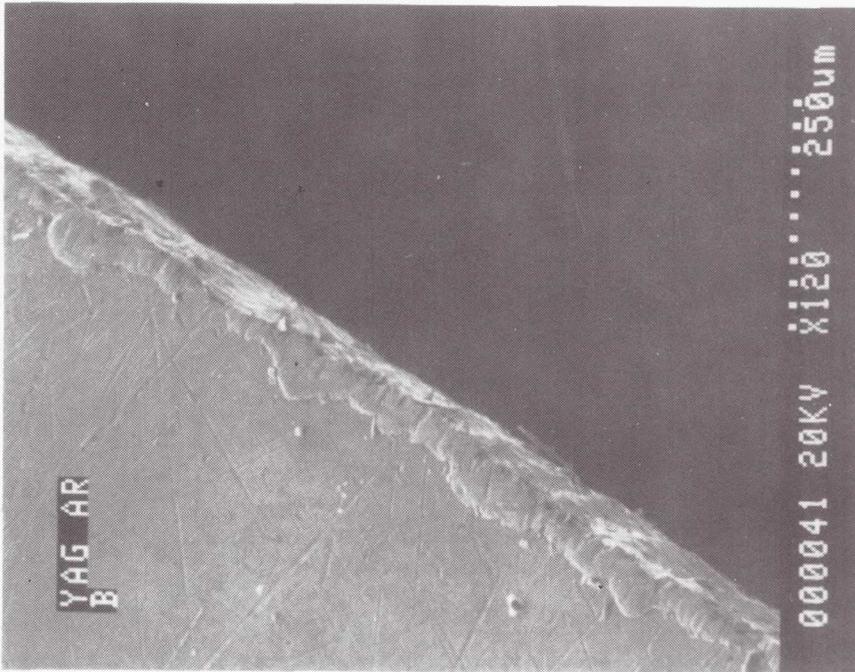
a)

Cut By EB Tec Using YAG Laser.
Vendor Made Effort to Mechanically
Remove Dross Along Laser Exit.
Note Smeared Appearance of Dross Layer.
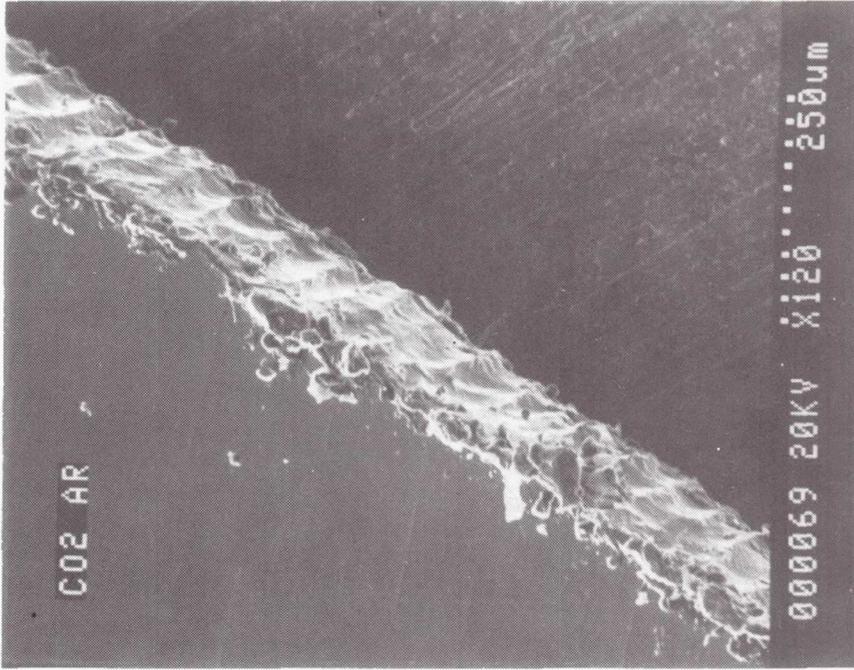
b)

Cut by Laser Tech Using C02 Laser.
No Clean Up Was Attempted by Vendor.
Oxygen Assist Used Which Should Aid in
Chemical Clean Up of Oxidized Recast Metal.

Figure 3.4.2-2. As-Received Condition of Laser Cut Platelets — Laser Beam Exit Surface
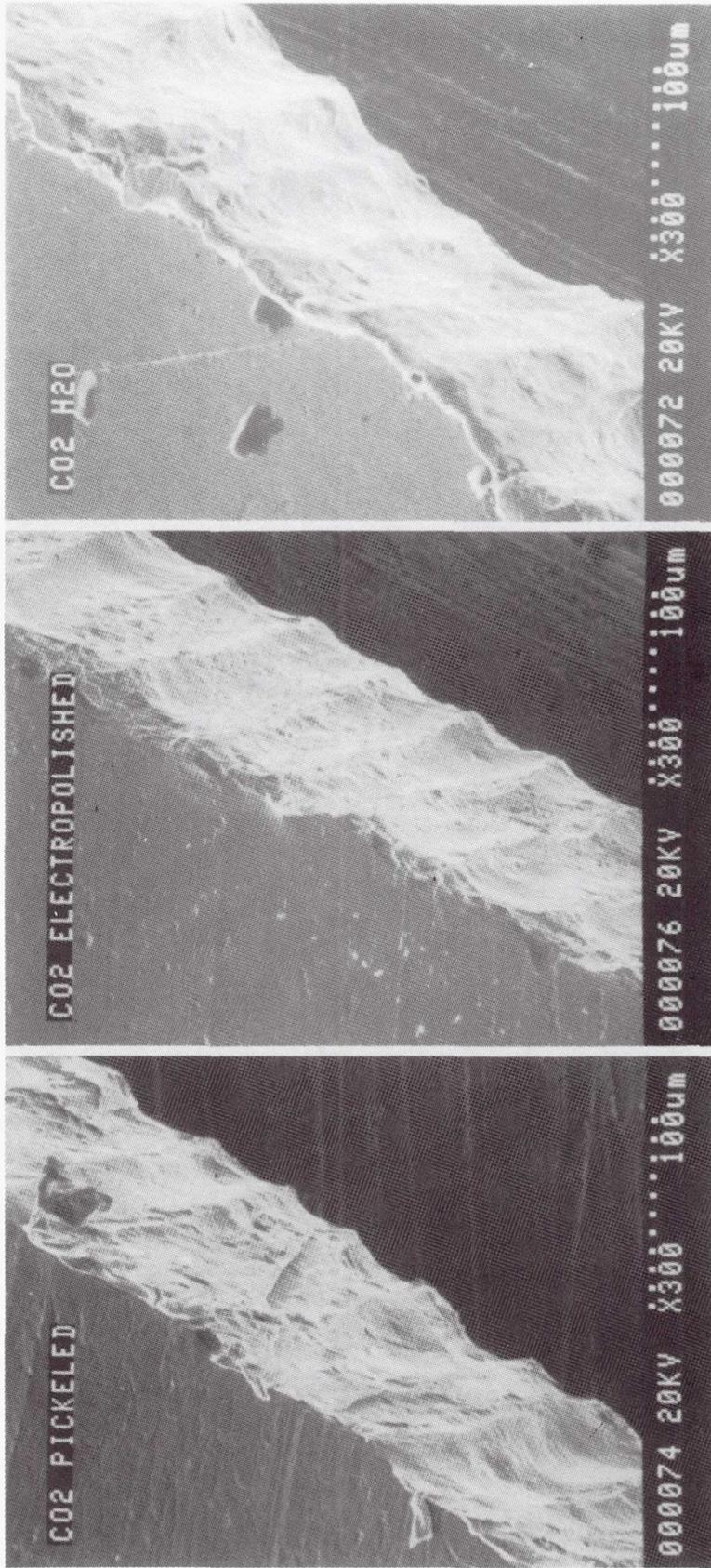
a) Platelet Immersed in a Nitric Acid Pickle for 30 Minutes at 140 to 185°F. Dress Formation at the Exit is Removed, No Gross Attack of Base Metal Noted.

b) Platelet Immersed in a Phosphoric Acid Electropolish Solution for 5 Minutes at 5.9 Amps Solution Very Aggressive in Clean Up, Note Pitted Appearance Where Base Material Is Being Attacked.

c) Platelet Mating Surfaces Lapped using 600 Grit Emery Cloth. Water Flow Removed Dross on Inside Surfaces. Slight Smearing Dross is Still Noted Along Edge.

Figure 3.4.2-3. Dross Removal Methods for Laser Cut Platelets

178

3.4, Injector Fabrication Studies (cont.)

Method #2 (Figure 3.4.2-3b):

The chemistry lab within Test Area "A" prepared and electropolished a platelet for 5 min at 5.9 amps. The solution was 75% phosphoric acid and water. Copper sheets were used for the anode. Starting weight was 8.62170 grams with a weight loss of 0.31110 grams.

Method #3 (Figure 3.4.2-3a):

The chemistry lab within Test Area "A" prepared and pickled a platelet for 30 minutes at 140 to 185 deg F. The solution used was a 300 series stainless pickle composed of 100 cc H_2O, 130 cc HNO_3, and 10 cc HF. Starting weight was 8.64523 grams with a weight loss of 0.13613 grams.

3.4.2.7 Conclusions

The initial findings on this study for stainless steel platelets are:

1) Laser cutting can be cheaper than chemical milling

2) Remaining dross on the platelets should be removed by exposure to a SS Pickle solution prior to inspection and use.

3) Operator skill is at least equally important as the type of equipment used.

4) Thicker platelets are more suitable for laser cutting than chemical etching.

5) Although not demonstrated within this study, laser cutting has the ability to make angular cuts.

REFERENCES

1. "Orbital Transfer Vehicle 3000 lbf Thrust Chamber Assembly Hot Fire Test Program," Interim Report, Contract/Task Order NAS 3-23772-C.2, NASA CR 182145, Prepared for National Aeronautics and Space Administration, September 1988.

2. "7.5K Thrust Level OTV Engine Preliminary Design," Final Report, Contract NAS 3-23772, Prepared for National Aeronautics and Space Administration, October 1988.

3. "Diffusion Bonding Procedure for Zirconium Copper," Aerojet TechSystems Materials and Processing Report, 7 August 1987.

4. Rocketdyne Materials Properties Manual, Vol. 3, Third Edition, Zirconium Copper - Alloy Class 7150, Jan. 1982.

5. Thermophysical Properties of Matter, Vol. 1, Thermal Conductivity - Metallic Elements and Alloys, IFI/Plenum Pub. N.Y., 1970.

6. Massalski, T.B., editor, "Binary Alloy Phase Diagrams," American Society for Metals, Metals Park, OH, 1986.

7. "Analysis of Copper and Copper Alloys in Combustion Chamber Liner Applications," Internal Memo, November 16, 1987.

8. SCM Metals Technical Bulletin #1428.

9. Conway, J.B., Stentz, R.H. and Berling, J.T., "High-Temperature, Low-Cycle Fatigue of Advanced Copper-Base Alloys for Rocket Nozzles; Part II - NASA 1.1, GlidCop and Sputtered Copper Alloys,"Contract NAS 3-17777, November 1974.

10. Calhoon, D.F., Ito, J.I. and Kors, D.L., "Investigation of Gaseous Propellant Combustion and Associated Injector/Chamber Design Guidelines," Final Report, Prepared for National Aeronautics and Space Administration.

11. Calhoon, D.F., Ito, J.I. and Kors, D.L., "Handbook for Design of Gaseous Propellant Injectors and Combustion Chambers," Prepared for National Aeronautics and Space Administration, July 31, 1973.

12. Advanced Regenerative Chamber Technology, IR&D Program 7983-08, Report 7983-08, February 1984 prepared by Berkman, D.K. and Schoenman, L.

13. Arcella, F.G., "Interdiffusion Behavior of Tungsten or Rhenium and Group V and VI Elements and Alloys of the Periodic Table - Part II (Appendices)," Report NASA CR-134526 - Prepared for National Aeronautics Administration, September 1974.

14. Schoenman, L., "Orbit Transfer Rocket Technology Program," Oxygen Compatible Materials Testing Task Order B.5, NASA CR 182195, Prepared for National Aeronautics and Space Administration, June 1988.

APPENDIX A

A COMPARATIVE ROD APPARATUS (CRA) FOR MEASURING THERMAL
CONDUCTIVITY TO 2000 DEG F

A COMPARATIVE ROD APPARATUS FOR MEASURING
THERMAL CONDUCTIVITY TO 2000 °F

Southern Research Institute's comparative rod apparatus is used to measure thermal conductivities of a wide variety of materials from -300 °F to 2000 °F. This apparatus shown schematically in Figure 1, consists basically of two cylindrical reference pieces of known thermal conductivity stacked in series with the cylindrical specimen. Heat is introduced to one end of the rod, composed of the references and specimen, by a small electrical heater. A cold sink or heater is employed at the opposite end of the rod as required to maintain the temperature drop through the specimen at the preferred level. Cylinders of zirconia may be inserted in the rod assembly to assist in controlling the temperature drop. Radial losses are minimized by means of radial guard heaters surrounding the rod and consisting of three separate coils of 16, 18 or 20-gage Kanthal wire wound on a 2 or 4- inch diameter alumina core. The annulus between the rod and the guard heaters is filled with diatomaceous earth, thermatomic carbon, bubbled alumina or zirconia powder. Surrounding the guard is an annulus of diatomaceous earth enclosed in an aluminum or transite shell.

The specimens and references (see Figure 2) are normally 1 inch diameter by 1 inch long. Thermocouples located 3/4 inch apart in radially drilled holes measure the axial temperature gradients. Thermocouples located at matching points in each guard heater are used to monitor guard temperatures, which are adjusted to match those at corresponding locations in the test section.

In operation, the apparatus is turned on and allowed to reach steady state. The guard and rod heaters are adjusted to minimize radial temperature gradients between the rod and guard sections consistent with maintaining equal heat flows in the references. Temperatures are measured on a Leeds and Northrup Type K-3 potentiometer, and the temperature gradients calculated. A typical temperature profile in the test section is shown in Figure 3.

The thermal conductivity of the specimen is calculated from the relation

$$K_s = \frac{K_1 \Delta T + K_2 \Delta T}{2 \Delta T_s} \qquad \frac{\Delta X_s}{\Delta X_r}$$

where K_1 and K_2 are the thermal conductivities of the upper and lower references; ΔT_1, ΔT_2 and ΔT_S are the temperature differences in the upper and lower references and specimen, respectively; ΔX_S and ΔX_r are the distances between thermocouples in the specimen and references.

Note that for purely axial heat flow, the products $K_1 \Delta T_1$ and $K_2 \Delta T_2$ should be equal. Due to imperfectly matched guarding and other factors, this condition is seldom attained in practice; therefore, the average of the two values is used in the calculations. Their difference is maintained as small as possible, usually within 5 percent of the smaller.

For identical specimens, the ratio $\Delta X_S/\Delta X_r$ should be unity but may vary due to the uncertainty in hole locations. To prevent introducing an additional error in calculations, ΔX is determined as follows: the depth of the hole is measured by inserting a snugly fitting drill rod in the hole, measuring the projecting length and subtracting it from the total length of the rod. The slope, or angle the hole makes with the perpendicular to the specimen axis, is determined by making measurements to the face of the hole and the outer end of the drill rod with respect to a datum plane, using a dial gage. From these measurements, the location of the bottom of the hole can be calculated.

Generally, measurements with the comparative rod apparatus are performed in an inert helium environment. The apparatus can also be operated in vacuum and at gas pressures of up to 100 psig. We have had experience operating under all conditions.

The primary reference materials which we use are Code 9606 Pyroceram and Armco iron for measurements on materials with low and high thermal conductivities, respectively. Primary standard reference sets are kept and are used to calibrate other references made from the same materials. The standards of Code 9606 Pyroceram were made from a batch of material which NBS purchased shortly after their measurements on a sample of Code 9606 Pyroceram. The curve which Flynn presented for the thermal conductivity of

the Pyroceram is given in Figure 4[1]. Note that the curve is in good agreement with the recommended values from NSRDS-NBS 8[2]. The standards of Armco iron were made from the stock which was used in the round-robin investigations from which Powell[3] developed the most probable values for Armco iron. The curve used for the Armco iron standards is shown in Figure 5. Powell estimated the uncertainty to be within ±2 percent over the temperature range from 0° to 1000 °C. Note in Figure 5 that numerous evaluations of Armco iron from other batches of material have agreed within ±3 percent (coefficient of variation about curve) with Powell's original data.

In addition to Code 9606 Pyroceram and Armco iron several other materials have been used as references. These include copper for high conductivity specimens, 316 stainless steel for specimens of intermediate thermal conductivity and Teflon or Pyrex for low conductivity materials.

Copper references have been calibrated against Armco iron and excellent agreement with literature data has been obtained. Thermal conductivity values obtained from calibrations of 316 stainless steel against Pyroceram, Armco iron and a set of 316 stainless steel standards are presented in Figure 6. Note the consistency of the data obtained with the three different sets of references. The coefficient of variation of the data shown in Figure 6, about the curve value, was ±3.3 percent. These data indicate the internal consistency of the stainless steel and the reference materials. Note that the thermal conductivity values for 316 stainless steel presented in Figure 6 lie between values reported by several steel manufacturers and Lucks and Deem.[4]

---

[1]Robinson, H. E. and Flynn, D. R., Proceedings of Third Conference on Thermal Conductivity, pages 308-321, 1963 (with author's permission).

[2]Powell, R. W., Ho, C. Y., and Liley, P. E. Thermal Conductivity of Selected Materials, NSRDS-NBS 8, Department of Commerce, November 25, 1966.

[3]Powell, R. W., Proceedings of Third Conference on Thermal Conductivity, pages 322-341, 1963.

[4]WADC TR58-476, "The Thermophysical Properties of Solid Materials," Armour Research Foundation, November, 1960.

The calibrations indicate that for materials with moderate to high
thermal conductivities the apparatus operates with a precision of about ±3
percent and a total uncertainty of about ±5 percent at temperatures above
0 °F if temperatures between the guard and test section are closely matched.
Below 0 °F, the precision achieved to date has been about ±7 percent with a
total uncertainty of about ±10 percent. We anticipate that the precision
and uncertainty at cryogenic temperatures can be improved by additional
calibrations.

Some additional data obtained on the comparative rod apparatus are
shown in Figure 7 and 8. Figure 7 shows thermal conductivity data for ATJ
graphite, with grain, using Armco iron as the reference material. These
data show excellent agreement with earlier data obtained here and by other
sources[5][7]. The maximum scatter of the comparative rod points was about 5
percent.

Figure 8 shows data for thermocouple grade constantan obtained on the
comparative rod apparatus using Armco iron references, and on Southern
Research Institute's high temperature radial inflow apparatus. Note the
excellent agreement. These data also show close agreement with data
obtained by Silverman[4] on an alloy of very similar composition.

---

[5]ASD-TDR-62-765, "The Thermal Properties of Twenty-Six Solid Materials
to 5000 °F or Their Destruction Temperatures", Southern Research Institute,
August, 1962

[6]Pears, C. D., Proceedings of Third Conference on Thermal Conductivity,
453-479 (1963)

[7]NSRDS-NBS 16, "Thermal Conductivity of Selected Materials", Part 2,
by C. Y. Ho, R. W. Powell and P. E. Liley, National Bureau of Standards, 1968
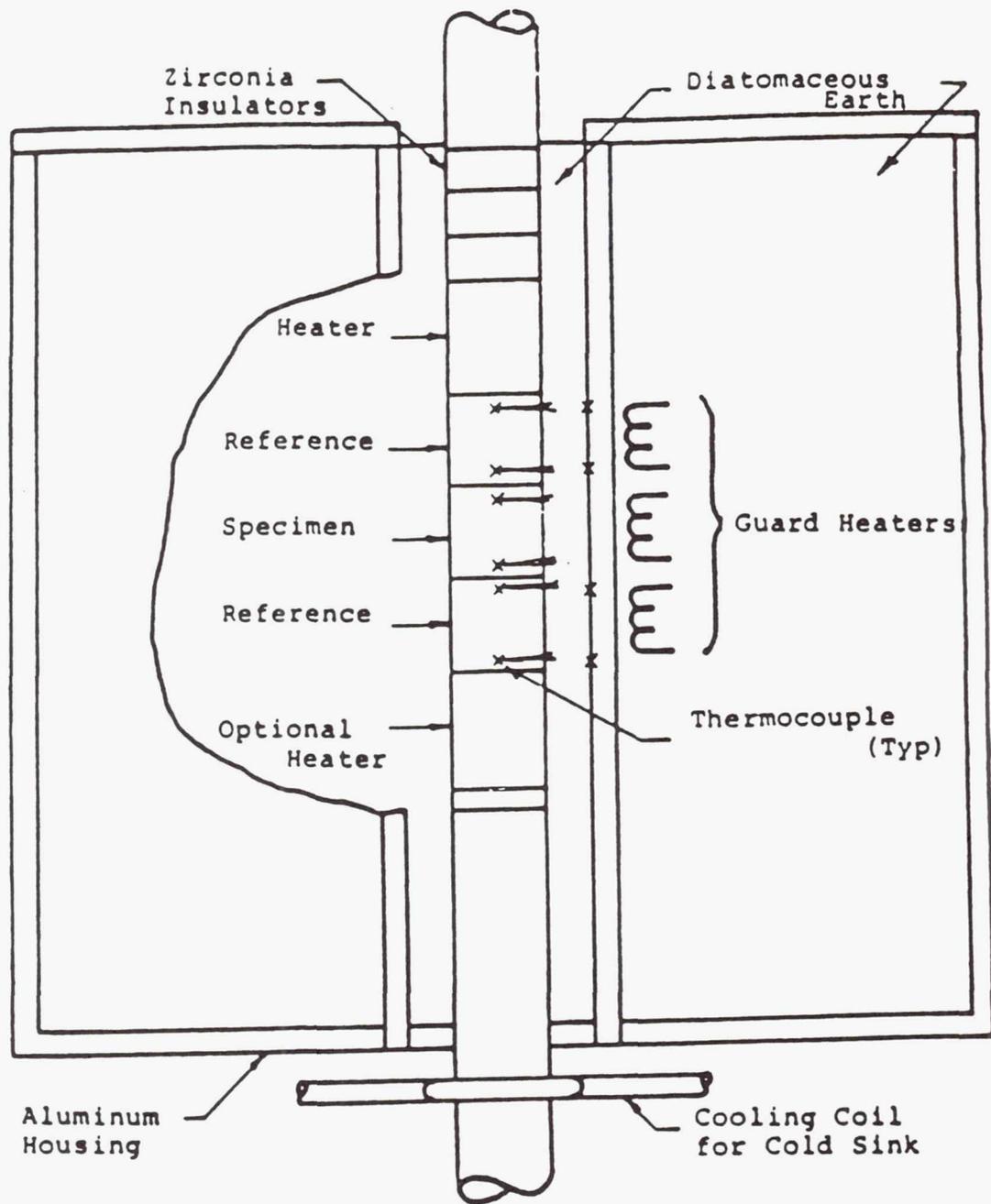
Figure 1. Schematic of Comparative Rod Thermal Conductivity Apparatus
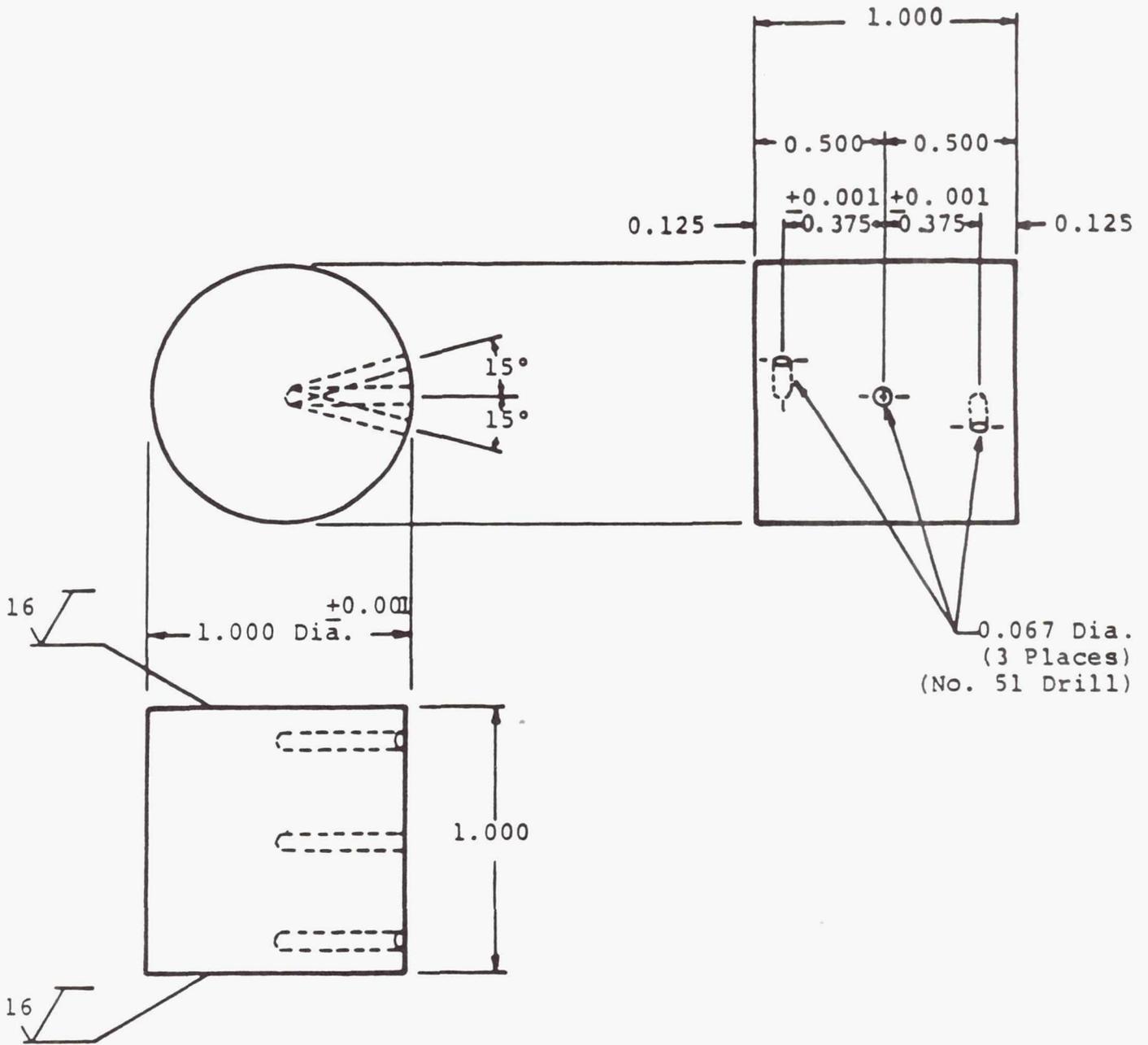
Note: All dimensions +0.005 except where noted

Figure 2. Drawing of specimen for Thermal Conductivity measurements in Comparative Rod Apparatus

A-7
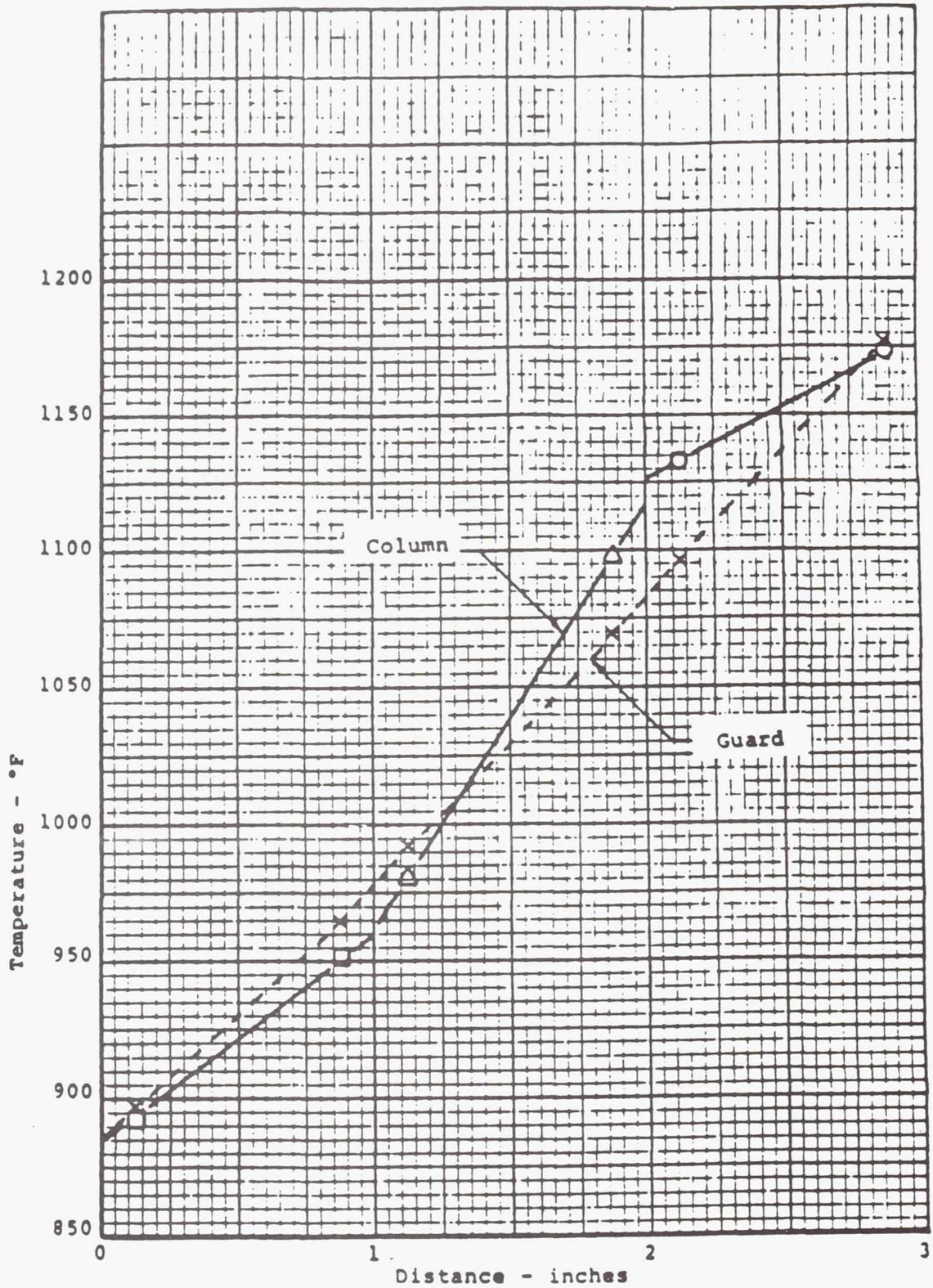
Figure 3. Typical temperature profile in test section
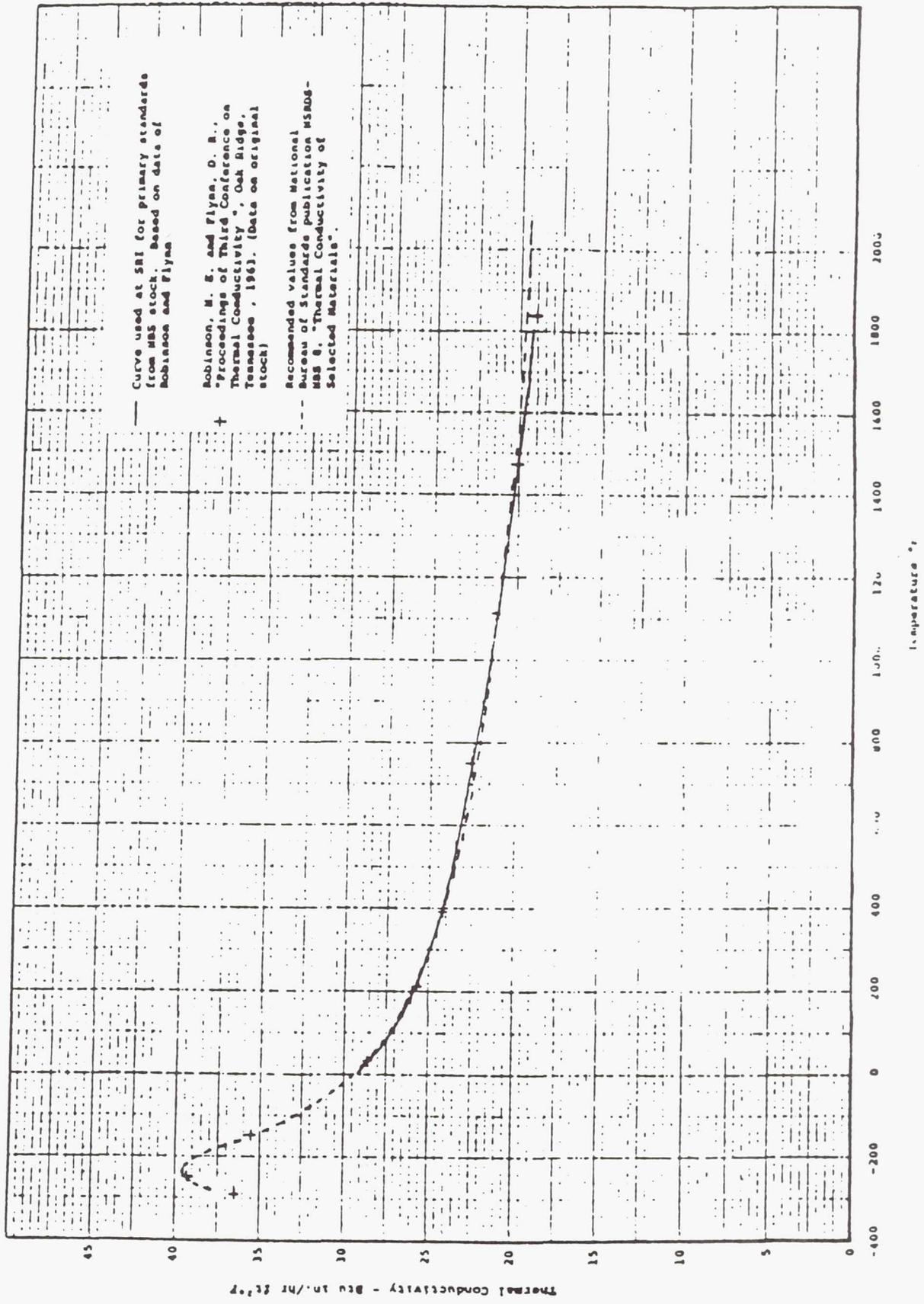
Figure 4. Thermal Conductivity of primary SRI standards from NBS stock of Code 9606 Pyroceram
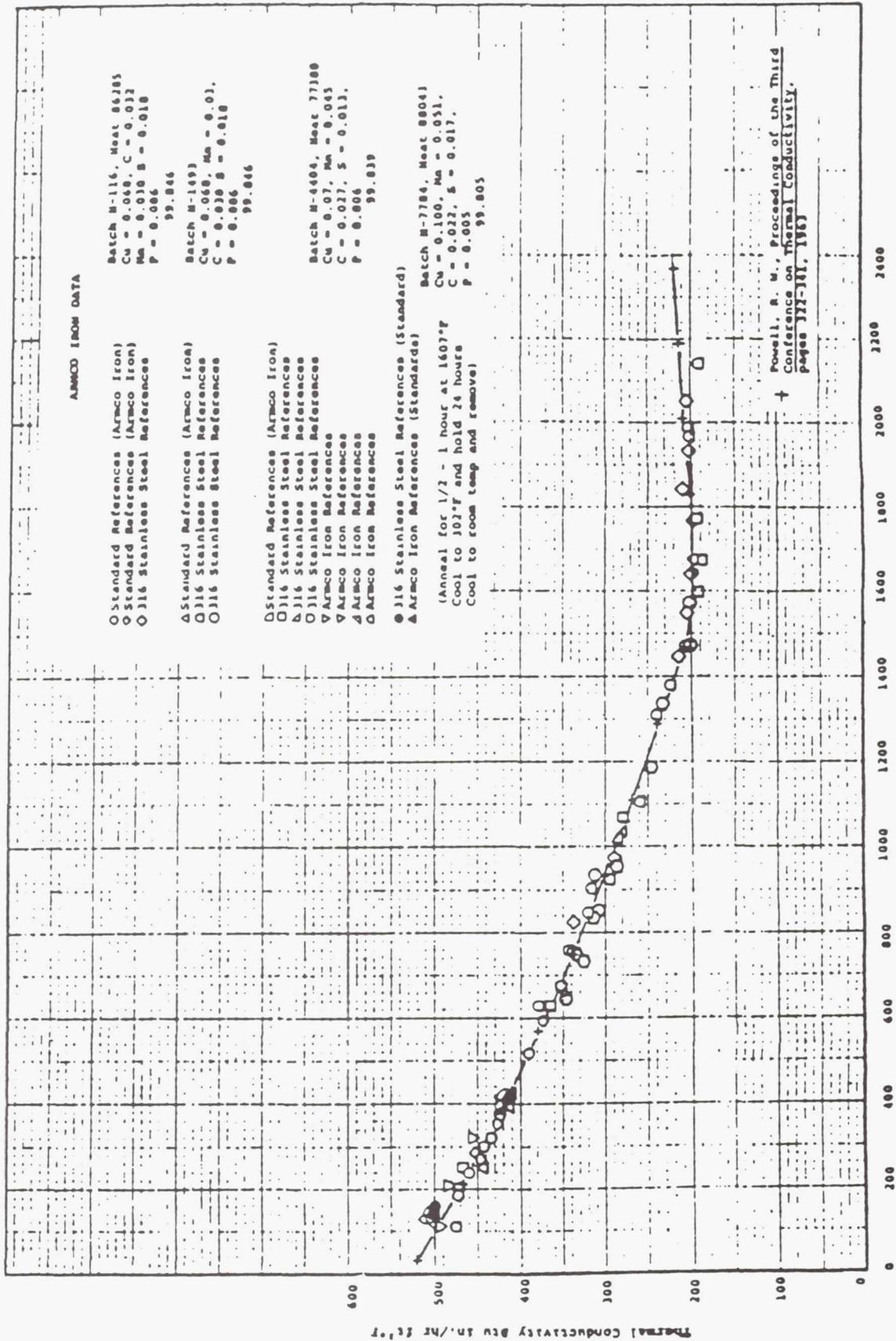
Figure 5. Thermal Conductivity of Armco Iron
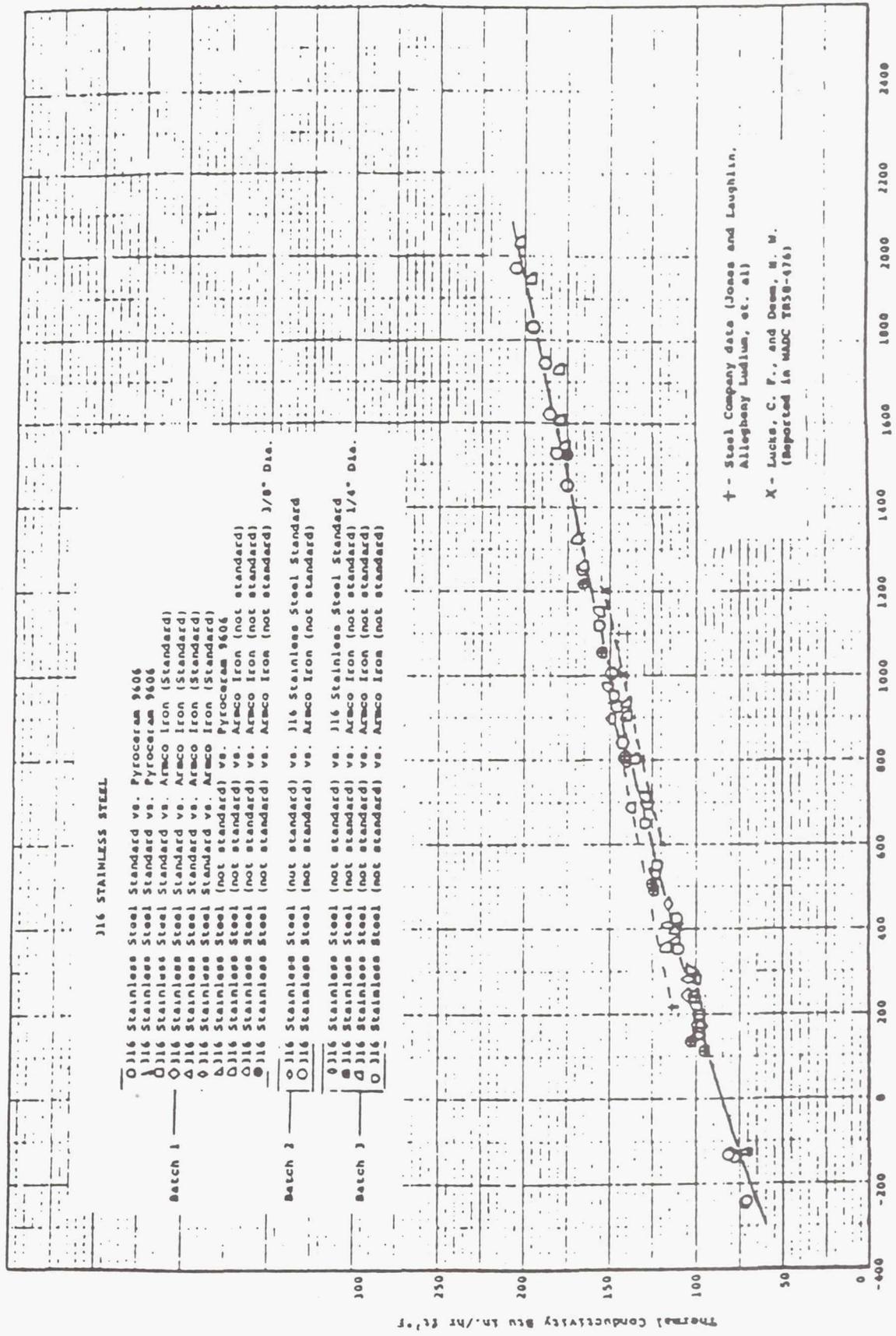
Figure 6. Thermal Conductivity of 316 Stainless Steel
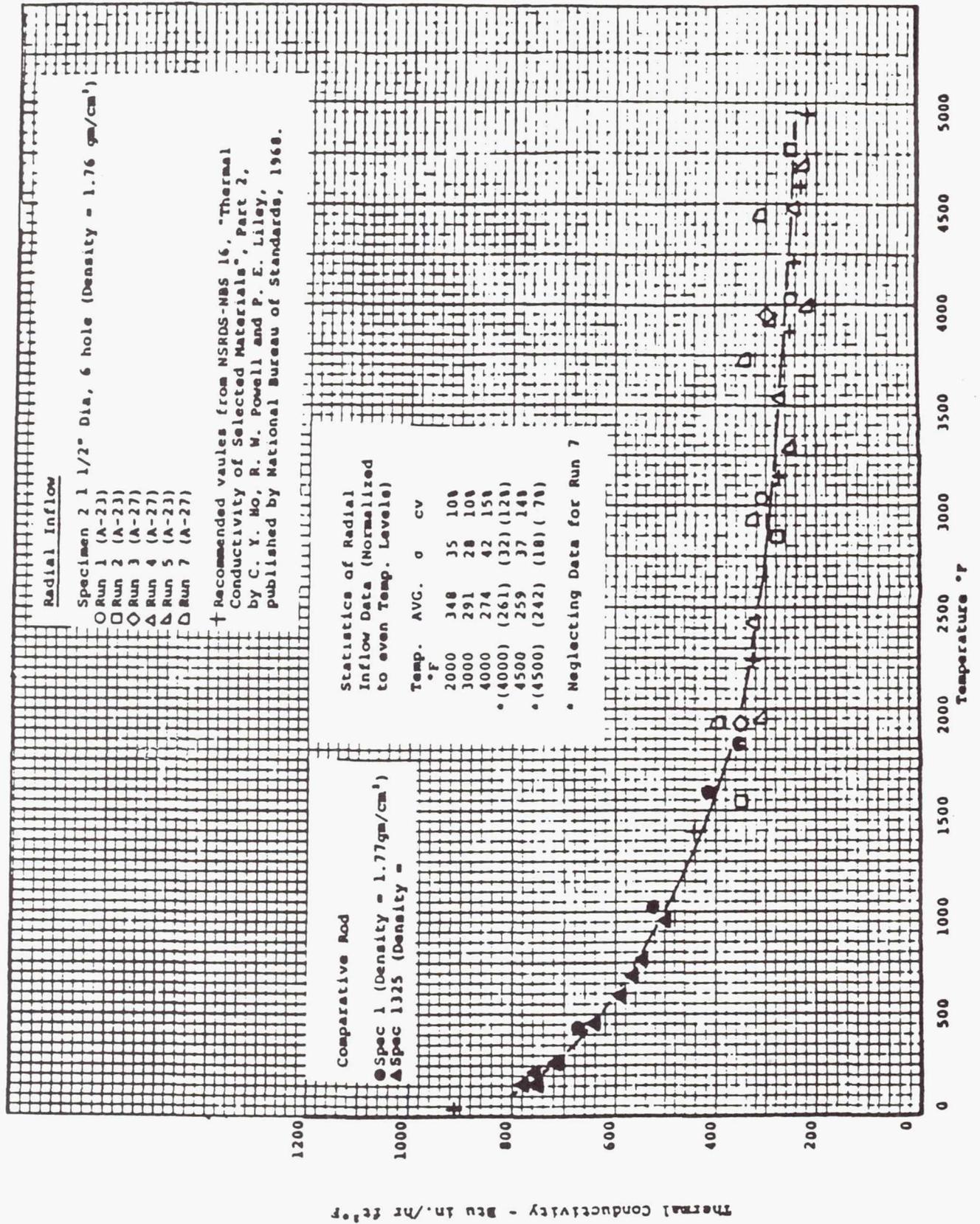
Figure 7. The Thermal Conductivity of ATJ Graphite, with Grain
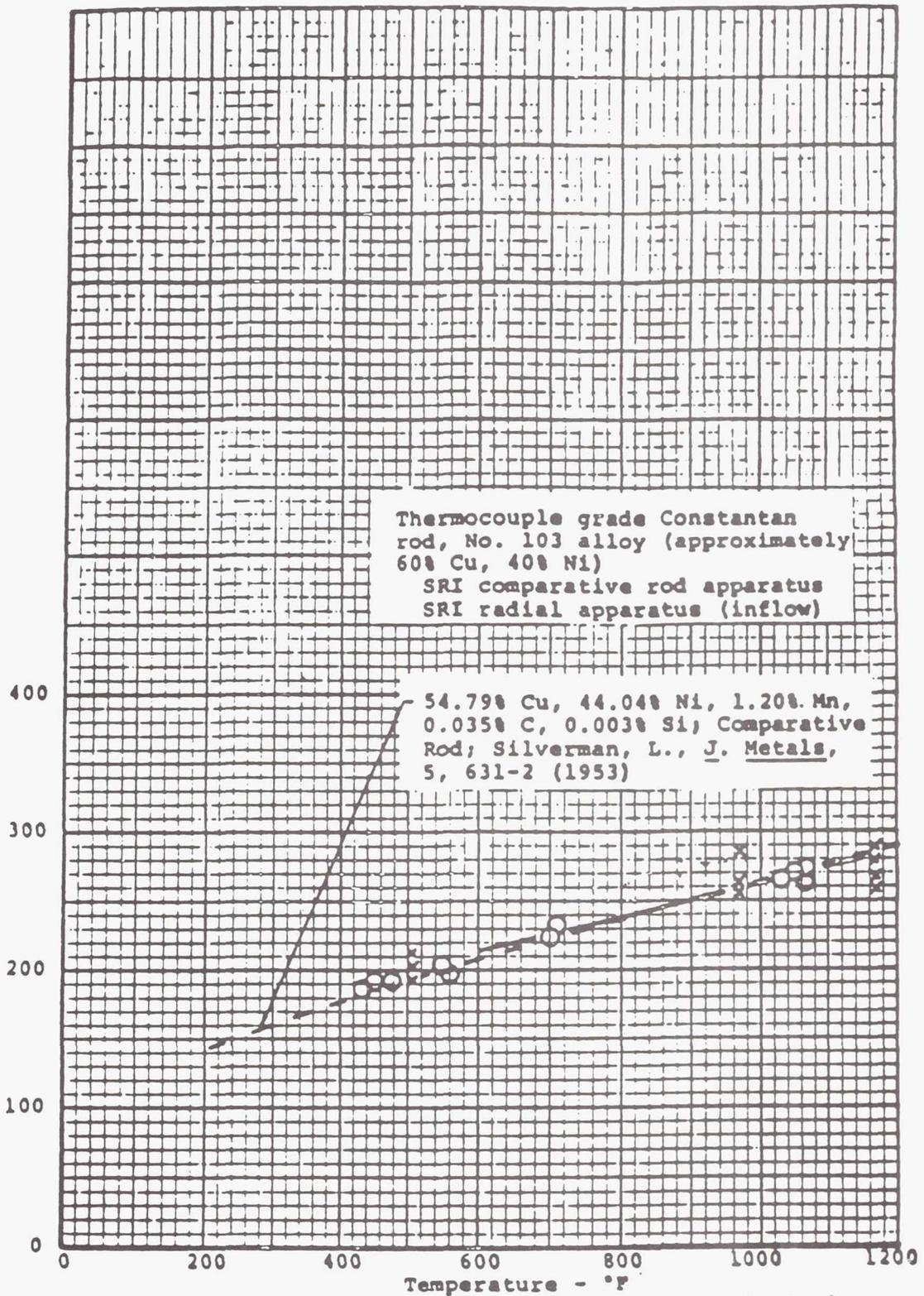
Figure 8. The Thermal Conductivity of Thermocouple Grade Constantan Rod

Thermocouple grade Constantan rod, No. 103 alloy (approximately 60% Cu, 40% Ni)
  SRI comparative rod apparatus
  SRI radial apparatus (inflow)

54.79% Cu, 44.04% Ni, 1.20% Mn, 0.035% C, 0.003% Si; Comparative Rod; Silverman, L., J. Metals, 5, 631-2 (1953)

APPENDIX B

INJECTOR ELEMENT SPLASH TEST RESULTS
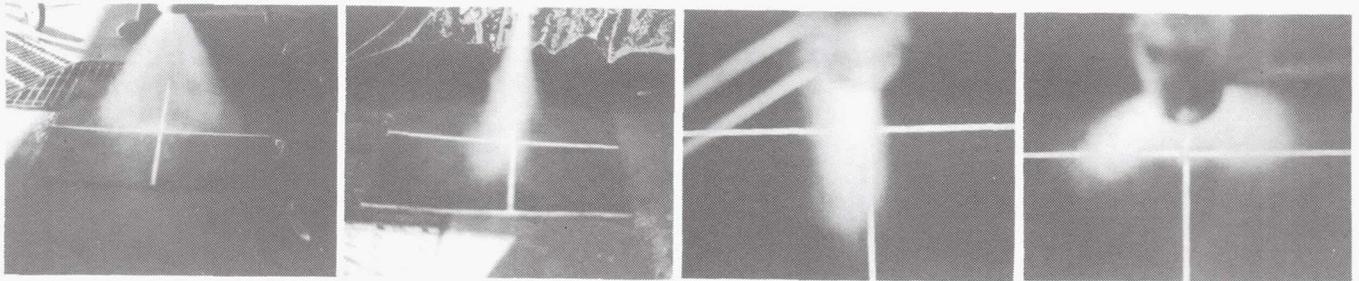
Baseline Element – Mod A
Momentum Ratio = 1.09
Wox = 0.4057
Wf = 0.0381
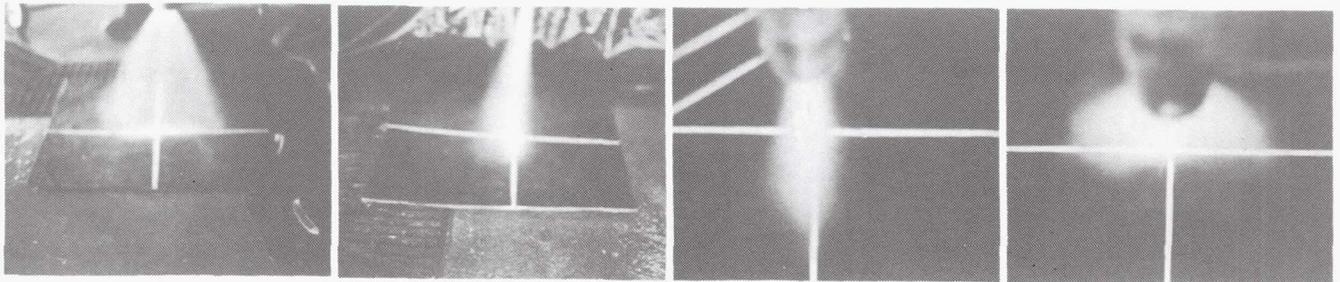
Baseline Element – Mod A
Momentum Ratio = 1.92
Wox = 0.5137
Wf = 0.0346
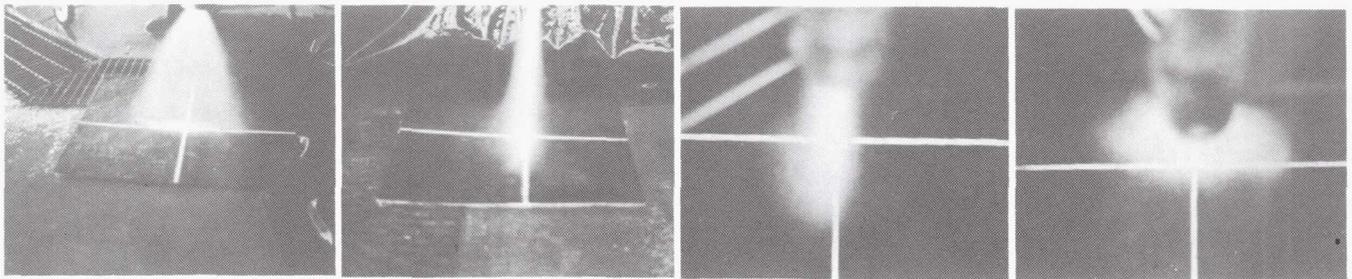
Baseline Element – Mod A
Momentum Ratio = 2.82
Wox = 0.5915
Wf = 0.0313
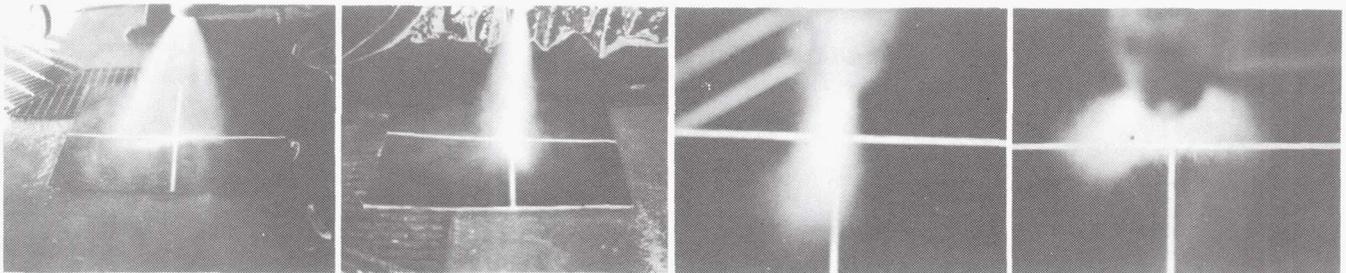
Baseline Element – Mod A
Momentum Ratio = 3.52
Wox = 0.6212
Wf = 0.0278
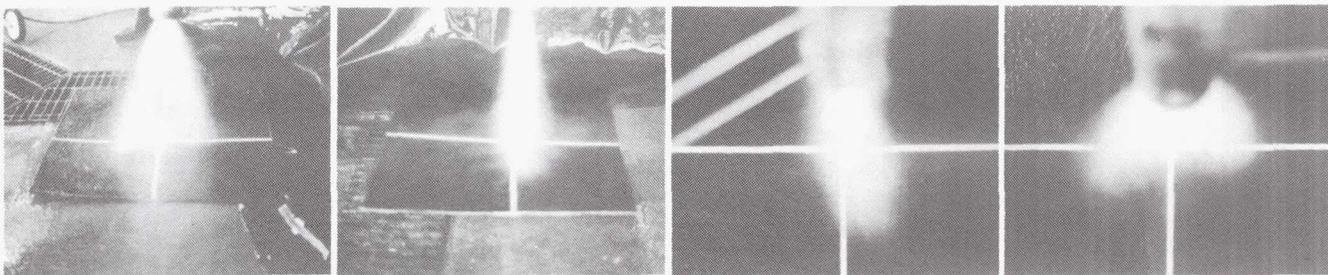
Center Element – Mod B
Momentum Ratio = 1.08
Wox = 0.4009
Wf = 0.0375
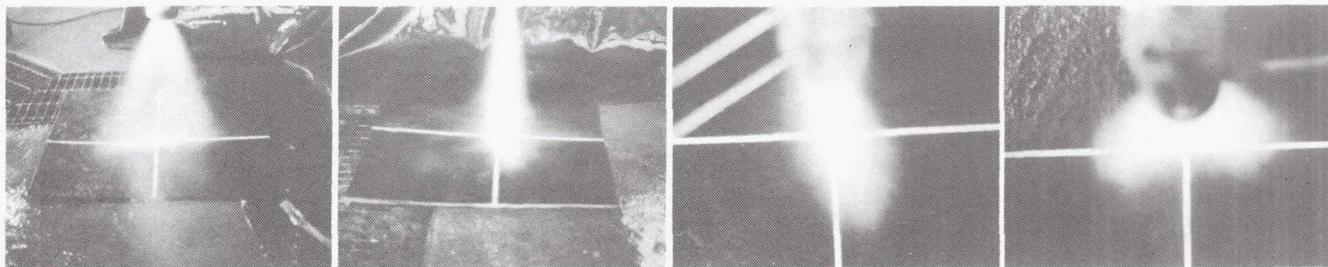
Center Element – Mod B
Momentum Ratio = 1.92
Wox = 0.5142
Wf = 0.0342
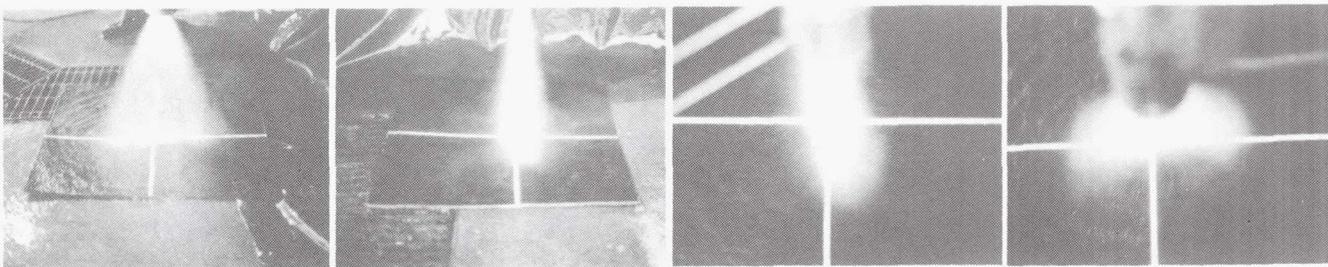
Center Element – Mod B
Momentum Ratio = 2.85
Wox = 0.5930
Wf = 0.0310
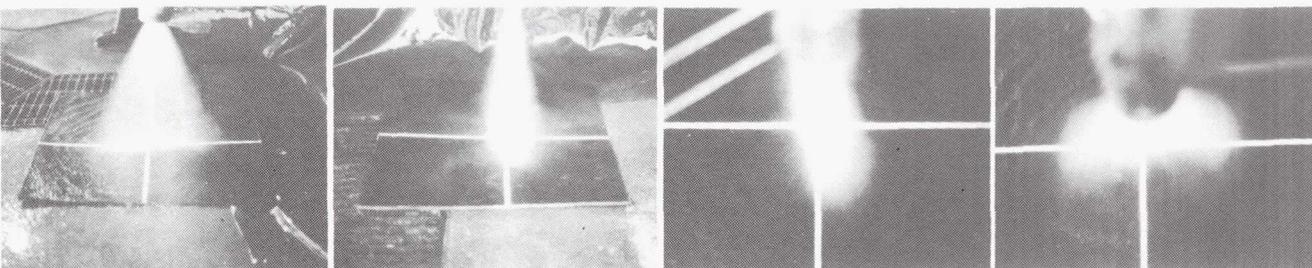
Center Element – Mod B
Momentum Ratio = 3.55
Wox = 0.6207
Wf = 0.0274
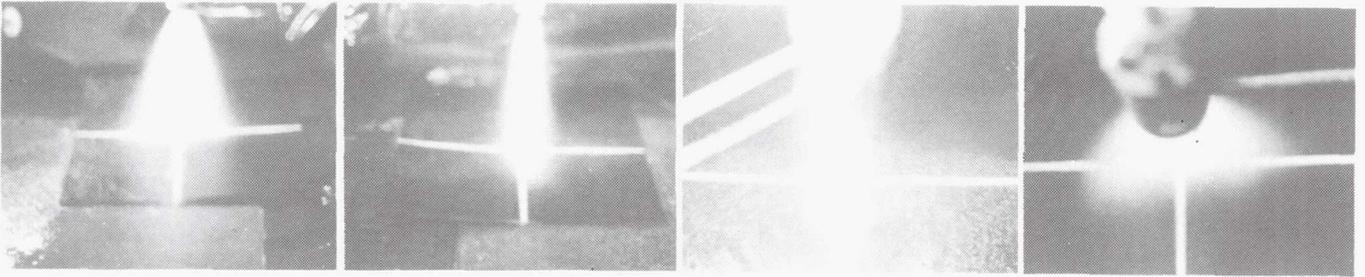
Center Element – Mod C
Momentum Ratio =1.08
Wox = 0.4029
Wf = 0.0378
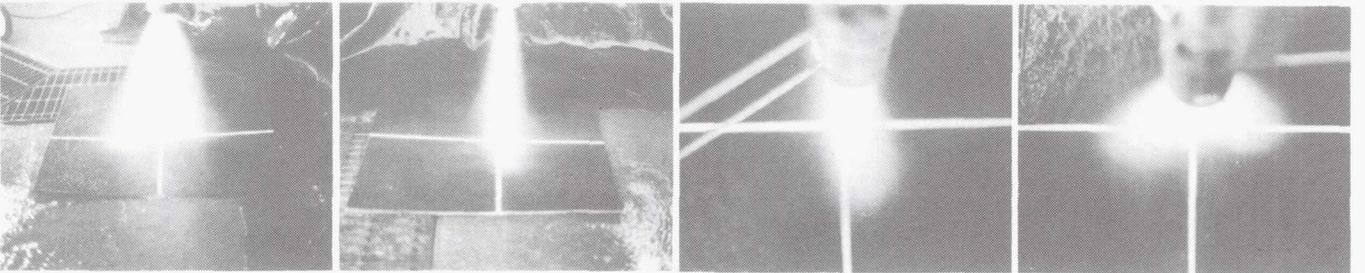
Center Element – Mod C
Momentum Ratio = 1.91
Wox = 0.5119
Wf = 0.0343
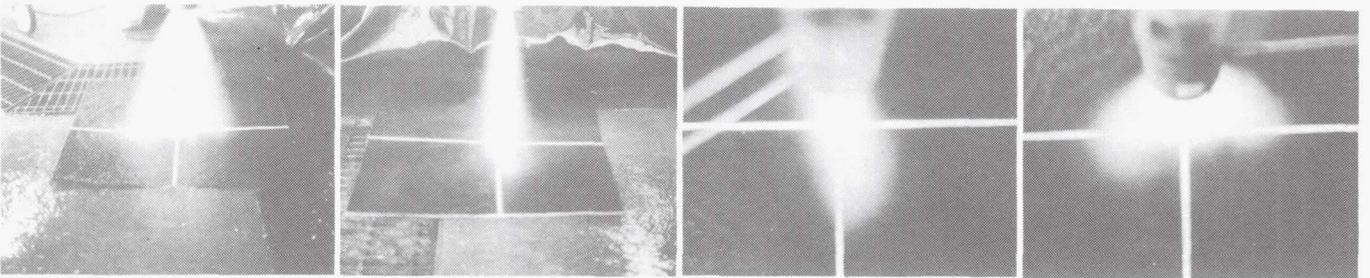
Center Element – Mod C
Momentum Ratio = 2.80
Wox = 0.5859
Wf = 0.0309
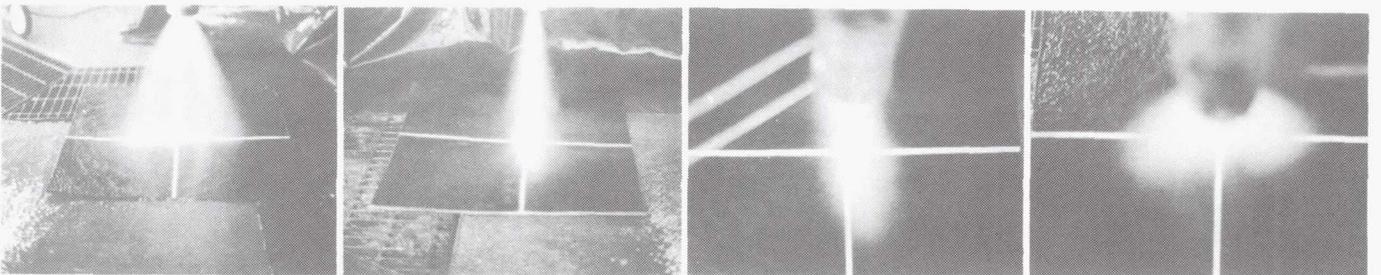
Center Element – Mod C
Momentum Ratio = 3.55
Wox = 0.6208
Wf = 0.0275
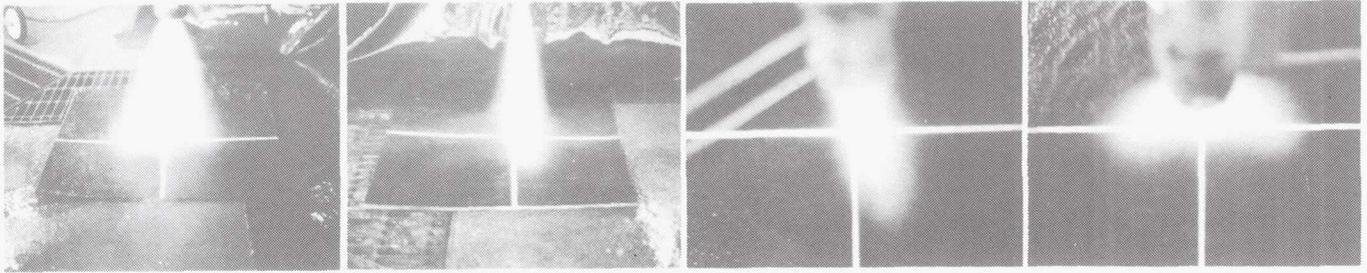
Center Element – Mod D
Momentum Ratio = 1.08
Wox = 0.4009
Wf = 0.0375
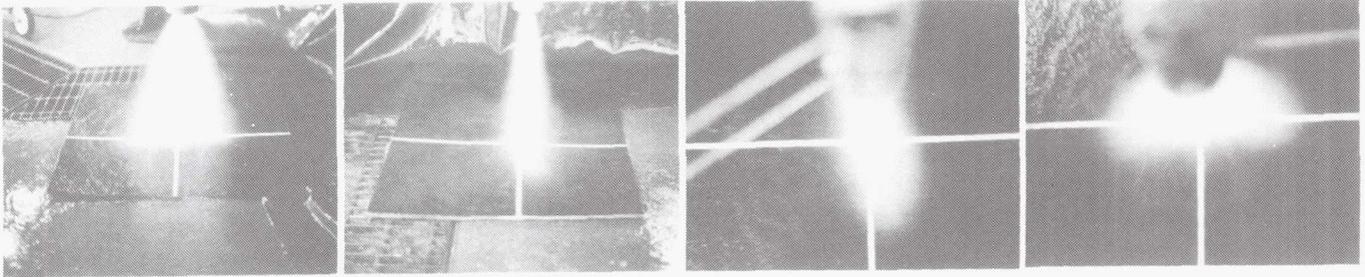
Center Element – Mod D
Momentum Ratio = 1.95
Wox = 0.5163
Wf = 0.0342

Center Element – Mod D
Momentum Ration = 2.82
Wox = 0.5877
Wf = 0.0309
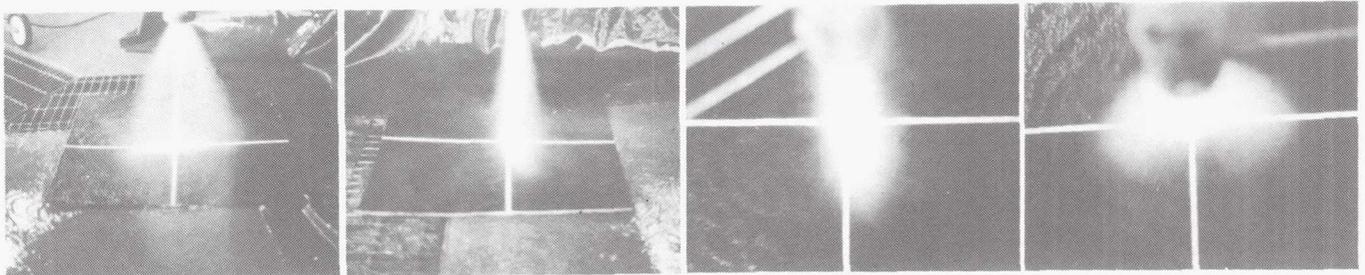
Center Element – Mod D
Momentum Ratio = 3.53
Wox = 0.6219
Wf = 0.0277
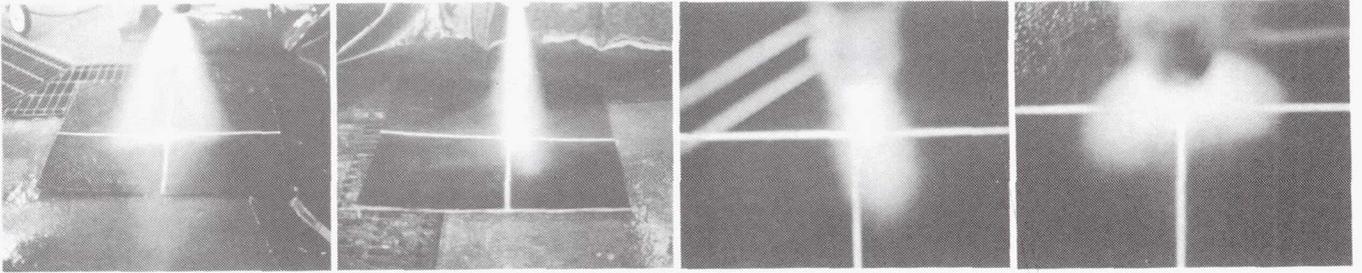
Center Element – Mod E
Momentum Ratio = 1.08
Wox = 0.4011
Wf = 0.0376
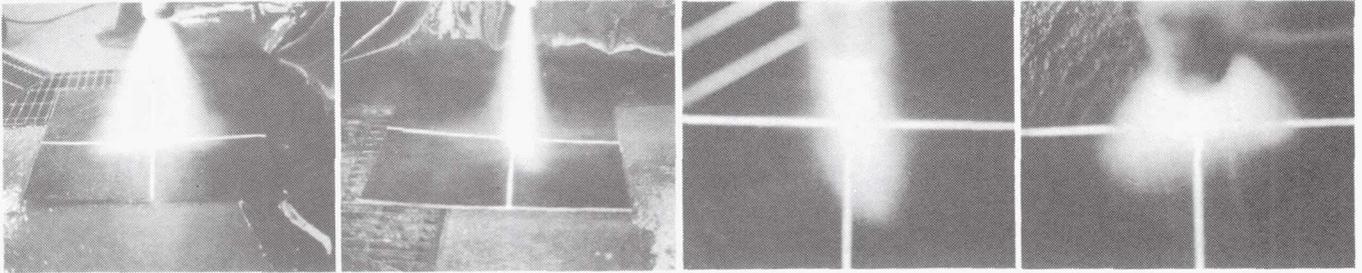
Center Element – Mod E
Momentum Ratio = 1.92
Wox = 0.5134
Wf = 0.0342
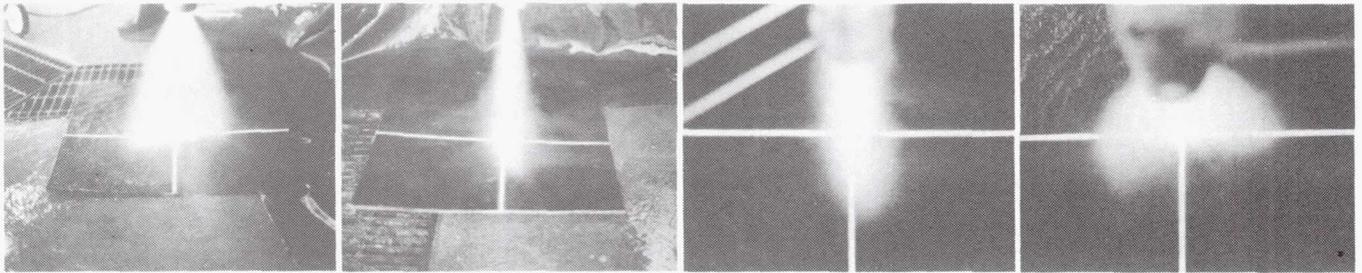
Center Element – Mod E
Momentum Ratio = 2.87
Wox = 0.5933
Wf = 0.0308
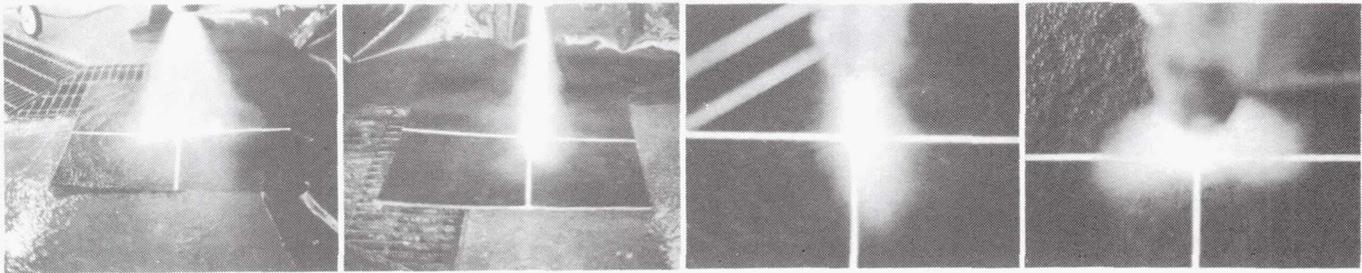
Center Element – Mod E
Momentum Ratio = 3.65
Wox = 0.6262
Wf = 0.0273
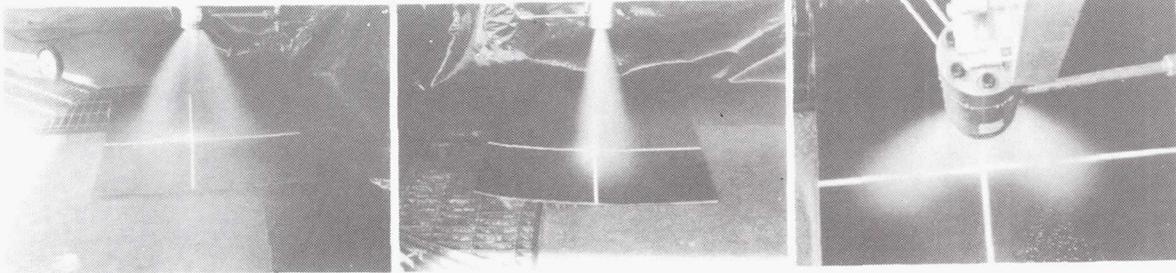
Baffle Element – Mod F
Momentum Ratio = 1.07
Wox = 0.3997
Wf = 0.0377
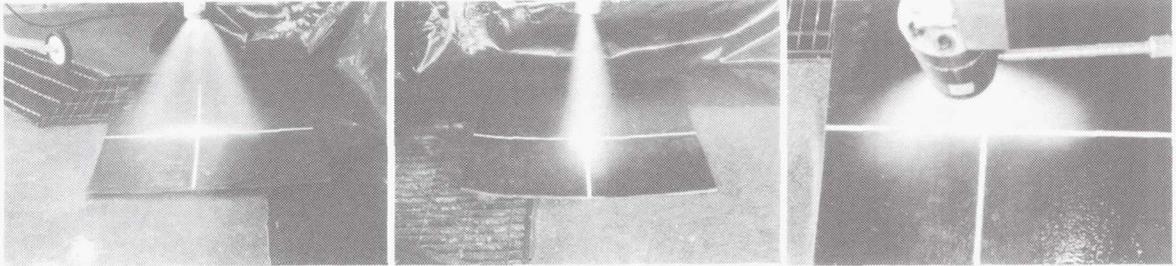
Baffle Element – Mod F
Momentum Ratio = 1.93
Wox = 0.5139
Wf = 0.0342
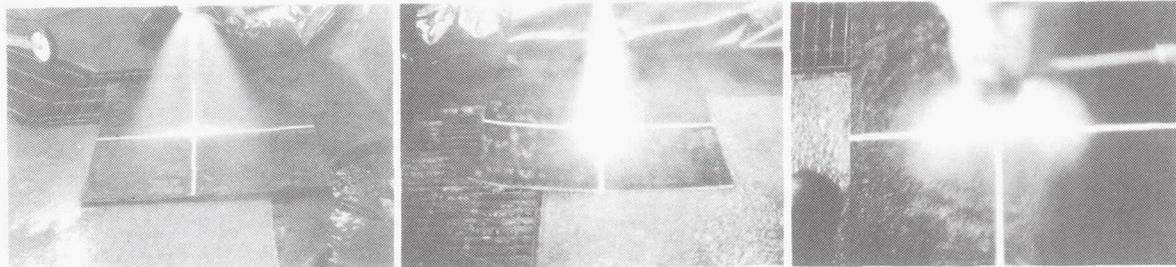
Baffle Element – Mod F
Momentum Ratio = 2.75
Wox = 0.5805
Wf = 0.0309

Baffle Element – Mod F
Momentum Ratio = 3.59
Wox = 0.6240
Wf = 0.0274
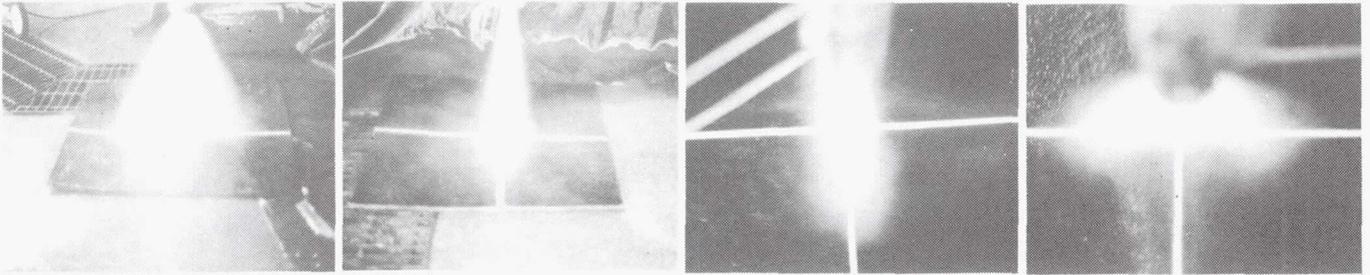
Baffle Element – Mod G
Momentum Ratio = 1.07
Wox = 0.4004
Wf = 0.0374
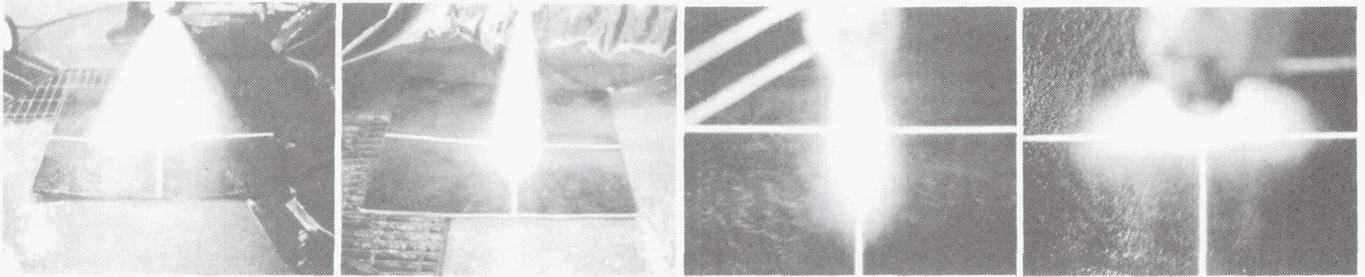
Baffle Element – Mod G
Momentum Ratio = 1.92
Wox = 0.5123
Wf = 0.0341
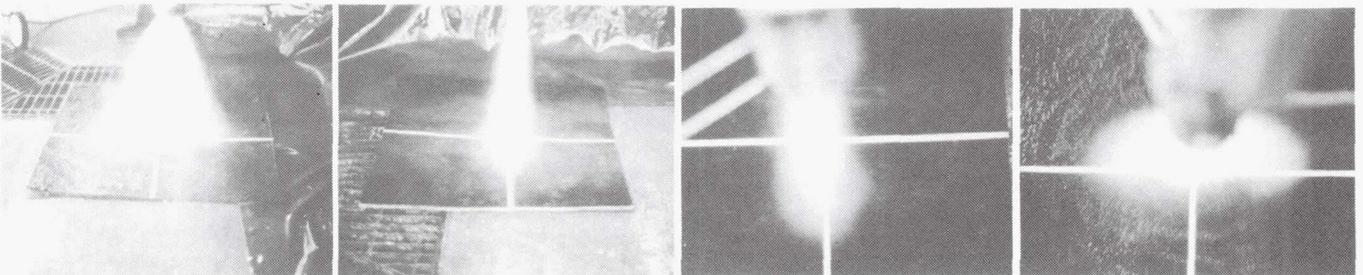
Baffle Element – Mod G
Momentum Ratio = 2.76
Wox = 0.5824
Wf = 0.0310
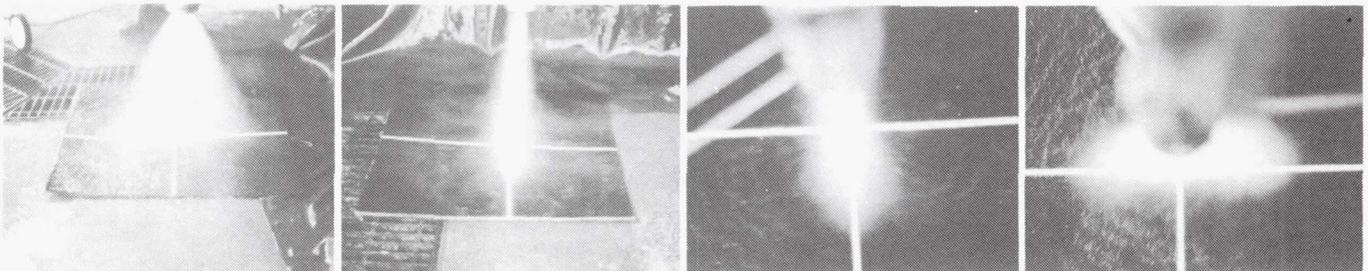
Baffle Element – Mod G
Momentum Ratio = 3.60
Wox = 0.6272
Wf = 0.0277
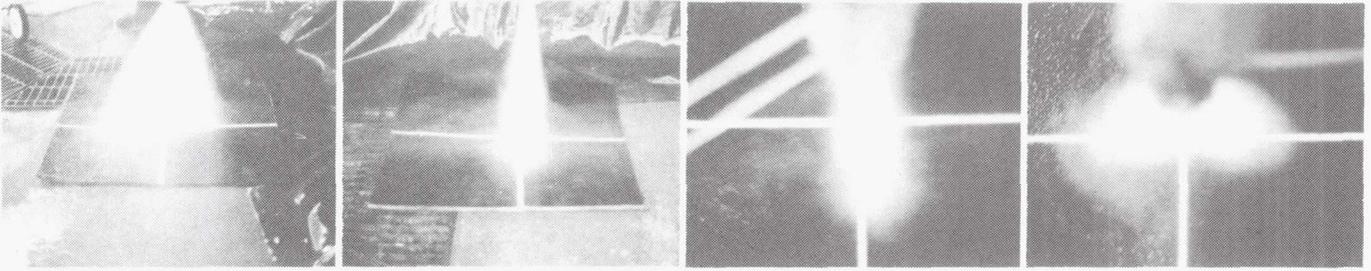
Baffle Element – Mod H
Momentum Ratio = 1.08
Wox = 0.4018
Wf = 0.0379
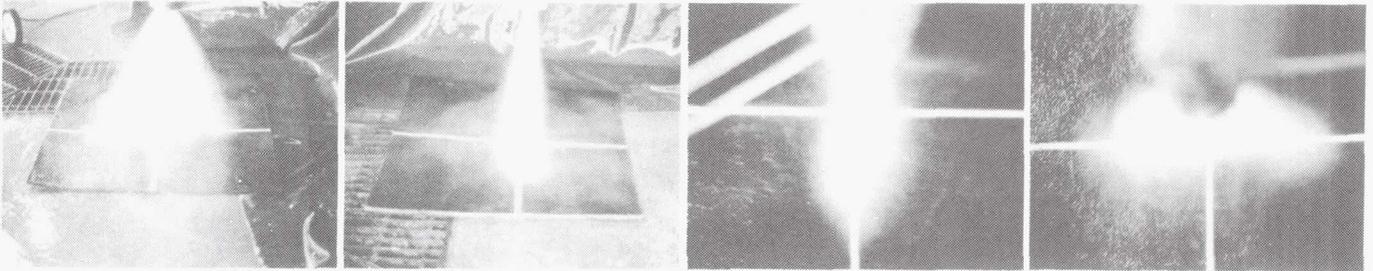
Baffle Element – Mod H
Momentum Ratio = 1.89
Wox = 0.5103
Wf = 0.0346
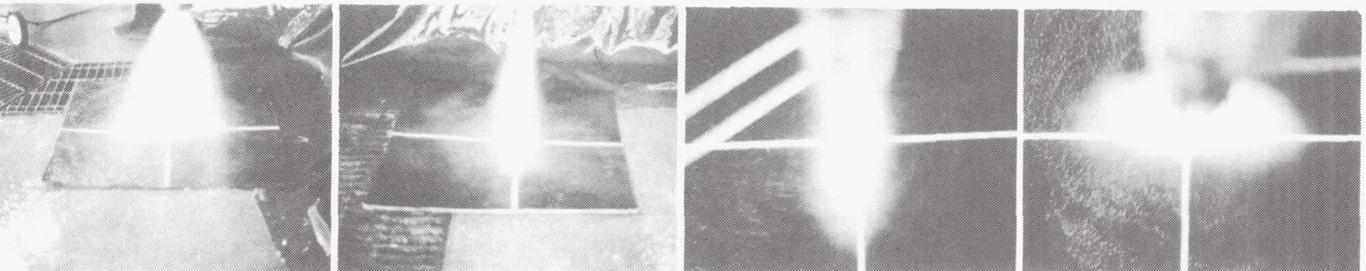
Baffle Element – Mod H
Momentum Ratio = 2.79
Wox = 0.5863
Wf = 0.0311
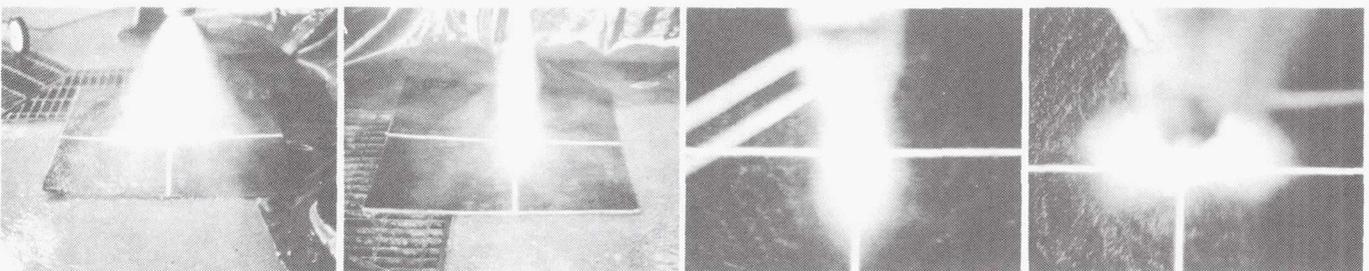
Baffle Element – Mod H
Momentum Ratio = 3.50
Wox = 0.6183
Wf = 0.0277
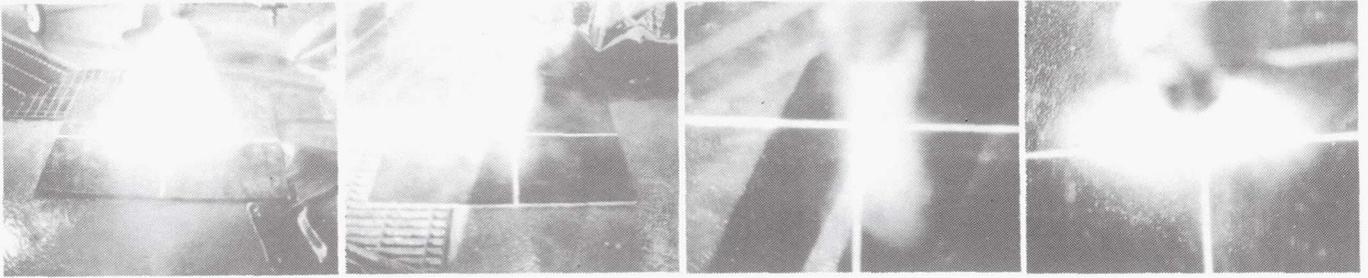
Baffle Element – Mod I
Momentum Ratio = 1.10
Wox = 0.4065
Wf = 0.0382
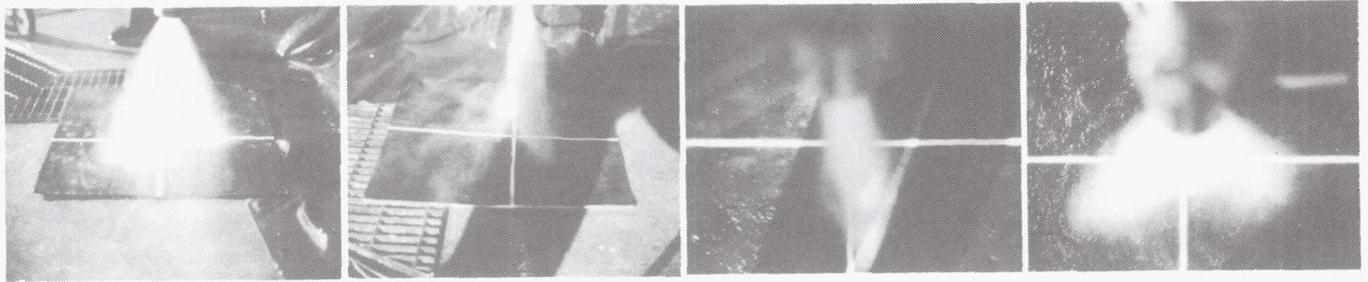
Baffle Element – Mod I
Momentum Ratio = 1.92
Wox = 0.5138
Wf = 0.0349
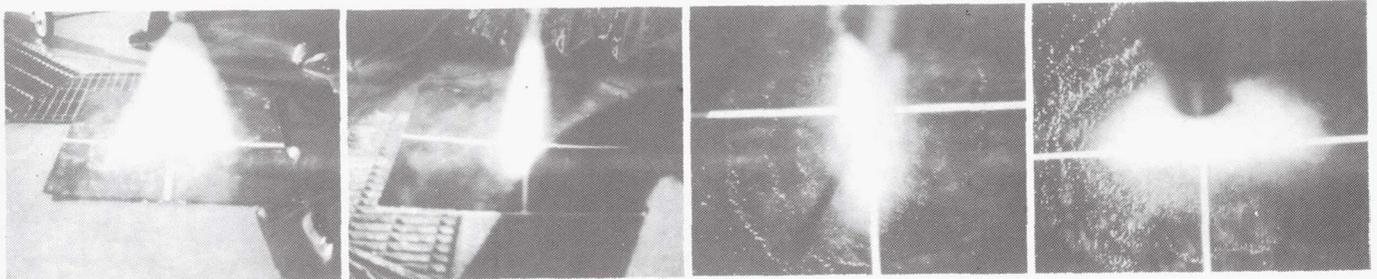
Baffle Element – Mod I
Momentum Ratio = 2.77
Wox = 0.5856
Wf = 0.0314
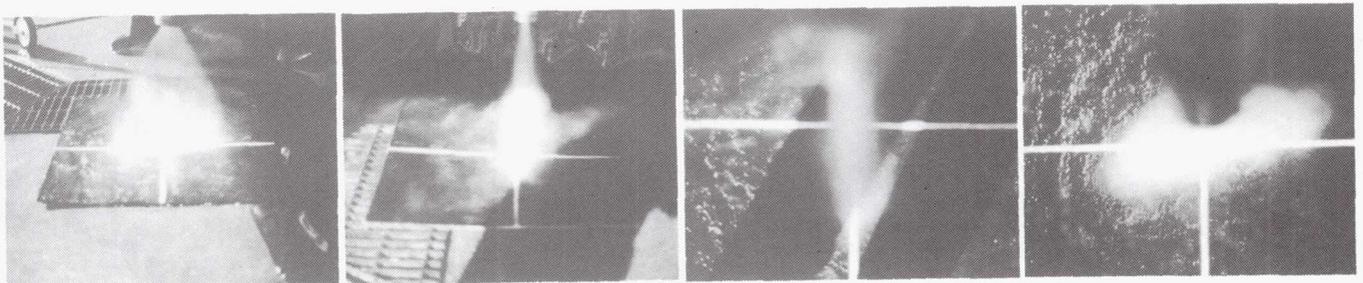
Baffle Element – Mod I
Momentum Ratio = 3.59
Wox = 0.6261
Wf = 0.0280

APPENDIX C

COMPUTER MODELS USED IN DATA REDUCTION FOR MILKMAID TEST
RESULTS

```
      PROGRAM SUGAR
C
C ******************
C CONVERTS LIQUID HEIGHTS IN CM TO CC FOR NEW ATC MILKMAID
C ******************
C
C     PROGRAM TO CONVERT MILK MAID VOLUME/ REFRACTIVE INDEX
(SUGAR
C     WEIGHT PERCENT) DATA INTO FUEL/OX MASS FLOW FOR USE BY
FD0073 AND LICOR
C
C     INPUT UNITS:
C
C       NAMELIST $PARAM:
C
C         TCOL:  COLLECTION TIME, SEC.
C       RINDX0:  UNDILUTED SUCROSE SOLUTION REFRACTIVE INDEX
C        CONC0:  UNDILUTED SUCROSE SOLUTION WEIGHT PERCENT
C         NROW:  NUMBER OF ROWS IN GRID
C         NCOL:  NUMBER OF COLUMNS IN GRID
C         ACEL:  CROSS-SECTIONAL AREA OF COLLECTOR CELL,
SQ.IN.
C        IFLAG:  INPUT FLAG; =0 FOR REFRACTIVE INDEX
(DEFAULT)
C                            =1 FOR WEIGHT PERCENT
C         ISUC:  SUCROSE CIRCUIT; =0 FOR OXIDIZER (DEFAULT)
C                            =1 FOR FUEL
C
C         REPEATED CELL DATA (FREE FORMAT):
C
C            I:  DATA ROW INDEX
C            J:  DATA COLUMN INDEX
C          VOL:  COLLECTED VOLUME (ACTUALLY MEASURED
HEIGHT), CM.
C       RINDEX:  REFRACTIVE INDEX
C          OR
C        CONCI:  SUCROSE WEIGHT PERCENT
C
C
      PARAMETER (NCONC=69, NROWM=50, NCOLM=50)
      CHARACTER INFILE*80, OUTFILE*80, TITLE*80
      DIMENSION CONC(NCONC), RI(NCONC), DENS(NCONC),
WO(NROWM,NCOLM),
     *           WF(NROWM,NCOLM)
      DATA WO, WF, DENSW, RINDX0, CONC0, IFLAG, ISUC
     *     /5000*0.0, 1.0, 2*0.0, 2*0/
      NAMELIST /PARAM/ TCOL, RINDX0, CONC0, ACEL, NROW,
NCOL, IFLAG,
     *                 ISUC
C
C     REFRACTIVE INDEX
C
      DATA RI /1.3344, 1.3351, 1.3359, 1.3367, 1.3374,
1.3381, 1.3388,
```

```
      *              1.3395, 1.3403, 1.3411, 1.3418, 1.3425,
   1.3433, 1.3411,                  .
      *              1.3448, 1.3456, 1.3464, 1.3471, 1.3479,
   1.3487, 1.3494,
      *              1.3502, 1.3510, 1.3518, 1.3526, 1.3533,
   1.3541, 1.3549,
      *              1.3557, 1.3565, 1.3573, 1.3582, 1.3590,
   1.3598, 1.3606,
      *              1.3614, 1.3622, 1.3631, 1.3639, 1.3647,
   1.3655, 1.3663,
      *              1.3672, 1.3681, 1.3689, 1.3698, 1.3706,
   1.3715, 1.3723,
      *              1.3731, 1.3740, 1.3749, 1.3758, 1.3767,
   1.3775, 1.3784,
      *              1.3793, 1.3802, 1.3811, 1.3820, 1.3829,
   1.3838, 1.3847,
      *              1.3856, 1.3865, 1.3874, 1.3883, 1.3893,
   1.3902/
   C
   C     SUCROSE WEIGHT % DATA (GM SUGAR/100 GM SOLUTION)
   C     (1-35 WEIGHT % AT 25 DEGREES C)
   C     REF: CRC HANDBOOK OF CHEMISTRY AND PHYSICS 59TH ED.
   PAGE E-358
   C
         DATA CONC /1.334, 1.836, 2.338, 2.840, 3.342, 3.844,
   4.346,
      *              4.848, 5.350, 5.851, 6.352, 6.853, 7.354,
   7.855,
      *              8.356, 8.857, 9.358, 9.859, 10.360, 10.861,
   11.362,
      *              11.863, 12.364, 12.865, 13.366, 13.867,
   14.368, 14.869,
      *              15.370, 15.871, 16.372, 16.873, 17.374,
   17.875, 18.376,
      *              18.877, 19.378, 19.879, 20.380, 20.880,
   21.380, 21.880,
      *              22.380, 22.880, 23.380, 23.880, 24.380,
   24.880, 25.380,
      *              25.881, 26.382, 26.883, 27.384, 27.885,
   28.386, 28.887,
      *              29.388, 29.889, 30.390, 30.891, 31.392,
   31.893, 32.394,
      *              32.895, 33.396, 33.897, 34.398, 34.899,
   35.400/
   C
   C     SUCROSE SOLUTION DENSITY DATA (GM/ML SOLUTION)
   C     (1-35 WEIGHT % AT 20 DEGREES C)
   C     REF: CRC HANDBOOK OF CHEMISTRY AND PHYSICS 59TH ED.
   PAGE D-308
   C
         DATA DENS /1.0021, 1.0040, 1.0060, 1.0079, 1.0099,
   1.0119, 1.0139,
      *              1.0158, 1.0178, 1.0198, 1.0218, 1.0238,
   1.0259, 1.0279,
```

```
      *                 1.0299, 1.0320, 1.0340, 1.0361, 1.0381,
     1.0402, 1.0423,
      *                 1.0444, 1.0465, 1.0486, 1.0507, 1.0528,
     1.0549, 1.0571,
      *                 1.0592, 1.0614, 1.0635, 1.0657, 1.0678,
     1.0700, 1.0722,
      *                 1.0744, 1.0766, 1.0788, 1.0810, 1.0833,
     1.0855, 1.0877,
      *                 1.0899, 1.0922, 1.0945, 1.0972, 1.0990,
     1.1013, 1.1036,
      *                 1.1059, 1.1082, 1.1105, 1.1129, 1.1152,
     1.1175, 1.1199,
      *                 1.1223, 1.1247, 1.1270, 1.1294, 1.1318,
     1.1342, 1.1366,
      *                 1.1391, 1.1415, 1.1440, 1.1464, 1.1489,
     1.1513/
C
C     FORMAT STATEMENTS
C
   10 FORMAT(1X,'INPUT FILE NAME ?')
   11 FORMAT(A)
   12 FORMAT(1X,'OUTPUT FILE NAME ?')
   13 FORMAT(/1X,A,//10X,'COLLECTION TIME=',F7.3,' SEC.',5X,
      *         'OXIDIZER SUGAR WEIGHT PERCENT=',F7.3,'%',/10X,
      *         'GRID CONTAINS ',I2,' ROWS AND ',I2,' COLUMNS')
   15 FORMAT(10X,'OXIDIZER DENSITY=',F7.4,' GM/ML',//)
   20 FORMAT(/1X,'*** WARNING ***',/1X,'OXIDIZER SUGAR
     WEIGHT PERCENT ',
      *       'IS GREATER THAN LARGEST VALUE IN TABLE,'
      *       /1X,'LARGEST WEIGHT PERCENT IS ',F7.3,' AND
     VALUES WILL ',
      *       'BE LINEARLY EXTRAPOLATED.')
   30 FORMAT(/1X,'REFRACTIVE INDEX GREATER THAN LARGEST
     VALUE IN TABLE',
      *       /1X,' VALUE LINEARLY EXTRAPOLATED.')
   31 FORMAT(/1X,'WEIGHT PERCENT GREATER THAN LARGEST VALUE
     IN TABLE',
      *       /1X,' VALUE LINEARLY EXTRAPOLATED.')
   40 FORMAT(//5X,'ROW=',I2,5X,'COLUMN=',I2,/5X,'REFRACTIVE
     INDEX=',
      *         F7.4,5X,'WEIGHT PERCENT
     SUGAR=',F7.4,/5X,'VOLUME % OX=',
      *         F7.2,5X,'VOLUME % FUEL=',F7.2,/5X,'OX MASS
     FLUX, LBm/S=',
      *         1PE10.3,5X,'FUEL MASS FLUX, LBm/S=',E10.3)
   41 FORMAT(//5X,'ROW=',I2,5X,'COLUMN=',I2,/5X,
      *         'WEIGHT PERCENT SUGAR=',F7.4,/5X,'VOLUME %
     OX=',
      *         F7.2,5X,'VOLUME % FUEL=',F7.2,/5X,'OX MASS
     FLUX, LBm/S=',
      *         1PE10.3,5X,'FUEL MASS FLUX, LBm/S=',E10.3)
   50 FORMAT(//10X,'FD0073/LICOR FLOWRATE INPUT DATA',//)
C
C     READ INPUT AND OUTPUT FILE NAMES
```

```fortran
                  WRITE(8,30)
                  N=NCONC-1
   250            CONTINUE
                  CONCI=CONC(N) + (CONC(N+1)-CONC(N))*(RINDEX-
RI(N))/
       *                (RI(N+1)-RI(N))
                  GOTO 400
              ELSE
                  CONCI=RINDEX
                  DO 300 N=1,(NCONC-1)
                     IF (CONCI .LE. CONC(N)) GOTO 350
   300            CONTINUE
                  WRITE(8,31)
                  N=NCONC-1
   350            CONTINUE
              END IF
   400        DENSI=DENS(N) + (DENS(N+1)-DENS(N))*(CONCI-
CONC(N))/
       *                (CONC(N+1)-CONC(N))
C
C      15.518 CONVERTS HEIGHT INTO VOLUME (CC'S) FOR ATC
MILKMAID
C
          VOL=VOL*15.518
          VO=(CONCI*DENSI)/(CONC0*DENS0)*VOL
          VF=VOL-VO
C
C      CALCULATE VOLUME PERCENTS
C
          PO=100.0*VO/VOL
          PF=100.0-PO
C
C      CALCULATE MASS FLUX IN LBm/SEC
C
          WO(I,J)=0.0022046226*DENS0*VO/TCOL
          WF(I,J)=0.0022046226*DENSW*VF/TCOL
          IF (ISUC .EQ. 1) THEN
              WFT=WO(I,J)
              PFT=PO
              WO(I,J)=WF(I,J)
              PO=PF
              WF(I,J)=WFT
              PF=PFT
          END IF
C
C      PRINT OUT DATA
C
          IF (IFLAG .EQ. 0) THEN
              WRITE(8,40) I, J, RINDEX, CONCI, PO, PF,
WO(I,J), WF(I,J)
              GOTO 500
          ELSE
              WRITE(8,41) I, J, CONCI, PO, PF, WO(I,J),
WF(I,J)
```

```
C
      WRITE(6,10)
      READ(5,11) INFILE
      OPEN(UNIT=7, FILE=INFILE, STATUS='OLD', ERR=9000)
      WRITE(6,12)
      READ(5,11) OUTFILE
      OPEN(UNIT=8,FILE=OUTFILE,STATUS='NEW')
C
C     READ TITLE AND NAMELIST $PARAM
C
      READ(7,11) TITLE
      READ(7,PARAM,ERR=9100)
C
C     CHECK DATA LIMITS
C
      IF (NROW .GT. NROWM) GOTO 9200
      IF (NCOL .GT. NCOLM) GOTO 9300
      IF (TCOL .LE. 0.0) GOTO 9400
C
C     CALCULATE OXIDIZER WEIGHT PERCENT AND DENSITY
C
      IF (RINDX0 .LE. 0.0 .AND. CONC0 .GT. 0.0) GOTO 175
      IF (RINDX0 .LE. 0.0) GOTO 9500
      DO 100 N=1,(NCONC-1)
         IF (RINDX0 .LE. RI(N)) GOTO 150
  100 CONTINUE
      WRITE(8,30)
      N=NCONC-1
  150 CONTINUE
      CONC0=CONC(N) + (CONC(N+1)-CONC(N))*(RINDX0-RI(N))/
     *       (RI(N+1)-RI(N))
      IF (CONC0 .GT. CONC(NCONC)) WRITE(8,20) CONC(NCONC)
      GOTO 190
  175 CONTINUE
      IF (CONC0 .GT. CONC(NCONC)) WRITE(8,20) CONC(NCONC)
      DO 185 N=1,(NCONC-1)
         IF (CONC0 .LE. CONC(N)) GOTO 190
  185 CONTINUE
      N=NCONC-1
  190 CONTINUE
      DENS0=DENS(N) + (DENS(N+1)-DENS(N))*(CONC0-CONC(N))/
     *       (CONC(N+1)-CONC(N))
      WRITE(8,13) TITLE, TCOL, CONC0, NROW, NCOL
      WRITE(8,15) DENS0
C
C     READ IN DATA POINTS AND CONVERT
C
      MAXIT=NROWM*NCOLM
      DO 500 ICOUNT=1,MAXIT
         READ(7,*,END=510,ERR=9600) I, J, VOL, RINDEX
         IF (IFLAG .EQ. 0) THEN
            DO 200 N=1,(NCONC-1)
               IF (RINDEX .LE. RI(N)) GOTO 250
  200       CONTINUE
```

```
            END IF
   500 CONTINUE
C
C     OUTPUT DATA IN FD0073 AND LICOR FORMAT
C
   510 CONTINUE
       WRITE(8,50)
       DO 600 I=1,NROW
          DO 600 J=1,NCOL
             WRITE(8,*) WO(I,J), WF(I,J)
   600 CONTINUE
C
C     STOP PROGRAM
C
  1000 CLOSE(7)
       CLOSE(8)
       STOP
C
C     ERROR CONTIDIONS
C
  9000 WRITE(6,*) 'INPUT FILE NOT FOUND, RUN ABORTED'
       STOP
  9100 WRITE(8,*) 'ERROR READING NAMELIST $PARAM, RUN
STOPPED'
       GOTO 1000
  9200 WRITE(8,*) 'NROW LARGER THAN PROGRAM LIMIT OF ',NROWM,
      *           ' RUN STOPPED'
       GOTO 1000
  9300 WRITE(8,*) 'NCOL LARGER THAN PROGRAM LIMIT OF ',NCOLM,
      *           ' RUN STOPPED'
       GOTO 1000
  9400 WRITE(8,*) 'COLLECTION TIME, TCOL, .LE. 0, RUN
STOPPED'
       GOTO 1000
  9500 WRITE(8,*) 'INITIAL OXIDIZER WEIGHT PERCENT, CONC0,
AND INITIAL ',
      *           'REFRACTIVE INDEX, RINDX0 .LE. 0; RUN
STOPPED'
       GOTO 1000
  9600 WRITE(8,*) 'ROW/COLUMN DATA READ ERROR, RUN STOPPED'
       GOTO 1000
       END
```

```
C       PROGRAM  PC73
C
C       PC VERSION OF FD0073; CONTOURING DONE WITH GOLDEN GRAPHICS SURFER
C
C       WRITTEN BY: J. MUSS                          DATE: 7/7/87
C
C       ********************************************************************
C       ******* Program to analyze injector flow collector data **********
C       ********************************************************************
C
C
C       D. FEFERMAN 4/87 -CONVERT TO VAX FROM UNIVAC
C       J. MUSS 5/6/87 - MODIFIED PROGRAM CONTROL, INPUT AND OUTPUT
C
C       OUTPUT DATA
C
C                       Oxidizer mass flow distribution
C                       Fuel mass distribution
C                       Total mass distribution
C                       Mixture ratio distribution
C                       Combustion gas temperature distribution
C                       Mixture ratio maldistribution ISP loss
C                       Theoretical ISP performance
C                       Theoretical CSTAR performance
C                       Injector mixing efficiency
C
C       INPUT FORMAT
C
C       Test series identification and date  (A80)
C       Injector identification  (A80)
C       Propellant combination name for performance data   (A80)
C
C
C       NAMELIST $DATAIN
C
C       XCOL      = Collector head size, (in.)
C       III       = Number of X-direction collection tubes, maximum = 28
C       JJJ       = Number of Y-direction collection tubes, maximum = 28
C       WOT       = Oxidizer simulant flowrate, (lbm/sec)
C       WFT       = Fuel simulant flowrate, (lbm/sec)
C       RHOO      = Oxidizer simulant density, (lbm/cu.ft.)
C       RHOF      = Fuel simulant density, (lbm/cu.ft.)
C       AOT       = Total EFFECTIVE oxidizer orifice area (INCLUDE CD), (sq.in.)
C       AFT       = Total EFFECTIVE fuel orifice area (INCLUDE CD), (sq.in.)
C       ITOTAL    = Normalize collected flows by total flows;
C                     0=NO (default)/ 1=YES
C       IFLAG     = MRD loss is calculated; 0=NO (default)/ 1=YES
C       CFLAG     = CSTAR loss is calculated; 0=NO (default)/ 1=YES
C       TFLAG     = Temperature distribution is calculated; 0=NO (default)/ 1=YES
C       EFLAG     = Injector mixing is calculated; 0=NO (default)/ 1=YES
C       ITAB      = No. of MRI, ISPI, CSTARI, and TCI values input (MAX=50)
C       MRI(1)    = Mixture ratios at which theoretical performance and
C                     temperature data are evaluated, ITAB inputs required
C       ISPI(1)   = Theoretical specific impulse at the corresponding
C                     MRI values, ITAB inputs required, (lbf/lbm/sec)
C       CSTARI(1) = Theoretical CSTAR at corresponding MRI values,
C                     ITAB inputs required, (ft/sec)
C       TCI(1)    = Theoretical combustion temperature at corresponding
C                     MRI values, ITAB inputs required, (R)
C
C       Collected TOTAL MASS data, III*JJJ ENTRIES REQUIRED. INPUT IS READ
```

```fortran
C                       ROW-WISE,FROM COLUMN 1-JJJ AS:
C
C
C                       DO 100 I=1,III
C                       DO 100 J=1,JJJ
C                          READ(7,*) WO(I,J), WF(I,J)
C                    100 CONTINUE
C
C
C     WO(I,J)  = Collected oxidizer simulant mass flow, (lbm/s)
C     WF(I,J)  = Collected fuel simulant mass flow, (lbm/s)
C
C     ****************************************************************
C
      PARAMETER (NAR=50, NTA=50)
C
      IMPLICIT REAL*4 (A-H,O-Z)
      INTEGER ITOTAL, CFLAG, IFLAG, EFLAG, TFLAG
      CHARACTER TITLE1*80, TITLE2*80, TITLE3*80
      REAL ISPM,ISPT,ISPI,MR,MRI,MRO,MRMDL
      COMMON /INPUT/ II,III,JJ,JJJ,XCOL,
     *               WOT,WFT,WOTT,WFTT,RHOO,RHOF,AOT,AFT,VO,VF,WV,RN,
     *               WO(NAR,NAR),WF(NAR,NAR),MR(NAR,NAR),TCL(NAR,NAR),
     *               MRO,EC,CMRO,EFC,EOC,EM,
     *               CSTARM,CSTARL,CSTART,ISPM,ISPT,MRMDL
      COMMON /TABLES/ CSTARI(NTA),MRI(NTA),ISPI(NTA),TCI(NTA)
      COMMON /FLAGS/ ITOTAL, CFLAG, IFLAG, EFLAG, TFLAG
      COMMON /TWO/ ITAB
C
      DATA II, JJ / 2*1/
      DATA  ITAB, ISKIP, IFLAG, CFLAG, EFLAG, TFLAG, ITOTAL / 7*0 /
C
      NAMELIST /DATAIN/ XCOL, III, JJJ, WOT, WFT, RHOO, RHOF, AOT, AFT,
     * ITOTAL, CFLAG, IFLAG, EFLAG, TFLAG, ITAB, CSTARI, MRI, ISPI, TCI
C
   10 FORMAT(A)
   11 FORMAT(1X,A4,/1X,2I4,/1X,1PE10.3,2X,E10.3,/1X,E10.3,2X,E10.3,
     *       /1X,E10.3,2X,E10.3)
C
C     READ INPUT DATA
C
      READ(7,10) TITLE1
      READ(7,10) TITLE2
      READ(7,10) TITLE3
      READ(7,DATAIN,ERR=9100)
      DO 100 I=1,III
         DO 100 J=1,JJJ
            READ(7,*,ERR=9200) WO(I,J), WF(I,J)
  100 CONTINUE
C
C     BEGIN CALCULATIONS
C
      CALL MASS
      IF (CFLAG .EQ. 1) CALL STAR
      IF (IFLAG .EQ. 1) CALL MRL
      IF (TFLAG .EQ. 1) CALL TEMP
      IF (EFLAG .EQ. 1) CALL EMIX
      CALL PRINT
C
C     BEGIN CONTOUR PLOTTING OUTPUT
C
      ZERO=0.0
```

```fortran
      YCOL=XCOL
      WRITE(6,*) 'GRID AXES IN 1) INCHES OR 2) CELLS (1/2)?'
      READ(5,*) IGRDA
      IF (IGRDA .EQ. 2) XCOL=FLOAT(JJJ)
      IF (IGRDA .EQ. 2) YCOL=FLOAT(III)
C
C     FUEL MASS FLOW CONTOURS
C
      ZMAX=0.0
      ZMIN=1.0E6
      DO 200 I=II,III
         DO 200 J=JJ,JJJ
            ZMAX=MAX(ZMAX,WF(I,J))
            ZMIN=MIN(ZMIN,WF(I,J))
  200 CONTINUE
      WRITE(9,11) 'DSAA',JJJ,III,ZERO,XCOL,ZERO,YCOL,ZMIN,ZMAX
      DO 250 I=II,III
         WRITE(9,*) (WF(I,J),J=JJ,JJJ)
         WRITE(9,*)
  250 CONTINUE
C
C     OXIDIZER MASS FLOW
C
      ZMAX=0.0
      ZMIN=1.0E6
      DO 300 I=II,III
         DO 300 J=JJ,JJJ
            ZMAX=MAX(ZMAX,WO(I,J))
            ZMIN=MIN(ZMIN,WO(I,J))
  300 CONTINUE
      WRITE(10,11) 'DSAA',JJJ,III,ZERO,XCOL,ZERO,YCOL,ZMIN,ZMAX
      DO 350 I=II,III
         WRITE(10,*) (WO(I,J),J=JJ,JJJ)
         WRITE(10,*)
  350 CONTINUE
C
C     TOTAL MASS FLOW
C
      ZMAX=0.0
      ZMIN=1.0E6
      DO 400 I=II,III
         DO 400 J=JJ,JJJ
            ZMAX=MAX(ZMAX,(WF(I,J)+WO(I,J)))
            ZMIN=MIN(ZMIN,(WF(I,J)+WO(I,J)))
  400 CONTINUE
      WRITE(11,11) 'DSAA',JJJ,III,ZERO,XCOL,ZERO,YCOL,ZMIN,ZMAX
      DO 450 I=II,III
         WRITE(11,*) ((WF(I,J)+WO(I,J)),J=JJ,JJJ)
         WRITE(11,*)
  450 CONTINUE
C
C     MIXTURE RATIO CONTOURS
C
      ZMAX=0.0
      ZMIN=1.0E6
      DO 500 I=II,III
         DO 500 J=JJ,JJJ
            ZMAX=MAX(ZMAX,MR(I,J))
            ZMIN=MIN(ZMIN,MR(I,J))
  500 CONTINUE
```

```
            WRITE(12,11) 'DSAA',JJJ,III,ZERO,XCOL,ZERO,YCOL,ZMIN,ZMAX
            DO 550 I=II,III
               WRITE(12,*) (MR(I,J),J=JJ,JJJ)
               WRITE(12,*)
       550 CONTINUE
C
C        LOCAL TEMPERATURE PROFILE
C
         IF (TFLAG .NE. 1) GOTO 1000
         ZMAX=0.0
         ZMIN=1.0E6
         DO 600 I=II,III
            DO 600 J=JJ,JJJ
               ZMAX=MAX(ZMAX,TCL(I,J))
               ZMIN=MIN(ZMIN,TCL(I,J))
       600 CONTINUE
         WRITE(13,11) 'DSAA',JJJ,III,ZERO,XCOL,ZERO,YCOL,ZMIN,ZMAX
         DO 650 I=II,III
            WRITE(13,*) (TCL(I,J),J=JJ,JJJ)
            WRITE(13,*)
       650 CONTINUE
C
C        END OF PROGRAM
C
  1000 STOP
C
C        ERROR MESSAGES
C
  9100 WRITE(6,*) 'ERROR IN NAMELIST $DATAIN, RUN STOPPED'
       WRITE(8,*) 'ERROR IN NAMELIST $DATAIN, RUN STOPPED'
       STOP
  9200 WRITE(6,*) 'ERROR READING FLOWS FOR CELL (',I,',',J,'), ',
      *             ' RUN STOPPED'
       WRITE(8,*) 'ERROR READING FLOW FOR CELL (',I,',',J,'), ',
      *             ' RUN STOPPED'
       STOP
       END
C
       SUBROUTINE MASS
C
C        MODIFIED BY J. MUSS 5/6/87
C
       PARAMETER (NAR=50, NTA=50)
C
       IMPLICIT REAL*4 (A-H,O-Z)
       INTEGER ITOTAL, CFLAG, IFLAG, EFLAG, TFLAG
       REAL ISPM,ISPT,ISPI,MR,MRI,MRO,MRMDL
       COMMON /INPUT/ II,III,JJ,JJJ,XCOL,
      *                WOT,WFT,WOTT,WFTT,RHOO,RHOF,AOT,AFT,VO,VF,WV,RN,
      *                WO(NAR,NAR),WF(NAR,NAR),MR(NAR,NAR),TCL(NAR,NAR),
      *                MRO,EC,CMRO,EFC,EOC,EM,
      *                CSTARM,CSTARL,CSTART,ISPM,ISPT,MRMDL
       COMMON /TABLES/ CSTARI(NTA),MRI(NTA),ISPI(NTA),TCI(NTA)
C
C        CALCULATE TOTAL OXIDIZER AND FUEL FLOW
C
       WOTT=0.0
       DO 100 I=II,III
        DO 100 J=JJ,JJJ
           WOTT=WOTT+WO(I,J)
```

```
               WFTT=WFTT+WF(I,J)
   100 CONTINUE
C
C       CALCULATE COLLECTED MR AND COLLECTION EFFICIENCY
C
        CMRO=WOTT/WFTT
        EFC=100.0*WFTT/WFT
        EOC=100.0*WOTT/WOT
        EC=100.*(WOTT+WFTT)/(WOT+WFT)
C
C       NORMALIZE COLLECTED BY NOMINAL FLOWRATE,
C
        IF (ITOTAL .NE. 1) GOTO 190
        FF=WFT/WFTT
        XF=WOT/WOTT
        WOTT=WOT
        WFTT=WFT
        DO 150 I=II,III
           DO 150 J=JJ,JJJ
              WO(I,J)=XF*WO(I,J)
              WF(I,J)=FF*WF(I,J)
   150 CONTINUE
C
C       CALCULATE LOCAL MIXTURE RATIO
C
   190 CONTINUE
        DO 200 I=II,III
           DO 200 J=JJ,JJJ
              MR(I,J)=99.99
              IF ((WO(I,J)+WF(I,J)) .LE. 0.0) MR(I,J)=0.0
              IF (WF(I,J) .LE. 0.0) GOTO 200
              MR(I,J)=WO(I,J)/WF(I,J)
   200 CONTINUE
C
C       CALCULATE OVERALL MIXTURE RATIO
C
        MRO=WOTT/WFTT
C
C       CALCULATE OXIDIZER AND FUEL VELOCITY
C
        VO=WOTT*144./RHOO/AOT
        VF=WFTT*144./RHOF/AFT
C
C       CALCULATE MOMENTUM RATIO
C
        WV=WOTT*VO/WFTT/VF
C
C       CALCULATE RUPE NUMBER
C
        RN=1.0/(1.0+(RHOO/RHOF*(VO/VF)**2.*SQRT(AOT/AFT)))
        RETURN
        END
C
        SUBROUTINE STAR
        PARAMETER (NAR=50, NTA=50)
C
        IMPLICIT REAL*4 (A-H,O-Z)
        INTEGER ITOTAL, CFLAG, IFLAG, EFLAG, TFLAG
        REAL ISPM,ISPT,ISPI,MR,MRI,MRO,MRMDL
        COMMON /INPUT/ II,III,JJ,JJJ,XCOL,
```

```
     *                    WOT,WFT,WOTT,WFTT,RHOO,RHOF,AOT,AFT,VO,VF,WV,RN,
     *                    WO(NAR,NAR),WF(NAR,NAR),MR(NAR,NAR),TCL(NAR,NAR),
     *                    MRO,EC,CMRO,EFC,EOC,EM,
     *                    CSTARM,CSTARL,CSTART,ISPM,ISPT,MRMDL
       COMMON /TABLES/ CSTARI(NTA),MRI(NTA),ISPI(NTA),TCI(NTA)
       COMMON /TWO/ ITAB
C
C      CALCULATE MASS AVERAGE CSTAR
C
       WDOT=WOTT+WFTT
       CSTARM=0.0
       DO 100 I=II,III
          DO 100 J=JJ,JJJ
          CSTAR = AINTP(MR(I,J),MRI,CSTARI,ITAB)
          IF (CSTAR .LT. 0.0) CSTAR=0.0
          CSTARM = CSTARM+CSTAR*(WF(I,J)+WO(I,J))/WDOT
   100 CONTINUE
C
C      CALCULATE OVERALL THEORETICAL CSTAR
C
       CSTART = AINTP(MRO,MRI,CSTARI,ITAB)
C
C      CALCULATE CSTAR LOSS
C
       CSTARL = (1.0-CSTARM/CSTART)*100.
       RETURN
       END
C
       SUBROUTINE MRL
       PARAMETER (NAR=50, NTA=50)
C
       IMPLICIT REAL*4 (A-H,O-Z)
       INTEGER ITOTAL, CFLAG, IFLAG, EFLAG, TFLAG
       REAL ISPM,ISPT,ISPI,MR,MRI,MRO,MRMDL
       COMMON /INPUT/ II,III,JJ,JJJ,XCOL,
     *                    WOT,WFT,WOTT,WFTT,RHOO,RHOF,AOT,AFT,VO,VF,WV,RN,
     *                    WO(NAR,NAR),WF(NAR,NAR),MR(NAR,NAR),TCL(NAR,NAR),
     *                    MRO,EC,CMRO,EFC,EOC,EM,
     *                    CSTARM,CSTARL,CSTART,ISPM,ISPT,MRMDL
       COMMON /TABLES/ CSTARI(NTA),MRI(NTA),ISPI(NTA),TCI(NTA)
       COMMON /TWO/ ITAB
C
C      CALCULATE MASS AVERAGED ISP
C
       WDOT=WFTT+WOTT
       ISPM=0.0
       DO 100 J=JJ,JJJ
          DO 100 I=II,III
             ISP= AINTP(MR(I,J),MRI,ISPI,ITAB)
             IF (ISP .LT. 0.0) ISP=0.0
             ISPM=ISPM+ISP*(WF(I,J)+WO(I,J))/WDOT
   100 CONTINUE
C
C      CALCULATE OVERALL THEORETICAL ISP
C
       ISPT = AINTP(MRO,MRI,ISPI,ITAB)
C
C      CALCULATE MR MALDISTRIBUTION LOSS
C
       MRMDL = (1.0-ISPM/ISPT)*100.
```

```
      RETURN
      END
C
      SUBROUTINE TEMP
      PARAMETER (NAR=50, NTA=50)
C
      IMPLICIT REAL*4 (A-H,O-Z)
      INTEGER ITOTAL, CFLAG, IFLAG, EFLAG, TFLAG
      REAL ISPM,ISPT,ISPI,MR,MRI,MRO,MRMDL
      COMMON /INPUT/ II,III,JJ,JJJ,XCOL,
     *               WOT,WFT,WOTT,WFTT,RHOO,RHOF,AOT,AFT,VO,VF,WV,RN,
     *               WO(NAR,NAR),WF(NAR,NAR),MR(NAR,NAR),TCL(NAR,NAR),
     *               MRO,EC,CMRO,EFC,EOC,EM,
     *               CSTARM,CSTARL,CSTART,ISPM,ISPT,MRMDL
      COMMON /TABLES/ CSTARI(NTA),MRI(NTA),ISPI(NTA),TCI(NTA)
      COMMON /TWO/ ITAB
C
C     CALCULATE LOCAL TEMPERATURE
C
      DO 10 I=II,III
         DO 10 J=JJ,JJJ
            TCL(I,J)= AINTP (MR(I,J),MRI,TCI,ITAB)
            IF (TCL(I,J) .LT. 0.0) TCL(I,J)=0.0
   10 CONTINUE
      RETURN
      END
C
      SUBROUTINE EMIX
      PARAMETER (NAR=50, NTA=50)
C
      IMPLICIT REAL*4 (A-H,O-Z)
      INTEGER ITOTAL, CFLAG, IFLAG, EFLAG, TFLAG
      REAL ISPM,ISPT,ISPI,MR,MRI,MRO,MRMDL
      COMMON /INPUT/ II,III,JJ,JJJ,XCOL,
     *               WOT,WFT,WOTT,WFTT,RHOO,RHOF,AOT,AFT,VO,VF,WV,RN,
     *               WO(NAR,NAR),WF(NAR,NAR),MR(NAR,NAR),TCL(NAR,NAR),
     *               MRO,EC,CMRO,EFC,EOC,EM,
     *               CSTARM,CSTARL,CSTART,ISPM,ISPT,MRMDL
      COMMON /TABLES/ CSTARI(NTA),MRI(NTA),ISPI(NTA),TCI(NTA)
C
C     CALCULATE OVERALL OXIDIZER MASS FRACTION
C
      WT=WOTT+WFTT
      RO=WOTT/WT
C
C     CALCULATE OXIDIZER MASS FRACTION AND MASS FRACTION FUNCTIONS
C
      SUMX=0.0
      SUMY=0.0
      DO 100 I=II,III
         DO 100 J=JJ,JJJ
         IF ((WO(I,J)+WF(I,J)) .LE. 0.0) GOTO 100
         WTL=WO(I,J)+WF(I,J)
         RL=WO(I,J)/WTL
         IF (RL .GT. RO) GO TO 50
         X=WTL/WT*(RO-RL)/RO
         SUMX=SUMX+X
         GO TO 100
   50    CONTINUE
         Y=WTL/WT*(RO-RL)/(RO-1.0)
```

```fortran
         SUMY=SUMY+Y
  100 CONTINUE
C
C     CALCULATE MIXING EFFICIENCY
C
      EM=100.*(1.0-(SUMX+SUMY))
      RETURN
      END
C
      SUBROUTINE PRINT
      PARAMETER (NAR=50, NTA=50)
C
      IMPLICIT REAL*4 (A-H,O-Z)
      INTEGER ITOTAL, CFLAG, IFLAG, EFLAG, TFLAG
      REAL ISPM,ISPT,ISPI,MR,MRI,MRO,MRMDL
      COMMON /INPUT/ II,III,JJ,JJJ,XCOL,
     *                WOT,WFT,WOTT,WFTT,RHOO,RHOF,AOT,AFT,VO,VF,WV,RN,
     *                WO(NAR,NAR),WF(NAR,NAR),MR(NAR,NAR),TCL(NAR,NAR),
     *                MRO,EC,CMRO,EFC,EOC,EM,
     *                CSTARM,CSTARL,CSTART,ISPM,ISPT,MRMDL
      COMMON /TABLES/ CSTARI(NTA),MRI(NTA),ISPI(NTA),TCI(NTA)
      COMMON /FLAGS/ ITOTAL, CFLAG, IFLAG, EFLAG, TFLAG
C
   10 FORMAT(1H1, T50,'AEROJET  LIQUID  ROCKET  COMPANY' / T55,'SACRAMEN
     1TO,  CALIFORNIA' //// T24,'ADVANCED  INJECTOR  DISTRIBUTION  (AID)
     2  DATA  ANALYSIS  COMPUTER  PROGRAM  (FD0073)' //// T46,
     3 '*********  TEST  SUMMARY  **********' ///)
   11 FORMAT(21X,A,/21X,A,/21X,A,///)
   12 FORMAT(40X,'COLLECTOR SIZE ................... ',F8.2,' INCHES',
     *        /40X,'TOTAL OXIDIZER FLOWRATE .......... ',F8.3,' LB/SEC',
     *        /40X,'TOTAL FUEL FLOWRATE .............. ',F8.3,' LB/SEC',
     *        /40X,'INJECTED MIXTURE RATIO ........... ',F8.2,
     *        /40X,'EFFECTIVE OXIDIZER ORIFICE AREA .. ',F8.4,
     *        ' SQ. INCHES',
     *        /40X,'EFFECTIVE FUEL ORIFICE AREA ...... ',F8.4,
     *        ' SQ. INCHES',
     *        /40X,'OXIDIZER VELOCITY ................ ',F8.2,' FT/SEC',
     *        /40X,'FUEL VELOCITY .................... ',F8.2,' FT/SEC',
     *        /40X,'MOMENTUM RATIO ................... ',F8.4,
     *        /40X,'RUPE NUMBER ..................... ',F8.3,
     *        /40X,'OXIDIZER COLLECTION EFFICIENCY ... ',F8.2,' PERCENT',
     *        /40X,'FUEL COLLECTION EFFICIENCY ....... ',F8.2,' PERCENT',
     *        /40X,'OVERALL COLLECTION EFFICIENCY .... ',F8.2,' PERCENT',
     *        /40X,'COLLECTED MIXTURE RATIO .......... ',F8.2,
     *        /40X,'NORMALIZED MIXTURE RATIO ......... ',F8.2)
   13 FORMAT(40X,'MIXING EFFICIENCY ................ ',F8.2,' PERCENT')
   14 FORMAT(40X,'THEORETICAL CSTAR ................ ',F8.2,' FT/SEC',
     *        /40X,'PREDICTED CSTAR .................. ',F8.2,' FT/SEC',
     *        /40X,'CSTAR LOSS ...................... ',F8.2,' PERCENT')
   15 FORMAT(40X,'THEORETICAL ISP .................. ',F8.2,' SEC',
     *        /40X,'PREDICTED ISP ................... ',F8.2,' SEC',
     *        /40X,'MR MALDISTRIBUTION LOSS .......... ',F8.2,' PERCENT')
   20 FORMAT(1X,'R\C',16(3X,I2,3X),/)
   21 FORMAT(1X,I2,1X,16F8.4/)
   22 FORMAT(1X,I2,1X,16F8.2/)
   23 FORMAT(1H1,30X,'****************** OXIDIZER MASS FLOW ********',
     *                '**************'//)
   24 FORMAT(1H1,30X,'************** OXIDIZER MASS FLOW (CONTINUED) ',
     *                '**************'//)
   25 FORMAT(1X)
```

```fortran
   30 FORMAT(1H1,30X,'******************** FUEL MASS FLOW ********',
     *                '*****************'//)
   31 FORMAT(1H1,30X,'**************** FUEL MASS FLOW (CONTINUED) ',
     *                '*****************'//)
   40 FORMAT(1H1,30X,'******************** TOTAL MASS FLOW ********',
     *                '***************'//)
   41 FORMAT(1H1,30X,'*************** TOTAL MASS FLOW (CONTINUED) ',
     *                '***************'//)
   50 FORMAT(1H1,30X,'******************** MIXTURE RATIO ********',
     *                '***************'//)
   51 FORMAT(1H1,30X,'*************** MIXTURE RATIO (CONTINUED) ',
     *                '***************'//)
   60 FORMAT(1H1,30X,'******************** TEMPERATURE PROFILE *******',
     *                '***************'//)
   61 FORMAT(1H1,30X,'*************** TEMPERATURE PROFILE (CONTINUED) ',
     *                '***************'//)
C
      WRITE(8,10)
      WRITE (8,11) TITLE1, TITLE2, TITLE3
      WRITE(8,12) XCOL, WOT, WFT, (WOT/WFT), AOT, AFT, VO, VF,
     *            WV, RN, EOC, EFC, EC, CMRO, MRO
      IF (EFLAG .EQ. 1) WRITE (8,13) EM
      IF (CFLAG .EQ. 1) WRITE(8,14) CSTART, CSTARM, CSTARL
      IF (IFLAG .EQ. 1) WRITE(8,15) ISPT, ISPM, MRMDL
C
C     OXIDIZER MASS FLOW
C
      WRITE(8,23)
      J1=JJ
      NRP=16
      IF (JJJ .LE. 16) NRP=JJJ
      WRITE(8,20) (I,I=J1,NRP)
      DO 100 I=II,III
         WRITE(8,21) I,(WO(I,J),J=J1,NRP)
         IF ((NRP-J1+1) .LT. 16) WRITE(8,25)
  100 CONTINUE
      DO 125 MN=1,10
         J1=NRP+1
         IF (J1 .GT. JJJ) GOTO 150
         WRITE(8,24)
         NRP=NRP+16
         IF (JJJ .LE. NRP) NRP=JJJ
         WRITE(8,20) (I,I=J1,NRP)
         IF ((NRP-J1+1) .LT. 16) WRITE(8,25)
         DO 125 I=II,III
            WRITE(8,21) I,(WO(I,J),J=J1,NRP)
            IF ((NRP-J1+1) .LT. 16) WRITE(8,25)
  125    CONTINUE
  150 CONTINUE
C
C     FUEL MASS FLOW
C
      WRITE(8,30)
      J1=JJ
      NRP=16
      IF (JJJ .LE. 16) NRP=JJJ
      WRITE(8,20) (I,I=J1,NRP)
      DO 200 I=II,III
         WRITE(8,21) I,(WF(I,J),J=J1,NRP)
         IF ((NRP-J1+1) .LT. 16) WRITE(8,25)
```

```
  200 CONTINUE
      DO 225 MN=1,10
         J1=NRP+1
         IF (J1 .GT. JJJ) GOTO 250
         WRITE(8,31)
         NRP=NRP+16
         IF (JJJ .LE. NRP) NRP=JJJ
         WRITE(8,20) (I,I=J1,NRP)
         IF ((NRP-J1+1) .LT. 16) WRITE(8,25)
         DO 225 I=II,III
            WRITE(8,21) I,(WF(I,J),J=J1,NRP)
            IF ((NRP-J1+1) .LT. 16) WRITE(8,25)
  225    CONTINUE
  250 CONTINUE
C
C     TOTAL MASS FLOW
C
      WRITE(8,40)
      J1=JJ
      NRP=16
      IF (JJJ .LE. 16) NRP=JJJ
      WRITE(8,20) (I,I=J1,NRP)
      DO 300 I=II,III
         WRITE(8,21) I,((WO(I,J)+WF(I,J)),J=J1,NRP)
         IF ((NRP-J1+1) .LT. 16) WRITE(8,25)
  300 CONTINUE
      DO 325 MN=1,10
         J1=NRP+1
         IF (J1 .GT. JJJ) GOTO 350
         WRITE(8,41)
         NRP=NRP+16
         IF (JJJ .LE. NRP) NRP=JJJ
         WRITE(8,20) (I,I=J1,NRP)
         IF ((NRP-J1+1) .LT. 16) WRITE(8,25)
         DO 325 I=II,III
            WRITE(8,21) I,((WO(I,J)+WF(I,J)),J=J1,NRP)
            IF ((NRP-J1+1) .LT. 16) WRITE(8,25)
  325    CONTINUE
  350 CONTINUE
C
C     MIXTURE RATIO
C
      WRITE(8,50)
      J1=JJ
      NRP=16
      IF (JJJ .LE. 16) NRP=JJJ
      WRITE(8,20) (I,I=J1,NRP)
      DO 400 I=II,III
         WRITE(8,22) I,(MR(I,J),J=J1,NRP)
         IF ((NRP-J1+1) .LT. 16) WRITE(8,25)
  400 CONTINUE
      DO 425 MN=1,10
         J1=NRP+1
         IF (J1 .GT. JJJ) GOTO 450
         WRITE(8,51)
         NRP=NRP+16
         IF (JJJ .LE. NRP) NRP=JJJ
         WRITE(8,20) (I,I=J1,NRP)
         IF ((NRP-J1+1) .LT. 16) WRITE(8,25)
         DO 425 I=II,III
```

```
                WRITE(8,22) I,(MR(I,J),J=J1,NRP)
                IF ((NRP-J1+1) .LT. 16) WRITE(8,25)
    425     CONTINUE
    450 CONTINUE
C
C       LOCAL TEMPERATURE
C
        IF (TFLAG .NE. 1) GOTO 550
        WRITE(8,60)
        J1=JJ
        NRP=16
        IF (JJJ .LE. 16) NRP=JJJ
        WRITE(8,20) (I,I=J1,NRP)
        DO 500 I=II,III
            WRITE(8,22) I,(TCL(I,J),J=J1,NRP)
            IF ((NRP-J1+1) .LT. 16) WRITE(8,25)
    500 CONTINUE
        DO 525 MN=1,10
            J1=NRP+1
            IF (J1 .GT. JJJ) GOTO 550
            WRITE(8,51)
            NRP=NRP+16
            IF (JJJ .LE. NRP) NRP=JJJ
            WRITE(8,20) (I,I=J1,NRP)
            IF ((NRP-J1+1) .LT. 16) WRITE(8,25)
            DO 525 I=II,III
                WRITE(8,22) I,(TCL(I,J),J=J1,NRP)
                IF ((NRP-J1+1) .LT. 16) WRITE(8,25)
    525 CONTINUE
    550 CONTINUE
        RETURN
        END
C
        FUNCTION AINTP (X,A,B,N)
C       Interpolation function
C       X= value of independent variable for interpolation
C       A= independent variable
C       B= dependent variable
C       N= no. of a and b pairs
        DIMENSION A(1), B(1), AM(3)
        DO 1 I = 2, N
         IF (A(I)-X) 1,2,3
    1   CONTINUE
    6   I= N-1
        GO TO 8
    3 IF (I-2) 5,5,4
    4 IF (I-N) 11,6,6
    2 AINTP = B(I)
        RETURN
   11 D= A(I)-A(I-1)
        AA= X-A(I-1)
        AB= X-A(I)
        DO 7 J=1, 3
         IIJ= I+ J
    7   AM(J)= (B(IIJ-2)-B(IIJ-3))/(A(IIJ-2)-A(IIJ-3))
        AINTP= (AA*B(I)-AB*B(I-1))/D+((AM(1)-AM(2))*AB+(AM(3)-AM(2))*AA)
     &   *AA*AB/(2.*D*D)
        RETURN
    5 J= I-1
        K= I
```

```
         L= I+1
         GO TO 20
     8 J= I+1
         K= I
         L= I-1
    20 D= A(K) - A(J)
         AA= X- A(J)
         AB= X- A(K)
         DD= (B(L)-B(K))/(A(L)-A(K))-(B(K)-B(J))/(A(K)-A(J))
         AINTP = AA*AB/(2.*D)*DD-(AB*B(J)-AA*B(K))/D
         RETURN
         END
```

Report Documentation Page

1. Report No. NASA CR-4387	2. Government Accession No.	3. Recipient's Catalog No.
4. Title and Subtitle Orbital Transfer Vehicle Engine Technology Baffled Injector Design, Fabrication and Verification		5. Report Date November 1991
		6. Performing Organization Code
7. Author(s) J.A. Schneider		8. Performing Organization Report No. None (E-6413)
		10. Work Unit No. 591-41-11
9. Performing Organization Name and Address GENCORP Aerojet Propulsion Division P.O. Box 13222 Sacramento, California 95813		11. Contract or Grant No. NAS3-23772
12. Sponsoring Agency Name and Address National Aeronautics and Space Administration Lewis Research Center Cleveland, Ohio 44135-3191		13. Type of Report and Period Covered Contractor Report Final
		14. Sponsoring Agency Code

15. Supplementary Notes

Project Managers, Sybil Morren and G. Paul Richter, Space Propulsion Technology Division, NASA Lewis Research Center, (216) 433-6603.

16. Abstract

New technologies for space-based, reusable, throttleable, cryogenic orbit transfer propulsion are being evaluated under NASA Contract NAS3-23772. Supporting tasks for the design of a dual-expander cycle engine thrust chamber design are documented in this report. The purpose of the studies was to research the materials used in the thrust chamber design, the supporting fabrication methods necessary to complete the design, and the modification of the injector element for optimum injector/chamber compatibility.

17. Key Words (Suggested by Author(s)) Dual expander cycle; Cryogenic, ZrCu Diffusion Bond, GlidCop AL-15; Uni-element cold flow test; Gas-Gas injector		18. Distribution Statement Unclassified - Unlimited Subject Category 20	
19. Security Classif. (of the report) Unclassified	20. Security Classif. (of this page) Unclassified	21. No. of pages 236	22. Price* A11